Molecular control of foam properties

Dissertation
zur Erlangung des Grades
„Doktor der Naturwissenschaften“
am Fachbereich 08: Physik, Mathematik und Informatik
der Johannes Gutenberg-Universität in Mainz

Judith Krom, geb. Hege
geboren in Kraichtal

Mainz, den 20.02.2025

1. Gutachter: Prof. Dr. Thomas A. Vilgis
2. Gutachter: Prof. Dr. Thomas Palberg
Tag der Prüfung: 05.05.2025

Judith Krom
Johannes Gutenberg University Mainz
Institute of Physics
Staudingerweg 7
D-55128 Mainz
jhege01@students.uni-mainz.de

Max Planck Institute for Polymer Research

Ackermannweg 10
D-55128 Mainz
kromj@mpip-mainz.mpg.de

Contents

Abstract

Protein-stabilized liquid foams are fascinating multiscale systems: the structural properties of a protein define its interfacial activity and interactions with other molecules. Its assembly at air-water interfaces together with drainage determine lamella stability. Coalescence and coarsening promote bubble growth affecting macroscopic foam stability represented by the foam height decay. This dissertation deepens the understanding of which structural properties of a protein promote increased foam stability. A method for monitoring the temporal evolution of the mean bubble size and circularity with common lab equipment and open-source software was developed. Comparing foams stabilized by hydrophobin and BSA, two proteins with fundamentally different properties, showed that large hydrophobic patches at the protein surface promote a higher foam stability. Adding polysaccharides to BSA-stabilized foams revealed that an increased solution viscosity enhances foam stability, but the stiffness and charge of the polysaccharide need to be considered. Modifying the tertiary structure of BSA by varying the solution pH revealed that uncharged proteins promote a more resilient interfacial arrangement facilitating an increased stability of dry foams. A high protein charge increases solution viscosity, thereby retarding drainage and improving the stability of wet foams. Investigating an oat drink showed that conformational changes provoked by heat and enzymatic treatment of oat proteins reduce foam stability.

Kurzzusammenfassung

Flüssige, durch Proteine stabilisierte Schäume sind faszinierende Multiskalensysteme: die strukturellen Eigenschaften eines Proteins definieren seine Grenzflächenaktivität und Interaktionen mit anderen Molekülen. Seine Anordnung an Luft-Wasser-Grenzflächen und das Abfließen von Flüssigkeit bestimmen die Lamellenstabilität. Koaleszenz und Vergröberung begünstigen Bläschenwachstum, welches die makroskopische Schaumstabilität, repräsentiert durch den Schaumzerfall, beeinflusst. Diese Dissertation vertieft das Verständnis davon, welche strukturellen Eigenschaften eines Proteins eine erhöhte Schaumstabilität begünstigen. Eine Methode zum Nachverfolgen der zeitlichen Entwicklung der mittleren Bläschengröße und Zirkularität mit gewöhnlicher Laborausstattung und Open-Source-Software wurde entwickelt. Der Vergleich von Schäumen, die durch Hydrophobin und BSA, zwei Proteine mit fundamental verschiedenen Eigenschaften, stabilisiert sind, zeigte, dass große hydrophobe Bereiche an der Proteinoberfläche eine höhere Schaumstabilität fördern. Zugabe von Polysacchariden zu BSA-stabilisierten Schäumen wies darauf hin, dass eine erhöhte Lösungsviskosität die Schaumstabilität verstärkt, aber auch die Steifheit und Ladung der Polysaccharide berücksichtigt werden müssen. Modifizieren der tertiären Struktur von BSA durch Variation des pH-Werts der Lösung zeigte, dass ungeladene Proteine die Schaumstabilität von Polyederschäumen (trockene Schäume) begünstigen. Eine hohe Proteinladung erhöht die Lösungsviskosität, welche das Abfließen von Flüssigkeit verlangsamt und die Stabilität von Kugelschäumen (nasse Schäume) verbessert. Untersuchungen eines Haferdrinks zeigten, dass Konformationsänderungen der Haferproteine, hervorgerufen durch Wärme- und enzymatische Behandlung, die Schaum-

stabilität senken.

1. Introduction

1.1. Introduction to the topic

Foams are ubiquitous systems with fascinating structures and properties. From playing with soap bubbles as a child over marveling at the light froths of juice spritzers, soda or sparkling wine to enjoying creamier and denser foam textures in whipped cream and mousse au chocolat, these systems surround us in our daily lives. In food specifically, many examples for protein-stabilized foams can be found, including milk foams [1], foams from plant-based dairy alternatives [2, 3], beaten egg white [4] and beer foams [5]. In contrast to these liquid foams, bread, cake, meringue and ice cream are foams with solidified lamellae, which are also referred to as set foams [6].
Culinary innovation continually aims for new combinations of flavors and textures. In this process, foam recipes with interesting flavors have been developed such as cauliflower foam [7], horseradish foam [6], green olive meringue [6] or fish meringue [8]. From a food technological point of view, the aim is to improve the texture and lifetime of foams. For example, with many plant-based dairy alternatives entering the market, questions arise about why the formed foam structures are different from cow's milk and how to adjust their functionality for barista use. Exploring such issues necessitates a physical understanding of the fundamental relationships between the properties of the contained molecules and the resulting foam properties.
Liquid foams contain gas bubbles dispersed in a liquid [9–12]. For such a foam to come into existence, surface-active molecules are required to stabilize the air bubbles in the liquid [13–15]. In food foams mostly proteins act as dominant foaming agents [16, 17]. However, also lipids, phospholipids and some polysaccharides can operate as emulsifiers in food foams and Pickering-type stabilizers such as protein aggregates, microgel particles and nanoparticles can contribute to foam stability [13, 17, 18]. Many food foams comprise a combination of different emulsifiers [16, 19]. For example, in dairy-based foams, phospholipids, various proteins and (solid) fat particles are included in the foam formation [20], in plant-based foams complex protein mixtures contribute to the interfacial activity [17], and even in simple egg whites a large number of different proteins [21, 22] provide foam stability. Furthermore, many food systems additionally contain polysaccharides such as naturally contained starch or added food thickeners, which may additionally affect foam stability.
From a physical point of view, exploring the fundamental relationships in these foams is complicated by their complexity. Also limited knowledge about the components hampers a molecular understanding of foam formation and foam stability. However, to improve the stability of a foam, knowledge of the fundamental relationships is essential. For this reason, the investigation of model systems is required for understanding

fundamental structure-function relationships. A model system contains less types of different interacting particles. Step by step other types of molecules can be added or conditions can be varied. This thesis focuses on model liquid foams stabilized by two different proteins, the addition of polysaccharides to one of them and an exemplary plant-based formulation as an application case for a real food system.
Protein-stabilized liquid foams are multiscale systems, which show different structures on various lengths scales [23–25]. The primary, secondary and tertiary structure of proteins determine their interfacial activity and the interactions of different proteins with one another. These properties influence the arrangement of the proteins at the air-water interface, which in turn stabilize the air bubbles in the foam by preventing their coarsening and coalescence [13, 25–29]. Also the properties of the liquid phase such as its viscosity are important for foam formation and stability. Viscosity influences the drainage of liquid from the foam [30–32]. As a consequence of drainage, the lamellae become thinner and the foam changes its texture from wet to dry over time [24, 31]. In this process the bubble shape changes from spherical to polyhedral [31–33]. Over time, the mean bubble size grows due to bubble coarsening (Ostwald-ripening) and coalescence [14, 19, 24, 34]. Macroscopically, a foam height reduction is observed together with a rising liquid height underneath the foam due to gravity (drainage) [25, 35]. These multiscale relationships demand for an investigation on different lengths scales to deepen the understanding of the underlying mechanisms and to draw structure-function relationships.
For this reason, solutions of bovine serum albumin (BSA) and H*B hydrophobin (HP) in ultrapure water were chosen as the basis for the model foam samples, as the structure and properties of BSA are well known and HP has a unique tertiary structure exposing large hydrophobic patches to the protein surface. Aeration by whipping and investigations on multiple scales then allowed to draw structure-function relationships.

1.2. Current state of research

Various methods have been applied to investigate molecular properties of emulsifiers on a microscopic scale, thin films and bubble sizes on a mesoscopic scale as well as macroscopic foam properties such as drainage and foam stability. Characterization of foaming capacity and foam stability include different forms of foam height and drainage measurements [34–54]. Another characteristic for foam stability is the bubble size evolution [14, 25, 34, 55]. Foam films are sometimes characterized by using thin film pressure balances [56–58]. The surface activity of emulsifiers is often characterized by measuring surface tension [59–62] and the dynamic properties of interfacial layers by dilatational surface rheology [63–67]. To investigate interfacial arrangements of emulsifiers, techniques such as ellipsometry [42, 60, 63] and atomic force microscopy [68–72] have been applied.
In recent years a multiscale approach is followed increasingly, which combines findings on different length scales to deepen the understanding of how molecular properties influence the macroscopic appearance of foams [42, 73–77]. This thesis also follows a

multiscale approach and contributes to the study of fundamental structure-function relationships. Most studies that investigate foams on different length scales use a foam analyzer for macroscopic foam characterization [42, 73–75]. These instruments are quite expensive and due to their specialization on foam formation and characterization, they are not readily available in each lab. In this thesis, simple lab equipment was used to measure foam and liquid heights and to develop a method to investigate the temporal evolution of the mean bubble size, size distribution and circularity. The developed method can easily be transferred to other labs and be applied for the investigation of other systems such as emulsions.

BSA is a well-characterized protein [65, 78–86], which is commercially available in high purity. It originates from the blood plasma of bovines [87] and is also found in cow's milk [88]. Its foam stabilizing ability has been studied in dependence of solution pH [40, 42, 89]. These studies focus on very low BSA concentrations and use the bubbling (sparging) method for foam formation. Whipping is often applied for foaming food systems [35, 90], but requires higher protein concentrations [35]. At such concentrations the solution viscosities have been investigated [91], however, to my knowledge no studies on foam formation have been performed. For this reason, foaming of BSA solutions at higher concentration (4 wt%) by whipping was investigated in this PhD project and showed that an interplay of different mechanisms influences foam stability.

The vast number of proteins found in nature and the improvement of extraction methods continually allow for investigation of novel proteins. A class of proteins that have aroused attention for their special structure including large hydrophobic surface patches and high surface activity are hydrophobins [16, 92–95]. Their fungal origin provides great potential for the use in food systems, due to a high consumer acceptance and reduced manufacturing costs [96, 97]. There are two classes of hydrophobins, class I and class II, which vary in their spacing between cysteine residues, the location of hydrophobic patches at the protein surface, solubility and the structures of their arrangements at hydrophobic-hydrophilic interfaces [98–100]. Many studies investigate different hydrophobin species directly extracted from various fungi [71, 72, 101–104]. However, meanwhile also an approach to produce hydrophins on industrial scale has been developed [93]. Such a hydrophobin is used in this thesis. Although many studies on the protein structure and interfacial arrangement have been performed for various hydrophobin species [68, 71, 72, 102, 105, 106], only some studies investigated bubble and foam stabilization by hydrophobins [26, 94, 107–109]. To my knowledge, these studies were performed exclusively with the class II hydrophobins HFBI and HFBII from *Trichoderma reesei*. Among these, only very few studies included the interaction of HFBII with other proteins and investigated bubble or foam properties of such systems [109–111]. This is where this thesis draws on. The class I H*B hydrophobin is compared with the larger and differently structured protein bovine serum albumin and the influence of their interactions on interfacial properties, foam texture and stability are explored. So far there is no other study that investigates the foaming properties of a class I hydrophobin in combination with another protein and provides a detailed study including not only macroscopic foam properties but also considers the interfacial assemblies and mutual interactions.

1.3. Research questions

This thesis aims to contribute to answering the following general research questions:

- Which molecular properties of a protein promote an increased foam stability?
- How does the combination of a protein and a polysaccharide affect foam stability?

To explore these topics this thesis focuses on:

- The development of a method to characterize the temporal evolution of bubble size and circularity using common lab equipment and open-source software.
- The comparison of foams stabilized by the two different proteins, H*B hydrophobin and BSA, and their mixtures. These proteins differ in the size of hydrophobic patches at their surface. The comparison of their molecular structure, interfacial arrangement and the stability of resulting foams contributes to answering the first general research question.
- The addition of the polysaccharides xanthan gum, iota-carrageenan and guar gum to BSA-based foams in order to investigate the effect on foam stability. In addition, it is aimed to clarify whether this effect is purely driven by changes in solution viscosity. This model system explores the second general research question.
- Variation of the solution pH of BSA-stabilized foams. Here, it is explored how these changes affect the molecular properties of BSA, the interfacial arrangements, the solution viscosity and the macroscopic foam stability. Investigation of this model system provides insights regarding the first general research question.
- The effects of heat and enzymatic treatment on the stability of oat drink foams, which affect the molecular properties of oat proteins and therefore contributes to answering the first general research question.

1.4. Outline of this thesis

First, some background information is provided (Chapter 2) including fundamental foam characteristics, an introduction of the investigated proteins and polysaccharides, relevant fundamental interactions in protein-stabilized liquid foam systems and the working principles of the applied measurement techniques.
Chapter 3 introduces the developed method for the analysis of foam stability. The method comprises automated analysis of the temporal evolution of the mean bubble size as a measure of foam stability. It applies foam formation by whipping, optical microscopy and image analysis using open-source software. Intermediate steps in the development of the method are also presented. The use of this method is exemplified

by comparing HP- and BSA-stabilized foams as well as foams stabilized by blends of these proteins.
Chapter 4 complements the investigations presented in Chapter 3 by exploring the interactions of HP and BSA with one another and their interfacial arrangements. Here, high performance liquid chromatography (HPLC), differential scanning calorimetry (DSC), surface tension measurements and atomic force microscopy (AFM) deliver insights.
Chapter 5 discusses the addition of the polysaccharides xanthan gum, iota-carrageenan, and guar gum to BSA-stabilized foams. By adding polysaccharides, the dynamic viscosity of the protein solution is increased. In addition, the structural properties of the polysaccharides and their interactions with BSA are relevant to foam stability. The influence of these variations on the temporal evolution of the mean bubble size is discussed.
Chapter 6 investigates the influence of changes in solution pH on the stability of BSA-based foams. pH changes impact the protein net charge and conformation. These in turn influence the interfacial protein assembly as well as the solution viscosity, which both affect foam stability and drainage behavior. A literature review provides information on pH-dependent conformational changes of BSA and layer formation at air-water interfaces. These insights are complemented by measuring zeta potentials, particle sizes and dynamic viscosities as well as monitoring the temporal evolution of foam and liquid heights as well as mean bubble sizes.
Additionally to these model systems, Chapter 7 investigates the foaming properties of a real food system. The development of an oat drink and study of its foaming properties was chosen as example. The impact of heat and enzymatic treatments are investigated by measurements of particle sizes, viscosities as well as foam and liquid heights and accompanied by optical microscopy. The relationships learned from the study of model systems comprised of pure components can be applied to learn about the fundamental relationships in such a complex system.
Last but not least, general conclusions and an outlook are provided in Chapter 8.

2. Theoretical background

2.1. Foam characteristics

Liquid foams are colloidal systems that contain gas bubbles (mostly air) dispersed in a liquid (aqueous) continuous phase [11]. To create such a foam, gas has to be incorporated into the liquid phase. The creation of an interface between a gas and a liquid requires energy. This additional energy is given by the product of the surface tension γ and the area of the created interface. γ has the unit of energy per unit area of the interface (or force per unit length) and is called *surface tension*, because it implies that an interface aims to reduce its area and therefore is under tension. [112] In addition, the stabilization of bubbles in the liquid necessitates, emulsifiers, which are surface-active molecules containing hydrophilic and hydrophobic parts [113]. This amphiphilic structure enables their arrangement air-water interfaces and stabilization of the foam [13, 16]. In food systems, proteins serve as emulsifiers [16, 17]. The resulting foam can be characterized on different length scales, from the microscopic arrangement of emulsifiers at the gas-liquid interface, over mesoscopic structures, such as the size and shape of bubbles and the thickness of the lamellae, to macroscopic foam height decay and increase of drainage.

2.1.1. Foam formation

Different methods are applied to incorporate air into the continuous phase: whipping, shaking, or sparging of the sample solution. Depending on the method chosen, the required concentration of protein in the solution varies between 3 % to 40 % of protein for whipping, about 1 % of protein for shaking and about 0.01 % to 2 % for sparging (bubbling) gas into the solution [35].

Whipping is a mechanical method of foam generation where whisks or blades move through the sample solution at high-speed and thereby beat atmospheric air into the liquid [90]. Tools used for whipping range from common food whisks [37, 50, 51] and milk frothers [37, 43] to laboratory equipment high-speed homogenizers [44–46, 48, 49, 52]. The foaming properties are influenced by the type and speed of the whisks as well as the shape and size of the bowl. In general, whipping produces the most stable foams, because with increasing whipping time the bubble size is progressively decreased and the liquid fraction of the foam increased. However, the top surface of these stiffer foams usually is not flat, which complicates the measurement of the foam volume. Furthermore, the protein concentration of the sample solution needs to be much higher, because the foam volume is usually significantly larger, which means

that the interfacial area is highly increased in whipped systems. [90] For the formation of food foams (e. g. meringues, mousses, or in baking), whipping is the most popular industrial method [35, 90].

Shaking In a closed system (e. g. a sealed measuring cylinder), foam is generated by mechanically or manually shaking the vessel containing the sample solution. Compared to sparging or whipping, shaking less efficiently produces bubbles and therefore leads to lower rates of foam production. In addition, the amplitude and frequency of shaking, the volume and shape of the vessel and the solution properties of the surfactant influence the foaming properties. [90]

Sparging or bubbling is a method, where gas is injected from below through a porous disk (e. g. a sintered glass filter), a single capillary or a set of capillaries into the sample solution. A foam is formed by gas bubbling into the solution, stabilization of the bubbles by emulsifiers present in the solution and rising of the gas bubbles due to buoyancy. [35, 40, 114, 115] An advantage of sparging is, that the type of gas incorporated in the foam can be varied. The flow rate and volume of the delivered gas can be controlled and a fixed volume of foam can be formed. [35, 90, 115] The foam generation by sparging is slower, but due to the glass frit the initial bubble size is constant. At a constant bubble size the pressure difference between the bubbles is minimized and therefore the Ostwald ripening is reduced. [90]
Commercially available foam analyzing instruments offer the possibilities of sparging and whipping (stirring) for foam formation [116, 117].

2.1.2. Foam structure

In a foam, bubbles are dispersed in a liquid and stabilized by emulsifiers [118]. The shape of the bubbles varies from spherical in a wet foam (or bubbly liquid) to polyhedral in a dry foam [16, 19, 112, 118]. A wet foam, also called *Kugelschaum*, contains a high liquid volume fraction and a low gas volume fraction. The spherical bubbles are separated by thick liquid films. In contrast, a dry foam contains a high volume fraction of gas and a low volume fraction of liquid. Here, the bubbles are separated by thin films and the dry foam can be regarded as space-filling packing of polyhedra. The dry foam is also called *Polyederschaum* or polyhedral foam. In general, dry foams develop from wet foams by sufficient drainage. Therefore, all intermediate states are also available. [118] The thin liquid films at the faces of the polyhedra between the bubbles are referred to as lamellae [13, 19]. These thin films contain a bilayer of emulsifiers, which assemble at the air-water interfaces between the thin film and the adjacent bubbles [13]. The liquid channels at the polyhedron edges are called Plateau borders [119]. The network of lamellae and Plateau borders, which is stabilized by the emulsifiers, entraps the bubbles in a foam and impedes their escape [13]. Figure 2.1 illustrates these elements of the foam structure.
The layers of emulsifiers at the interfaces of bubbles and lamellae stabilize the foam, since they modify the properties of the interface. For the ability of a solution to form

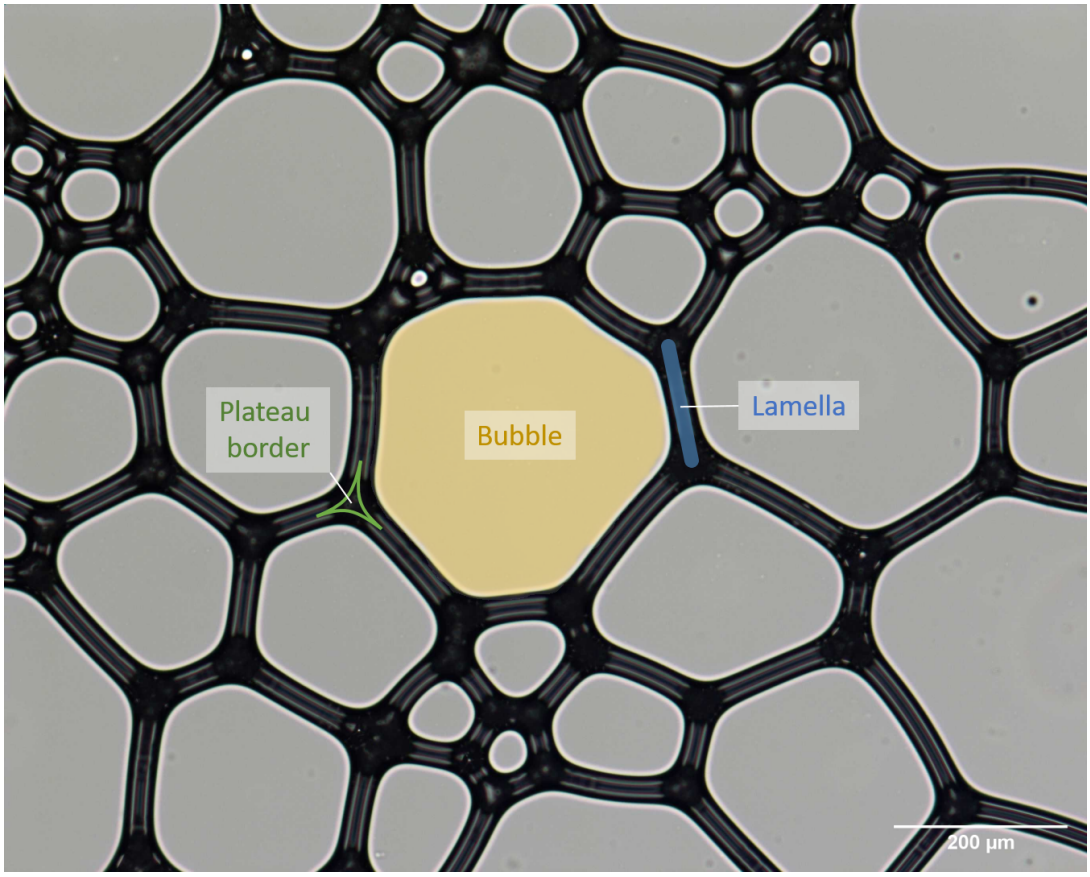

Figure 2.1.: Microscope image of a foam stabilized by a protein (BSA) at 10-fold magnification. The elements of the foam structure are highlighted: air bubble in polyhedral shape, thin films (lamellae) at the faces of the polyhedron and Plateau borders at the edges.

a foam and its stability, the speed with which the surfactants cover the interface, the concentration of emulsifiers at the interface and the viscoelasticity of the interface are relevant [112]. The capacity of an emulsifier to reduce surface tension is a crucial factor in this context, as the Laplace pressure, in conjunction with gravity, represents a primary driving force behind the destabilization of a foam [13, 112, 120–122].

2.1.3. Foam ripening

Liquid foams are not thermodynamically stable. Several mechanisms destabilize the foam and cause it to decay gradually. The foam decay is characterized by drainage of liquid from the foam and an increase in the mean bubble size. [32, 34, 118]
Regarding foam stability the *Young-Laplace law* (or just *Laplace law*) is of importance, which correlates the pressure difference at an interface to the curvature of the interface. The pressure difference causes the interface to bend. However, the surface tension reduces the curvature and therefore counteracts the pressure difference.

$$\Delta P = P_A - P_B = \gamma\Big(\frac{1}{r_1} + \frac{1}{r_2}\Big) \tag{2.1}$$

where P_A and P_B are the pressures of the interfacing phases, γ is the surface tension and r_1 and r_2 are the principal radii of curvature of the interface. [112]

Drainage describes the flow of liquid through the network of Plateau borders due to gravity, which causes the system to separate into a foam phase at the top and an aqueous phase at the bottom. In addition, the foam becomes drier at the top than further down. [107, 112, 119]
In addition to gravity, the phenomenon of *Plateau border suction* or *capillary suction* contributes to the drainage. It is caused by the capillary pressure, which is given by the Young-Laplace law (cf. Equation 2.1). The liquid in a foam is confined between gas-liquid interfaces. The local curvature and shape of the Plateau borders and vertices is determined by the pressure difference of gas phase and liquid phase. In a foam, the pressure in the dispersed phase is higher than in the continuous phase. For sufficiently long Plateau borders ($r_1 << r_2$) the capillary pressure is given by

$$P_c = P - p \simeq \frac{\gamma}{r} \tag{2.2}$$

where P and p are the pressure of the gas and the liquid, respectively, γ is the surface tension and r is the radius of curvature of the Plateau border [112]. The interface between a lamella and its adjacent bubble has only a low curvature and therefore the pressure difference is small. However, at the interface of Plateau border and bubble, the pressure difference is much larger due to the stronger curvature of the Plateau border. Therefore, inside the lamella there is a radial pressure gradient from its center towards the Plateau borders at its outer periphery. This pressure gradient leads to a drainage from the lamellae to the Plateau borders [112, 123–125]. Since the radius of curvature of the Plateau borders is smaller for small bubbles (cf. Figure

2.1), the lamellae between smaller bubbles tend to drain faster than that between large bubbles. Emulsifiers decrease the surface tension of the bubbles and thereby slow down the drainage of the thin films.

Coalescence expresses the merging of two or more bubbles into a single large bubble caused by rupture of the thin liquid film (lamella) between the bubbles [19, 112, 126]. When considering the stability of a lamella, two opposing forces are relevant: the capillary pressure and the disjoining pressure. The capillary pressure has been described above in the paragraph about drainage. If the curvature of the Plateau border is larger than the curvature of the lamella, the Plateau border is at lower pressure and capillary suction acts, which means that it sucks much of the liquid from the lamella into the Plateau border. This leads to a thinning of the lamella and eventually to its rupture. [112]
The disjoining pressure is caused by the interactions between emulsifiers adsorbed at the interface. The interaction forces between the surfactant layers tend to increase the thickness h of the lamella and by this prevent its thinning. The most important intermolecular forces contributing to the disjoining pressure are van der Waals interactions Π_{vdW}, electrostatic repulsion Π_{ele} and steric forces Π_{steric}.

$$\Pi_{net}(h) = \Pi_{ele} + \Pi_{vdW} + \Pi_{steric} + ... \tag{2.3}$$

The contribution of van der Waals interactions is attractive whereas those of electrical and steric forces are repulsive. [19, 127] The dependence of these contributions from the film thickness is sketched in Figure 2.2.

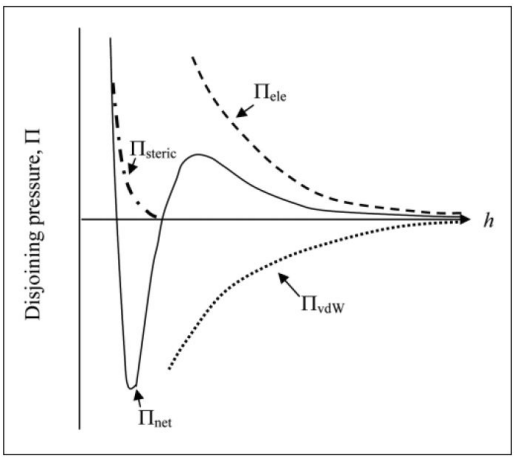

Figure 2.2.: Contributions of the disjoining pressure Π_{net} in dependence of the film thickness h: van der Waals Π_{vdW}, steric Π_{steric} and electrostatic forces Π_{ele}. Reproduced from [19], who adopted from [127]. Permission obtained from John Wiley and Sons © Institute of Food Technologists and IOP Publishing © IOP Publishing. Reproduced with permission. All rights reserved.

As the lamella thins, its interfaces approach each other. This results in a local increase

of the concentration of counterions in the lamella compared to that in the Plateau border. Furthermore, protruding chains of adsorbed polymeric surfactants overlap and increase the local concentration gradient. This leads to an osmotic pressure gradient, which retards drainage from the lamella and further thinning of the film. [19]
Hydrodynamic forces can cause surface waves in the thin lamella film, when it thins below a critical thickness [128]. These ripples become more pronounced, the lower the interfacial tension and the larger the size of a bubble. Furthermore, interface waves affect the local thickness of the film and can cause holes, which lead to rupture of the film and coalescence of the bubbles. Surface-active polymers and strong intermolecular interactions facilitate the formation of highly viscoelastic interfacial films. Due to their connectivity and viscoelastic properties such films can mitigate the intensity and propagation of ripples across the interface. For this reason, flexible proteins with strong intermolecular interaction can better stabilize the thin foam films against rupture than small low molecular weight surfactants. [19, 129]
Indeed, the choice of emulsifier is relevant regarding the kinetic stability of the foam, since the physicochemical properties of the surface-active molecule determine the viscoelastic properties of the adsorbed interfacial film as well as the steric repulsion between the adsorbed emulsifier layers located at both interfaces of the lamella. [19]
If the stabilizing mechanisms are too weak or absent, a film between adjacent bubbles breaks. Dynamic effects contribute to film rupture as the lamellae approach their equilibrium thickness. However, also at equilibrium and with stabilization of the thin films by repulsive forces between its surfaces, spontaneous fluctuations in thickness or density, or external perturbations such as dust, grease and evaporation of liquid at the top of the foam can cause films to rupture. Dust and grease form additional hydrophobic-hydrophilic interfaces and attract emulsifiers, which then are unavailable at air-water interfaces. Coalescence results in a reduction of the total number of bubbles. The rupture of lamellae at the top of the foam causes loss of gas and a decrease in foam volume. [112]

Coarsening / Ostwald Ripening Ostwald ripening, also known as disproportionation represents the diffusion of gas from smaller to larger bubbles, which is driven by the pressure difference between bubbles of different sizes (Laplace pressure given by the Young-Laplace law) [19, 130]. A more general term to describe the bubble size changes caused by gas diffusion is coarsening [112, 130]. Any gas is soluble in any liquid to some extent. For this reason, the liquid films between bubbles in a foam are no absolute barriers to the gas. Therefore, gas may diffuse from one bubble to another through the liquid phase, if there is a pressure difference between bubbles (as is the case for differently sized bubbles). The gas diffusion leads to an increase in average bubble size and a reduction in the number of bubbles. Coarsening is thus a sufficiently slow process, so that the foam is still close to mechanical equilibrium. [112]
In a bubbly liquid the liquid fraction is high, bubbles are spherical and well separated from each other. Gas diffuses between bubbles and liquid. The liquid acts as a reservoir of gas. The pressure of a bubble is proportional to its curvature and for a spherical

bubble it is inversely proportional to its radius as is seen from the Young-Laplace law (Equation 2.2). For this reason, the smallest bubbles have a higher overpressure relative to the liquid than larger bubbles. Therefore, small bubbles lose more gas to the liquid than receiving from it. On the other hand, the largest bubbles receive more gas from the liquid than losing to it. Consequently, small bubbles shrink and eventually disappear, whereas large bubbles continue to grow. This leads to an increase of the mean bubble size and to a decrease of the total number of bubbles, since no new bubbles are created. The growth rate of bubbles is determined by $\Omega_{bl} = \frac{dr^3}{dt}$ and the average bubble radius increases with $t^{1/3}$ assuming a constant growth rate. This process is called Ostwald ripening (or Lifshitz-Slyozov-Wagner ripening). [112, 131–134] In experiments often exponents larger than 1/3 are determined [133, 134].
In a dry foam the gas diffuses directly from bubble to bubble, since the lamellae are very thin. Here, the pressure of the bubble is still proportional to its curvature, however since bubbles are not spherical the curvature depends on the bubble shape. The bubble growth rate is rather determined by the number of faces than the bubble volume and given by $\Omega_{df} = \frac{dr^2}{dt}$. The average equivalent bubble radius increases with $t^{1/2}$ and the coarsening in a dry foam is described as von Neumann-Mullins coarsening. [112, 133–136]
These two scenarios represent the two extremes. In actual foams, the liquid fraction can assume any value in between and the behavior of the foam can be considered somewhere between these two extremes. [112]
Three main strategies are applied to slow down the ripening of a foam. First, the viscosity of the continuous phase can be increased [17]. Second, a less soluble gas can be used for foam formation. However, this option is limited in case of food foams due to the edibility of the gas. And third, the choice of emulsifier is relevant for the stability of a foam. Efficient foaming agents produce highly elastic interfaces that can resist film rupture and / or gas diffusion. [26]

2.1.4. Characterization of foaming capacity and foam stability

To characterize a foam, two properties are investigated: foaming capacity and foam stability. The foaming capacity, or foamability, is the capacity of the solution to entrap gas, i. e. to form a foam, and is described by the initial increase in foam volume. On the other hand, foam stability is the ability of a foam to keep the gas inside the foam, i. e. it is the capacity of an existing foam to persist. [17, 119]
Several methods have been applied to characterize foaming capacity and foam stability. The foamability of a solution depends not only on the intrinsic properties of the protein and solution parameters, but also on the methods applied for foam formation and measurement of foaming capacity and foam stability [35, 119]. The manifold techniques used for foam formation and characterization complicate a comparison of the results of different studies [35]. In the following an overview of common methods for foam characterization is given.
Foaming capacity is most commonly calculated by the ratio of the foam volume directly after foam formation or the increase of total volume to the volume of the solution

before foaming [38, 42, 45–47, 49–54]. Alternatively, conductivity measurements are considered to characterize foaming capacity [84]. In case of sparging, the gas volume and gas flow rate can be considered. The foaming capacity is then given by the ratio of foam volume directly after foam formation to the volume of sparged gas [137, 138].
To quantify foam stability, the temporal evolution of either the liquid drained from the foam or the decrease in foam volume is considered [35]. Often the foam volume immediately after foam formation ($V_{f,0}$) and after a certain time ($V_{f,t}$) is measured and the ratio $V_{f,t}/V_{f,0}$ or $(V_{f,0} - V_{f,t})/V_{f,0}$ is used to describe the foam stability. Typical time intervals are 5 min [42], 10 min [43], 30 min [44–47], 60 min [48] and 90 min [49]. Similarly, also the volume of liquid retained in the foam (foam liquid stability) is used to describe the stability of a foam [35, 50, 51].
Alternatively, the half-life time of the foam or the liquid in the foam is used to characterize its stability [38–40]. Furthermore, the rate of collapse of the foam [41] and the rate of drainage [34, 40] are considered. Alternatively, the foam height is monitored over time [36, 37].
Besides observing the temporal evolution of the macroscopic foam height, the growth of the mean bubble size is also a relevant measure of foam stability [25, 34, 55].

2.2. Proteins

Mainly the primary and tertiary structure of proteins determine their applicability as foaming agents: Depending on the presence and sequence of hydrophobic amino acid residues in the primary structure and the spacial folding, proteins can develop hydrophobic regions [16]. Exposure of such hydrophobic regions to the protein surface increases their interfacial activity and improves foaming properties [139, 140]. However, in most proteins, the tertiary structure hides hydrophobic regions from the polar solvent water. Exposure of the shielded hydrophobic regions to the aqueous phase can be obtained from unfolding the protein by heat supply or addition of detergents and chemical agents. [16, 119]
Protein adsorption at interfaces is thermodynamically favorable because of the simultaneous dehydration of the hydrophobic parts of the protein and the hydrophobic interface. Upon adsorption of a protein to an air-water interface, hydrophobic parts of the protein are directed towards the gas phase. Additionally, the protein loses some of its tertiary structure but most of its secondary structure is retained. [32, 141]
Due to the surface structure of proteins, they often have multiple adsorption sites per molecule. Spontaneous desorption of the entire molecule is therefore statistically very unlikely. [16] Many proteins strongly adsorb to air–water interfaces and form layers with reasonably high surface rheological moduli due to steric and electrostatic inter-protein interactions. [16]
In the following the molecular structures and the fundamental properties of the proteins applied in this study are introduced.

2.2.1. Bovine Serum Albumin

Bovine serum albumin (BSA) is a protein found in the blood serum of cattle (*Bos taurus*). With 3.3 % it is the main protein in the blood plasma [87], where its main function is to regulate the colloidal osmotic pressure of the blood. Moreover, BSA binds water, ions and other molecules such as fatty acids, hormones, and drugs and is the major zinc, calcium, and magnesium transporter in the plasma. [142] Besides being an important component of the blood serum, BSA represents a whey protein with a concentration of $0.4\,\mathrm{g\,L^{-1}}$ to $0.8\,\mathrm{g\,L^{-1}}$ BSA present in cow's milk [88].
The presence and assembly of hydrophobic and hydrophilic amino acids at its surface make BSA a surface-active molecule and enable it to act as an emulsifier in a liquid foam. Gräff et al. [56] investigated protein stabilized foam films. These authors found that the assemblies of BSA at the air-water interface are quite immobile. However, their stabilization ability might be lower than that of β-lactoglobulin networks [56, 60].
The primary, secondary and tertiary structure of BSA has been well investigated [65, 78–86]. It is a heart-shaped protein with a molecular weight of about 66.5 kDa [143–145]. The primary structure contains 583 amino acids (607 amino acids including the signal peptide) [146]. The tertiary structure of BSA is shown in Figure 2.3. Structurally relevant properties (location of helices and cysteines) are highlighted as

well as properties relevant for interactions with other molecules (surface charges and hydrophobic areas).

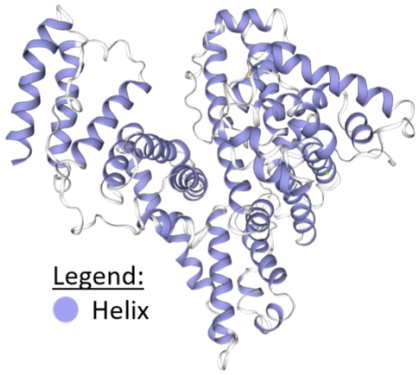

(a) Helical content.

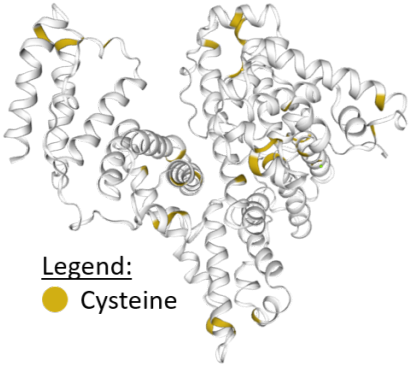

(b) Location of cysteines.

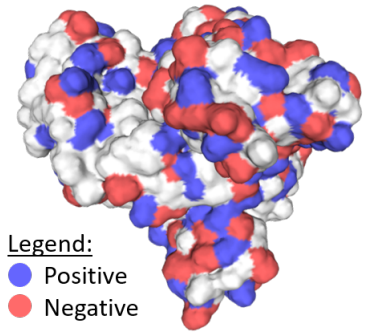

(c) Charged amino acids at the surface of BSA.

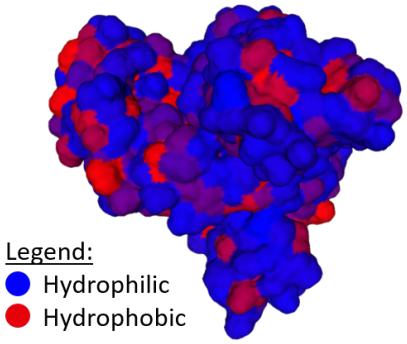

(d) Hydrophobic amino acids at the surface of BSA.

Figure 2.3.: Tertiary structure and surface properties of BSA (UP-ID: P02769). Reproduced from `https://swissmodel.expasy.org/` [146], licensed under CC BY-SA 4.0 license. For more information, visit `https://swissmodel.expasy.org/docs/terms_of_use`.

BSA can be divided into three domains with repeating structure: domain I, domain II, and domain III. The domain structure is shown in Figure 2.4. Each domain consists of three double loops formed by disulfide bonds. Thereby, a large double loop is connected to a small double loop by a short connecting segment. The small double loop is followed by a large connecting segment and another large double loop, which is connected to the next domain. The amino acids 1-190 belong to domain I, amino acids 191-382 form domain II, and domain III consists of amino acids 383-583. The structure of domain I differs from the other two domains in missing one disulfide bond (position 8 and 54) and therefore contains one single loop instead of the first large

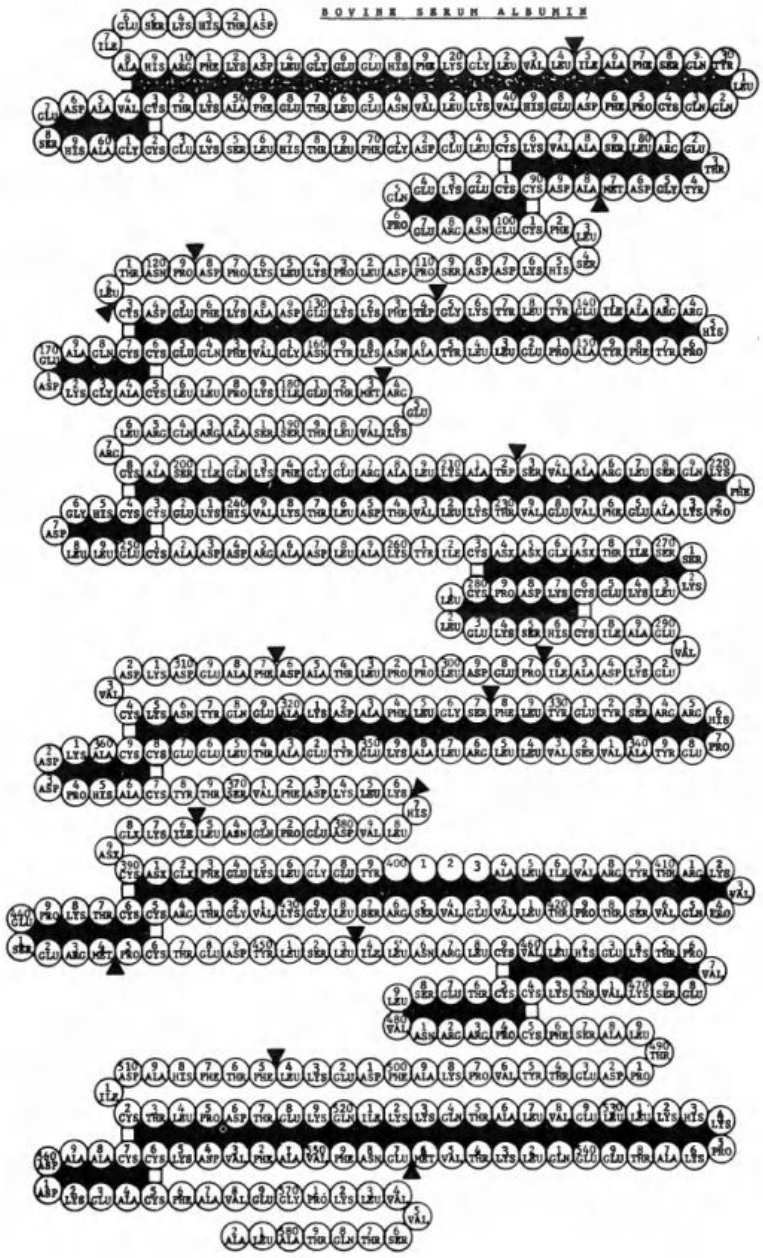

Figure 2.4.: Primary structure of BSA with cysteine bonds. Reprinted from [147] with permission from Elsevier.

double loop.[147]
In three dimensions, the native globular shape of BSA is arranged in a heart-like shape, which is called Normal (N) form. Domains I and II form one half, whereas domain III builds the other half of the heart-like shape. [146, 148–150]
Depending on the solution pH, BSA changes its conformation, as illustrated in Figure 2.5. The N form (Normal form) exists at the IEP, where the net charge of the protein

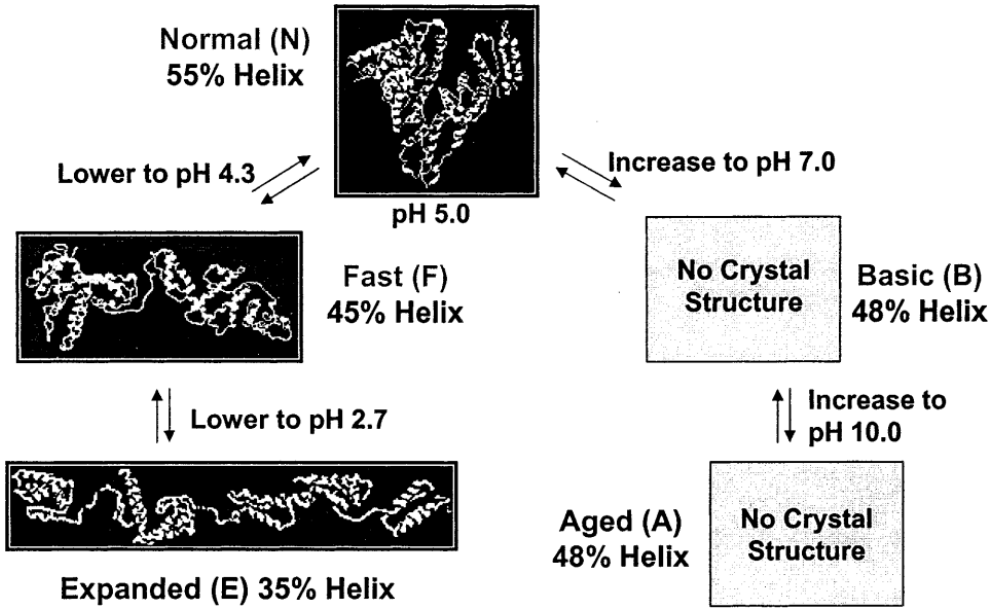

Figure 2.5.: pH-dependent conformational changes of BSA. Reprinted with permission from [65]. Copyright 2003 American Chemical Society.

is neutral. The IEP of BSA is at about pH 5 (reported values are in the range of pH 4.2 to pH 5.5) [42, 83, 151–155]. In its compact globular shape the two parts of the heart-like shape cohere due to electrostatic attraction of oppositely charged amino acids [147].
Changing the pH of the solution will affect the charges of the amino acids. At pH values lower than the IEP of the protein some of the before negatively charged amino acids become neutral or positively charged. Overall the number of positive charges in the protein increases. As a consequence of the induced repulsion, the BSA molecule unfolds between domain II and domain III [65, 148–150]. The obtained conformation is called Fast (F) form and occurs at pH values below pH 4 [149]/ pH 4.5 [79]. Figure 2.6 shows the conformational change of BSA from N-form to F-form as obtained from all-atom molecular dynamics simulations [150]. At even lower pH values the shape of BSA extends further reaching Expanded (E) form below pH 3.5 [149]. The low pH conformational changes are associated with a loss in helical content [65].
Under alkaline conditions the number of negatively charged amino acids increases. Their repulsion leads to a conformational change, which is associated with a volume increase of the BSA molecule and a loss in helical content occurs. The Basic (B) form

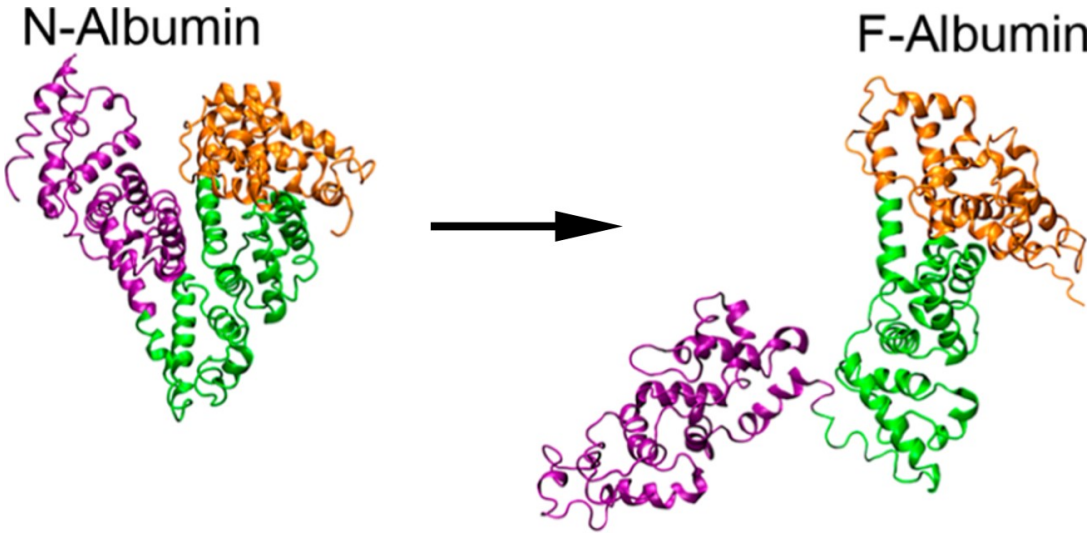

Figure 2.6.: Conformational change of BSA at low pH. The N-form unfolds between domain II and domain III. Reprinted from [150] (with slight layout change). ACS public use license. Copyright 2014 American Chemical Society.

is typically found between pH 7 and pH 9 [65] / above pH 8 [149].

2.2.2. Hydrophobin

Hydrophobins are small, highly surface-active proteins discovered in filamentous fungi [71, 72, 94]. Their ability to form amphipathic protein layers by spontaneous self-assembly at hydrophobic-hydrophilic interfaces supports multiple processes in the development of filamentous fungi [68, 71, 72, 94, 95, 104, 156–161]. Hydrophobins inhibit the wetting of aerial spores during dispersal, allow fungi to breach air–water interfaces by lowering the surface tension, and facilitate their attachment to surfaces for germination and infection of hosts [104, 157, 162–166].
Various fungi such as *Neurospora crassa*, *Schizophyllum commune*, *Trichoderma reesei* contain hydrophobins [162]. In bacteria (*Bacillus subtilis* and *Streptomyces tendae*), proteins with similar function but different structure were discovered, which are sometimes referred to as bacterial hydrophobins [156, 167–169]. Meanwhile, industrial scale production of hydrophobins has been achieved by use of recombinant production processes [93].
The molecular weight of hydrophobins is about 10 kDa [159, 170] and their primary structures cover about 100 amino acids [156, 162]. All hydrophobins contain eight cysteine residues, which form four disulfide bonds [98, 99, 105, 171, 172]. These show a distinct conserved pattern: X_{2-38}-C-X_{5-9}-C-C-X_{11-44}-C-X_{8-23}-C-X_{5-9}-C-C-X_{6-18}-C-X_{2-14}, where C denotes cysteine and X indicates any other amino acid [99, 171]. Two disulfide bridges stabilize the core of the hydrophobin, while the other two disulfide bonds hold relatively loose parts close to the core. For this reason, hydrophobins show a very stable and compact core structure [71, 72, 159, 162, 172,

173] and increased resistance to denaturation [160, 174].
Hydrophobins are divided into two classes, which vary in solubility, location of hydrophobic patches at the protein surface, and structures formed upon assembly at hydrophilic-hydrophobic interfaces [98, 99]. Class I and class II hydrophobins differ in their spacing between cysteine residues [100] as shown in Figure 2.7. Class I hydrophobins tend to be larger than class II hydrophobins and exhibit major variations in the total number of amino acids and the length of the inter-cysteine segments [172].

Figure 2.7.: Comparison of amino acid sequences from various class I and class II hydrophobins. Cystein residues are highlighted in yellow. Brackets indicate the conserved disulfide bonding pattern. Compared hydrophobins: SC3 from *Schizophyllum commune* (UP-ID: P16933); SC4 from *Schizophyllum commune* (UP-ID: P16934); EAS from *Neurospora crassa* (UP-ID: Q04571); MPG1 from *Magnaporthe oryzae* (UP-ID: P52751); HCF1 from *Cladosporium fulvum* (UP-ID: Q00367); ABH1 from *Agaricus bisporus* (UP-ID: P49072); PRI2 from *Agrocybe aegerita* (UP-ID: Q9Y8F0); RODA from *Aspergillus fumigatus* (UP-ID: P41746); HFBI from *Trichoderma reesei* (UP-ID: P52754); HFBII from *Trichoderma reesei* (UP-ID: P79073); CU from *Ophiostoma ulmi* (UP-ID: Q06153); CRP from *Cryphonectria parasitica* (UP-ID: P52753); HCF6 from *Cladosporium fulvum* (UP-ID: Q9C2X0); MGP from *Magnaporthe grisea* (UP-ID: O94196); HYD4 from *Gibberella moniliformis* (UP-ID: Q6YF29) and SRH1 from *Trichoderma harzianum* (UP-ID: P79072). Reprinted from [172] with permission from Elsevier.

The structure of class II hydrophobins is, in general, more ordered and compact and consists of a β-barrel, a single tethered α-helix and two relatively ordered loops [71]. The core of class II hydrophobins is also described as "closed" β-barrel [105]. For class I hydrophobins the loops are longer and more flexible [71]. Its structure is also described as "open" or half-barrel structure [105]. Figure 2.8 compares the structure and surface properties of the two most investigated hydrophobins: class I hydrophobin SC3 from *Schizophyllum commune* and class II hydrophobin HFBII from *Trichoderma reesei*. To illustrate the structural variations within class I hydrophobins, the tertiary structures of four representatives are shown in Figure 2.9.
Furthermore, hydrophobins are highly surface-active proteins due to large hydropho-

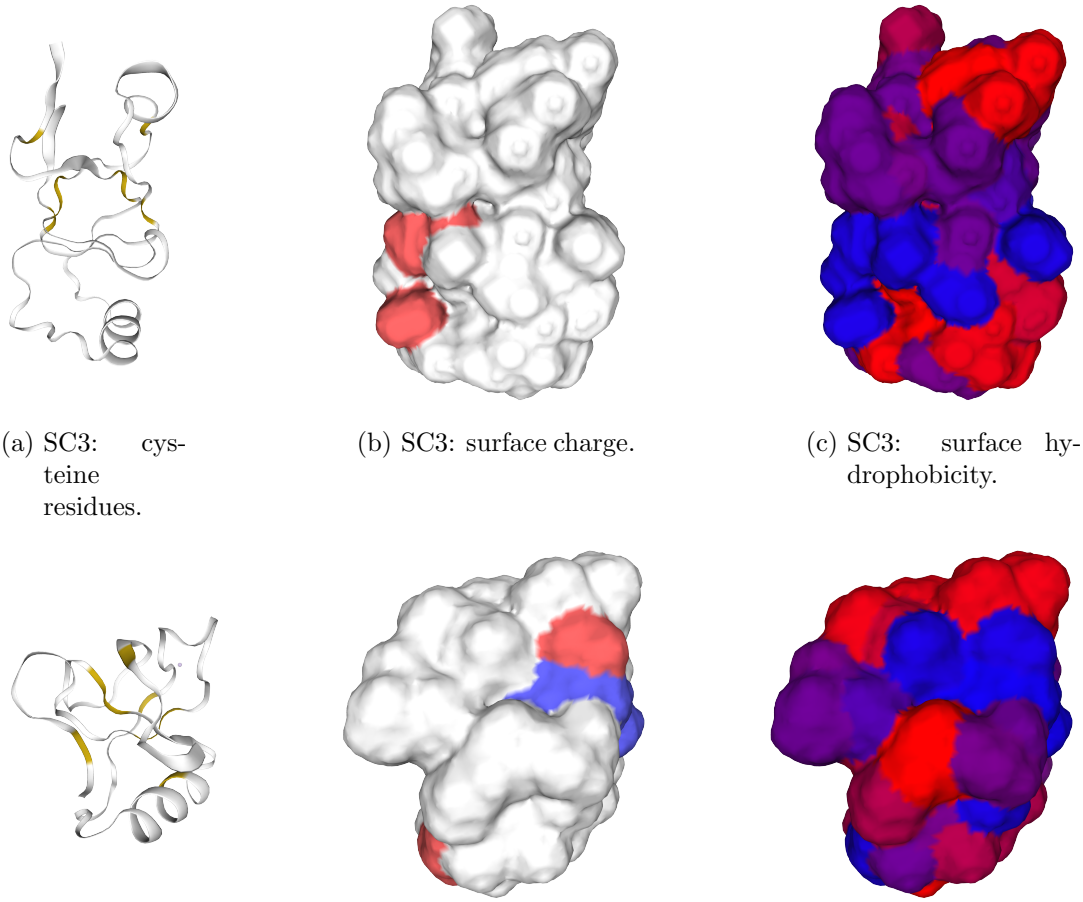

(a) SC3: cysteine residues.

(b) SC3: surface charge.

(c) SC3: surface hydrophobicity.

(d) HFBII: cysteine residues.

(e) HFBII: surface charge.

(f) HFBII: surface hydrophobicity.

Figure 2.8.: Comparison of class I and class II hydrophobins. First row: class I hydrophobin SC3 (UP-ID: P16933) from *Schizophyllum commune*. Second row: class II hydrophobin HFBII (UP-ID: P79073, PDB-ID: 2b97) from *Trichoderma reesei*. (a, d) Location of cysteine residues (yellow) in the tertiary structure. (b, e) Surface with positively (blue) and negatively (red) charged amino acids. (c, f) Surface with hydrophobic (red) and hydrophilic (blue) amino acids. In (f) the typical large hydrophobic patch of HFBII is shown on the top. [146] Reproduced from `https://swissmodel.expasy.org/` [146], licensed under CC BY-SA 4.0 license. For more information, visit `https://swissmodel.expasy.org/docs/terms_of_use`.

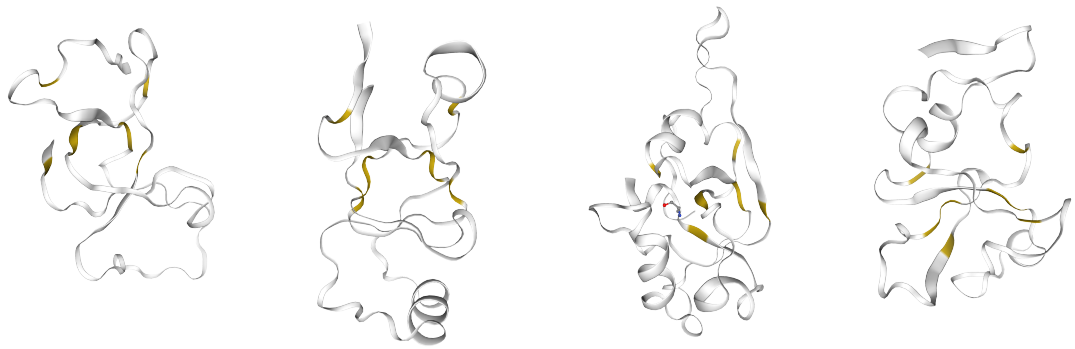

(a) EAS. (b) SC3. (c) rodA. (d) MPG1.

Figure 2.9.: Examples of different class I hydrophobins. (a) EAS (UP-ID: Q04571, PDB-ID: 2fmc) from *Neurospora crassa* (b) SC3 (UP-ID: P16933) from *Schizophyllum commune*. (c) rodA (UP-ID: P41746) from *Aspergillus fumigatus*. (d) MPG1 (UP-ID: P52751, PDB-ID: 2n4o) from rice blast fungus *Magnaporthe oryzae*. Locations of cysteine residues are highlighted in yellow. [146] All representatives show eight cysteine residues and the compact core, however, they vary in length and location of flexible loops. Reproduced from `https://swissmodel.expasy.org/` [146], licensed under CC BY-SA 4.0 license. For more information, visit `https://swissmodel.expasy.org/docs/terms_of_use`.

bic patches on the protein surface [71, 102, 159, 160, 175] and are sometimes compared to janus-like particles in the literature [94, 176]. The high core stability ensures the exposition of a large hydrophobic patch to the protein surface [71, 95, 162], which provides hydrophobins with surfactant like characteristics [72, 160]. Due to their compact structure and high surface activity, hydrophobins spontaneously self-assemble into an amphipathic protein layer at a hydrophilic-hydrophobic interfaces and thereby can change hydrophobic surfaces into hydrophilic ones and vice versa [162, 177]. The patterns in which hydrophobins self-assemble at hydrophobic-hydrophilic interfaces vary between class I and class II hydrophobins. Class I hydrophobins form highly stable rodlet structures, which can only be dissolved by trifluoroacetic acid and formic acid [71]. Depending on the hydrophobin the rodlet diameters vary between 5 nm to 15 nm and their lengths are in the range of hundreds of nanometers [159]. Class II hydrophobins on the contrary assemble in less stable layers, which can be dissolved using ethanol and hot SDS [71]. Class II hydrophobin monolayers consist of highly ordered networks with hexagonal structure [160, 178–180]. The fundamentally different structures formed by class I and class II hydrophobins are shown in Figure 2.10.

Hydrophobins lower the surface tension significantly [92, 94, 161, 162, 174]. Their intermolecular packing at air-water interfaces is very compact and they form strong films at interfaces [17, 94]. These layers of self-assembled hydrophobins at air-water interfaces show a high elasticity due to the strong hydrophobic interaction between hydrophobins [68, 94, 107, 160] and can resist bubble shrinkage caused by Ostwald ripening as well as coalescence [17, 94, 107]. These unique properties make hydrophobins excellent candidates for the stabilization of individual bubbles and assembled foams. Indeed, class II hydrophobins are claimed to form some of the most stable aqueous foams [26, 68, 94, 107, 160] and hydrophobins are also connected to the phenomenon of beer gushing [182].
The industrial applications of hydrophobins are manifold. Their specific properties and ability to alter, bridge and stabilize interfaces are useful in fields such as pharmaceuticals, food products, electronics and microfluidics [183]. In biomedicine, hydrophobins are particulartly advantageous for formulation and delivery of hydrophobic drugs as they improve their solubility in aqueous environments [184–191]. Furthermore, hydrophobins have been used as antimicrobial coatings [192–194], for cell and protein immobilization [195–197] and for surface modification of textile materials [177].

2.2.3. Oat proteins

Oat grains contain 9.70 % to 17.30 % protein [198]. Osborne fractionation classifies grain proteins depending on their solubility. Proteins soluble in salt solution are called globulins, the water-soluble fraction was named albumins, prolamins are soluble in ethanol, and glutelins indicate the insoluble fraction. [199]
In oats, globulins represent 50 % to 80 % [200, 201] of the total protein content and consequently constitute the majority of grain storage proteins. Oat globulins have been further identified as three main fractions with 3S, 7S, and 12S sedimentation

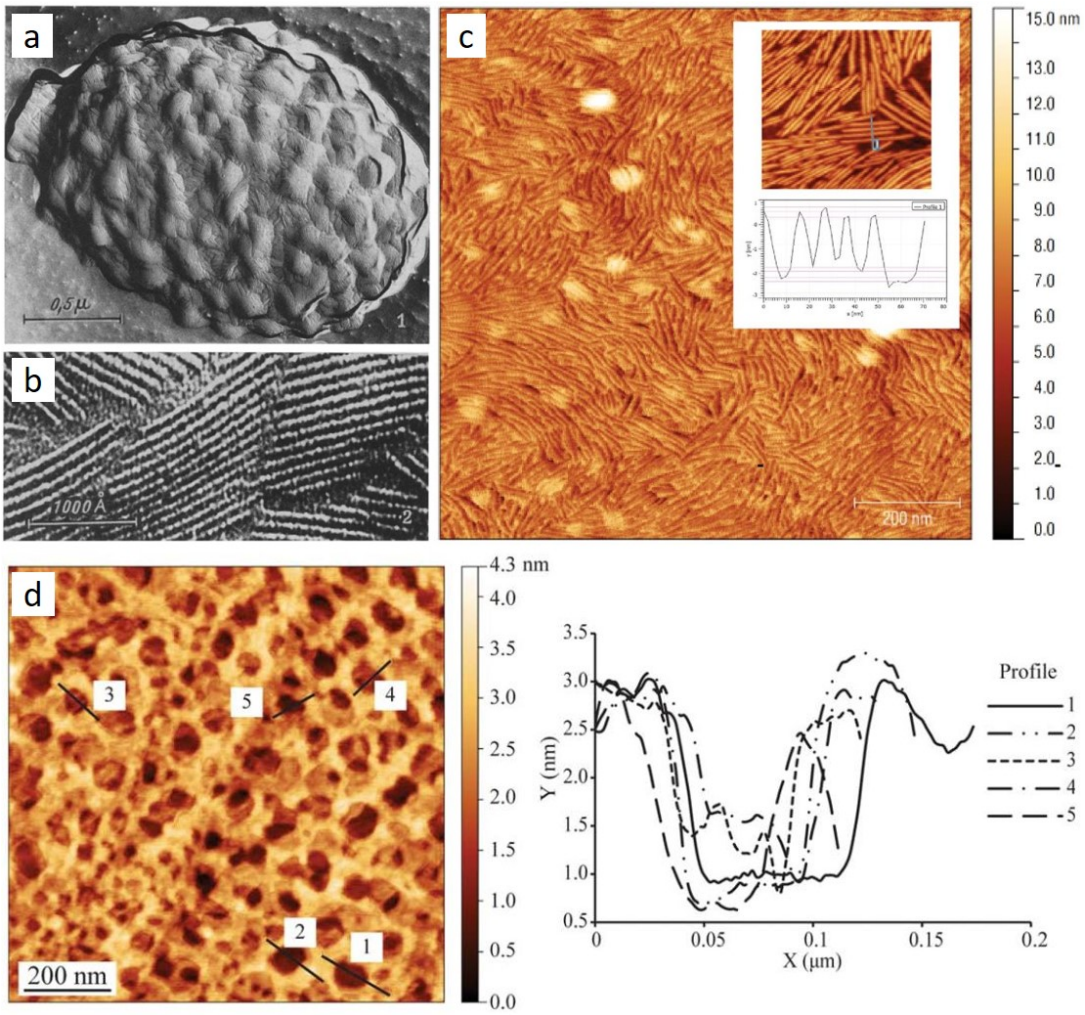

Figure 2.10.: (a) Rodlets at the surface of a spore from *Penicillium herquei*. (b) Fine structure of (a). (c) AFM image of rodlets formed by class I hydrophobin MPG1 from *Magnaporthe oryzae* on highly-oriented pyrolytic graphite (HOPG). The inset shows a height profile of the rodlets. (d) AFM image of a monolayer formed by class II hydrophobin NC2 from *Neurospora crassa* on HOPG. Height profiles of the marked cross sections are shown on the right. (a,b) Reproduced from [181] with permission from Springer Nature. (c) Reproduced from [72] licensed under Creative Commons Attribution 4.0 International License. To view a copy of this license, visit `http://creativecommons.org/licenses/by/4.0/`, no changes made. (d) Reproduced from [71] with permission from Wiley Online Library, © 2013 Wiley Periodicals, Inc.

coefficients [202], where (unlike other grains) the major component in oats is 12S globulin [200]. The 12S storage protein fraction has a molecular weight of 53 kDa to 58 kDa [201] and contains two subunits, the α- and β-subunit. The α-subunit is an acidic polypeptide with a molecular weight of 32 kDa to 37 kDa and an IEP of 5.5. The β-subunit, on the other hand, is a basic polypeptide with a molecular weight of 22 kDa to 24 kDa and an IEP between 8.0 and 10.0 [201, 203]. These α-subunit and β-subunits are disulfide-bound [202]. In its native form, 12S globulin exists as 320 kDa hexamer consisting of 54 kDa subunits, which are held together by disulfide bonds [202, 204]. The shape of 12S globulin is an oblate cylinder with a height of 8.5 nm. This cylinder is formed by two annular trimeric rings with diameters of 11.8 nm stacked on top of each other. [205] The tertiary structure of the 12S globulin is shown in Figure 2.11. The 7S globulins have a molecular weight of 50 kDa to 70 kDa [201] and the 3S fraction has a molecular weight of about 48 kDa to 52 kDa [201].

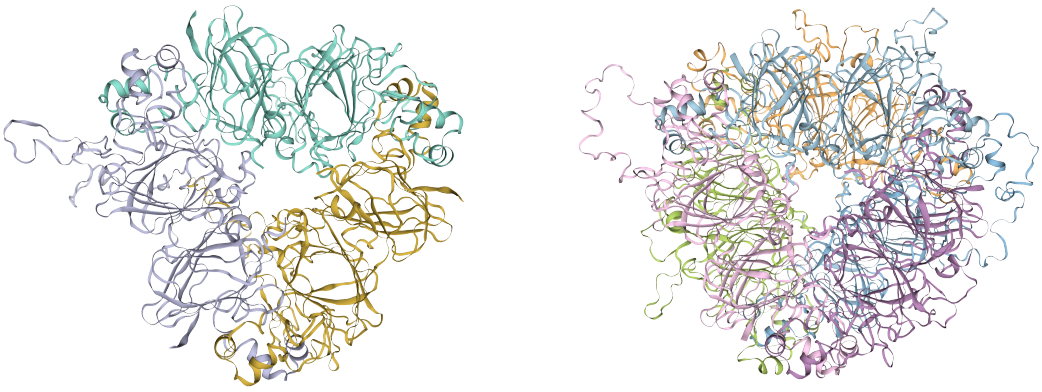

(a) Trimer. (b) Hexamer.

Figure 2.11.: 12S globulin (UP-ID: O49258) [146]. Each chain is highlighted with a different color. Reproduced from `https://swissmodel.expasy.org/` [146], licensed under CC BY-SA 4.0 license. For more information, visit `https://swissmodel.expasy.org/docs/terms_of_use`.

Oats show a low prolamin content with 4 % to 15 % of the total protein ([206, 207] as cited in [200]). These alcohol soluble proteins have a size of 17 kDa to 34 kDa and IEPs between pH 5.0 and 9.0 [201]. Albumins represent 1 % to 12 % of the oat proteins [206]. Different albumin fractions exhibit molecular weights of 14 kDa to 17 kDa, 20 kDa to 27 kDa, and 36 kDa to 47 kDa and IEPs between pH 4 and 7.5 [201]. Glutelins are with less than 10 % a minor fraction and include unextracted globulins and prolamins as well as minor polypeptides [200, 201].

The divers types of oat proteins show fundamentally different structures and vary strongly in surface activity. Figure 2.12 presents an overview of different examples of oat proteins. Globulins are much larger and only little surface-active. Most surface-active are albumins and some prolamins, because their tertiary structure contains a

hydrophobic tail, which facilitates an alignment along hydrophilic-hydrophobic interfaces.

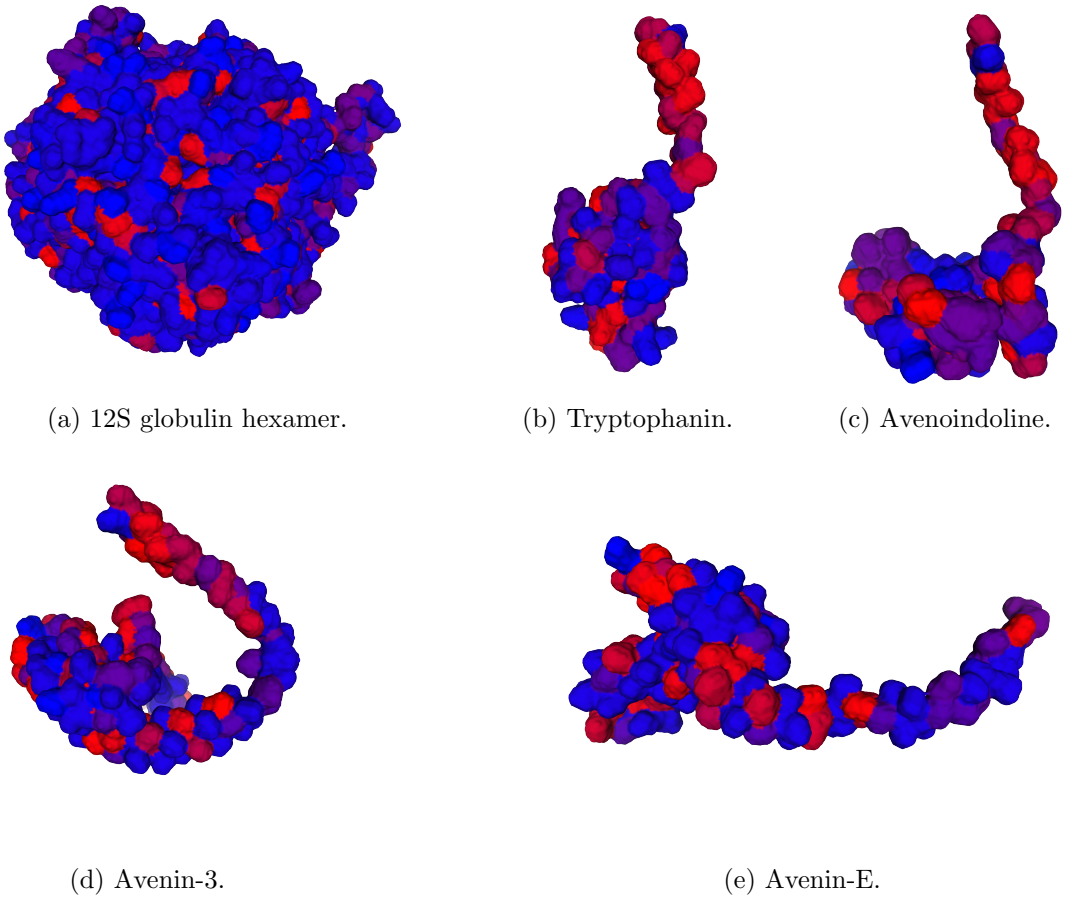

(a) 12S globulin hexamer. (b) Tryptophanin. (c) Avenoindoline.

(d) Avenin-3. (e) Avenin-E.

Figure 2.12.: Examples of oat proteins: (a) 12S globulin (UP-ID: O49258), the albumins (b) tryptophanin (UP-ID: A7U440) and (c) avenoindoline (UP-ID: Q9M4E2) and the prolamins (d) avenin-3 (UP-ID: P80356) and (e) avenin-E (UP-ID: Q09114) [146]. Shown are protein surfaces with hydrophobic amino acids colored in red and hydrophilic amino acids in blue. Reproduced from `https://swissmodel.expasy.org/` [146], licensed under CC BY-SA 4.0 license. For more information, visit `https://swissmodel.expasy.org/docs/terms_of_use`.

2.3. Hydrocolloids

Besides the surface activity of the foaming agent, also other factors such as the viscosity of the solution influence the stability of a foam [208–210]. In many food systems, coarsening is slowed down by gelling or solidifying the continuous phase of the foam [26]. Famous examples are mousses, marshmallows or meringues. Some food systems naturally contain polysaccharides which can act as food thickeners, for example oats contain fibers which thicken oat drink under heating cf. Chapter 7. However, often thickening agents are added to control the texture of a food product [211–215].

Hydrocolloids are long chain hydrophilic polymers, which form viscous solutions or gels when dispersed in water. Their affinity for binding water arises from a large number of hydroxyl groups. In dispersions these molecules show the properties of a colloid and the formed dispersions are intermediate between a suspension and a true solution [216]. Hydrocolloids include polysaccharides extracted from seaweeds, plants and microbial sources, gums derived from plant exudates and biopolymers derived from starch or cellulose by enzymatic treatment [215].

The polysaccharides chosen in this thesis vary in their physical properties e. g. molecular weight, radius of gyration, chain length, charge and flexibility.

The AFM images and representations of the chemical structures of the polysaccharides shown in Section 2.3 originate from my master project and have been published in manuscript [217].

2.3.1. Xanthan gum

Xanthan gum is a polysaccharide produced by bacteria from the genus *Xanthomonas*, mostly *Xanthomonas campestris*, by fermentation of saccharated substrates. In food systems, it is applied to stabilize emulsions, foams and particulate suspensions by significant viscosity enhancement. [211]

Figure 2.13 shows the chemical structure of a xanthan gum repeating unit and an AFM image indicating the stiffness of the molecule. The cellulose backbone of the xanthan gum polymer chain consists of two D-glucose units linked by a glycosidic bond (β-(1→4)-D-glucose). Every second glucose exhibits a trisaccharide side-chain linked to the C-3 atom. This side chain consists of an inner mannose with an acetate group, a glucoronic acid containing a carboxy group, and an outer mannose with a pyruvate group. [211, 212] The pyruvate and carboxy groups provide the side chains with negative charges and impart the xanthan gum molecule a highly negative charge. In a previous study a zeta potential of (-75.0 ± 5.6) mV was measured for the xanthan gum used in this thesis [217]. The negatively charged side chains lead to electrostatic stiffening of the polymer chain. Therefore, in a very simple model xanthan gum molecules can be approximated by stiff negatively charged rods. The length of a xanthan gum molecule has been estimated to be about 1.5 µm [217] and its molecular weight is about 2 MDa [212].

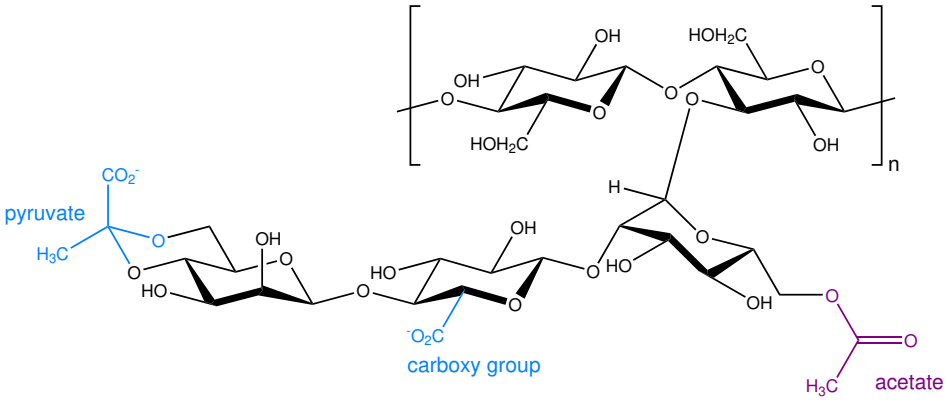

(a) Chemical structure.

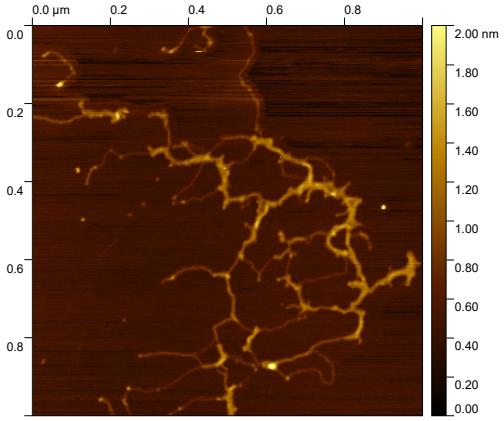

(b) AFM image.

Figure 2.13.: Xanthan gum: (a) Chemical structure of the repeating unit. (b) AFM image of an argon dried droplet of a xanthan gum solution with a concentration of $1\,\mu g\,g^{-1}$.

2.3.2. Guar gum

Guar gum is produced from the seeds of the guar plant *Cyamopsis tetragonoloba* [212]. To produce a powdered guar gum, these seeds are dried, milled and sifted multiple times to remove the hull, followed by washing, flaking, drying and grinding of the guar splits (endosperm halves of the seed) [212].
Figure 2.14 shows the repeating unit of guar gum and an AFM image of the guar gum used in this thesis. The backbone repeating unit of guar gum consists of two β-D-mannopyranose units linked by a (1-4)-glycosidic bond. Every second β-D-mannopyranose unit is linked to a α-D-galactopyranose unit by a (1-6)-glycosidic bond. Guar gum shows a high polydispersity (high variation in degree of polymerization), which is characterized by the ratio of the weight average molecular weight M_w and the number average molecular weight M_n [218]. Weight average molecular weights of guar gum range from 0.4 MDa to 1.7 MDa [218–220]. Thus, its molecular weight is similar to that of xanthan gum or up to a factor 10 smaller. Furthermore, guar gum consists of polar chains and is thus flexible. The flexibility of guar gum is represented in the AFM image, where a self-avoiding walk confined to two dimensions during drying of guar gum is shown.

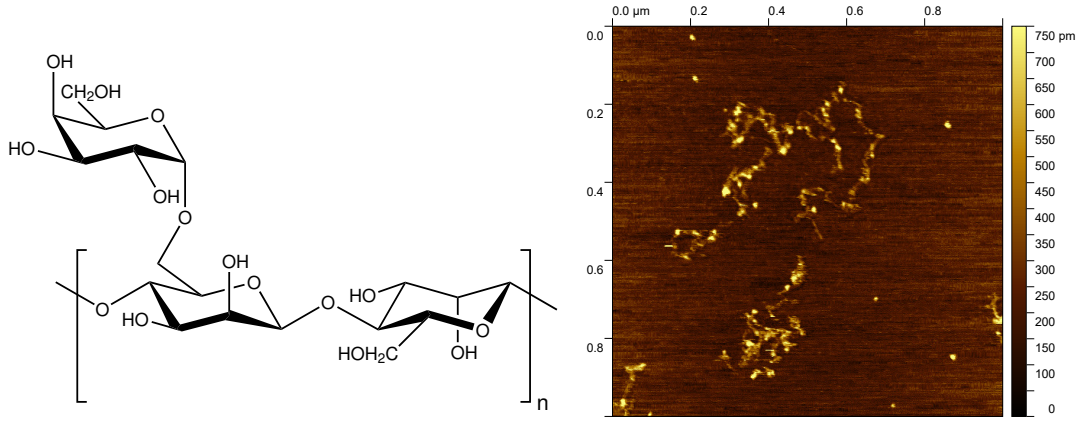

(a) Chemical structure. (b) AFM image.

Figure 2.14.: Guar gum: (a) Chemical structure of the repeating unit. (b) AFM image of an argon dried droplet of a guar gum solution with a concentration of $1\,\mu g\,g^{-1}$.

2.3.3. Iota-carrageenan

Iota-carrageenan is gained from the species *Eucheuma denticulatum* of red seaweed (*Rhodophyceae*), where it fills voids in the cellulose structure. To produce carrageenan gum powders, red seaweed is washed and various alkalis (e. g. sodium, potassium, calcium hydroxide) are applied to extract the polysaccharide. Subsequently, it is filtered, centrifuged, concentrated, precipitated with isopropyl alcohol and dried. [212]

The chemical structure of iota-carrageenan and an AFM image are depicted in Figure 2.15. The repeating unit of carrageenans consists of a disaccharide of a galactose unit

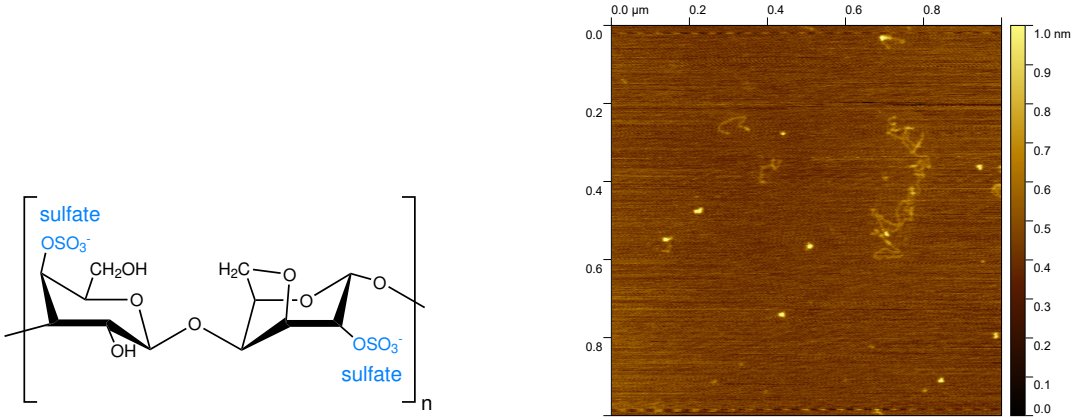

(a) Chemical structure. (b) AFM image.

Figure 2.15.: Iota-carrageenan: (a) Chemical structure of the repeating unit. (b) AFM image of an argon dried droplet of a iota-carrageenan solution with a concentration of $1\,\mu g\,g^{-1}$.

and a 3,6-anhydrogalactose, which are linked by alternating alpha-(1,3) and beta-(1,4) glycosidic links. The galactose units can be sulfated or non-sulfated. Varying anhydrogalactose contents, sulfate contents and sulfate distributions lead to different types of carrageenans. For iota-carrageenan both galactose units are sulfated and it contains an 3,6-anhydrogalactose content of 26 % and a sulfate content of 32 %. The sulfates are negatively charged and make iota-carrageenan a negatively charged polyelectrolyte. [212] However, the iota-carragenan used in this thesis is less negatively charged than the employed xanthan gum [217]. Since it does not contain any side chains the molecule is still quite flexible and in a simple model behaves like a negatively charged polymer chain. In the AFM image, the iota-carrageenan chain appears very flexible and performs a self-avoiding walk (during drying confined to two dimensions), which is stretched due to the negative charge of the molecule.
The molecular weights of carrageenans are typically in the range of 200 kDa to 800 kDa [212] and thus lower than for xanthan gum and similar to low molecular weight guar gum.

2.4. Interactions

2.4.1. Molecular interactions

Due to their molecular properties, particles such as proteins or polysaccharides interact with each other. Some of these interactions shall be shortly introduced here. The following section on molecular interactions is based on the information provided in the textbooks by Butt et al. [118], Raychaudhuri [221], Israelachvili [222], Dhont [223], Atkins et al. [224], and Lyklema [225].

Electrostatic interaction describes the force acting between electrical charges. In the vicinity of an electrical point charge, an electrical field is generated which exerts a force on other electrical charges. The force between two point charges is directed along the line that joins the two charges. The interaction between like charges is repulsive, whereas the interaction between unlike charges is attractive. The resulting force acting on one point charge is determined by the linear superposition of the forces caused by other surrounding charges. Coulomb's law provides a mathematical description of the long range interaction of electrical point charges. For two point charges with magnitudes e_1 and e_2 located at a distance R from each other in vacuum, the force $\vec{F}_2$ acting on e_2 is given by:

$$\vec{F}_2 = \frac{1}{4\pi\varepsilon_0}\frac{e_1 e_2}{R^3}\vec{R} \tag{2.4}$$

where $\vec{R}$ is the vector joining the two charges and is directed from e_1 to e_2 and ε_0 is the permittivity of the free space. The potential energy in this case is given by

$$W_{el} = \frac{e_1 e_2}{4\pi\varepsilon_0 R} \tag{2.5}$$

In the frame of this study, proteins and hydrocolloids dissolved in water are investigated. Water is a good solvent for ions due to its high relative permittivity. For charged particles in a suspension, the surface charges cause an electric field and attract counterions, which then form a layer along the charged surface. The term *electric double layer* denotes the layer of surface charges together with the counterions. In a simple model, the counterions are considered to be directly bound to the surface and to neutralize the surface charges. Therefore, the electric field caused by the surface charges is restricted to the thickness of a monolayer of counterions. This layer is called *Helmholtz* layer. However, thermal fluctuations cause the counterions to move, which was considered by *Gouy-Chapman*. Due to the thermal motion, the counterions tend to move away from the surface and consequently form a diffusive layer, which is thicker than a monolayer of molecules. *Debye-Hückel* determined the potential and the ion distribution around spherical surfaces for this approach. In this case, the molecular nature of the solvent is neglected and instead it is treated as a continuous medium. For an infinitely extended planar surface with a low potential ($e|\psi| \ll k_b T$),

the solution of the linearized *Poisson-Boltzmann* equation is the potential given by

$$\psi(x) = \psi_0 \exp(-\kappa x) \tag{2.6}$$

with

$$\kappa = \Big(\frac{2c_0e^2}{\varepsilon\varepsilon_0 k_B T}\Big)^{1/2} \tag{2.7}$$

where e is the elementary charge, c_0 is the ion concentration, ε and ε_0 are the relative permittivity and the permittivity of free space, k_B is the Boltzmann constant and T is the temperature. The potential decreases exponentially with the decay length, called Debye length,

$$\lambda_D = \kappa^{-1} \tag{2.8}$$

The *Graham* equation gives the relationship between the charge of the surface σ and the potential ψ_0 based on the Gouy-Chapman theory. A requirement is that the total charge (charges of the surface plus all ions in the double layer) is zero. For low potentials it holds

$$\sigma = \frac{\varepsilon\varepsilon_0\psi_0}{\lambda_D} \tag{2.9}$$

The ideas of Helmholtz were combined with that of a diffuse layer by *Stern*. In this model the electric double layer is devided into two parts. The inner part contains an immobile layer of ions directly adsorbed to the surface, which is called Stern layer. The outer part comprises mobile ions obeying Poisson-Boltzmann statistics and is called Gouy or diffusive layer. Due to the finite size of the counterions, which may include a hydration shell in water, there is a distance δ between the charged surface and the center of the counterions in the Stern layer. The distance δ marks the outer Helmholtz plane. Figure 2.16 illustrates the Helmholtz, Gouy-Chapman and Stern models.

Van der Waals interactions (vdW interactions) consider dipole-dipole interactions between molecules. Three contributions are distinguished: The Keesom, Debye and London interactions:

$$C_{total} = C_{orient} + C_{ind} + C_{disp} \tag{2.10}$$

where C_{total} is the total van der Waals coefficient, C_{orient} the coefficient of the Keesom contribution, C_{ind} the coefficient of the Debye interaction and C_{disp} the coefficient of the London or dispersion interaction. The potential energy of vdW interactions scales with R^{-6}:

$$W_{vdW} = -\frac{C_{total}}{R^6} \tag{2.11}$$

where R is the distance between the considered molecules.

Molecules with neutral net charge can develop an uneven distribution of electric charge resulting in a more positively charged and a more negatively charged side of the

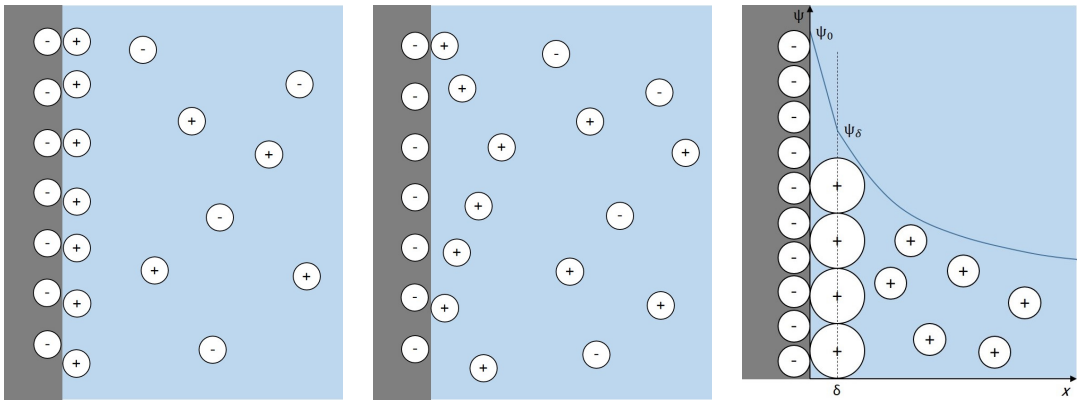

(a) Helmholtz (b) Gouy-Chapman (c) Stern

Figure 2.16.: Electric double layer: (a) Helmholtz model, (b) Gouy-Chapman model and (c) Stern model with δ the distance of the outer Helmholtz plane from the surface, ψ_0 the potential at the surface and ψ_δ the potential at the outer Helmholtz plane.

molecule. In this case, their electric properties are described by the dipole moment μ

$$\vec{\mu} = \int \rho_e(\vec{r})\vec{r}dV \tag{2.12}$$

where ρ_e is the charge density and integration is over the volume of the whole molecule. Freely rotating dipoles such as in mobile molecules orient themselves with regard to other charges or dipole moments. However, thermal fluctuations impede a perfect orientation. Still, a net preferential orientation remains on average.

The *Keesom* interaction describes the interaction of two freely rotating dipoles. These attract each other since they preferentially orient in a way that their opposite charges face each other. The Helmholtz free energy of this randomly oriented dipole-dipole interaction is given by

$$W_{orient} = -\frac{C_{orient}}{R^6} = -\frac{\mu_1^2\mu_2^2}{3(4\pi\varepsilon_0)^2 k_B T R^6} \tag{2.13}$$

where entropic effects are considered, which means that the orientation of one dipole is affected by the field of the other dipole. μ_1 and μ_2 denote the dipole moments, R the distance between the two dipoles, ε_0 the permittivity of free space, k_B the Boltzmann constant and T the temperature.

A charge approaching a molecule without static dipole moment induces a dipole moment in the before non-polar molecule, which interacts with the approaching charge. The *Debye* interaction describes the interaction of a molecule containing a static dipole moment with a polarisable molecule. For different molecules the Helmholtz free energy

for a freely rotating dipole is

$$W_{ind} = -\frac{C_{ind}}{R^6} = -\frac{\mu^2 \alpha}{(4\pi\varepsilon_0)^2 R^6} \tag{2.14}$$

where μ is the dipole moment and α is the polarizability. For identical molecules a factor of two has to be multiplied.
The attraction of non-polar molecules is described by the *London* force, which is also called dispersion force. Consider an atom with a positively charged nucleus and electrons circulating around the nucleus with a high frequency. Then, the atom is polar with the direction of the polarity changing with high frequency. If two such oscillators approach, these influence each other. The probability of attractive orientations is higher than that of repulsive ones leading to an attractive force on average. To calculate this interaction, quantum mechanical perturbation theory is used. For two molecules with ionization energies $h\nu_1$ and $h\nu_2$ the Helmholtz free energy is approximated by

$$W_{disp} = -\frac{C_{disp}}{R^6} = -\frac{3}{2}\frac{\alpha_1 \alpha_2}{(4\pi\varepsilon_0)^2 R^6}\frac{h\nu_1\nu_2}{(\nu_1+\nu_2)} \tag{2.15}$$

where α_1 ans α_2 denote the polarizabilities of the two molecules, ν_1 and ν_2 are the frequencies of their electrons and h is the Planck constant. This interaction increases with the polarizability of the two molecules.

Hydrophobic interactions act between hydrophobic surfaces, molecules or parts of molecules and cause these to attract each other. This interaction is mainly of entropic reason and decays roughly exponentially. The origin of hydrophobic interactions comes from a change in the water structure when two hydrophobic surfaces approach or a hydrophobic molecule is inserted into water. Because such molecules are apolar, water cannot form hydrogen bonds with hydrophobic molecules and forms a "cage" around the hydrophobic molecule. This requires a reorientation of the water molecules and is entropically unfavorable. For this reason, water expels hydrophobic molecules, which leads to a spontaneous aggregation of hydrophobic molecules or their adsorption to air-water interfaces. The rearrangement of water molecules involves a high number of molecules and therefore leads to a long range of this interaction. Hydrophobic interactions have important implications on the dynamics of micelle formation, interfacial self-assembly of amphiphilic molecules and protein folding.

Steric interactions When the outer segments of two polymer coated particles interpenetrate, the segment concentration in the overlap region increases. The confinement of the chains reduces their entropy. Due to osmosis, solvent molecules are drawn into the overlap region and a repulsive force between the particles occurs. Also the conformation of a single polymer chain is determined by steric interaction. The spatial extent and the excluded volume of the polymer segments reduce the configuration entropy and result in repulsive forces. If two polymer chains approach, their thermal movement becomes limited and the entropy of the individual polymer chain decreases.

Comparison of interaction ranges The interplay of electrostatic, van der Waals, hydrophobic and steric interactions defines protein and polysaccharide conformations as well as the intermolecular interactions in the foam system and the arrangement of proteins at air-water interfaces.

Electrostatic interactions can be attractive or repulsive depending on the signs of the charges. At long distances the net molecular charge dominates the intermolecular interaction. However, at short distances the charges of single amino acids of a protein interact with other amino acids within the protein or of a neighbor. These short range electrostatic interactions define protein conformations and intermolecular interactions of proteins with neutral net charges. The potential energy of electrostatic interactions decays with

$$W_{el} \sim \pm\frac{1}{R} \tag{2.16}$$

which means that the strength of the interaction is defined by the distance R between the charge.

Van der Waals interactions are attractive forces and their potential energy decays with

$$W_{vdW} \sim -\frac{1}{R^6} \tag{2.17}$$

It decays much faster with the distance R than electrostatic interactions and is therefore only relevant at short distances, i. e. when molecules come close to each other.

Steric interactions are very short ranged and become important when particles are squeezed together such as during a collision of two molecules. This interaction is repulsive and the potential energy is often estimated by

$$W_s \sim \frac{1}{R^{12}} \tag{2.18}$$

At very short interparticle distances, steric repulsion dominates van der Waals attraction, however it decays rapidly and is therefore dominated by other interactions at increasing interparticle distances.

Hydrophobic interactions in water are much stronger than van der Waals interactions and show a longer range than typical covalent bonds [226, 227]. The potential energy of hydrophobic interaction decays exponentially

$$W_h \sim -\exp\left(-\frac{R}{D_0}\right) \tag{2.19}$$

with a decay length $D_0 \sim 1\,\mathrm{nm}$ and an effective range of the interaction of roughly up to 20 nm [226–229].

The R-dependency of the discussed interactions is shown in Figure 2.17. Due to prefactors the strength of the interaction may vary according to the investigated system. For better comparison only the magnitudes are shown without considering whether the interaction is attractive or repulsive. However, a rough impression of the interaction is gained from the plot.

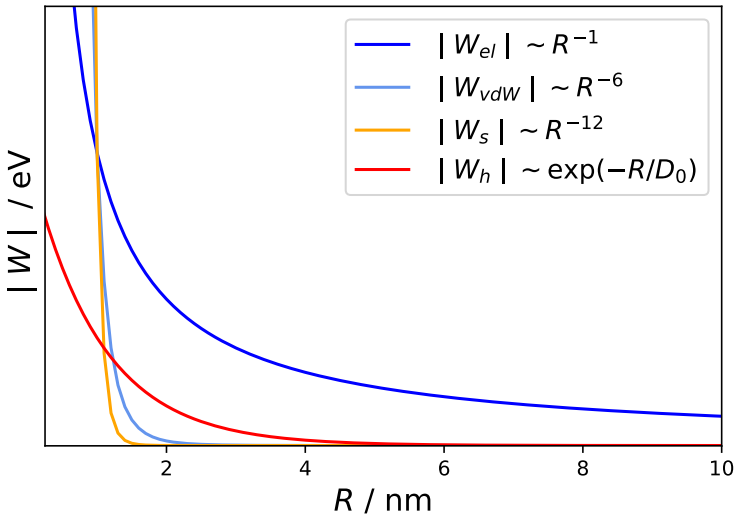

Figure 2.17.: Range of electrostatic, van der Waals, steric and hydrophobic interactions.

This short discussion shows, that electrostatic interactions have the longest range and that the dynamics of interfacial protein arrangements is mainly an interplay of electrostatic and hydrophobic interactions. At short distances also van der Waals attraction plays a role and at further decreasing distances steric interactions contribute.

2.4.2. Influence of particle size and shape on solution viscosity

The viscosity of a suspension of very small rigid spheres in a liquid is increased compared to the pure liquid as shown by Einstein:

$$\eta_{sus} = \eta(1 + 2.5v) \tag{2.20}$$

where η is the viscosity of the liquid and v is the total volume of the spherical particles [230, 231]. The spherical particles do not need to be of the same size. However, the suspension should be sufficiently dilute and the particles should not form aggregates [232]. Jeffery extended this equation to ellipsoidal particles and showed that it is of the same form, but the factor 2.5 needs to be replaced by a coefficient, which depends on the ellipticity of the spheroid [232]. For ellipsoidal particles, there are two opposing effects acting on their orientation: the hydrodynamic shear tends to align them in the direction of flow, whereas the Brownian motion tends to randomize their orientations [233]. In flow, anisotropic particles change their orientation and thereby alter the behavior of the suspension. Various simulations show that the precise orientation depends on various parameters such as the initial orientation and the Deborah number [234].
Besides the particle shape also the size (volume) of the particles influences the viscosity

of a particle suspension. Therefore, the intrinsic viscosity of dilute polymer solutions is given by

$$[\eta] = \nu \cdot v_s \tag{2.21}$$

where ν denotes the molecular shape parameter (also called viscosity increment) and v_s is the swollen specific volume. Due to solvent association, an anhydrous molecule swells when it is dissolved or suspended. v_s is given by the volume of the macromolecule in solution per unit anhydrous mass of the molecule and is a measure of the solvent association with the macromolecule. [233]

Also the flexibility of the molecules reflects in the viscosity of the suspension. The Mark-Houwink-Kuhn-Sakurada (MHKS) relations describe the dependence of the intrinsic viscosity $[\eta]$ on the molecular weight M for such molecules.

$$[\eta] = K' M^a \tag{2.22}$$

where K' and a are both parameters which depend on the polymer conformation and M is the molecular weight of the regarded molecule. There are three extremes of particle conformations to be distinguished: the compact sphere, rigid rod and random coil, which are reflected in the value of a. The values for a vary between 0 for a compact sphere, 0.5 to 0.8 for a random coil and 1.8 for a rigid rod. [233] For this reason, different viscosities are expected for guar gum, iota-carrageenan and xanthan gum, which vary in flexibility as described above (Section 2.3). Foams containing these polysaccharides are investigated in Chapter 5.

2.4.3. Influence of particle charge on solution viscosity

Electroviscous effects describe the component of the viscosity caused by the particle charge [235]. These cause an additional resistance to the flow of the sample and consequently increase the solution viscosity [91]. Therefore, for protein solutions the viscosity is minimal at the isoelectric point (net charge of protein is zero) and increases with increasing or decreasing pH. For BSA solutions this behavior has been observed at concentrations below $150\,\mathrm{mg\,mL^{-1}}$; for higher concentrations contributions of short-range attractive interactions increase and a different pH-dependency of the viscosity is observed. [91]

Electroviscous effects are classified into three contributions. The primary effect describes the resistance caused by the diffuse double layer which surrounds the charged molecule. The secondary effect is based on intermolecular repulsions between double layers of different molecules. Furthermore, the interparticle repulsion may affect the shape of the molecule, which influences the viscosity of the sample and is described by the tertiary effect. [91, 233] As the net charge of a protein increases, the protein conformation may also change to increase the distance between charges. In this case, the volume increase of the molecule also contributes to an increase in the viscosity [236].

The viscosity increase caused by the primary electroviscous effect is given by:

$$\eta_{el} = \eta_0 \left[1 + \frac{5v}{2V} \left\{ 1 + \sum_{1}^{\infty} b_n \left(\frac{e\zeta}{k_B T} \right)^n \right\} \right] \tag{2.23}$$

where η_0 denotes the viscosity of the liquid, v the volume of the solid and V the total volume of the mixture, b_n are coefficients, e is the electronic charge, ζ the zeta-potential, k_B Boltzmann's constant and T the absolute temperature [237].
Tanford et al. [236] investigated BSA solutions at varying pH (i. e., molecular charge) and stated that the viscosity increases as the molecule becomes charged due to two factors: the electrostatic interaction with the surrounding ions and a volume increase caused by conformational changes.

2.4.4. Influence of viscosity on foam stability

The bulk viscosity of the continuous phase affects the drainage of liquid from the lamellae. An increased viscosity slows down drainage. Due to the reduced drainage the lifetime of the film between bubbles is extended, which means that the rate of coalescence is lower, and therefore the foam stability is enhanced. [90, 210, 238] Furthermore, a higher viscosity of the continuous phase slows down the mobility of gas bubbles and thereby reduces the creaming rate of the bubbles [107, 238, 239].
To stabilize a foam by enhancing the viscosity of the continuous phase, thickening agents can be added to the solution [208, 238]. Such continuous phase stabilizers are not surface-active and usually polymers such as polysaccharides are used. However, depending on their molecular properties, these may also cause destabilizing effects such as isotropic/anisotropic phase separations, bridging and depletion flocculation (if the emulsifier (protein) and the thickening agent (polysaccharide) interact) and the inhibition of protein adsorption. [238] Geometrical differences between rod-like stabilizer molecules and spherical bubbles can cause a phase separation which is in agreement with Flory's theory [217, 238, 240–243]. Furthermore, also the formation of aggregates of surfactants in the bulk leads to a viscosity increase [244].

2.5. Methods

2.5.1. Atomic force microscopy

Atomic force microscopy (AFM) is a 3D surface mapping technique to investigate soft and rigid samples with sub-nanometer to micrometer resolution in vacuum, air, or liquids. [245, 246]
The method of AFM was invented by Binnig et al. [247] in 1986. The sample surface is scanned with a sharp tip (atomic-sized) attached to a cantilever and the forces created on the tip by the proximity to the sample surface are measured [247]. Contact mode or dynamic mode, which is also called AC mode, intermittent contact mode or tapping mode, are applied. During operation in contact mode a constant contact force between tip and sample surface is maintained. Using dynamic mode the oscillation amplitude is kept constant as the tip bounces off the surface of the sample. Therefore, dynamic mode involves an oscillation of the cantilever just above the sample surface at a frequency close to its resonance frequency. The most common form of dynamic mode uses an amplitude of the free oscillation of the cantilever, which is slightly larger than the nominal tip/surface distance. When the tip approaches the sample surface, the oscillation amplitude, phase and frequency are modulated. To keep the amplitude of the oscillation at a constant level, a feedback loop is used. [245]
Figure 2.18 shows the working principle of a typical AFM instrument in dynamic mode. At the center of the figure, the cantilever with the sharp tip (probe), which

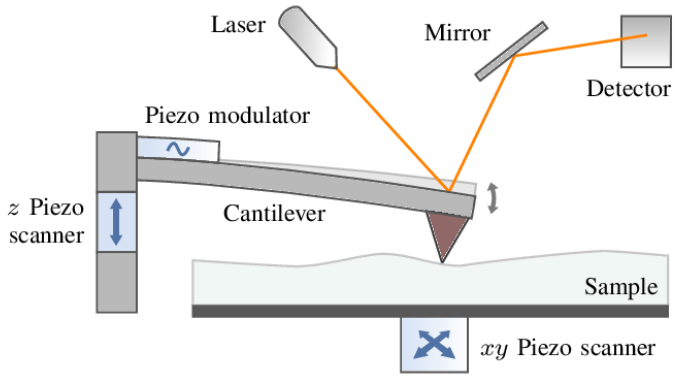

Figure 2.18.: Setup of the AFM dynamic mode. © 2019 IEEE. Reprinted, with permission, from [246].

is used to scan the sample, is shown. The very thin tip allows for a very high x-y resolution [248]. The cantilever beam is oscillated at its resonance frequency by a small piezoelectric element, the piezo modulator [247]. Piezoelectric materials convert electrical potential into mechanical motion and vice versa. Piezo scanners are used to move the AFM tip relative to the sample surface and to adjust and maintain the tip-sample distance [248]. Below the cantilever the sample holder with the sample is placed. A laser beam is focused on the cantilever above the probe, where it is

reflected and guided to the detector. The signal is used to measure the deviation of the cantilever tip (optical lever). AFM instruments typically also contain an optical microscope, control electronics and a computer. The optical microscope is used to locate the tip above the sample surface. Control electronics generate signals that drive the scanners and digitize AFM signals to be recorded and displayed on the computer. With the computer parameters can be set by the instructor. The control electronics uses these values to drive the AFM accordingly while handling the signals coming from the force sensor. With these information the piezoelectric scanner is operated in a way that the tip-sample distance is maintained. If there is a particle on the sample surface, i. e. the height profile goes up, the force between tip and surface is increased. The feedback control then moves the piezoelectric scanner away from the sample. On the other hand, if the force sensor measures a smaller force than before, the piezoelectronics move the tip closer to the surface. By detecting these signals a height profile of the sample surface is obtained. [248]
Because of its high resolution (structures in the nm- and µm-range can be seen), AFM is used in this thesis to obtain a detailed view on the interfacial arrangement of HP and BSA. To mimic the air-water interface, the hydrophobic substrate highly-oriented pyrolytic graphite (HOPG) is used.

2.5.2. Brewster angle microscopy

Brewster angle microscopy (BAM) is a reflection technique used for real-time visualization of the lateral organization of monolayers at the air-water interface including phase separation and domain formation. [249] The method of BAM was developed by two groups independently and published in 1991 [250, 251]. Figure 2.19 shows the working principle of BAM. A parallel (p) polarized laser beam is directed onto

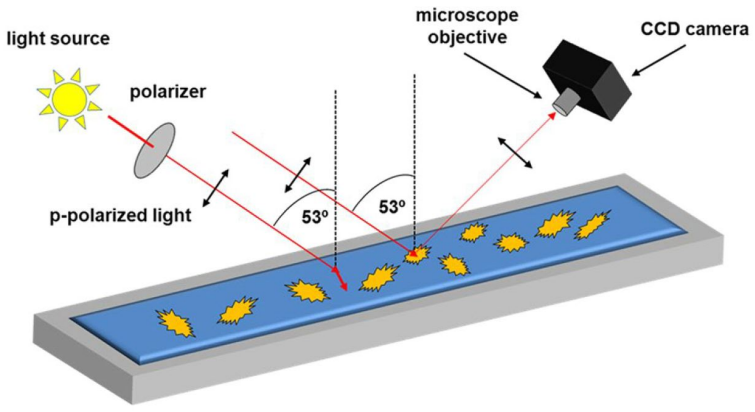

Figure 2.19.: Working principle of BAM. Reproduced from [252] with permission from Springer Nature.

an air-water interface at the Brewster angle, which is roughly 53° for pure water. If p-polarized light is directed at an interface under the Brewster angle, the reflected

p-polarized beam has zero intensity. Therefore, for pure water, no light is reflected. Adding a monolayer of surface-active molecules at the air-water interface results in a change of the refractive index. Consequently, the Brewster angle changes and p-polarized light is reflected by the interface, which is detected by the camera. [249, 252, 253]
Advantages of BAM are the real-time imaging under full hydration of the interface and that no labeling is required, which could disturb the molecular interactions. In comparison to other microscopic techniques a disadvantage is however, that a poorer contrast is achieved, which cannot be tuned by using different types of dyes. [249, 252] Although the resolution is not as precise as with AFM (several µm-range for BAM), BAM is tested in this thesis, because it allows to image the air-water interface directly.

2.5.3. Differential scanning calorimetry

Differential scanning calorimetry (DSC) determines thermodynamic properties of macromolecules [254]. The method was developed by Watson et al. [255] in 1962 [255]. The fundamental working principle is represented in Figure 2.20. At the center

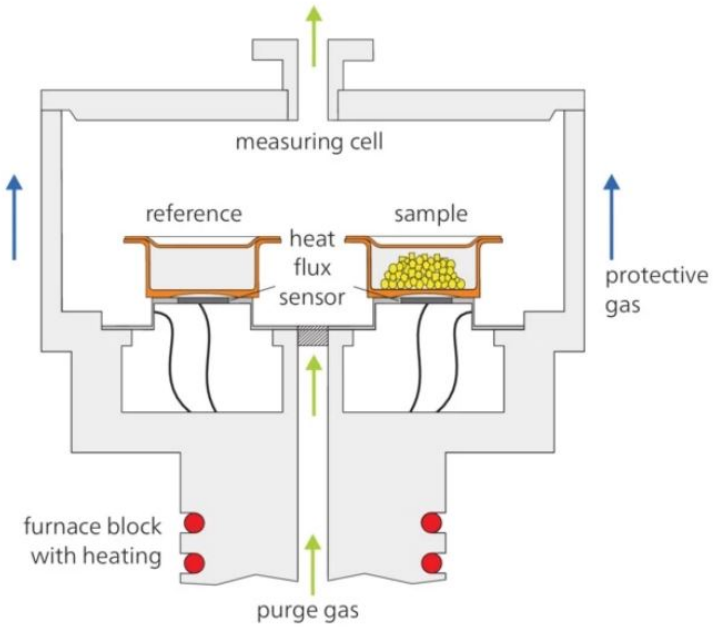

Figure 2.20.: Working principle of DSC. Reproduced from [256] with permission of NETZSCH-Gerätebau GmbH, Selb, Germany.

of the DSC instrument, there are two crucibles, the measurement cell, which contains the sample, and a reference cell. These cells are surrounded by an adiabatic jacket (or several adiabatic jackets), which prevents heat exchange with the environment. The cells and adiabatic jacket are heated with a precise temperature ramp. Heat

flux sensors measure and control the temperature in the measurement and reference cell. Heating triggers thermal transformations in the sample. In a protein solution for example, the native conformation of the protein unfolds into a self-avoiding coil, which can happen at once or with several intermediate, partly unfolded states. When a transformation occurs induced by heating the sample, a part of the supplied heating capacity is needed for the transformation of the molecule. The heating of the sample cell becomes slower and a temperature difference between sample cell and reference cell occurs. This temperature difference is detected by the sensors and the sample cell is supplied with an additional heating capacity to compensate for the temperature difference. This differential heating capacity is the actual measurement parameter, which is recorded as a function of time or temperature, respectively. [257] Depending on whether the transition is endothermic or exothermic, heat is absorbed or released by the sample. [258]
When a mixture of proteins is investigated and a shift of their denaturation temperature as compared to that of the pure components is observed, it can be concluded that these proteins interact. Therefore, DSC is used in the current study to learn about whether HP and BSA interact with each other.

2.5.4. Dynamic light scattering

Dynamic light scattering (DLS) is used to determine the size distribution of nanomaterials. More precisely, the hydrodynamic radius R_h of particles in solution is measured without shearing or the need for filtration or chromatographic separation. [259] This method can be applied, for example, to investigate the homogeneity of proteins, nucleic acids, or protein–protein complexes as well as interactions of proteins with small molecules [260].
Particles in solution perform a random movement (Brownian motion). For polymers, every monomer underlies Brownian motion restricted by the connectivity of the monomers in the polymer chain. In DLS, monochromatic light from a laser is focused on the sample, where it is scattered at the sample particles. Their motion causes local density fluctuations and concentration changes. When scattered light from two or more such macromolecules interferes, there is a changing destructive and constructive interference creating speckles, which leads to temporal fluctuations in the measured intensity of the scattered light. [261–263] The diffusion of smaller particles is faster, which leads to more rapid intensity fluctuations. In contrast, larger particles diffuse slower and show slower intensity fluctuations. [261] Figure 2.21 illustrates the working principle of DLS.
These temporal fluctuations are detected by a single photon counting module [261]. From that, the intensity correlation function $G_2(\tau)$ is obtained, which describes the motion of the investigated particles

$$G_2(\tau) = \langle I(t)I(t+\tau)\rangle \tag{2.24}$$

where $I(t)$ is the intensity at the time t and $I(t+\tau)$ is the intensity at a delayed time

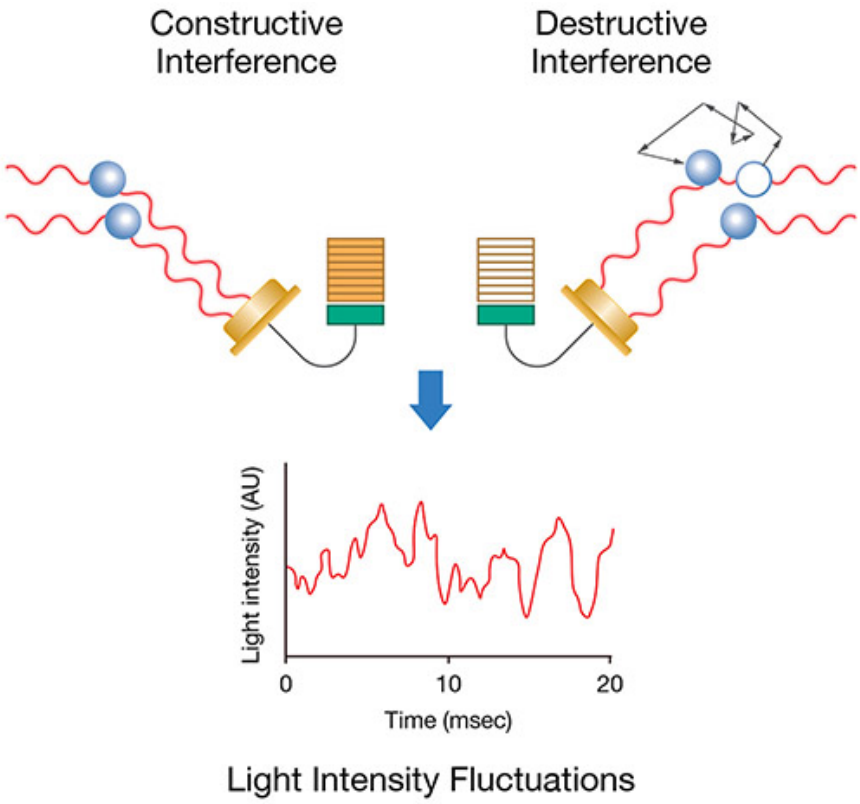

Figure 2.21.: Working principle of DLS. The light scattered at moving particles (Brownian motion) interferes constructively and destructively, which results in time-dependent fluctuations in the intensity of the scattered light. From the rate of fluctuations the diffusion coefficient and finally the hydrodynamic radius is obtained. Reproduced from [261] with permission of Wyatt Technology™, a portfolio of Waters Corporation™, Santa Barbara, CA, USA.

$(t + \tau)$, τ denotes the lag time between the two time points and $\langle\rangle$ means averaging over t. [260, 262, 263] $G(\tau)$ can be normalized as

$$g_2(\tau) = \frac{\langle I(t)I(t+\tau)\rangle}{\langle I(t)\rangle^2} \tag{2.25}$$

Electric field correlation functions $G_1(\tau)$ and $g_1(\tau)$ are analogously defined for the electric field instead of the intensity. [260] $g_1(\tau)$ and $g_2(\tau)$ are related by the Siegert equation, which assumes homodyne scattering and a random Gaussian process for photon counting:

$$g_2(\tau) = B + \beta|g_1(\tau)|^2 \tag{2.26}$$

with the baseline $B \sim 1$ and the coherence factor β, which depends on the measurement setup [260, 264]. Short time delays result in a high correlation, because the macromolecules do not have the chance to move and the signal remains unchanged. For longer time delays on the other hand, the correlation decays exponentially. [262]
For monodisperse particles, a single exponential decay is detected:

$$g_1(\tau) = \exp(-\Gamma\tau) \tag{2.27}$$

where Γ denotes the decay rate. [260, 262]
The translational diffusion coefficient D_τ is derived from

$$\Gamma = -D_\tau q^2 \tag{2.28}$$

with the Bragg wave vector q

$$q = \frac{4\pi n_0}{\lambda}\sin\frac{\theta}{2} \tag{2.29}$$

where λ denotes the wavelength of the incident light from the laser, n_0 the refractive index of the solvent and θ the angle at which the detector is located. [260, 262]
Signals from the scattered light can be detected at one angle or at a range of angles. Also the angular dependency tells something about the nature of the particles in the sample. This is especially relevant for polydisperse samples with unknown particle size distributions. In this case, each particle species in the sample causes an exponential decay and the autocorrelation function is a sum of these exponential decays. [262]
Figure 2.22 shows an autocorrelation function typical for a monodisperse sample.
The translational diffusion coefficient D_t is determined by automated non-linear least squares fitting of the autocorrelation function. For fitting the autocorrelation function different methods are used depending on the sample composition. For samples with only one exponential decay the cumulant method can be applied. This method assumes one population of particles, which has a single average diffusion coefficient with a single standard deviation. It is used to fit monomodal samples, which are monodisperse or polydisperse, e. g. nanoparticles or proteins with populations of monomers, dimers and small oligomers. The hydrodynamic radius R_h is the radius of a hard sphere with the same diffusion coefficient as the particles in the sample. It is calcu-

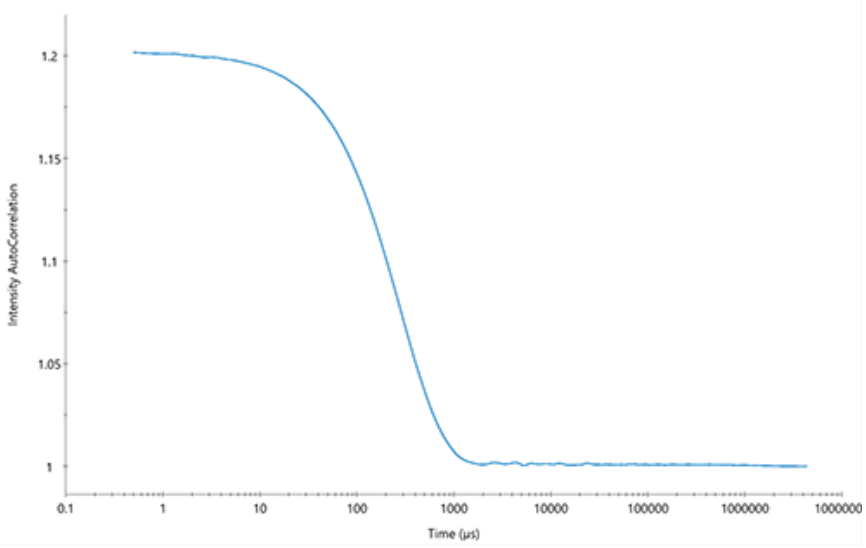

Figure 2.22.: Typical autocorrelation function of a monodisperse sample as obtained from DLS. The particles have a $R_h = 50\,\mathrm{nm}$. Reproduced from [261] with permission of Wyatt Technology™, a portfolio of Waters Corporation™, Santa Barbara, CA, USA.

lated from the Stokes-Einstein equation

$$R_h = \frac{k_B T}{6\pi\eta D_\tau} \tag{2.30}$$

where k_B denotes the Boltzmann constant, T the absolute temperature and η the solvent viscosity. [260–262] Additionally, the polydispersity of the sample can be obtained as a fit parameter.

For multimodal, heterodisperse, and polydisperse systems the cumulant method is not sufficient to obtain good fit results as is demonstrated in Figure 2.23. An alternative is the CONTIN algorithm [265–267], also known as regularized fit or regularization method, which uses an inverse Laplace transform for analysis of the autocorrelation function. The regularization method can be applied for samples where any number of populations of particles is present, where each population has its own diffusion coefficient, polydispersity, and standard deviation. This method can resolve particle species differing by more than 2 times in size and can therefore be used for the identification of large aggregates and insoluble species in protein samples. [261, 262]

The size of proteins may vary depending on the solution pH due to changes in the charges of the amino acids and aggregation may occur at pH values close to the isoelectric point [60, 268]. For this reason, dynamic light scattering is used in this project to measure the size of dissolved BSA molecules at varying pH.

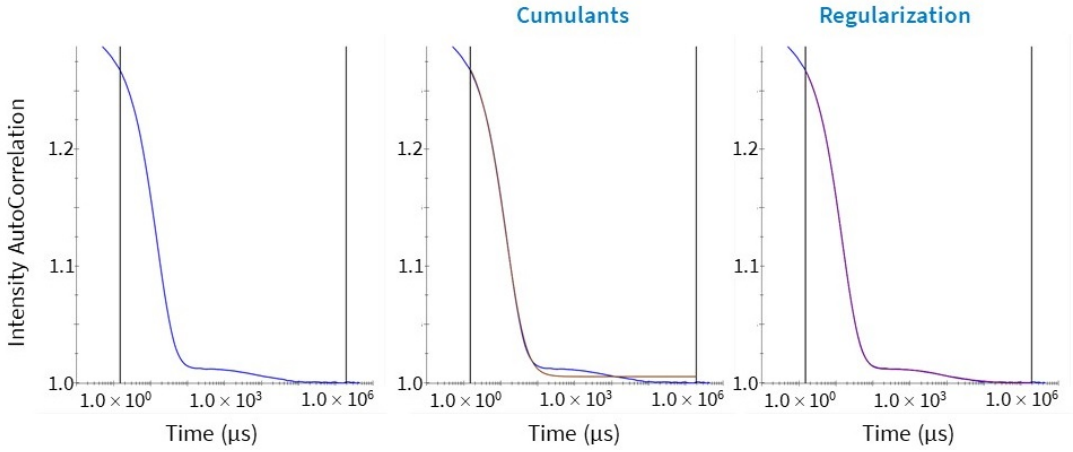

Figure 2.23.: Fitting the autocorrelation function of a multimodal sample with different methods. Left: The autocorrelation function (shown in blue) of the multimodal sample. Middle: The cumulants fit (shown in brown) is used for monodisperse samples and does not provide a suitable result for the multimodal sample. Right: For such systems the regularization fit (shown in purple) is more appropriate. Reproduced from [261] with permission of Wyatt Technology™, a portfolio of Waters Corporation™, Santa Barbara, CA, USA.

2.5.5. High-performance liquid chromatography

High-performance liquid chromatography (HPLC) is an analytical chemistry technique, which is a fully automated version of chromatography. With HPLC molecular compounds such as proteins and peptides of a chemical mixture can be separated and characterized with high precision. The separation of the sample components is facilitated by a pressure-driven flow of a mobile phase through a column containing a stationary phase and is based on adsorption of the sample components on the particles of the stationary phase. [257, 269] A method of adsorption chromatography using a column was presented by Tsvet [270, 271] in 1903. Martin et al. [272] improved the method and presented a theory of chromatographic separations in 1941.

Figure 2.24 shows the principal setup of an HPLC device. The mobile phase (solvent or eluent) is pumped through the column to the detector. A liquid sample is injected into the mobile phase and is carried by the mobile phase through the column and the detector. The column contains a (solid) stationary phase. In the column, the components of the sample separate due to varying degrees of interaction with the stationary phase, which lead to different velocities. When interacting with the stationary phase the elution of the sample component is retarded, which is described by the retention time t_R (or elution volume V_R). The retention factor describes the retention of the analyte independently from the column properties and the flow rate and can take values between 0 (no retention) and ∞ (irreversable adsorption), where values between

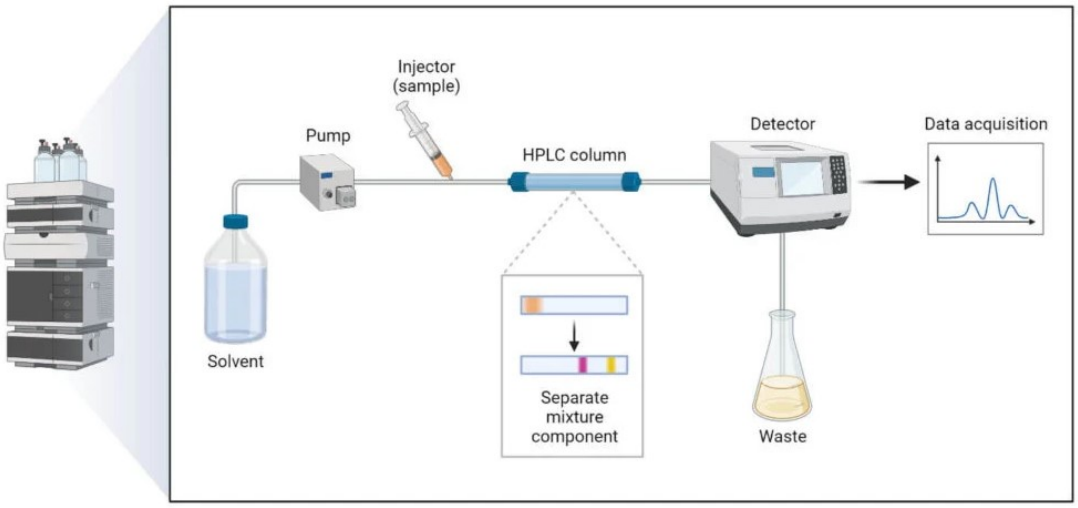

Figure 2.24.: Working principle of HPLC. Reproduced from [273] with permission of S. Aryal, Microbe Notes, Kathmandu, Nepal.

1 and 20 are preferred due to practical and economic reasons. After elution from the column, the signals of the different sample components are detected by a UV-detector and translated by the chromatography data system (CDS). The data is displayed in a chromatogram, where the x-axis represents time or elution volume and the y-axis shows the specific signal from the detector. Hereby, the concentration of the eluted analytes is represented by elution peaks in the chromatogram. [257, 269]
Since with HPLC the different components of a liquid sample can be separated, it is used in the current study to check the purity of the proteins as received by the supplier. Furthermore, it is applied to see, whether HP and BSA strongly interact with each other, if in a mixed solution.

2.5.6. Optical microscopy

Optical microscopy magnifies structures and objects by using visual light and glass lenses [274]. The first microscope composed of two lenses was invented by Hooke [257]. The magnification of a lens is given by

$$M = -\frac{x'}{f} \tag{2.31}$$

where x' is the distance between the second focal point and the image (eye), f is the focal length and the negative sign denotes an upside down image [257, 275].
Magnification is increased by arranging two lenses consecutively on the optical axis [257]. The operation principle of such a compound optical microscope is shown in Figure 2.25. The two lenses used in a microscope are called objective and ocular. The objective magnifies the object and provides a magnified real, upside down image

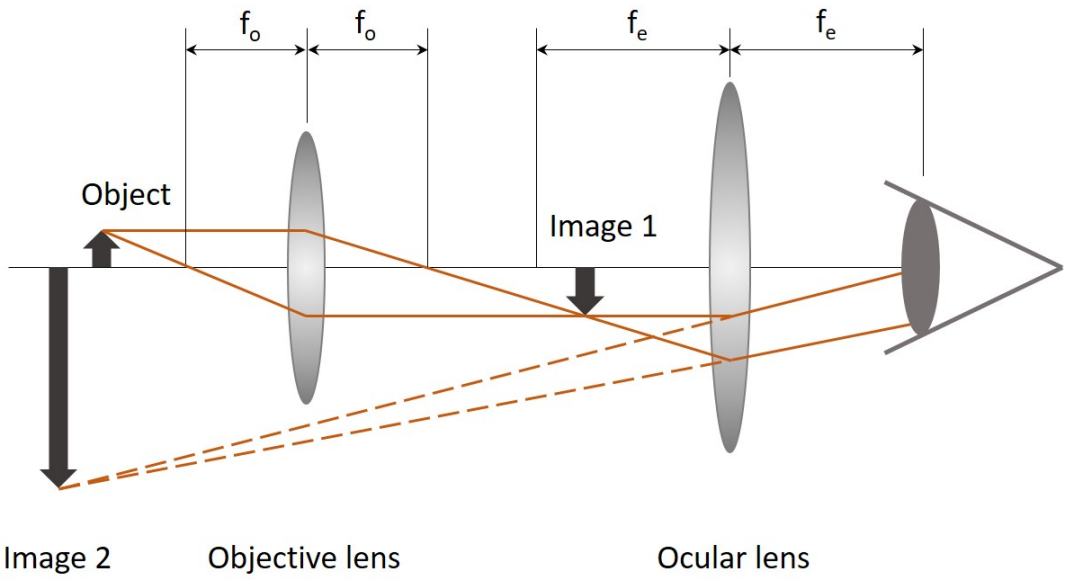

Figure 2.25.: Working principle of optical microscopy. By using two lenses, objective and ocular, a magnified image of the object is viewed by the eye of the observer. f_0 and f_e denote the focal lengths of the objective and the ocular, respectively. Image 1 is a real image magnified by the objective lens, whereas image 2 is a virtual image magnified by the ocular lens.

located within the focal length of the ocular. The ocular provides a magnified virtual image, which is viewed by the eye. [257, 275] The magnification of a microscope is calculated by the multiplication of the magnifications of objective and ocular:

$$M_{microscope} = M_{objective} M_{ocular} = \left(-\frac{L}{f_0}\right)\left(\frac{254\,\mathrm{mm}}{f_e}\right) \tag{2.32}$$

where L is the tube length, which is standardized to 160 mm in most optical microscopes, f_0 and f_e denote the focal lengths of the objective and ocular, respectively and the standardized near point is 254 mm [257, 275].
Resolution describes the ability to distinguish two points from each other and is measured as the shortest distance between those points. The resolution of the unaided eye is about 0.1 mm. [257, 274, 275] With the help of magnifying lenses, the resolution limit can be increased. However, due to the wavelength of visible light (400 nm to 800 nm), the resolution of an optical microscope is limited to about 100 nm to 200 nm [276].
In this study, brightfield mode is applied, which is a classical microscopic method used to magnify objects directly [257]. Illuminating the sample with transmitted light leads to observing dark objects on a bright background. The resolution of optical microscopy in the (several) µm-range is well suited to image the sizes of a large number of bubbles in the studied foams. A camera with timer function mounted to the optical setup facilitates the observation and documentation of the temporal evolution.

2.5.7. Sodium dodecyl sulfate-polyacrylamide gel electrophoresis

Sodium dodecyl sulfate-polyacrylamide gel electrophoresis (SDS-PAGE) is an analytical method used to separate a mixture of substances such as proteins according to their molecular sizes and charges. In SDS-PAGE, the sample will run through a polyacrylamide gel to which an electric current is applied. The size and charge of the protein determine the velocity with which it migrates through the gel. For this reason, different sizes of proteins can be separated. Typically, the molecular weight is classified with the help of a marker. [257, 277]
Figure 2.26 shows the general setup of SDS-PAGE on the left. The gel contains several wells for different samples. The applied current defines the direction of migration. After running the gel, the proteins are typically stained with the dye Coomassie blue. On the right side, the result is shown with the marker (molecular mass standards) in the first well and the result of the investigated protein in the second well. From comparison of the result of the analysis with the marker, the molecular mass is estimated. [257, 277, 278]
Different polyacrylamide gels are available which vary in their pore size and are therefore suitable for the investigation of molecules in different size ranges. For gel formation, acrylamide monomers polymerize with an appropriate crosslinking agent, which is most commonly *N,N'*-methylene-*bis*-acrylamide (BIS). Usually ammonium persulfate (APS) is used to initiate gel polymerization and *N,N,N',N'*-tetramethylenediamine (TEMED) to accelerate the reaction. Crosslinking of ran-

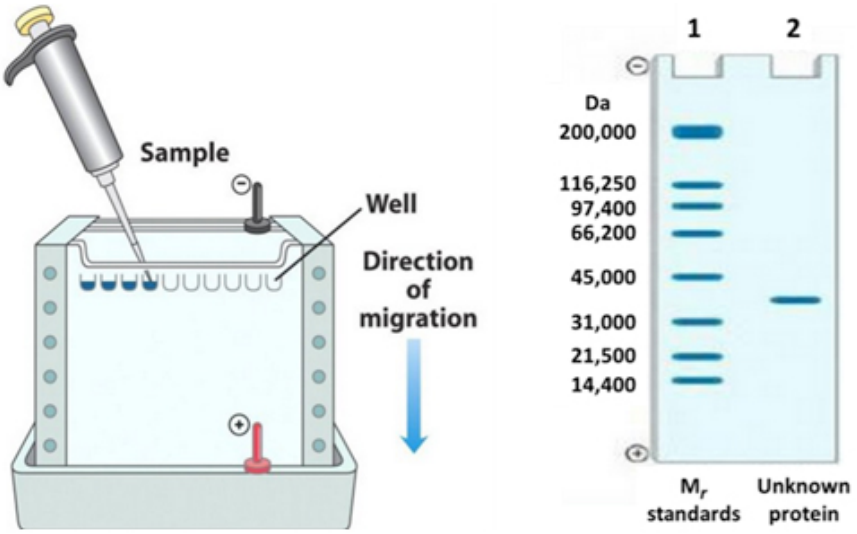

Figure 2.26.: Working principle of SDS-PAGE. Reproduced from [278] with permission of Creative Proteomics, Shirley, NY, USA.

domly growing polyacrylamide chains leads to the formation of a three-dimensional network. The acrylamide concentration and crosslinking agent concentration determine the polymer length and the extent of crosslinking, which affect the physical properties of the gel such as the pore size. The pore size of the gel is important in the separation of the proteins, since large pore sizes allow for faster migration of large proteins, whereas a smaller pore size slows large proteins down and provides for a better separation of smaller molecules. [277]

For precise separation of the proteins, usually a standard procedure introduced by Laemmli is applied, which uses a sodium dodecyl sulfate (SDS)-containing, discontinuous Tris-HCl/Tris-Glycin-buffer system [257]. Boiling the sample with SDS denatures the proteins, masks their charges and results in a negative charge of all proteins, which is proportional to their molecular size [257, 277]. The charge influences the velocity of the motion through the gel and enables a separation according to the size of the molecule. Smaller proteins travel faster through the gel. [277] In addition, equipping all molecules with a negative charge ensures a common direction of migration in the applied electric field and prevents protein aggregation [257]. When heating the sample with SDS, the tertiary and secondary structures of the proteins are unfolded by cleaving the hydrogen bonds and expansion of the molecule. Disulfide bonds can be cleaved by adding a reducing thiol compound such as β-mercaptoethanol or dithiothreitol (DTT). [257, 277] Both, the reducing and the non-reducing method, are applied in practice. When using a reducing thiol agent the proteins in the sample unfold completely and can be separated according to their molecular weight. The non-reducing method is chosen when sensitive proteins should not be destroyed and disulfide bonds not cleaved. However, some polypeptides may not be unfolded completely, which leads to a faster migration of the molecule through the gel than that correlating to its

molecular mass. [277]
In this study, SDS-PAGE is used to check the purity of the proteins, since this method allows for a separation of sample components based on their molecular mass.

2.5.8. Surface tension measurement

To measure the surface tension of a liquid, various types of tensiometers can be used such as force tensiometers, bubble pressure tensiometers or spinning drop tensiometers [279]. Regarding international standards, force tensiometers are used more commonly to determine the surface tension of surface-active agents, whereas optical methods such as pendant drop shape analysis are more commonly used for the investigation of the wettability of paints and varnishes [280].
A force tensiometer measures the tensile force, which results from the wetting of an immersed probe. The most common probes are a plate (Wilhelmy plate method) or a ring (Du Noüy ring method). [279] In this study the Wilhelmy plate setup was used, which was proposed by Wilhelmy in 1863 [281, 282]. Figure 2.27 illustrates the method. A rectangular plate is immersed into the sample. When it touches the liquid

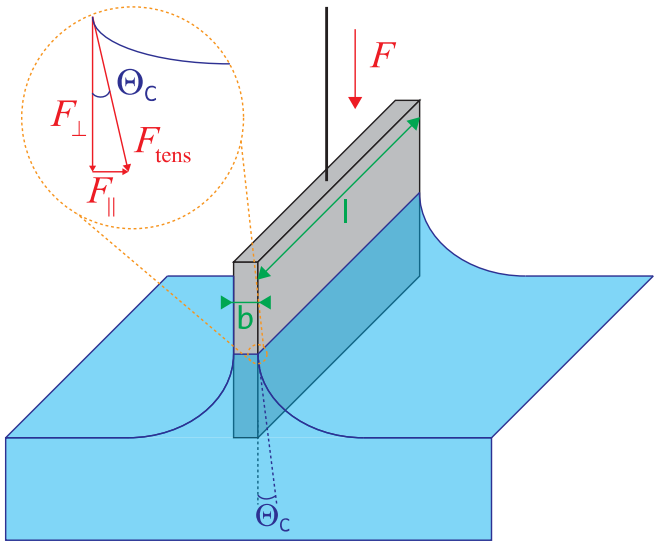

Figure 2.27.: Working principle of measuring the surface tension with the Wilhelmy plate probe. The wetted length is $L = 2l + 2b$. Reproduced from [283] with permission of DataPhysics Instruments GmbH, Filderstadt, Germany.

surface, a force F acts on the plate. This force depends on the surface tension σ, the wetted length L, which equals the perimeter of the plate, and the contact angle θ:

$$\sigma = \frac{F}{L \cos \theta} \tag{2.33}$$

The force F is measured with a force sensor, which is attached to the plate. The plate is commonly made of platinum, because it is chemically inert and easy to clean.

Furthermore, platinum has a very high surface free energy which leads to optimal wetting ($\theta = 0°$). The surface tension is calculated directly from equation 2.33. [284]
Comparing the different geometries of force tensiometers, the Wilhelmy plate method offers certain advantages over the Du Noüy ring method. When applying the Du Noüy ring method, the surface is stretched, which disturbs the arrangement of emulsifiers and can lead to significantly different results. The Wilhelmy plate is not moved during measurement, which ensures a constant surface area of the sample and facilitates determining the surface tension at equilibrium. [285]
In this thesis, the surface tension of protein solutions was measured, which is relevant for foam stability. The Wilhelmy plate method has been chosen for these measurements, because it provides more accurate results, especially for systems, where the surface tension is determined by the interfacial arrangement of surface-active molecules.

2.5.9. Viscosity measurement

To determine the viscosity of a liquid, different approaches are adopted. In the low-viscosity range the use of a rolling-ball viscometer, such as the Lovis 2000 M microviscometer from Anton Paar used in this work, is suitable [286]. Such viscometers measure the time a ball needs to roll through a transparent liquid by applying Hoeppler's falling ball principle [287]. The principle of this method is shown in Figure 2.28.

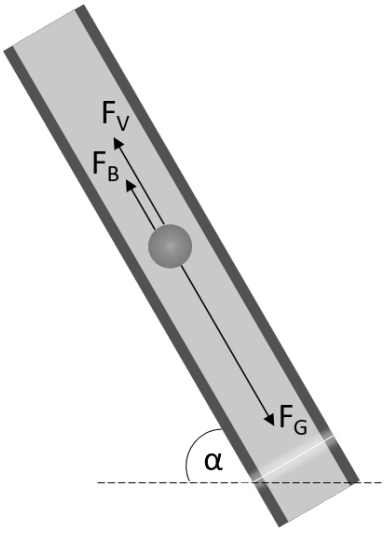

Figure 2.28.: Working principle of rolling ball method to determine the sample viscosity. The main forces acting on the descending ball are the effective portions of the gravitational force F_G, the buoyancy force F_B and the viscous force F_V. α denotes the inclination angle of the capillary.

In a closed capillary filled with the sample liquid a ball of known dimensions and density moves through the sample due to gravity. The inclination angle of the capillary

is preset by the operator and determines the speed of the ball. It should not be chosen too steep, since a too high speed of the ball causes turbulent flow conditions [286]. The transition from laminar to turbulent flow conditions is marked by the critical Reynolds number Re_{crit} [288, 289]. The Reynolds number describes the relation of inertial force and flow resistance force [289] and is given by

$$Re = \frac{uh\rho}{\eta} = \frac{uh}{\nu} \tag{2.34}$$

where u is the average velocity of the liquid between ball and tube, $h = D - d$ is a characteristic length defined by the tube diameter D and the ball diameter d, ρ is the density of the liquid, η is the dynamic viscosity of the liquid and $\nu = \eta/\rho$ is the kinematic viscosity [290].

Provided there is laminar flow in the sample-filled capillary, the relevant forces acting on the ball are the gravitational force, the buoyancy force and the viscous force [286]. The gravitational force

$$F_G = mg = \rho_b V g \tag{2.35}$$

where m and V denote the mass and volume of the ball, respectively, g is the acceleration of gravity and ρ_b the density of the ball, is directed downwards and accelerates the ball. On the other hand, the buoyancy force

$$F_B = \rho_l V g \tag{2.36}$$

where ρ_l is the density of the sample liquid, and the viscous force (Stoke's law)

$$F_V = 6\pi\eta R v \tag{2.37}$$

where η is the dynamic viscosity, R the radius of the ball and v the flow velocity, slow down the ball. [286, 289]

From this it can be derived that the viscosity of the sample is proportional to the time the ball needs to move a defined distance. Therefore, the dynamic viscosity η can be obtained from

$$\eta = K(\rho_b - \rho_l)t \tag{2.38}$$

where K is a proportionality constant, ρ_b and ρ_l are the ball density and sample density, respectively, and t is the ball rolling time. The proportionality constant K is obtained from a viscosity reference standard. [286, 289]

To measure the dynamic viscosity of samples with higher viscosities, rotational viscometers (rheometers) are used [286]. In this case the sample is placed between a stator and a rotor. The rotation or oscillation of the rotor shears the sample and different properties describing the viscoelastic behavior of the sample can be measured. If the molecules of a sample are shifted relative to each other, friction forces appear. The occurring resistance to flow can be evaluated as viscosity of the fluid. [289] The fundamental working principle of a shear test for a sample between plates is shown in Figure 2.29.

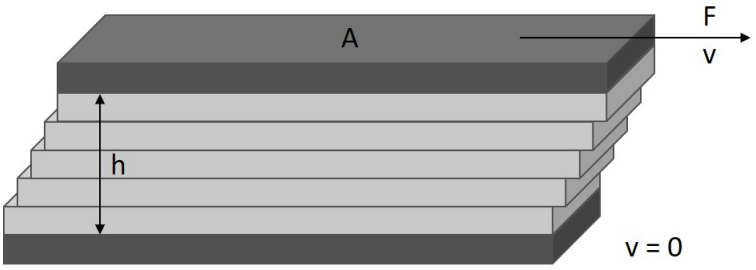

Figure 2.29.: Two plate model for shear tests. The lower plate rest, whereas the upper plate is moved to the right. As a consequence, the sample between the plates is sheared. A denotes the area of the plates, h the distance between the two plates, F the applied force and v the velocity of the upper plate.

In such a test, the viscosity is given by

$$\eta = \tau/\dot{\gamma} \tag{2.39}$$

where τ is the shear stress and $\dot{\gamma}$ is the shear rate. The shear stress is given by

$$\tau = \frac{F}{A} \tag{2.40}$$

where F is the (shear) force and A is the (shear) area. The shear rate is given by

$$\dot{\gamma} = \frac{v}{h} \tag{2.41}$$

where v is the velocity and h is the distance between the plates. Also here laminar flow conditions are important and furthermore, it needs to be assured that the sample does not slip at the walls of the geometry. [289] By the help of a motor drive higher forces than earth's gravitational force are obtained. The dynamic viscosity measured with these devices is also referred to as shear viscosity. Different geometries are possible such as cup-vane geometry, coaxial cylinders, or cone-plate and parallel-plate geometries. [286]

For geometries with a cup and a bob two principles are to be distinguished. In the Couette principle, the cup is rotated, whereas in the Searle principle, a bob is rotated inside a fixed cup [286, 289]. Here, the bob was rotated in the stationary cup. To rotate the measuring bob, a certain motor torque is needed, which has to overcome the viscous forces [286]. Figure 2.30 shows the setup of the concentric cylinder geometry used in this study to measure the viscosities of oat drink samples and BSA-polysaccharide solutions. Two different rotor geometries were applied, the conical cylinder rotor and the vane rotor, which are shown in Figure 2.31. The vane rotor is used for samples with higher viscosity to prevent wall slippage. This rotor was applied to investigate the starch gelatinization appearing in the oat drink at heat

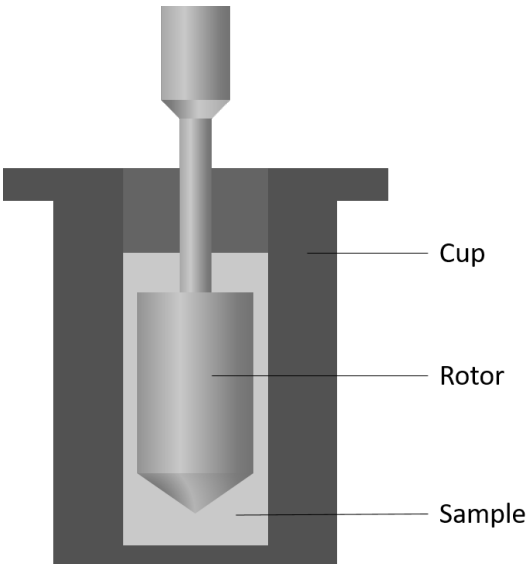

Figure 2.30.: Setup of the concentric cylinder geometry.

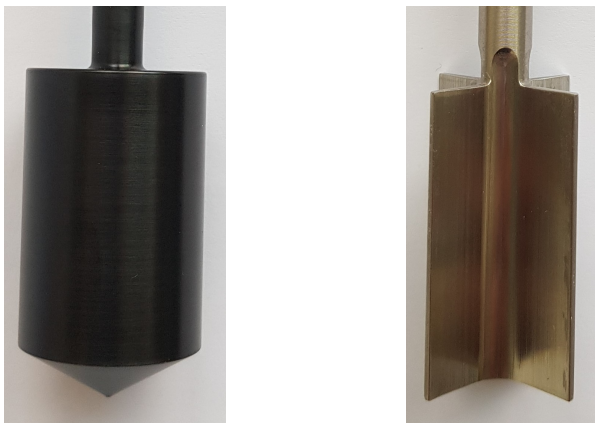

(a) Conical rotor. (b) Vane rotor.

Figure 2.31.: The two rotor geometries used in this project.

treatment. Concentric cylinders are used for samples of lower viscosity, because the measurement is more precise. The conical rotor was applied when investigating BSA-Polysaccharide solutions as well as the enzymatic treatment of the oat drink. For investigating the viscosity of BSA solutions at different pH, the rolling ball viscometer was applied, because the viscosities are much lower. At such low viscosities the flow becomes turbulent at high shear rates in the rheometer and therefore the viscosity cannot be measured correctly at high shear rates (cf. Section C.1).

2.5.10. Zeta potential measurement

As described above (in Paragraph 2.4.1), charged particles, colloids or droplets in a suspension attract counterions. The charged particle is surrounded by a double layer of ions. Close to the charged surface an immobile layer of adsorbed counterions is formed, which is referred to as *Stern layer*. At a larger distance from the particle surface, a *diffuse layer* (also "diffusive layer") of mobile counterions and ions of the same sign as the particle assembles. When moving through the suspension, some ions of the diffuse layer move with the particle, which defines the slipping plane (also "shear plane"). [118, 291, 292] These layers are illustrated in Figure 2.32. The potential of the electric field of the particle decays with the distance from the particle surface. The zeta potential (ζ-potential, also "electrokinetic potential") describes the potential at the slipping plane [291, 293].
Zeta potential measurement is based on electrophoresis, i. e. the movement of charged particles in an electric field. Consider a particle with charge Q in an electrical field E. On such a particle act the electrical force

$$F_{el} = QE \tag{2.42}$$

and the friction force (Stokes law) acting in opposite direction, which is for spherical particles given by

$$F_f = 6\pi\eta r v \tag{2.43}$$

with v the velocity of the particle, r its radius and η the viscosity of the solvent. In equilibrium both forces are equal and

$$v = \frac{zeE}{6\pi\eta r} \tag{2.44}$$

However, this approximation is not exact, since the particle is surrounded by a cloud of counterions from the solvent. The force

$$F_{el} = -QE \tag{2.45}$$

acts on the counter ions and is also referred to as electrophoretic retardation force. Due to their opposite charge, the counterions move in opposite direction than the particle in the applied electrical field, which slows down the particle. The extend of the retardation, however, depends on the spatial distribution of the charges (double

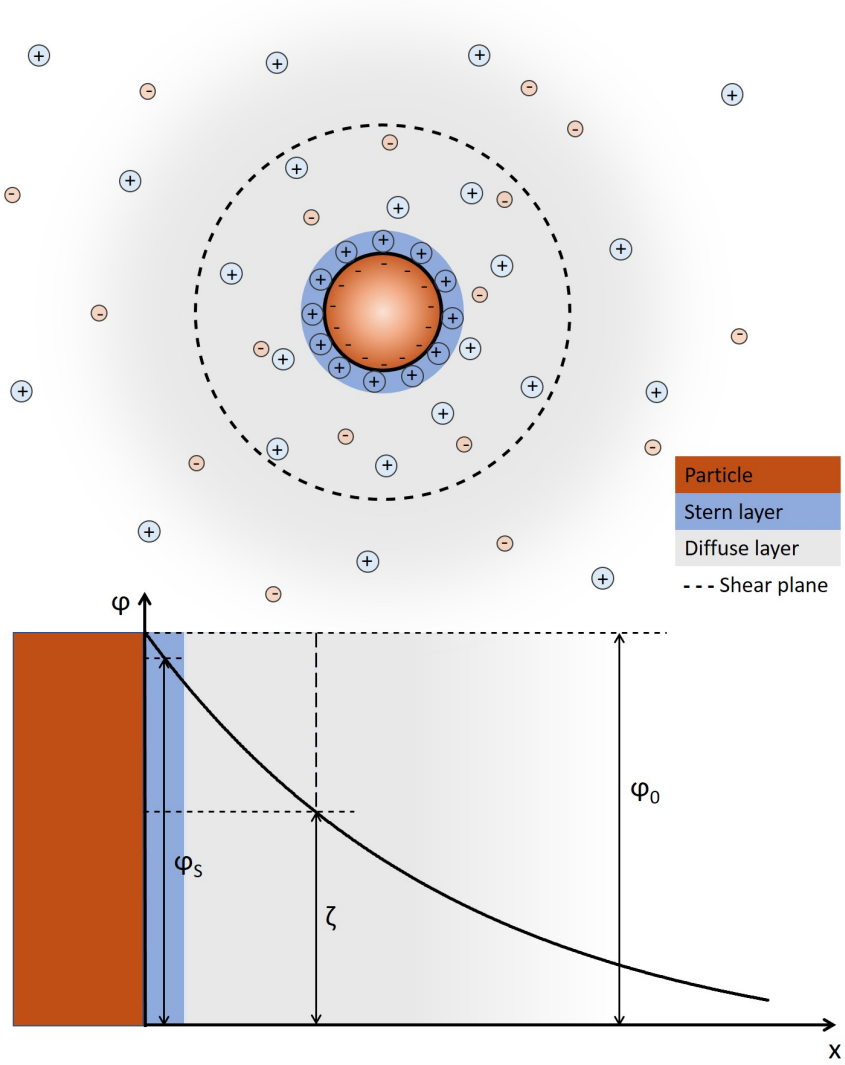

Figure 2.32.: Schematic of the electrical double layer of charged particles and definition of the zeta potential. Counterions firmly adsorb at the surface of a charged particle and form the Stern layer. The potential at the particle surface is called surface potential φ_0 and the potential at the Stern plane is the Stern potential φ_S. Further away from the particle follows the diffusive layer. Ions closer to the particle than the slipping plane are carried with the particle when it moves. The slipping plane is marked by the dashed circle. The potential at the slipping plane is the zeta potential ζ. [291–293]

layer composition) and their ionic mobilities. As a consequence, the ion cloud is deformed; its shape becomes more narrow at the front side of the particle and more extended at its back. For such an asymptotic charge distribution in the vicinity of the moving particle, the center of the countercharge does not conincide with the center of the particle charge. This distance creates an additional electric field, which leads to a polarization force acting on the particle and further retarding its motion. [118, 292, 294] For a particle performing a steady, linear motion, the electrophoretic motion is given by

$$U = \frac{v}{E} \tag{2.46}$$

By solving the hydrodynamic equations, Henry derived an equation for calculating the electrophoretic mobility

$$U = \frac{\varepsilon_0 \varepsilon_r \zeta}{\eta} f(\kappa r) \tag{2.47}$$

where ε_0 is the electrical field constant and ε is the relative permittivity, η the viscosity of the solvent and $f(\kappa r)$ the Henry function. The expansion of the Henry function leads in first approximation to

$$f(\kappa r) = \begin{cases} 1 - ... & \text{for} \quad 1 \ll \kappa r \\ \frac{2}{3} + ... & \text{for} \quad 1 \gg \kappa r \end{cases} \tag{2.48}$$

The first expression holds for thin Debye layers and is called Helmholz-Smoluchowski equation. The second expression holds for thick Debye layers and is called Hückel-Onsager equation. [294–298]

For the Debye-Hückel parameter it holds

$$\kappa^{-1} = \sqrt{\frac{\varepsilon_0 \varepsilon k_B T}{2e^2 c}} \tag{2.49}$$

where ε_0 is the electrical field constant, ε the relative permittivity, k_B the Boltzmann constant, T the temperature, e the elementary charge and c the ion concentration. The Debye-Hückel parameter is coupled to the Debye length λ_D by $\lambda_D = \kappa^{-1}$. [118, 222, 294]

Devices such as the Zetasizer Nano-Z from Malvern, which was used in this thesis, apply an electrical field to a sample in a capillary. The velocity v of the charged particles in the sample is measured using Laser Doppler Velocimetry. Thereby, a fluctuating intensity signal is received from focusing laser light on the sample and comparing the scattered light with a reference beam. In this signal, the rate of fluctuation is proportional to the particle velocity. Characteristic frequencies are extracted using a digital signal processor. As the applied field strength E is known and the particle velocity v is measured, the zeta potential ζ can be calculated from equation 2.47. [293] A schematic showing the working principle of the zeta potential measurement is shown in Figure 2.33.

In this thesis, the zeta-potential is measured to study the changes in surface charge

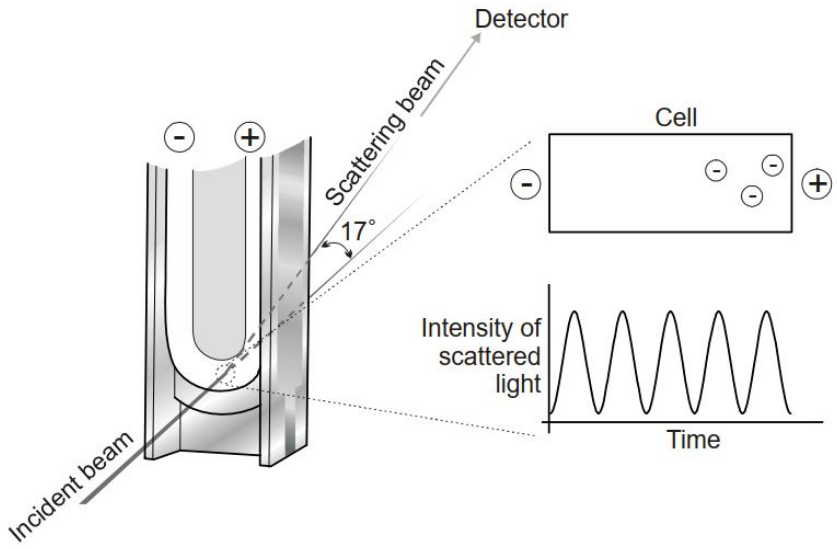

Figure 2.33.: Working principle of the zetasizer. The charged particles in the sample move towards the electrode of opposite charge. A laser is focused at the sample and the intensity of the scattered light is monitored over time. Comparison with a reference beam leads to a characteristic fluctuating intensity pattern from which the particle velocity can be extracted and the zeta potential calculated. [293] Reproduced from [293] with permission of Malvern Panalytical B.V., Almelo, Netherlands.

of BSA at varying solution pH. With this, the isoelectric point (IEP) of BSA is determined.

3. Development of a simple method for automated foam characterization

The stability and bubble shape of foams are influenced by the properties and arrangement of surface-active molecules at air-water interfaces. The investigation of such multiscale-relationships requires a well-done analysis of microscopic foam properties. At the beginning of this PhD project, it was a challenge to adequately analyze foams with the equipment available in our laboratory. Therefore, one of the aims of the thesis was to develop a method to accurately characterize foam stability and bubble shape using open-source software and existing laboratory equipment. This method should provide a quantitative analysis and allow for a comparison of the properties of foams stabilized by different proteins and under varying conditions (pH, viscosity). To study bubble size and shape, microscopy of foams and image analysis proved to be a good solution for characterization. For reliable statistics a large number of bubbles per image is investigated. The considerable quantity of data requires the implementation of an automated approach to image analysis.

Two different approaches were tested: one based on thresholding the microscope images, the other one based on applying the machine learning algorithm *Cellpose* [299, 300]. For both options, *Python* scripts were written for image analysis (see Section A). Applying *Cellpose* proofed to be the method with higher precision and better control over the results. To enhance the precision of analysis, two sets of masks are merged, a set for tiny bubbles and one for large bubbles. The graphical user interface (GUI) of *Cellpose* offers the option to visually control and manually correct bubble shapes. Furthermore, areas of cut edge bubbles are not considered in the analysis. The area of a bubble at the image edge is incorrectly represented, if the bubble is not shown entirely. For this reason, the removal of such edge bubbles enhances the precision of the analysis.

By investigating a time series of microscope images, the temporal evolution of bubble size and shape are monitored. Over time, the mean bubble size increases due to Ostwald ripening and coalescence. For this reason, conclusions on the foam stability are drawn from the temporal evolution of the mean equivalent bubble diameter. The physical properties of the emulsifiers define characteristic bubble shapes [301, 302]. The bubble shape changes during foam ripening from spherical for a wet foam to polyhedral for a dry foam [16, 19, 112, 118]. Therefore, the circularity (roundness) of the foam bubbles decreases with time. Ostwald ripening is represented in the temporal evolution of the bubble size distribution.

3.1. Method of foam formation

A simple and reproductive method for foam formation is necessary for foam studies. In our laboratory, a T 25 easy clean control ULTRA-TURRAX (IKA-Werke GmbH & Co. KG, Staufen, Germany) with dispersion tool (in the following: T 25) and an ULTRA-TURRAX Tube Drive control (in the following: tube drive) are available. Figure 3.1 shows the two different devices. These are dispersing tools, which can be used for the formation of smooth, creamy foams by whipping the sample solution. Foam formation with these devices was preferred over manual shaking, because of better control of the experimental parameters and better reproducibility of the settings.

(a) (b)

Figure 3.1.: Devices for foam formation: (a) tube drive and (b) T 25.

Due to limited protein resources, especially for hydrophobin, in this thesis, the sample volumes are minimized. This affected the choice of foaming device. The minimum sample volume needed when using the tube drive is 20 mL for the large tube and 15 mL for the small tube. Figure 3.2 shows photos of the tubes used with the tube drive. The top views displayed in Subfigure 3.2 (b) and (c) show the interior of the tubes with the rotating pins used for foam formation. In both cases, static pins are combined with rotating pins to disperse the sample. The foam formed by using the tube drive was not transferable by pouring, because it was too stiff and therefore adhered to the beaker. Furthermore, the milky structure of the tube drive walls hampers the reading of the foam height. Therefore, using the tube drive was not suitable for measuring

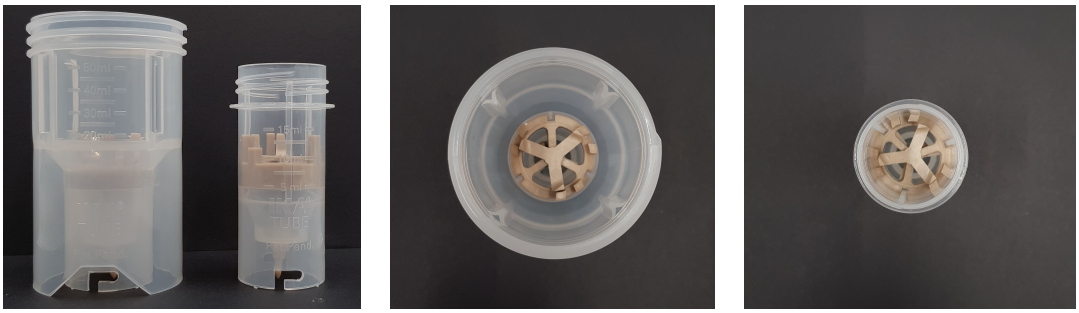

(a) (b) (c)

Figure 3.2.: Tubes used with tube drive (a) side view and top view of (b) large and (c) small tube.

the foam height.
Figure 3.3 shows photos of the T 25 tool S 25 N - 10 G. It consists of a spherical stator

(a) (b)

Figure 3.3.: Ultra turrax T 25 tool S 25 N - 10 G as viewed from the side (a) and from below (b).

at the outside and two rotor pins, which move fast inside the tool. When using the T 25, the size of the vessel containing the sample is not fixed. Therefore, by choosing a glass vessel with optimized size, the required sample volume can be minimized. Sample volumes of 2 mL already sufficiently cover the tool, which is much smaller than the minimum sample volume required when using the tube drive. During foam formation, the volume of the sample extends due to the incorporation of air into the liquid sample. Therefore, a glass vessel with overflow protection was manufactured by the in-house glass blower.
The glass vessel with overflow protection used for foaming is shown in Figure 3.4. The inner diameter of the glass cylinder is 13.6 mm, the height of the cylinder without overflow protection is 65 mm and the total height of the glass vessel is 90 mm. The larger diameter in the upper part prevents overflowing of the foam.
By using the T 25 and the custom-built glass vessel, the sample volume could be reduced to 2 g of protein solution. All samples were dispersed at a speed of 20 000 rpm for 1 min [52]. Higher rotational speeds during emulsification (whipping) lead to smaller

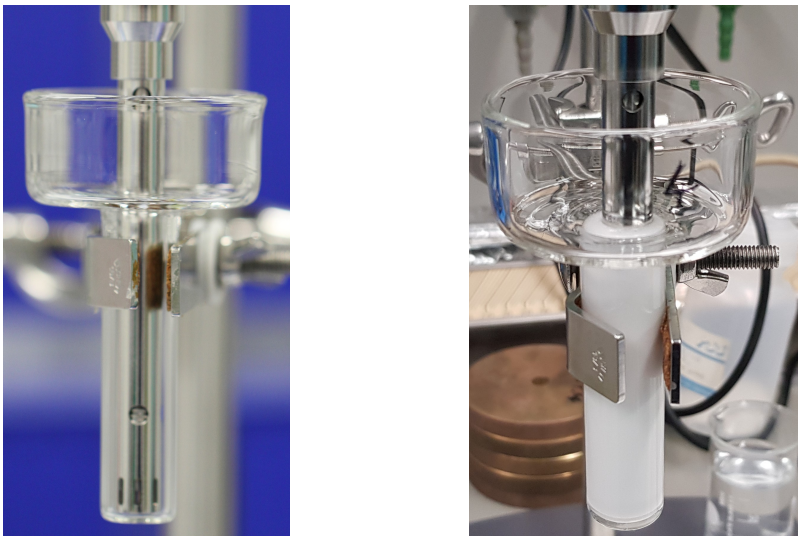

(a) (b)

Figure 3.4.: Glass vessel used for foam formation with ultra turrax T 25 tool inserted: (a) without sample and (b) with foamed sample. The upper part with larger diameter prevents the foam from overflowing during foam formation.

bubble sizes [303, 304]. First, longer whipping also leads to smaller bubbles and a higher liquid fraction of the foam [90]. However, for long processing times only insignificant improvements in fineness of the foam are obtained. Furthermore, at the high shear rates applied, long whipping can heat up the sample [305]. To prevent an increase in the temperature of the sample, the duration of the whipping process is kept relatively brief.

3.2. Protein concentration

Waniska et al. [35] mention a required protein concentration of 3 % to 40 % for foam formation by whipping the sample solution. Preliminary tests in this study showed, that for a protein concentration of 4 wt% smooth, creamy foams are obtained. Figure 3.5 shows images of foams prepared by using 0.1 wt% and 4 wt% of BSA, respectively. At 0.1 wt% the foam volume is much smaller and the foam appears coarser. In such foams, the bubbles are too large to be well processed and observed under the microscope. At a concentration of 4 wt% protein, smooth foams are prepared under identical conditions, which are suitable to be investigated with the proposed method.

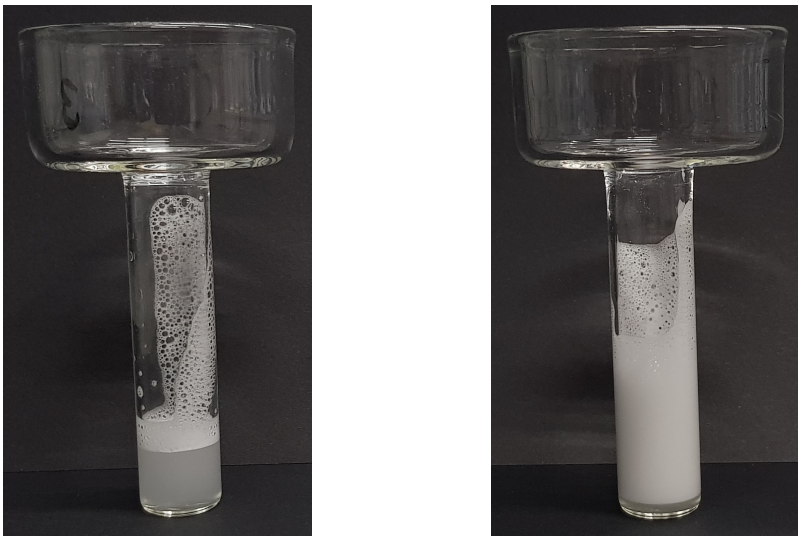

(a) (b)

Figure 3.5.: Foam formed with (a) 0.1 wt% BSA and (b) 4 wt% BSA. At 4 wt% BSA the foam volume is much larger and the foam is much finer.

3.3. Choice of the optical microscope

In the process of developing the method, different magnifications for imaging the foam samples are tested. First, an Axio Scope.A1 light microscope from Carl Zeiss (Oberkochen, Germany) with an objective providing a magnification of 10 × was used. Figure 3.6 shows microscope images of a BSA-stabilized foam at the beginning and after 25 min. Over time, the bubble size increases and the number of bubbles decreases. The images show that the number of bubbles in the field of view decreases and already after 25 min there are not enough bubbles visible in the image to quantitatively describe the bubble size and facilitate a comparison with other samples. Therefore, an imaging method with better statistics is required.
As the second approach to image the foams, a Canon EOS 7D camera equipped with objective Canon Macro Lens EF 100mm 1:2.8 L IS USM and a Canon TC-80N36D remote release with timer function (Canon Inc. Headquarters, Tokyo, Japan) is used. The camera is mounted to a repro stand RS 2 XA from Kaiser Fototechnik (Kaiser Fototechnik GmbH & Co. KG, Buchen, Germany) and samples under the camera are placed on top of a luminous plate LED Slimlite plano (Kaiser Fototechnik GmbH & Co. KG, Buchen, Germany).
By this method, a large number of bubbles can be viewed, as is seen in Figure 3.7. Therefore, the statistics are reliable. However, the contrast of the images is low, especially at later times. In addition, the lamellae between the bubbles are very thin, which can complicate the correct detection during image analysis.
For this reason, as a third imaging technique, a microscope with lower magnification was used. With a Leica MS5 stereomicroscope (Leica Microsystems GmbH, Wetzlar,

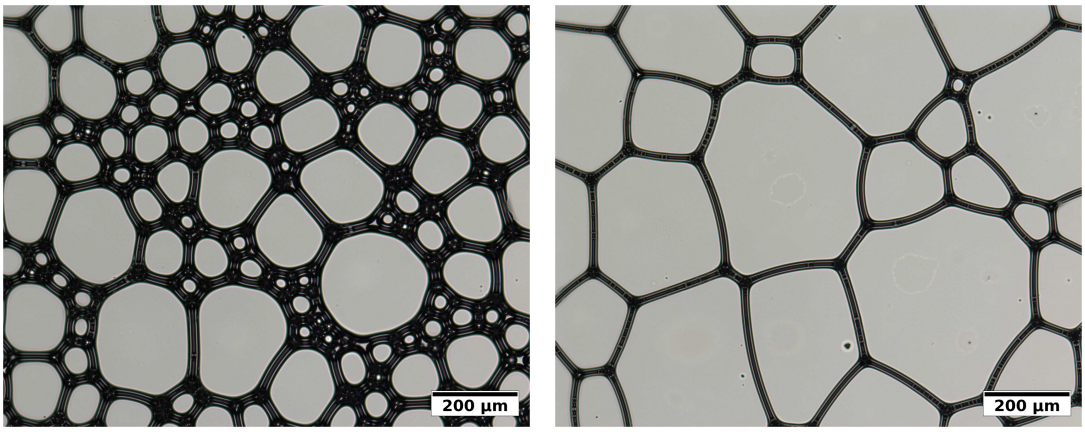

(a) 0 min (b) 25 min

Figure 3.6.: Images taken with Axio Scope.A1 light microscope in transmission bright-field mode with 10 × magnification (a) immediately after foam formation and (b) 25 min later.

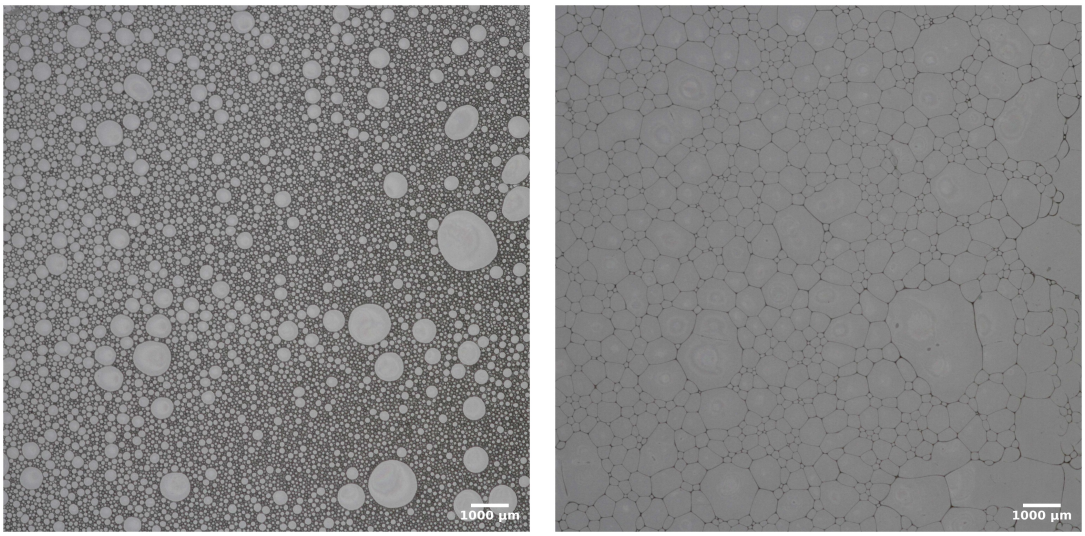

(a) 0 min (b) 25 min

Figure 3.7.: Images taken with Canon EOS 7D camera (a) immediately after foam formation and (b) 25 min later.

Germany), images were taken in brightfield transmission mode at a magnification of 1.6 ×. Such images of a BSA-stabilized foam are shown in Figure 3.8. As can be seen

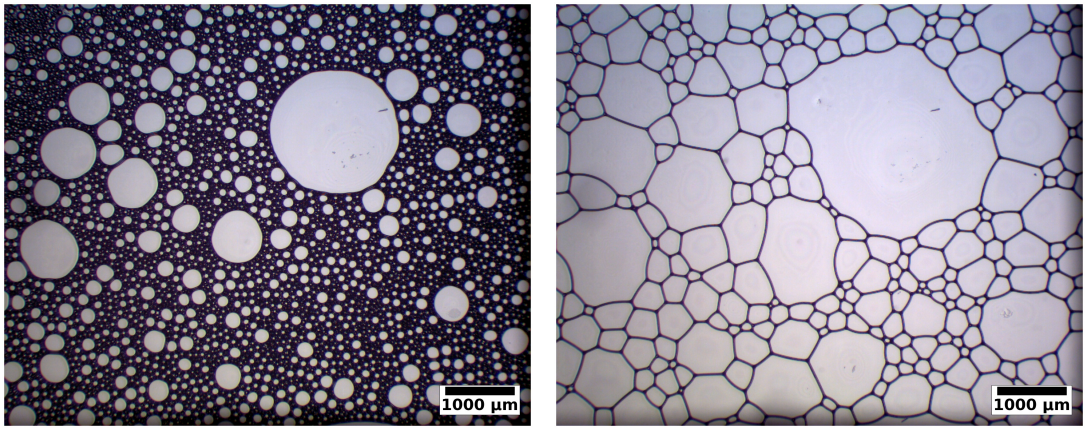

(a) 0 min (b) 25 min

Figure 3.8.: Images taken with Leica MS5 stereomicroscope (a) immediately after foam formation and (b) 25 min later.

from the images, the contrast and statistics are suitable for analysis. The number of bubbles in one image varies between 200 and 5000 bubbles depending on the sample and the measuring time.

3.4. Evaporation during the measurements

Evaporation dries a foam. By covering the foam on the microscope slide with a cover slip, the surface of foam that is exposed to air is small. Therefore, it was assumed that not much liquid evaporates over the time of observation. Furthermore, the usage of a 50 µm spacer between microscope slide and cover slip (of constant sizes) ensures that the exposed area is constant throughout the measurement and for all measured samples. The impact of changing environmental factors such as temperature and air humidity was minimized by measuring all different samples of one series within the same day. For each replication, all sample types were prepared and measured within another day.
Sealing of the sample with a varnish was not considered. First, application and drying of the varnish would have taken too long, since the sample has to be put under the microscope as soon as possible after foaming. Second, a varnish could cause further surface effects or changes in gas pressure.
Evaporation from the foam on the microscope slide was not investigated in more detail. It was considered a constant factor for all samples, because changes in environmental influences were minimized and the surface area was kept constant. In any case, the results show clear differences between the samples of different composition, which was the aim of this study.

3.5. Threshold-based approach for image analysis

A typical approach in image analysis is to set a threshold for segmentation of objects from the image. Thereby, objects are considered as foreground and are separated from the background. Objects are clusters of same-color foreground pixels. After detecting them, the size and shape of these clusters can be determined. A threshold is a value, which divides two regions: below the threshold and above the threshold. The technique of thresholding compares the value of each pixel of an image with the threshold and assigns it relative to the threshold. A pixel value smaller than the threshold is then set to 0 (black), whereas larger pixel values are set to a maximum value (generally 255 (white)). [306, 307]
When applying thresholding to an image using the function cv2.threshold (cv2 version 4.6.0) in *Python* (Python Software Foundation, version 3.8.8), the source, threshold value, maximum value and thresholding technique have to be provided. The source is the input image array, which must be in grayscale. The threshold value is the threshold, which is used to assign the pixel values and the maximum value is the value to which the upper pixel values are assigned, which is usually 255. The thresholding technique is the type of thresholding, which is applied to the image. In the current study, two techniques are combined: cv2.THRESH_BINARY_INV (inverted thresholding), which indicates that pixel values less than the threshold are set to the maximum value, and Otsu's thresholding (cv2.THRESH_OTSU), which computes the optimum threshold value based on the input image automatically. [306, 307]
The threshold-based approach was applied to images taken with the camera. Figures 3.9 and 3.10 visualize the approach. First, the obtained photo needs to be cropped to show only foam and no surroundings such as the empty microscope slide. Consequently, the whole image is filled with objects of interest (bubbles and lamellae, cf. Subfigure 3.9b). For better discrimination between bubbles and lamellae the contrast is enhanced (Subfigure 3.9c). Then, the image is converted into a binary image by thresholding (Subfigure 3.9d). From the thresholded image, bubbles are detected by measuring the areas of connected same color pixels. These areas are used to calculate the equivalent bubble diameters. The equivalent diameter of a bubble is the diameter of a sphere, which has the same area as the bubble. These equivalent diameters are used to describe the bubble size. A histogram of the sizes (equivalent diameters) of all bubbles in the image is shown in Subfigure 3.9e). Furthermore, the mean equivalent bubble diameter of all bubbles in the image is calculated. A disadvantage of the threshold-based approach is, that parts of lamellae have the same color as the bubbles and are therefore also counted as objects. For a discussion on this issue refer to Section 3.6.3. To reduce the number of detected lamella pieces, tiny objects are left out in the histogram and the calculation of the mean value.
The described procedure is repeated for all time steps of the measurement to obtain the temporal evolution of the mean equivalent bubble diameter. The analysis is repeated for three identical samples and mean and standard deviation of the three samples are calculated as shown in Figure 3.10.

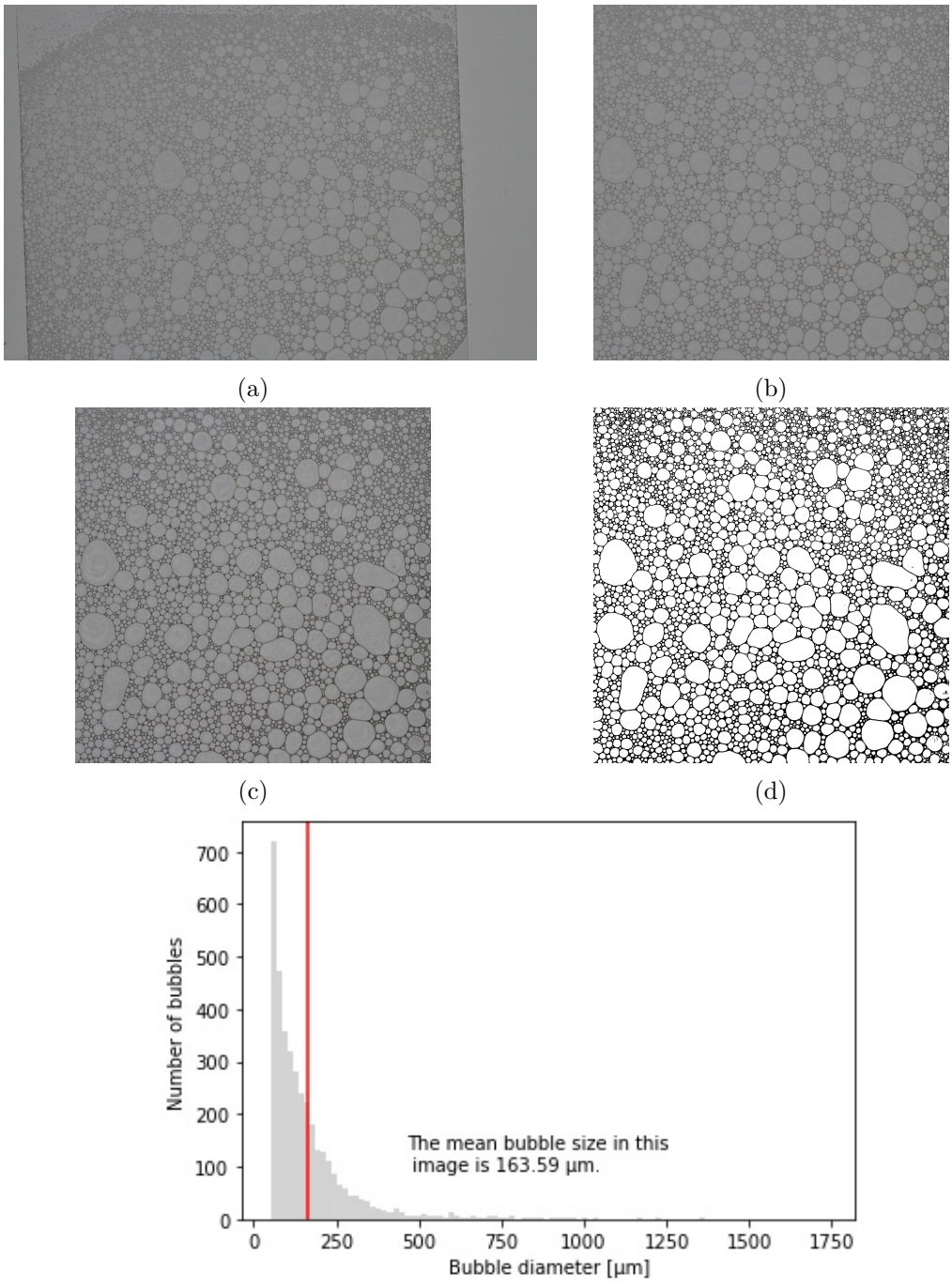

Figure 3.9.: Operating principle of the threshold-based approach: (a) Camera image, (b) cropped image, (c) contrast enhanced image and (d) binary image. Analysis of the bubble size provides a histogram of the bubble sizes and the mean bubble size as shown in (e).

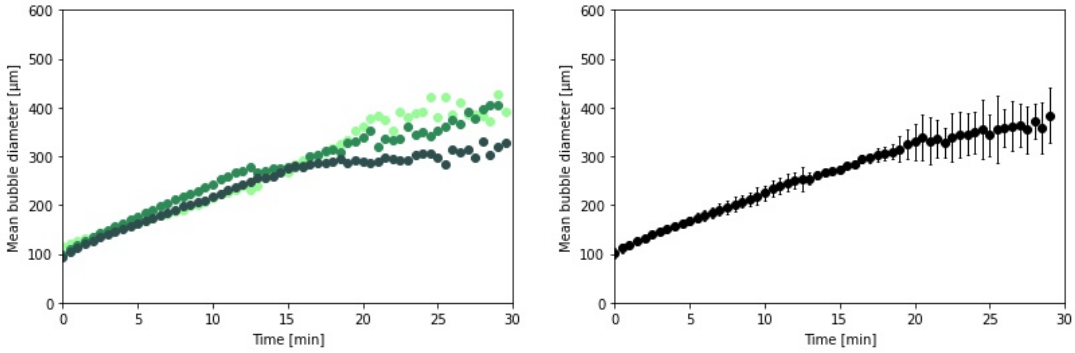

(a) (b)

Figure 3.10.: Mean bubble size over time: (a) Three measurements of identical samples and (b) mean and standard deviation of three measurements.

3.6. Machine learning-based approach for image analysis

This section is based on the manuscript

Simple method to assess foam structure and stability using hydrophobin and BSA as model systems
Judith Krom, Konrad Meister, Thomas A. Vilgis
ChemPhysChem (2024)
DOI: 10.1002/cphc.202400050.[302]

Author contributions
Judith Krom: Formal analysis, Investigation, Methodology, Project administration, Software, Visualization, Writing - original draft; **Konrad Meister:** Resources, Supervision; **Thomas A. Vilgis:** Resources, Supervision, Writing - review & editing.

The following is quoted from [302]. Only the numbering of the captions, figures and references as well as the typesetting (including the capitalization of captions) were adjusted to the numbering and style of the thesis.

Abstract The properties and arrangement of surface-active molecules at air-water interfaces influence foam stability and bubble shape. Such multiscale-relationships necessitate a well-conducted analysis of mesoscopic foam properties. We introduce a novel automated and precise method to characterize bubble growth, size distribution and shape based on image analysis and using the machine learning algorithm *Cellpose*. Studying the temporal evolution of bubble size and shape facilitates conclusions on foam stability. The addition of two sets of masks, for tiny bubbles and large bubbles, provides for a high precision of analysis. A python script for analysis of the evolution of bubble diameter, circularity and dispersity is provided in the Supporting Informa-

tion. Using foams stabilized by bovine serum albumin (BSA), hydrophobin (HP), and blends thereof, we show how this technique can be used to precisely characterize foam structures. Foams stabilized by HP show a significantly increased foam stability and rounder bubble shape than BSA-stabilized foams. These differences are induced by the different molecular structure of the two proteins. Our study shows that the proposed method provides an efficient way to analyze relevant foam properties in detail and at low cost, with higher precision than conventional methods of image analysis.

3.6.1. Introduction

Protein-stabilized foams are ubiquitous in everyday life - from milk foam in a morning cappuccino to whipped cream on an afternoon cake to beer foam in the evening. The macroscopic appearance of foams is determined by their complex microstructure. Therefore, reliable characterization of the microstructure of different foams is a fundamental requirement for understanding how molecular differences influence foam stability and coarseness.

To characterize foam stability, traditionally the foam volume at two different points in time is measured and the foam stability is calculated by $FS = V_t/V_0$, where V_t is the foam volume at the later point in time and V_0 is the initial foam volume [42, 44–48, 137]. Commercially available foam analyzing instruments additionally allow for analysis of bubble size [308]. However, these instruments are quite cost-intensive and not readily available in most labs. In contrast, the method developed in the following can be applied to images taken with a common optical microscope and freely available open-source software.

Image analysis of microscope images is a powerful tool that allows for a quantitative analysis of microstructures [300, 309, 310]. To determine the sizes of objects, such as bubbles in a foam, cells in biological systems or ice crystals, diameters of these objects can be measured manually using programs such as *Fiji/ImageJ* [311–313]. This is easy to perform and does not require special programming skills or financial investment in expensive instruments. However, for large numbers of objects it can become extremely time intensive. Therefore, a common method is to just measure the ten largest objects with the drawback that precision is compromised [312].

Another method is, to set a threshold and convert the image into a binary image. From the connected same contrast pixels, objects can then be identified [314–317]. However, for objects, which are not sufficiently separated from each other, whose intensity profiles do not decay smoothly from the center, or if the center of the object has the same color as the background, the correct identification of the objects by this method is difficult [299].

Foams consist of air bubbles dispersed in a liquid, which are stabilized by emulsifiers (surfactants, proteins). The thin liquid films between bubbles are referred to as lamellae [13, 19]. Wet foams, which contain a higher liquid fraction, show larger areas of liquid in between the bubbles. In a microscope image, such parts of the continuous (liquid) phase have the same contrast as the bubble interior. Therefore, methods of image analysis, which are based only on a threshold are not sufficient to adequately

determine the bubble areas.
To provide additional criteria for segmentation and analyze microscope images in an automated way, deep neural network-based methods are frequently applied in the fields of cell biology and biomedical applications [299, 318–327]. These usually require large training datasets to estimate the parameters for segmentation. Mostly, such models are trained on specialized datasets and come with the drawback of not generalizing well to other types of data [299]. Thus, Stringer et al. used a variety of different training data in the process of developing the open-source software *Cellpose* [299]: large datasets of cell images obtained from different types of microscopy and using a variety of fluorescent markers were collected and manually segmented, as well as non-microscopy images containing large numbers of repeated objects.
By including such data in the training set a neural network was trained that generalizes more robustly and more widely. When analyzing an image in *Cellpose*, the neural network predicts horizontal and vertical contrast gradients and whether a pixel belongs to any cell. These maps are then combined into a gradient vector field, which is used to assign the pixels to their eventual fixed point. All pixels converging to the same fixed point are then assigned to the same mask. This approach provided *Cellpose* a high precision compared to other segmentation algorithms [299], and avoids the above-mentioned disadvantages of an exclusively contrast-based segmentation.
When applying software developed for segmenting cells to foams, a challenge is the heterogeneous nature of foams. Since cells of one tissue have a rather homogeneous size, segmentation software programs can have difficulties to detect very small and very large objects at the same time. However, due to Ostwald-ripening, foams offer a very broad size distribution. Therefore, adequate analysis necessitates a procedure that can detect tiny as well as large bubbles. Indeed, when reviewing different methods of foam analysis, it becomes apparent, that tiny bubbles are often not considered and their relevance is not discussed [316, 328].
In the current article, a method is presented to precisely analyze the temporal evolution of bubble shape and size over the whole range of bubble sizes. Our considerations are based on a script we wrote in the programming language *Python* to analyze microscope images of liquid foams. We provide this script in the Supporting Information accompanying this manuscript. For pre-processing of the microscope images, we follow similar steps as described by Bonilla et al., who used *ImageJ* [328]. The images are then analyzed using *Cellpose* [299, 300]. *Cellpose* offers several pretrained models and can be further trained on own data [300]. Additionally, it offers the possibility for manual corrections of bubble masks via a graphical user interface (GUI).
In contrast to Bonilla et al. [328] or Saad et al. [312], we here implement a method to overcome the shortcomings of Cellpose in terms of size range. Therefore, to improve the precision of the method we append the possibility to merge two sets of masks for each image to cover a larger size distribution. This is unique and offers a higher precision in detecting the whole bubble size range. Furthermore, we remove bubbles at the edge of the microscope image, which are not shown completely. Removal of such edge bubbles adds to the precision of analyzing the shape and correct size of the investigated bubbles. The use of a machine learning algorithm and the supplied

script provide for a faster and more detailed analysis than with conventional methods. Therefore, the presented approach offers a fast and easy analysis of a large amount of bubbles.
Furthermore, in contrast to Bonilla et al. [328], we consider a time series of microscope images to quantify foam stability. The evolution of bubble sizes over time correlates with the stability of a foam, since the mean bubble size increases with time due to coalescence and Ostwald ripening [19, 329, 330]. The bursting of bubbles and the escape of air from the foam leads to a macroscopically observed foam decay.
To monitor the mean bubble size, we use the equivalent bubble diameter, which is the diameter of a sphere with the same area as the bubble. Furthermore, we characterize the bubble size distribution by analyzing the dispersity of the bubble sizes (areas). In addition, the bubble shape is considered by analyzing the circularity of the bubbles in the foam. By these means, we offer a method to quantify foam structure and stability simultaneously.
Two model foams with different bubble characteristics, stabilized by two proteins with different structures, bovine serum albumin (BSA) and hydrophobin (HP), are considered to illustrate how the method works. Due to their characteristic primary and secondary structure, the proteins show different arrangements at air-water interfaces, leading to very distinguishable foam structures. Consequently, it is useful to consider mixtures of these proteins to test the method.
BSA is a "heart-shaped" protein with a molecular weight of about 66.5 kDa [143–145]. It contains 583 amino acids (607 amino acids including the signal peptide) [146] and is found in the blood serum of bovines and cow's milk [87, 88, 142]. HP on the other hand is a small protein with a molecular weight of about 10 kDa [159] and a primary structure containing about 100 amino acids [156, 162].
HPs are secreted by filamentous fungi and have multiple biological functions [99, 156, 159–161]. This protein family is divided into two classes, class I and class II hydrophobins. Representatives of these two classes differ in their spacing between cysteine residues, which are generally longer and vary more for class I HPs [100, 172]. Furthermore, class I and class II HPs differ in their solubility, the location of hydrophobic patches at the protein surface, and the structures they form upon assembly at hydrophilic:hydrophobic interfaces [98, 99]. In the current study a class I hydrophobin is used.
Furthermore, HPs are highly surface-active proteins due to their almost janus-like amphipathic nature [94] and their rigidity [95]. HPs contain 4 disulphide bonds which stabilize the core [162]. The high core stability ensures the exposition of a large hydrophobic patch to the protein surface [71, 162], which provides HPs with surfactant like characteristics [72, 160]. At a hydrophilic:hydrophobic interface, HPs spontaneously self-assemble into an amphipathic protein layer [162]. Due to their properties, HPs lower the surface tension significantly [92, 161, 162, 174] and the HP layers at the air-water interface show a high elasticity [94]. They are known to form some of the most stable aqueous foams [26, 68, 107, 160].
The tertiary structures of BSA and HP are shown in Figure 3.11 to illustrate their fundamental differences in shape and primary structure, which determine their surface

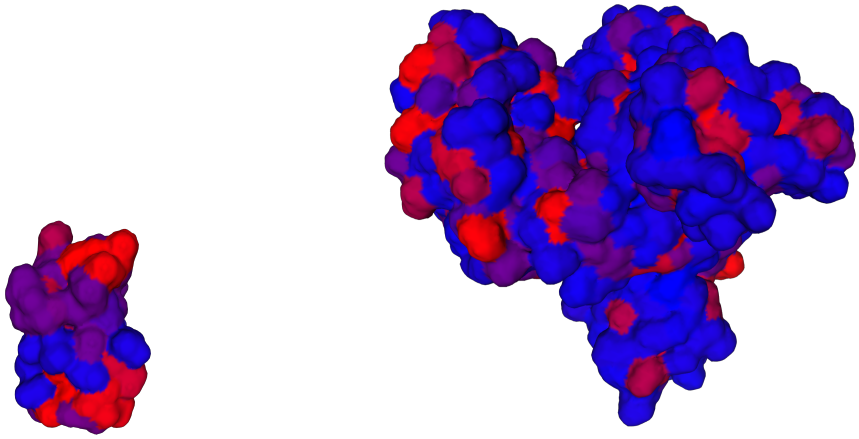

(a) (b)

Figure 3.11.: Surfaces of the protein structures of (a) HP (UP-ID: P16933, containing 136 amino acids) and (b) BSA (UP-ID: P02769, containing 583 amino acids). Hydrophobic amino acids are colored in red and hydrophilic ones in blue. [146]

activity and cause distinct variations in bubble shape, size distribution, and growth rate after foam preparation.

3.6.2. Materials and methods

Sample preparation

BSA (A7030, heat shock fraction, protease free, fatty acid free, essentially globulin free, pH 7, $\geq$ 98 %) from Sigma-Aldrich (Saint Louis, MO, USA) and HP (H*B hydrophobin) from BASF (Ludwigshafen, Germany) were used as-received. To ensure complete dissolution, HP solutions were stirred for 48 h (cf. [100, 188]). Solutions of 4 wt% protein in ultrapure water (18.2 MΩ cm) were prepared. This protein concentration was chosen, because whipping requires a protein concentration of 3 % to 40 % [35] and because it resulted in smooth foams.

Foam formation

For foam formation a T 25 easy clean control ULTRA-TURRAX (IKA-Werke GmbH & Co. KG, Staufen, Germany) equipped with dispersion tool S 25 N - 10 G was used. 2 g of protein solution were dispersed at a speed of 20 000 rpm for 1 min. The glass vessel used for foaming the protein solution was a custom-built glass cylinder with overflow protection in the upper part. The inner diameter of the glass cylinder was 13.6 mm, the height of the cylinder without overflow protection was 65 mm and the total height of the glass vessel was 90 mm. An image of the glass vessel is shown in

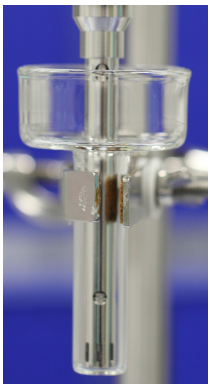

Figure 3.12.: Glass vessel used for foam formation with ultra turrax tool inserted. The upper part with larger diameter prevents the foam from overflowing during ultra turrax treatment.

Figure 3.12. The larger diameter in the upper part prevents overflowing of the foam (overflow protection).

Optical microscopy

Immediately after preparation, 0.01 g of foam were transferred to a microscope slide using a microspoon and then covered with a cover slip. Three little pieces of teflon film with a thickness of 50 µm served as spacer between microscope slide and cover slip. Bright field optical microscopy with 1.6-fold magnification was performed in transmission mode using a Leica MS5 stereomicroscope (Leica Microsystems GmbH, Wetzlar, Germany). Microscope images were taken every 5 min for 30 min. Microscopy was performed for three identical samples.

Image analysis

Data was analyzed using a Fujitsu (Minato, Tokyo, Japan) Esprimo P757 computer with Intel®Core™i7-6700 CPU @ 3.40 GHz, 3408 MHz, 4 cores, 8 logical processors and 16.0 GB of RAM operating in Microsoft (Redmond, WA, USA) Windows 10 Pro. For image analysis *Cellpose*[299, 300] and *Python* (Python Software Foundation, version 3.8.8) were used.
Pre-processing was performed in *Python* applying gaussian blur filter (cv2.GaussianBlur), image subtraction (cv2.subtract (2 times)), kuwahara filter (pykuwahara 0.3.2), background subtraction (skimage.restoration.rolling_ball, skimage.restoration.ellipsoid_kernel) and contrast enhancement (PIL.ImageEnhance.Contrast) to the original images.
Cellpose was trained on microscope images using the GUI. The pre-defined model 'CP' was taken as starting point and was adjusted by training on one own image to adjust for tiny bubbles and another own image to adjust for large bubbles. To identify the foam bubbles, the images were processed in the *Cellpose* GUI with the

trained model. Slight corrections to bubble masks have been made in individual cases. *Cellpose* provides a '_seg.npy'-file, which contains an array of the bubble masks. In this array, each pixel of the image is labelled with a number. The background is labelled with 0 and all masks are labelled with ascending integers.

Further analysis was performed in *Python* to add masks of small and large bubbles, remove edge bubbles and analyze bubble properties. To obtain the equivalent diameter, the area, and the crofton perimeter of each mask, we used the package skimage.measure.regionprops_table. The mean equivalent bubble diameter of all bubbles in an image, the mean circularity, and the dispersity were calculated from these data. When calculating the mean circularity, only circularities of bubbles with an equivalent diameter larger than 10 pixels were considered to minimize uncertainties caused by image resolution.

Mean and standard deviations of measurements of three identical samples were calculated. For each quantity the time-dependent cause was evaluated.

3.6.3. Results and discussion

Image processing and analysis

Figure 3.13 shows the workflow of the image analysis.

An optical microscope image is shown in Subfigure a (upper left). The edges of the bubbles are darker, however, the insides of the bubbles have the same contrast as the lamellae. Subfigure b (upper right) displays the pre-processed image. A gaussian blur filter, image subtraction and kuwahara filter are applied to reduce image noise. Subsequently, the background subtraction is used to smooth the background. Finally, the contrast of the image is enhanced. All pre-processing steps are performed using *Python*.

After image pre-processing, *Cellpose* is used to identify the bubbles, as shown in Subfigure c (lower right). The contrast of the edges is used to identify the bubbles. In the segmentation, the bubbles become individual masks and are colored randomly to improve the discriminability. An array containing all bubble masks is saved. The quantification and evaluation of the bubbles is done in *Python*. If there is a very heterogeneous size distribution of the bubbles, *Cellpose* is not able to detect all bubbles in an image. Our *Python* script allows to add two sets of masks (one for small bubbles and one for large bubbles) to solve this problem and to identify bubbles in a larger size range.

In our *Python* code, edge bubbles are neglected. The image in Subfigure d (lower left) shows the remaining bubble masks in different colors. These are overlaid with the pre-processed microscope image so that removed bubbles are shown in white. If only a small part of a bubble is visible in the image, treating that part as a whole bubble can distort the statistical analysis, especially in the case of large bubbles. To remove

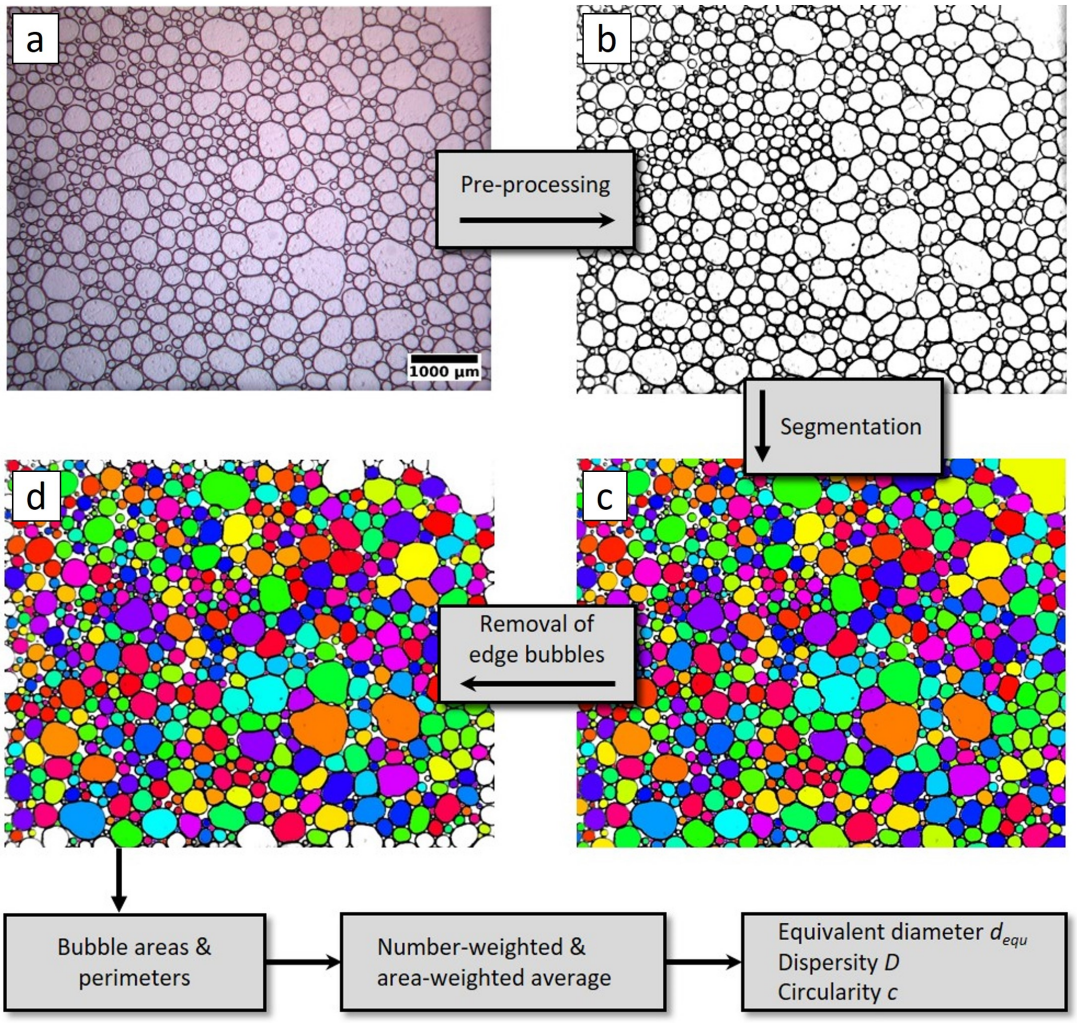

Figure 3.13.: Image processing: The original microscope image is pre-processed to reduce background noise and enhance contrast. Bubble masks are detected using *Cellpose* (Segmentation). Subsequently, masks of edge bubbles are removed. From the remaining masks bubble areas and perimeters are determined, averages are calculated and the mean equivalent diameter, mean circularity and dispersity are calculated for each image.

edge bubbles the criterion

$$l = \begin{cases} < \frac{1}{4} d_{equ} \Rightarrow & \text{consider bubble} \\ > \frac{1}{4} d_{equ} \Rightarrow & \text{do not consider bubble} \end{cases} \tag{3.1}$$

is applied, where l is the length (number of pixels) the bubble shares with the edge of the image and d_{equ} the equivalent diameter of the bubble. Figure 3.14 illustrates this approach.
Cellpose provides an array with bubble masks, that can be analyzed in *Python*. The bubble areas, equivalent diameters, and perimeters (in pixels) for all detected masks can be obtained using the scikit-image library. The equivalent diameter is the diameter of a circle with the same area as the bubble, as noted in eq. 3.2:

$$d_{equ} = \sqrt{\frac{4}{\pi} A} \tag{3.2}$$

where A is the actual bubble area in the microscope image. For each image, we calculate the mean equivalent bubble diameter of all bubbles in the image.
To characterize the shape of the bubbles, the circularity of each bubble is calculated as

$$c = \frac{4\pi A}{p^2} \tag{3.3}$$

where A is the area of the bubble and p is the perimeter. The circularity is 1.0 for a perfect circle and as it approaches 0.0, it indicates an increasingly elongated shape. Subsequently, the mean circularity of all bubbles in one image is calculated.
The characterization of the bubble size distribution in an image is done by calculation of the dispersity. Analogously to polymer chemistry, where the dispersity of molar masses is given by [331, 332]

$$D = \frac{\overline{M_w}}{\overline{M_n}} \tag{3.4}$$

with M_w mass weighted average of the molar mass and M_n number weighted average of the molar mass, we define the bubble dispersity

$$D := \frac{\overline{A_a}}{\overline{A_n}} \tag{3.5}$$

where $\overline{A_a}$ is the area weighted average of the bubble areas and $\overline{A_n}$ is the number weighted average (=mean) of the bubble areas.

Optical microscopy of HP- and BSA-stabilized foams

Figure 3.15 shows pre-processed optical microscope images of HP- and BSA-stabilized foams at different time steps. Clear differences in the temporal behavior can be distinguished between foams only containing HP and those only containing BSA. The bubble shape, size distribution and growth rate vary significantly between these foams.

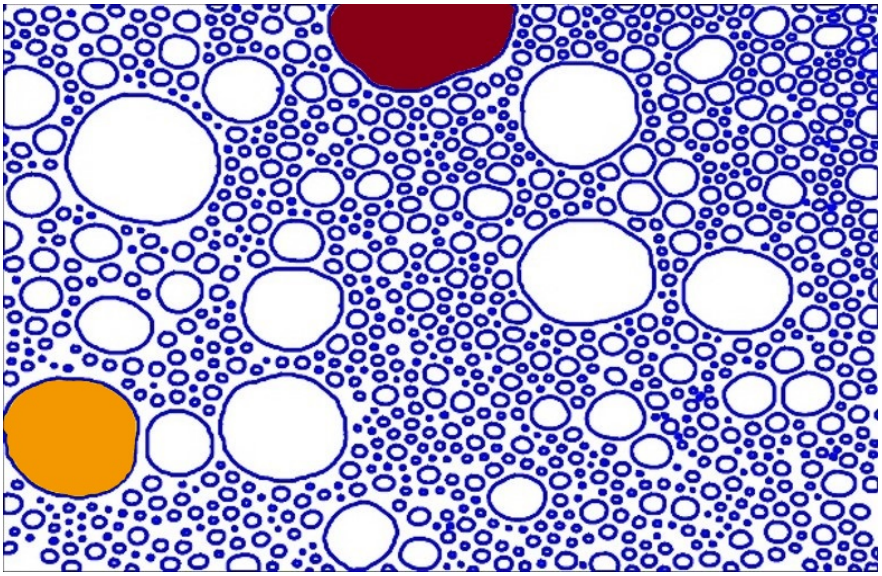

(a) Outlines of all detected bubble masks are shown in blue. Bubbles like the orange one should be evaluated, bubbles like the red one should not be considered.

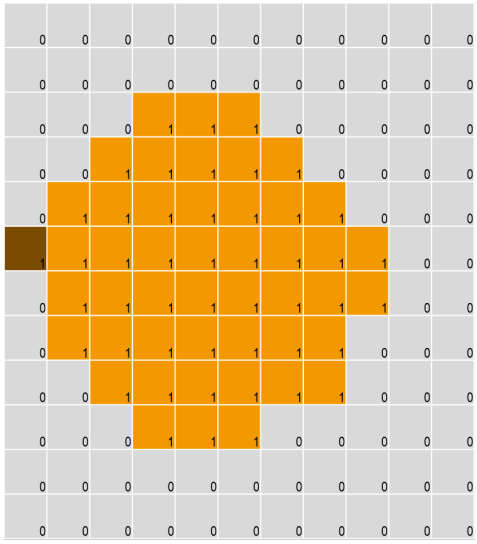

(b) $A = 48$
$d_{equ} = 8$
$l = 1$
$\Rightarrow l < \frac{1}{4} d_{equ}$
$\Rightarrow$ Bubble will be evaluated.

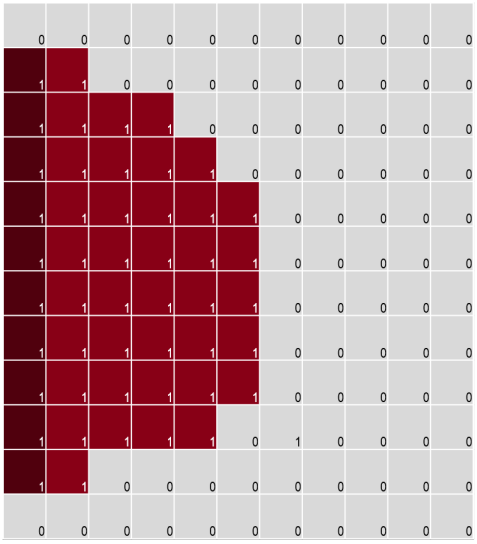

(c) $A = 48$
$d_{equ} = 8$
$l = 10$
$\Rightarrow l > \frac{1}{4} d_{equ}$
$\Rightarrow$ Bubble will be removed.

Figure 3.14.: Illustration of the removal of edge bubbles. Edge bubbles with $l > \frac{1}{4} d_{equ}$ are removed. l is the length the bubble shares with the image edge, d_{equ} is the equivalent diameter of the bubble calculated from its area.

A visual comparison of the microscope images of these two different foams (first and last row in Figure 3.15) shows that the bubbles in the BSA-stabilized foam have a broader size distribution and their increase in size is more pronounced. Over time, the bubble shape changes from spherical to polyhedral. The bubbles in the HP-stabilized foam not only have a narrower size distribution and remain smaller over time, but also have a different shape. Although the HP-stabilized foam bubbles become less spherical over time, the vertices remain rounded.
Additionally, Figure 3.15 also shows microscope images of foams stabilized by blends of HP and BSA (rows two through four). Three different ratios of HP to BSA were considered (3:1, 2:2, and 1:3). The foams stabilized by mixtures of HP and BSA are less stable than foams stabilized by HP alone, but more stable than foams stabilized by BSA, since the bubble sizes grow faster than for HP- but slower than for BSA-stabilized foams. BSA-stabilized foams have the widest bubble size distribution. The bubble shapes of foams stabilized with blends of HP and BSA look more like the purely BSA-stabilized foams. To quantify these visually observed differences, the temporal evolution of the mean equivalent bubble diameter was analyzed and the dispersity and mean circularity of the bubbles were calculated.

Temporal evolution of mean bubble size

As foams age, the mean bubble size increases due to coalescence and Ostwald ripening [19, 329, 330]. As the bubbles grow and burst, the foam decays. Therefore, the mean bubble size over time is a measure of foam stability. Figure 3.16 shows the mean equivalent bubble diameter over time for HP- and BSA-stabilized foams. Throughout the measurement period, the mean bubble size of HP-stabilized foams remains significantly smaller than that of BSA-stabilized foams. Proteins can adsorb at an air-water interface due to hydrophobic amino acid residues [16]. As with most proteins, the majority of the surface amino acid residues of BSA are hydrophilic [16, 146].
However, BSA also has some hydrophobic amino acids on its surface that allow it to attach to the bubble surfaces and thus stabilize the foam. HP has a different molecular structure with a large hydrophobic part on its surface, which makes it a very surface-active molecule [16, 162]. At air-water interfaces, HP molecules pack very tightly and form very strong films that can significantly resist bubble shrinkage [16].
Class I hydrophobins form insoluble rodlet films at air-water interfaces when the surface membrane gets compressed [160]. Since foams are dynamic systems where bubbles shrink and others grow at their expense (Ostwald ripening [26, 333, 334]), the HP films at the interface are not static either. The HPs at the surface of a shrinking bubble experience compression and can therefore form rodlet structures. These very stable films around the small bubbles prevent further shrinkage. As a result, larger bubbles cannot grow at their expense and the foam becomes more stable as observed by optical microscopy.
In addition, HP has a lower molecular weight than BSA. Therefore, it can move faster to the interface, assemble at the interface while the bubbles are still small, and stabilize the bubbles in the liquid. By forming stable HP films, the bubbles stay

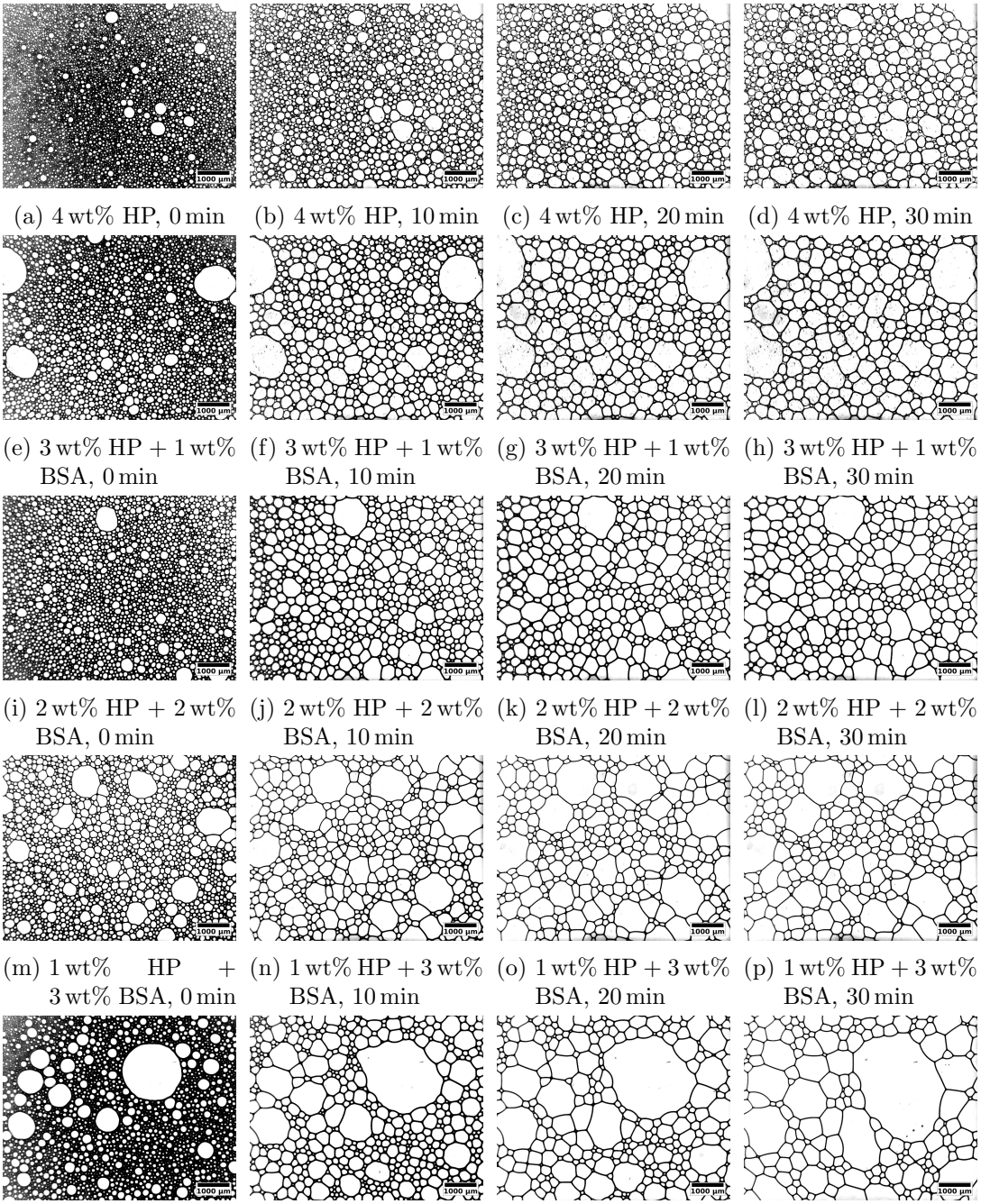

(a) 4 wt% HP, 0 min (b) 4 wt% HP, 10 min (c) 4 wt% HP, 20 min (d) 4 wt% HP, 30 min

(e) 3 wt% HP + 1 wt% BSA, 0 min (f) 3 wt% HP + 1 wt% BSA, 10 min (g) 3 wt% HP + 1 wt% BSA, 20 min (h) 3 wt% HP + 1 wt% BSA, 30 min

(i) 2 wt% HP + 2 wt% BSA, 0 min (j) 2 wt% HP + 2 wt% BSA, 10 min (k) 2 wt% HP + 2 wt% BSA, 20 min (l) 2 wt% HP + 2 wt% BSA, 30 min

(m) 1 wt% HP + 3 wt% BSA, 0 min (n) 1 wt% HP + 3 wt% BSA, 10 min (o) 1 wt% HP + 3 wt% BSA, 20 min (p) 1 wt% HP + 3 wt% BSA, 30 min

(q) 4 wt% BSA, 0 min (r) 4 wt% BSA, 10 min (s) 4 wt% BSA, 20 min (t) 4 wt% BSA, 30 min

Figure 3.15.: Microscope images of foams stabilized by HP (first row), HP-BSA mixtures (second to forth row), and BSA (last row). Time proceeds from left to right.

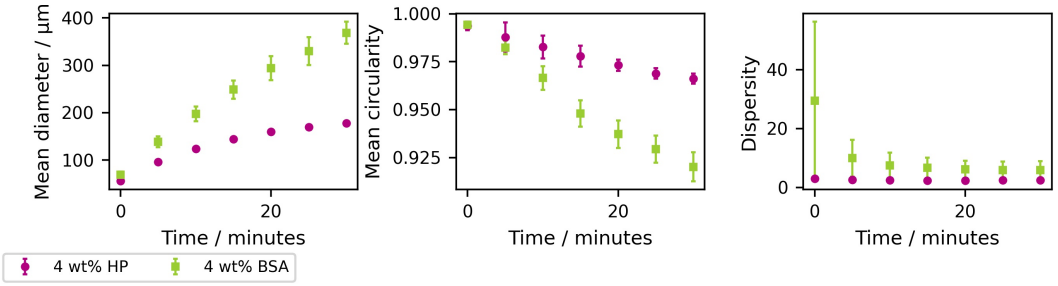

Figure 3.16.: Comparison of the temporal evolution of mean equivalent bubble diameter, mean circularity and dispersity of HP- and BSA-stabilized foams.

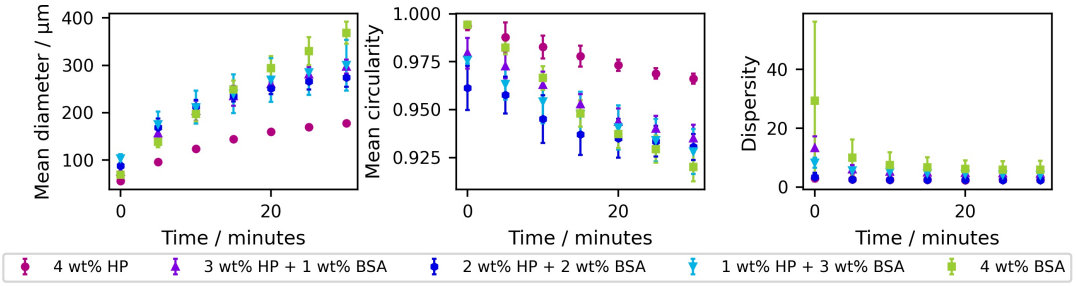

Figure 3.17.: Comparison of the temporal evolution of mean equivalent bubble diameter, mean circularity and dispersity of HP- and BSA-stabilized foams, as well as differently concentrated mixtures of HP and BSA.

smaller. Furthermore, HP has the ability to significantly lower the surface tension and achieves lower surface tensions than BSA [92, 162]. A lower surface tension allows for a larger surface area. The surface of more smaller bubbles adds up to a larger area than a smaller number of larger bubbles filled with the same total volume of air. The lower surface tension caused by HP favors the many small bubbles observed in HP-stabilized foams.

Temporal evolution of circularity

As discussed in the literature, foams dry during aging and the bubble shape changes from spherical to polyhedral [33, 126, 335]. These changes in bubble shape can also be seen in the microscope images in Figure 3.15. When looking at the microscope images, it is noticeable that the bubble shape varies between HP-stabilized and BSA-stabilized foams. BSA-stabilized foams form polygonal shapes as they age. Although the overall shape of the bubbles in HP-stabilized foams is similar to polygonal, the vertices are rounded.
Circularity compares the area of the bubble to the area that a circle with the perimeter of the bubble would have, and is therefore a measure of how close the shape of the bubble under consideration is to that of a perfect circle. We use circularity to compare the bubble shapes of BSA-stabilized and HP-stabilized foams. Figure 3.16 shows the temporal evolution of the bubble circularity of HP- and BSA-stabilized foams. Over time, the circularity of the bubbles decreases as the bubble shape changes from circular to polygonal. This decrease in circularity with time is observed for both systems. At $t = 0$, both, HP- and BSA-stabilized foams show a mean circularity close to 1. This means that the bubbles are spherical, which is consistent with what can be observed in the microscope images. However, at all later time steps, the circularity of the HP-stabilized foams is significantly higher than that of the BSA-stabilized foams, which means that the bubbles in the HP-stabilized foams have a rounder shape (their shape is closer to a circle). The bubbles in the HP-stabilized foams are less elongated than some bubbles in the microscope images of the BSA-stabilized foams. In addition, the vertices of the bubbles in the HP-stabilized foams are rounded. Both of these effects cause the higher circularity observed in the HP-stabilized foams.

Temporal evolution of dispersity

To quantify the variation in bubble size within an image, we calculated the dispersity of the bubble size. The temporal behavior of the dispersity of HP- and BSA-stabilized foams is shown in Figure 3.16. Especially in the beginning there are many small bubbles and few large bubbles. Therefore, a higher dispersity is observed (especially for BSA-stabilized foams). Over time, Ostwald ripening and coalescence cause small bubbles to disappear. Therefore, the distribution of bubble sizes shifts and the dispersity decreases.
HP-stabilized foams show a more homogeneous bubble size distribution and smaller dispersity than BSA-stabilized foams. This result is consistent with the visually ob-

served foam properties in the microscope images. The narrower size distribution observed for HP-stabilized foams can be explained by the adsorbed HP-film at the air-water interface. Due to their special properties, HPs pack very tightly and form strong films at the air-water interface [16]. These films stabilize the air bubbles well in the liquid. As a result, they remain smaller.

HP-BSA mixtures

Figure 3.17 shows the temporal evolution of the mean equivalent bubble diameter, mean circularity and dispersity of foams stabilized by mixtures of HP and BSA compared to systems stabilized by one of these proteins. Mixtures were investigated at different ratios: 3 wt% HP + 1 wt% BSA, 2 wt% HP + 2 wt% BSA, and 1 wt% HP + 3 wt% BSA. The differences in between the foams stabilized by mixtures are distinctly less pronounced as compared to purely HP-stabilized foams.
HP forms monolayers with very regular patterns (rodlets) at the air-water interface [160]. As explained above, these highly amphipathic layers stabilize the foam well. Foam stability decreases significantly when BSA is added to HP foams: All foams stabilized by blends of HP and BSA show mean bubble diameters closer to those of BSA-stabilized foams than to those of HP-stabilized foams. Only at the end of the measurement period, the mean bubble diameter of foams stabilized by HP-BSA mixtures becomes distinguishably smaller than that of BSA-stabilized foams, but still remains significantly larger than that of HP-stabilized foams. Therefore, BSA seems to impede the regular arrangement of HP molecules at the interface. Consequently, the structures of the protein networks at the air-water interface are less regular and the emulsifying proteins are not able to achieve the same stability as in HP-stabilized foams.
The microscope images and the results of the analysis also show that the bubble shapes of foams stabilized by blends of HP and BSA are more similar to BSA-stabilized foams. The circularity of foams stabilized by HP-BSA blends is comparable to that of foams stabilized by BSA alone, while HP-stabilized foams show significantly higher circularity. For the dispersity, the trend is less pronounced. Mixtures of HP and BSA show dispersities in between those of BSA- and HP-stabilized foams with 2 wt% HP + 2 wt% BSA showing a similar dispersity as 4 wt% HP.
These investigations show that differences in foam structure in relation to molecular differences can be well characterized by choosing the three parameters equivalent bubble diameter, circularity, and dispersity resulting from image analysis. This can be achieved using simple methods and freely available software. Therefore, the developed method can be used to study different systems and understand how they influence foam stability and structure.

Bubble diameter distribution

The dispersity of the equivalent bubble diameters offers a measure of the bubble size distribution. However, to investigate the bubble diameter distribution in more de-

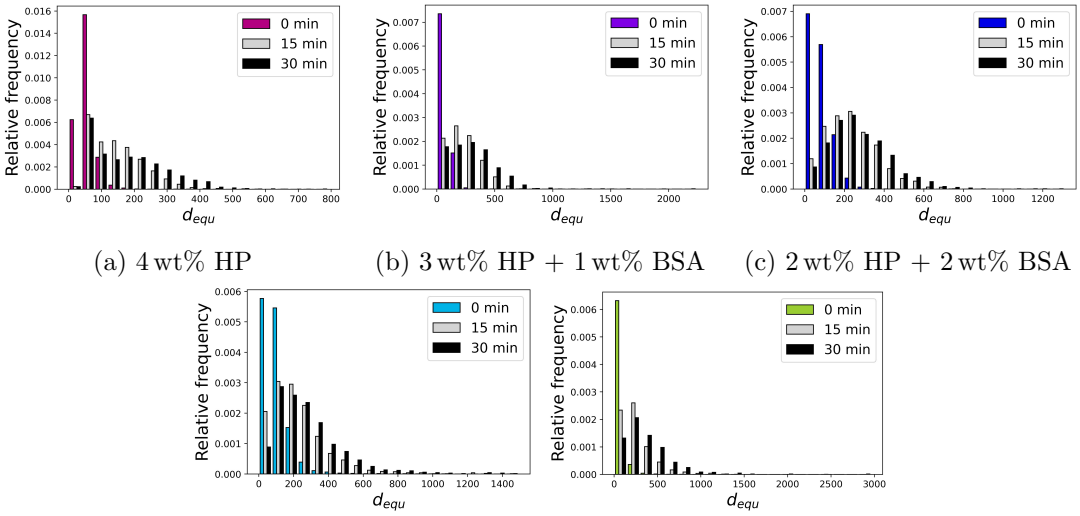

(a) 4 wt% HP (b) 3 wt% HP + 1 wt% BSA (c) 2 wt% HP + 2 wt% BSA

(d) 1 wt% HP + 3 wt% BSA (e) 4 wt% BSA

Figure 3.18.: Temporal evolution of the equivalent bubble diameter distribution. Ostwald ripening leads to a broader size distribution in the course of time.

tail, histograms of the equivalent bubble diameters are shown in Figure 3.18. Each histogram includes the bubbles detected for three identically prepared samples. Additionally, in each plot the histograms of the bubble size distributions at the beginning, after 15 min and after 30 min are shown to investigate the temporal evolution. Over time, the bubble size distribution becomes broader in every investigated case. This trend can be explained by Ostwald-ripening. Over time, large bubbles grow and small bubbles shrink due to the pressure differences between differently sized bubbles (Laplace pressure) [19, 112, 130]. The growth of large bubbles at the expense of small bubbles leads to a broader bubble size distribution. The disappearance of tiny bubbles due to Ostwald ripening is further observed in the histograms and represents one of the most obvious temporal changes, especially at the beginning of the process. Therefore, the detection of tiny bubbles is important to study Ostwald ripening.
To compare the different proteins and their mixtures see Figure 3.19. With increasing BSA content, the size distribution becomes broader, which is in agreement with the higher dispersity and the presence of larger bubbles at the beginning of the measurements.

Economic aspect

The employed software in the current method for automated analysis of the temporal evolution of foams is freely available and we provide the code for data analysis in the Supporting Information. Therefore, the costs for using the proposed method are lower than commercially available software.
Furthermore, the time investment is lower by using the proposed method than by

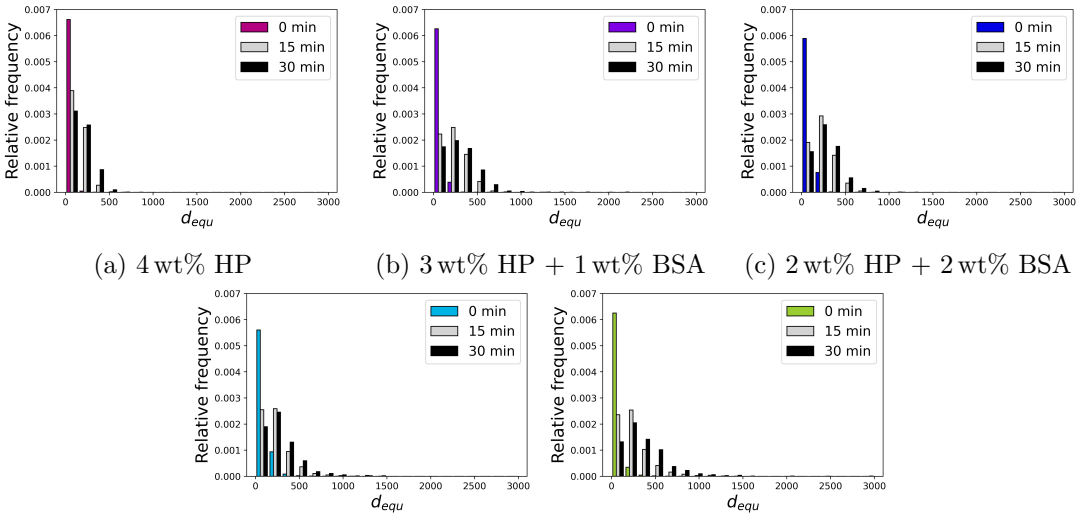

(a) 4 wt% HP (b) 3 wt% HP + 1 wt% BSA (c) 2 wt% HP + 2 wt% BSA

(d) 1 wt% HP + 3 wt% BSA (e) 4 wt% BSA

Figure 3.19.: Temporal evolution of the equivalent bubble diameter distribution. Samples with a higher BSA content show a broader size distribution.

using uncommercial analytical methods classically applied in fundamental research. A classical way of analyzing the sizes of bubbles in a foam is to measure the bubble size by hand [311–313]. The microscope images used in this study contain about 200 to 5000 bubbles each. Measuring 100 bubble diameters manually by drawing corresponding lines in *ImageJ* takes about 4 min to 10 min, which corresponds to about 2.5 s to 5 s per bubble. The needed time depends on the bubble size. To measure all bubble sizes in one image would then take between 17 min and 7 h depending on the number of bubbles contained in the image. Therefore, this method is very time intensive. Alternatively, one could only measure a few bubbles by hand to reduce the invested time. However, this approach biases the precision of the analyzed data.
The segmentation with *Cellpose* takes, depending on the number of bubbles, between 5 s and 60 s (about 70 s for two sets of masks) per image. Including the data analysis with our script, the total time of segmentation and analysis is about 2 min. Figure 3.20 shows a comparison of measuring the bubble diameters manually and analyzing the bubble properties with the presented approach. Manual measurement of the bubble diameter not only takes more time, but also does not provide information about the bubble shape.
Another approach is to threshold an image and determine the object sizes from the areas of connected same color pixels in the binary image. Figure 3.21 shows a section of a microscope image of a HP foam and the same image where a threshold was applied using *ImageJ* [336]. Since the interior of the bubble and of the continuous phase have the same gray level, the difference cannot be extracted using a threshold. Therefore, thresholding is not sufficient for detecting objects in these kinds of samples. For this reason, the use of a machine learning algorithm and / or the possibility for manual

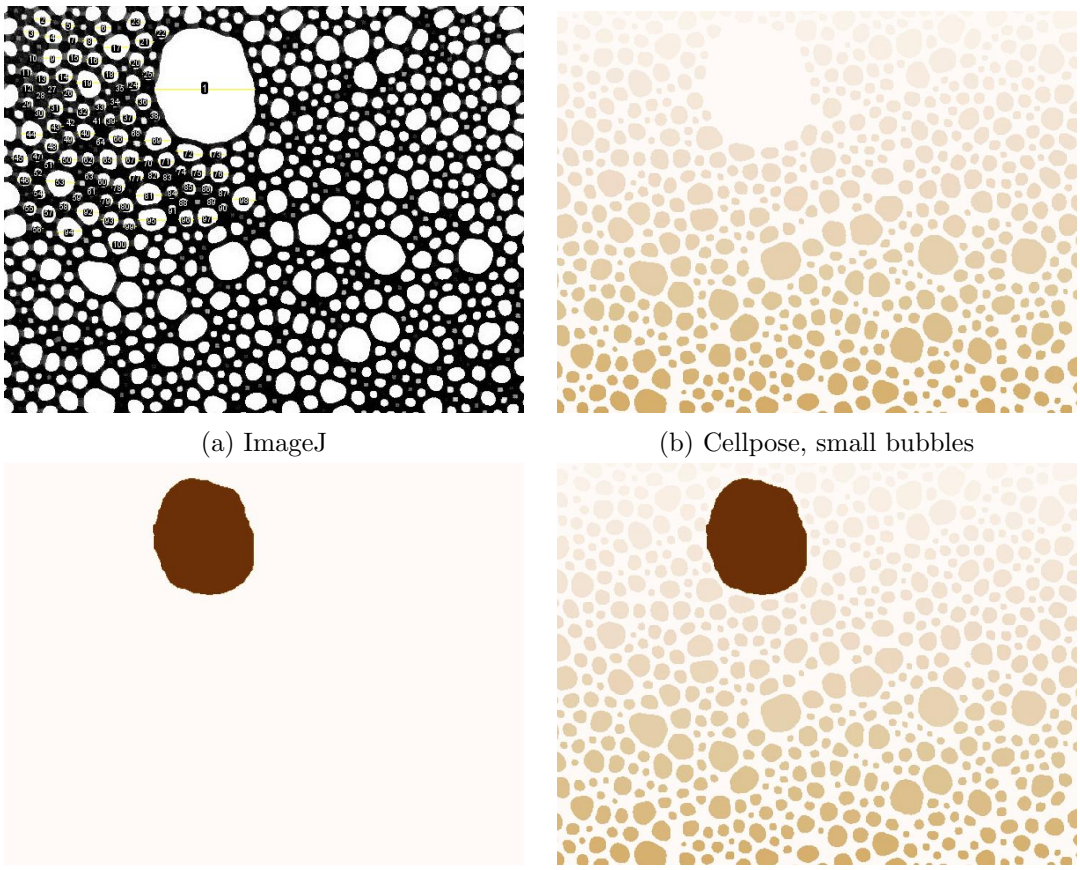

(a) ImageJ

(b) Cellpose, small bubbles

(c) Cellpose, large bubbles

(d) Small and large bubbles combined

Figure 3.20.: (a) Microscope image of foam, where 100 bubble diameters where measured by hand using *ImageJ* [336]. The required time was 4 min 26 s. (b) Segmentation of small bubbles performed with *Cellpose* on the same microscope image. The required time was 57 s. (c) Segmentation of large bubbles. The required time was 5 s. (d) Addition of small and large bubble masks. The required time for adding the masks and analyzing the bubble properties was 35 s. Therefore, in total 1 min 37 s were required to analyze the image with the proposed method. For better visability, cutouts of the images are shown. To see the whole image, refer to Subfigure 3.15i.

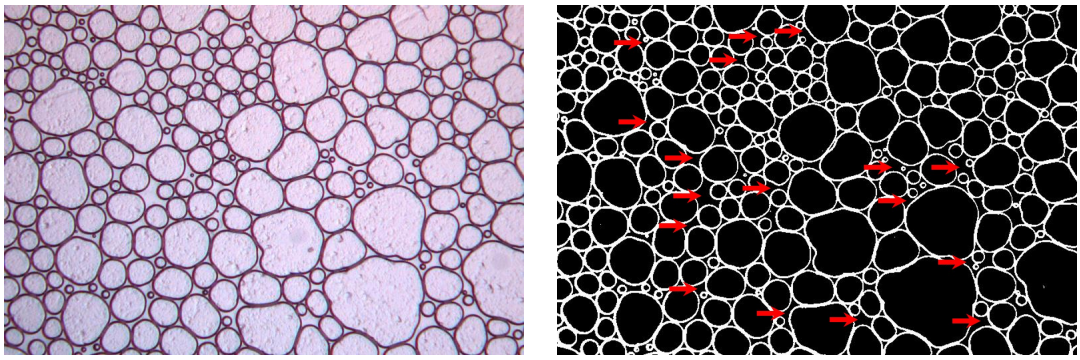

(a) Microscope image (b) Thresholded image

Figure 3.21.: (a) Microscope image and (b) thresholded image of a HP foam. The red arrows mark example areas of continuous phase, which cannot be distinguished from bubble interior by contrast alone.

correction leads to higher precision in detecting the bubbles correctly.
Furthermore, the *Cellpose* GUI offers the possibility to manually correct bubble masks to improve the precision. To what extend this option is used, is up to the user.
With the addition of two (or more) sets of masks for tiny bubbles and larger bubbles, our suggested method provides a greatly improved precision.

3.6.4. Conclusion

The developed method proves to be a useful and relevant tool for quantitative analysis of microscope images. It allows automated analysis of the temporal evolution of foams, including bubble growth, size distribution and bubble shape. Variations caused by different emulsifiers can be detected and analyzed quantitatively and economically, offering great advantages over expensive setups commonly used to determine bubble stability. The investigations show that the data analysis is consistent with visual observation. The large number of bubbles detected in each image provides significant statistics to ensure the reproducibility of the calculated quantities.
The example analysis of HP- and BSA-stabilized foams shows that the choice of emulsifier influences the foam structure and stability. Bubble size and shape vary depending on the properties of the emulsifier. The two proteins selected have different molecular structures. HP has a large hydrophobic patch on its surface and assembles into very strong films with regular patterns at the air-water interface [16, 160, 162]. These properties result in a significantly more stable foam and a rounder bubble shape. By analyzing microscope images with the presented method, it is demonstrated how mixing the two proteins influences their arrangement and the resulting stability.
Thus, using simple laboratory equipment and open-source software, we are able to introduce our developed method as a way to analyze foams and draw meaningful conclusions.
Here the quotation from [302] ends.

4. Interaction of bovine serum albumin and hydrophobin

4.1. Introduction

Many food systems comprise a mixture of several proteins. Examples are cow's milk and cream [337, 338] as well as plant-based milk-alternatives [200, 201, 339]. The protein composition is defined by the natural composition of the milk or the grain kernel, respectively, or may be varied by addition of proteins from other crops or legumes. The properties of the contained proteins define the characteristics of the foam prepared from the milk or plant-based alternative.
The interactions of the different proteins with each other influence their arrangement at the air-water interface and consequently the foam stability. For this reason, a model system containing two proteins with different molecular structure is regarded in this study: bovine serum albumin (BSA) and H*B hydrophobin (HP). Systems consisting of one protein type as well as mixtures of both proteins at varying ratios were investigated.
The mesoscopic properties of these systems including foam stability and foam structure are presented and discussed in Section 3.6.3. The investigations show that foams stabilized by HP alone retain a smaller bubble size over time than those stabilized by protein mixtures or BSA alone, which means that HP solutions produce more stable foams. Furthermore, also the bubble shape is influenced by the protein type. HP shows rounder bubble shapes with rounded vertices in contrast to BSA, which shows polyhedral bubbles with angular vertices.
In this chapter, the results of additional measurements are presented and discussed. These measurements investigate the protein arrangement at the interface and the interfacial properties. The aim of this study is to learn more about the behavior of HP and BSA at the interface as well as about their interactions with each other. To achieve this, the interaction of HP and BSA with each other is investigated by measuring differential scanning calorimetry (DSC), the properties of the interface are determined by measuring the surface tension and the protein arrangement at the interface is explored by atomic force microscopy (AFM) studies. In addition, molecular interactions are discussed.

4.2. Materials and methods

4.2.1. Proteins

BSA (A7030, heat shock fraction, protease free, fatty acid free, essentially globulin free, pH 7, $\geq$ 98 %) from Sigma-Aldrich (Saint Louis, MO, USA) and HP (H*B hydrophobin) from BASF (Ludwigshafen, Germany) were used as-received and dissolved in ultrapure water (18.2 MΩ cm). To ensure complete dissolution, HP solutions were stirred for 48 h (cf. [100, 188]). The total protein concentration in the sample solution is given at the description of the methods. For HP-BSA mixtures, the HP:BSA mass fraction ratios of 3:1, 1:1 and 1:3 were investigated, which means for a 4 wt% protein solution: the 3:1 ratio solution contains 3 wt% HP + 1 wt% BSA in water, the 1:1 ratio 2 wt% HP + 2 wt% BSA, and the 1:3 ratio 1 wt% HP + 3 wt% BSA.

4.2.2. Sodium dodecyl sulfate-polyacrylamid gel electrophoresis

BSA and HP aqueous solutions with a concentration of 0.1 wt% protein in ultrapure water were prepared. For sodium dodecyl sulfate-polyacrylamid gel electrophoresis (SDS-PAGE), 4 µL LDS running buffer (Novex MES SDS running buffer from Thermo Fisher Scientific, Waltham, MA, USA) and 1.6 µL reducing agent (NuPAGE sample reducing agent from Thermo Fisher Scientific, contains dithiothreitol (DTT)) were added to 10.4 µL sample. The samples were heated at 90 °C for 10 min in a Thermomixer comfort (Eppendorf SE, Hamburg, Germany). SDS-PAGE was performed in an Invitrogen Mini-Gel-Tank (Thermo Fisher Scientific) at 120 V for 1 h. The gel was a NuPAGE 4 % to 12 % Bis-Tris Gel. As marker Page Ruler Plus from Thermo Fisher Scientific was used. The samples were stained over night with Coommassie blue and destained several times the next day.

4.2.3. High performance liquid chromatography

High performance liquid chromatography (HPLC) was performed on an HPLC arrangement containing a 7725i injection valve with 20 µL loop from Rheodyne (IDEX Corporation, Lake Forest, Illinois, US), a Series 1260 quarternary gradient pump from Agilent Technologies (Santa Clara, California, US), a Series 1200 column oven from Agilent Technologies, a Series 1200 photodiode array detector (DAD) from Agilent Technologies measuring at a wavelength of 220 nm and a 385-LC evaporative light scattering detector (ELSD) from Varian (Palo Alto, California, US). The system is equipped with the software OpenLAB CDS Chemstation from Agilent Technologies. Measurements were performed using the BioBasic column from Thermo Scientific (Waltham, MA, USA), which contains three columns with pore sizes of 300 Å, 60 Å and 60 Å. The column length is 100 mm, the diameter 4.6 mm and the grain size 5 µm. According to the manufacturer's specifications, it is designed for the analysis of proteins and peptides or other biomolecules with a high hydrophobicity. The column temperature during measurement was 37 °C. The isocratic mobile phase contained 40 % acetonitrile (CH_3CN) and 60 % TFA (trifluoroacetic acid) solution (0.1 %

TFA in water). The applied flow rate was $1\,\mathrm{mL\,min^{-1}}$. HPLC measurements were performed by a trained service technician inhouse.

4.2.4. Differential scanning calorimetry

Protein solutions of a concentration of 10 wt% in ultrapure water (18.2 MΩ cm) were prepared and filled into DSC sample aluminium pans (100 µL volume, Mettler-Toledo GmbH, Gießen, Germany). Additionally, the dry powders of HP and BSA were filled into DSC sample aluminium pans. DSC was measured with a DSC 3+ from Mettler-Toledo GmbH. Measurements were performed with a heating rate of $2\,\mathrm{K\,min^{-1}}$ in a temperature range from 5 °C to 90 °C under nitrogen atmosphere with a flow of $30\,\mathrm{mL\,min^{-1}}$. DSC measurements were performed by a trained service technician inhouse. All measurements were performed for at least three identically prepared samples. Melting peaks were determined using the software STARe Excellence Thermal Analysis Software (Mettler-Toledo GmbH). From the minima of three measurements mean and standard deviation were calculated. In the figures representative single measurements are shown.

4.2.5. Surface tension

Surface tension was measured on a DCAT 21 from DataPhysics Instruments GmbH (Filderstadt, Germany) with Wilhelmy plate setup by a trained service technician inhouse. The rectangular plate had a length of 19.9 mm, a width of 0.2 mm and a wetted length of 40.2 mm. The contact angle was 0°. Measurements were performed at 25 °C. Every sample was measured four times and measurements were repeated for two identical samples. Mean and standard deviation were calculated from all eight measurements for each sample type. Measurements for a third identical sample could not be performed because the device was sent in for maintenance and was not repaired afterwards.

4.2.6. Brewster angle microscopy

BAM imaging was performed using an EP3-BAM instrument equipped with EP3 View software from Park Systems GmbH (Göttingen, Germany; previously Accurion GmbH respectively Nanofilm Technologie GmbH). The laser had a wavelength of 658 nm. For the measurements an objective with 20-fold magnification was used and the sample was placed in a white Teflon trough. Ultrapure water (18.2 MΩ cm) was used as subphase and the protein solution was pipetted onto it. Films were formed for 1 µL or 2 µL of 0.4 wt% protein solutions pipetted to the water surface after about 1 h resting time. Before film formation, a dust particle moves fast across the water surface, whereas at film formation, it swings slightly at one point. Measurements were performed at a Brewster angle of 52.857°, which is the Brewster angle for water at room temperature. The sample stage height, laser power, polarizer angle, compensator angle and analyzer angle were adjusted to optimize the signal-to-noise ratio and the image contrast.

4.2.7. Atomic force microscopy

AFM was performed on a Dimension ICON Fast Scan from Bruker Corporation (Billerica, MA, USA). All measurements were performed in tapping mode using OTESPA cantilevers, which are aluminium coated and have a resonance frequency of 300 kHz and a spring constant of 26 N m^{-1}. For each image 512 samples/line were used. Scan sizes were in the range of 0.3 µm to 3 µm and the applied scan rates between 0.5 Hz and 1 Hz.
Protein solutions were transferred to highly-oriented pyrolytic graphite (HOPG) by different methods. Using the "dried droplet"-method a 100 µL droplet of protein solution was pipetted to freshly cleaved HOPG and let to dry over night under a cover. Alternatively, the "surface transfer"-method was used. Therefore, 10 mL of protein solution were filled in a trough and let rest for about 1.5 h to 4 h or over night under a glass cover. Subsequently, the surface was transferred to freshly cleaved HOPG as described in Figure 4.1.

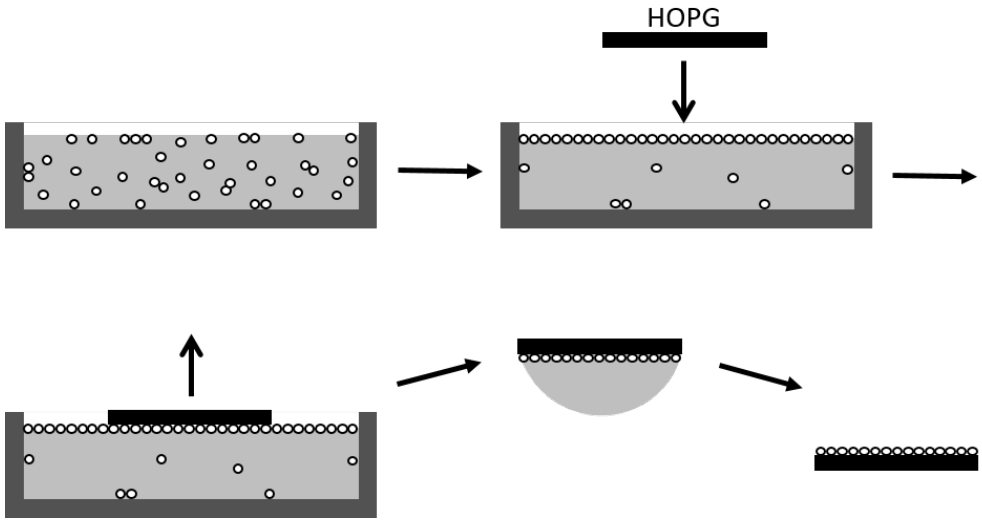

Figure 4.1.: Surface transfer method. The sample solution rests in a trough and forms an interfacial film after some time. Freshly cleaved HOPG is moved towards the sample surface until touching it and subsequently withdrawn. Afterwards, the transferred sample is left to dry.

4.3. Results and discussion

4.3.1. Sodium dodecyl sulfate-polyacrylamid gel electrophoresis

The purity of the proteins is described by the supplier as $\geq 98\,\%$ for BSA and about 80 % for HP. To check the purity of the proteins, SDS-PAGE and HPLC were performed. Figure 4.2 shows the results of SDS-PAGE.

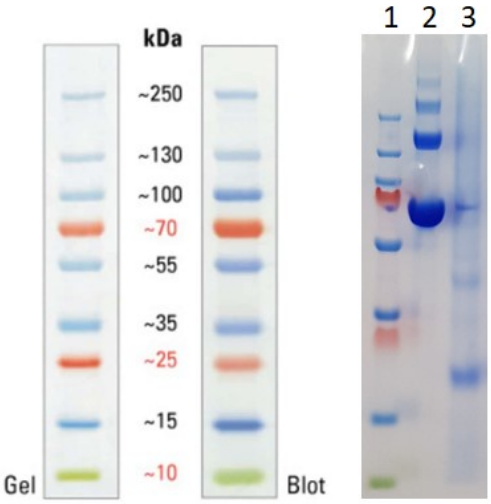

Figure 4.2.: SDS-PAGE of aqueous solutions of HP and BSA. (1) Marker, (2) BSA, (3) HP.

The molecular weight is about 66.5 kDa for BSA [143–145] and about 10 kDa for HP [159, 170]. For BSA, SDS-PAGE shows a pronounced bar below the red 70 kDa marker, which represents the BSA monomer (66.5 kDa) and suggests that BSA monomers constitute the largest fraction. In addition, bars with decreasing markedness are shown above the 130 kDa and above the 250 kDa markers, which imply the presence of dimers and tetramers as well as small fractions of larger aggregates. Aggregate formation can be imaged via electrostatic interactions of surface charges and hydrophobic interactions via hydrophobic amino acids located at the BSA surface. The bars of BSA are more clear than those of HP, which suggests a higher purity of BSA. For HP, the largest fraction is found at about 20 kDa, which reveals that HP is mainly represented by dimers. Additionally, bars are observed at about 40 kDa and 60 kDa, which suggest the presence of tetramers and hexamers. Indeed, the tendency of hydrophobins to aggregate into dimers or other oligomers due to their large hydrophobic surface patches was also described by Wang et al. [340] and Torkkeli et al. [341] for other hydrophobins.

4.3.2. High performance liquid chromatography

HPLC was performed to check the purity of the proteins and also to see whether HP and BSA interact with each other in solution. HPLC allows for a separation of the components of a sample according to polarity with high resolution. However, it does not provide the identification of the components. These can only be determined and examined by comparison with standards. The signals of each measurement were recorded by two different detectors simultaneously. Figure 4.3 shows chromatograms measured with the UV detector (DAD) at 220 nm and Figure 4.4 chromatograms measured with the evaporative light scattering detector (ELSD). Each figure shows the elution of HP, BSA and a 1:1 mixture thereof. Each sample was prepared at a concentration of 0.1 wt% protein in ultrapure water.
For BSA both chromatograms show mainly 1 peak at about 3.3 min, which reveals that the samples are quite pure. This result is consistent with the specifications provided by the manufacturer, which state a purity of $\geq 98\,\%$.
For HP the ELSD detected mainly one peak at about 5.6 min, whereas with UV detection several peaks were found. In this case, the manufacturer mentions a purity of about 80 %. This suggests that some impurities are present in the HP powder. These impurities are not further specified. However, since they are detected by the DAD, they must be able to absorb UV-light of a wavelength of 220 nm. Furthermore, since these molecules are not detected in the ELSD, it can be assumed that they are quite small.
In the elugrams obtained from both detectors, the mixture of HP and BSA shows all peaks that are present in either HP or BSA. Therefore, no sign of interaction between HP and BSA is obtained. This indicates that HP and BSA either do not interact or that the interaction is not strong enough to withstand the pressure and shear forces caused by the flow through the column. The aforementioned conditions have the effect of disintegrating the aggregates, which in turn precludes the possibility of detecting non-covalent interactions by HPLC. This implies that interactions between HP and BSA are non-covalent. Non-covalent interactions comprise (different types of) electrostatic and hydrophobic interactions [342–345].

4.3.3. Differential scanning calorimetry

In a next step, the interaction of HP and BSA with each other should be investigated. Since HP is highly hydrophobic and hardly to dissolve completely [159, 160, 341, 346] Isothermal Titration Calorimetry (ITC) could not be performed as aggregation and sedimentation leads to additional heat flow signals and unstable baselines, which hampers the interpretation of the results. Another method, which is typically applied to measure the denaturation temperatures of proteins is Nano Differential Scanning Fluorimetry (NanoDSF). This method uses the intrinsic tryptophan or tyrosine fluorescence of a protein to monitor its unfolding. However, HP does neither contain tryptophan nor tyrosine. Therefore, NanoDSF could not be measured.
To investigate the interaction of HP and BSA, Differential Scanning Calorimetry

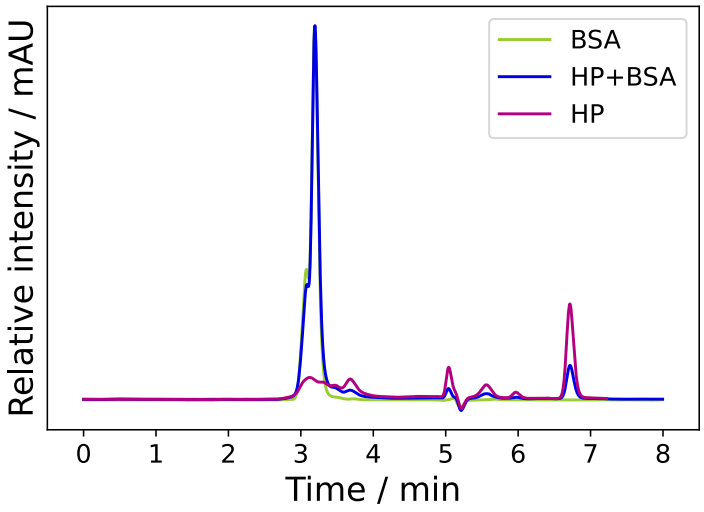

Figure 4.3.: Chromatogram measured with DAD.

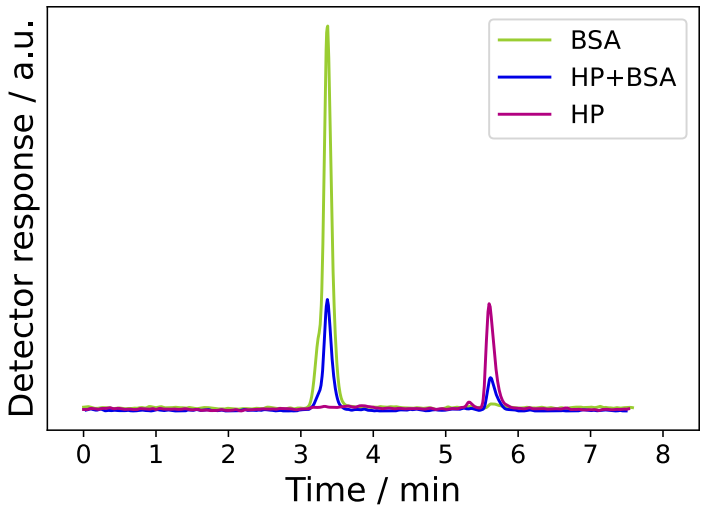

Figure 4.4.: Chromatogram measured with ELSD.

(DSC) was used. The native structure of a protein is stabilized by forces such as electrostatic, hydrophobic and van der Waals interactions. During heating of the sample, energy is required to disrupt these forces at the respective melting or denaturation points. This leads to a peak in the heat flow, that is measured by DSC. [258]
Figure 4.5 shows the measured heat flow during heating at a rate of $2\,\mathrm{K\,min^{-1}}$ for dry HP and BSA. The denaturation temperature of HP is with about 67.8 °C higher than

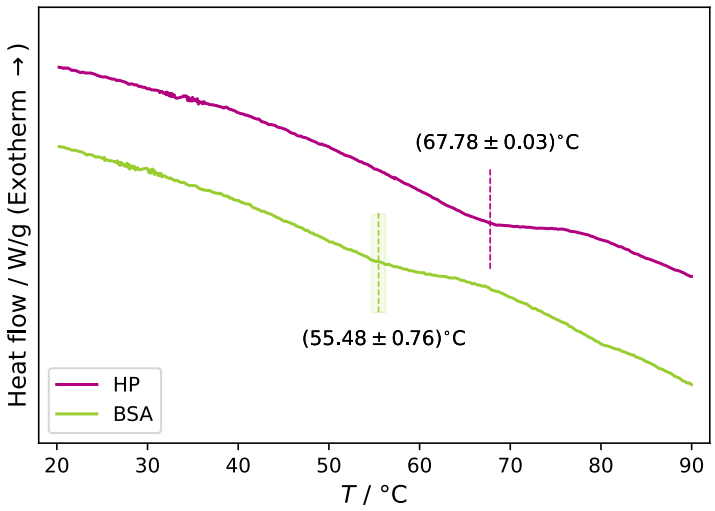

Figure 4.5.: DSC of dry HP and BSA. Shown are representative single measurements. Vertical lines show the mean and standard deviation.

that of BSA with about 55.5 °C. Relevant for the higher stability of HP may be its compact tertiary structure [162, 347].
Electrostatic and hydrophobic forces constitute not only intramolecular but also intermolecular interactions. Examples for relevant intermolecular interactions are shown in Figure 4.7. Because of such intermolecular interactions, the thermograms reveal information about the interaction of HP and BSA when comparing the different mixture ratios among each other and with the pure proteins. A shift of a peak to higher temperatures shows that the protein structure is stabilized by the other protein upon heating.
Figure 4.6 shows the measured heat flow during heating for 10 wt% aqueous solutions of HP, BSA and mixtures in HP:BSA mass fraction ratios of 3:1, 1:1, and 1:3. The two minor peaks between 30 °C and 40 °C at the ratio of 3:1 are an artefact. Peak minima, which are representing the denaturation temperature of the protein, are summarized in Table 4.1. For HP no peak was detected. HP was not completely soluble at a concentration of 10 wt%. For this reason, the concentration could not be further increased. Although the sample was shaken directly before filling the crucible, the concentration within the sample was likely insufficient for the detection of a peak. For BSA a peak is observed at $(58.3 \pm 0.2)\,°\mathrm{C}$. This melting point of BSA is in

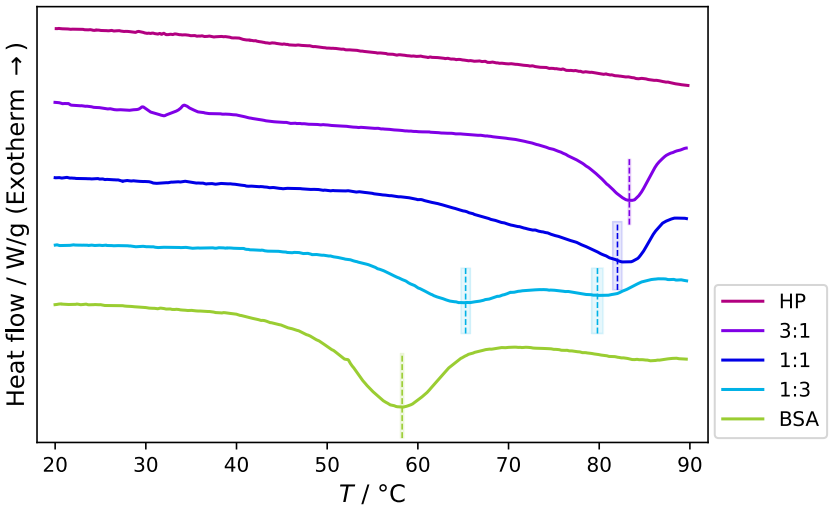

Figure 4.6.: DSC of HP and BSA solutions as well as solutions containing HP-BSA mixtures. Shown are representative single measurements. Vertical lines show the mean and standard deviation of three measurements of identically prepared samples.

HP:BSA	Protein concentration	Peak 1 °C	Peak 2 °C
1:0	10 wt% HP	–	–
3:1	7.5 wt% HP + 2.5 wt% BSA	–	83.3 ± 0.1
1:1	5 wt% HP + 5 wt% BSA	–	82.0 ± 0.5
1:3	2.5 wt% HP + 7.5 wt% BSA	65.3 ± 0.5	79.8 ± 0.6
0:1	10 wt% BSA	58.3 ± 0.2	–

Table 4.1.: Peak minima of DSC thermograms of HP-BSA mixtures.

agreement with reported values [348–350]. At the mass fraction ratio of 1:3, the peak is shifted to $(65.3 \pm 0.5)\,^{\circ}\mathrm{C}$ and an additional peak occurs at $(79.8 \pm 0.6)\,^{\circ}\mathrm{C}$. A precise quantitative comparison between the measurements of dry samples and proteins in solution is not possible, because the protein concentrations are not equal. The different concentrations change intermolecular interactions and the measured heat flow, which can lead to slight shifts in the denaturation temperature. However, the measurement of dry HP and BSA still provides additional information. Since significant differences in the peak location are observed, it can still be concluded that the second peak is located at a higher temperature than both, the denaturation temperature of pure BSA and that of pure HP. This peak shift suggests that HP and BSA stabilize each other. Although the overall mass fraction ratio is 1:3, the ratio of interacting HPs and BSAs can vary locally. The existence of two peaks suggests that different ratios of interacting HP and BSA molecules are present. Furthermore, the presence of BSA could enhance the solubility of HP. In this case, the first peak detected for the 1:3 ratio could be caused by HP, because it is localized at a similar temperature as the peak of dry HP. For a mass fraction ratio of 1:1, the thermogram shows only the second peak, but with a clearly visible shoulder towards smaller temperatures. This suggests, that locally still different ratios of interacting HPs and BSAs are present. However, the interaction ratio causing the second peak dominates, because the peak at higher temperature is more pronounced. At a mass fraction ratio of 3:1 only one peak at $(83.3 \pm 0.1)\,^{\circ}\mathrm{C}$ occurs. In this case, all BSAs and HPs seem to interact and stabilize each other with uniform interaction ratio. In conclusion, higher HP concentrations lead to increased thermostability of the HP-BSA interactions and more uniform interaction ratios as the second peak becomes slightly shifted to higher temperatures and more pronounced.

HP molecules are much smaller than BSA molecules. Their molecular weight and number of amino acids are about 1/6 of that of BSA [143–146, 156, 159, 162, 170]. Therefore, the ratios of the particle fraction differ from those of the mass fraction. Table 4.2 shows the according particle fractions. These were calculated using the following molar masses: $M_{BSA} = 66.5\,\mathrm{kg\,mol^{-1}}$ for BSA [143–145], $M_{HP} = 10\,\mathrm{kg\,mol^{-1}}$ for hydrophobin [159], and $M_{H2O} = 18\,\mathrm{g\,mol^{-1}}$ for water [351, 352]. At the mass fraction ratio of 1:3 two to three HPs are present per one BSA. In this case, the number of HP molecules is not high enough to stabilize all BSAs and therefore some BSAs

	Mass fraction			Particle fraction / $\cdot 10^{-4}$			
HP:BSA	HP	BSA	Water	HP	BSA	Water	HP:BSA
1:0	0.1	0	0.9	2	0	9998.0	1:0
3:1	0.075	0.025	0.9	1.5	0.1	9998.4	20:1
1:1	0.05	0.05	0.9	1	0.2	9998.8	6.7:1
1:3	0.025	0.075	0.9	0.5	0.2	9999.3	2.2:1
0:1	0	0.1	0.9	0	0.3	9999.7	0:1

Table 4.2.: Mass and particle fractions of HP-BSA mixtures.

interact with more HPs than other BSAs. For equal mass fractions, there are 6 to 7 HPs per BSA. This ratio is sufficient to stabilize most BSAs as shown by the one peak at larger temperature with a pronounced shoulder. At the 3:1 mass fraction ratio, there are 20 HPs per BSA molecule. This ratio provides for stabilization of all BSA molecules and the peak at lower temperature disappears. However, not necessarily all HPs interact with BSAs at such high HP fractions. Furthermore, the investigation of pure HP solutions shows that a peak caused by HP might also just not be detectable. Due to their large hydrophobic surface patches, HPs like to interact with each other and form aggregates [159, 341]. With BSA electrostatic and hydrophobic interactions can be well imagined. Different configurations of HP and BSA are possible due to their surface hydrophobic and charged amino acids and their size differences. An example of possible arrangements caused by hydrophobic and electrostatic interactions between HP and BSA molecules is shown in Figure 4.7.

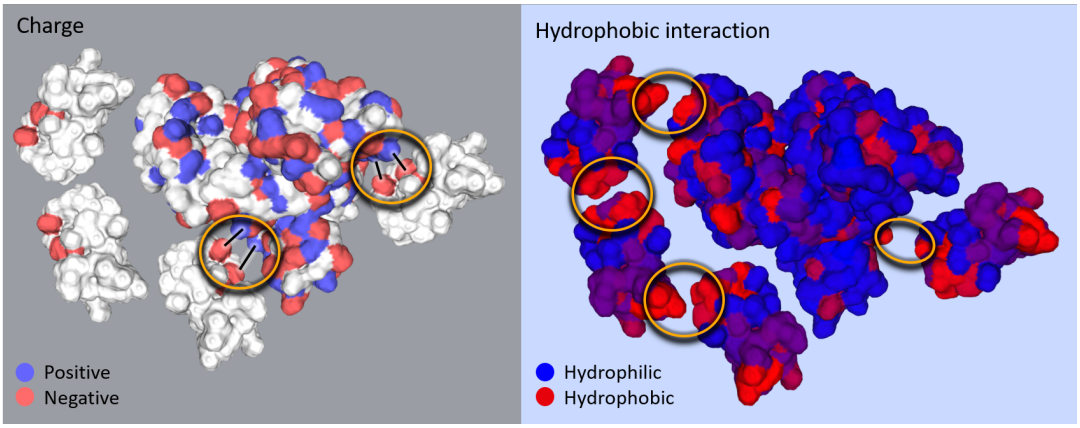

Figure 4.7.: Examples of relevant interactions and resulting arrangement of HP and BSA. Electrostatic interactions are marked by black lines and both types of interaction are highlighted with yellow circles. Charged surface amino acids are colored on the left and hydrophobic surface amino acids are colored on the right to show both properties for the presented possible configuration.

4.3.4. Surface tension

Figure 4.8 shows the surface tensions measured for samples of HP, BSA and mixtures thereof at different ratios. A clear trend is observed: The purely HP-stabilized solutions show the lowest surface tension and with increasing BSA content the surface tension increases. The surface tension for pure BSA solutions is markedly higher than for the mixtures or pure HP solution. Compared to pure water, which has a surface tension of $(71.99 \pm 0.36)\,\mathrm{mN\,m^{-1}}$ at $25\,^{\circ}\mathrm{C}$ [353], BSA lowers the surface tension already significantly by about $20\,\mathrm{mN\,m^{-1}}$. Since the decrease in surface tension with rising hydrophobin concentration is not linear, the measurement data suggests, that

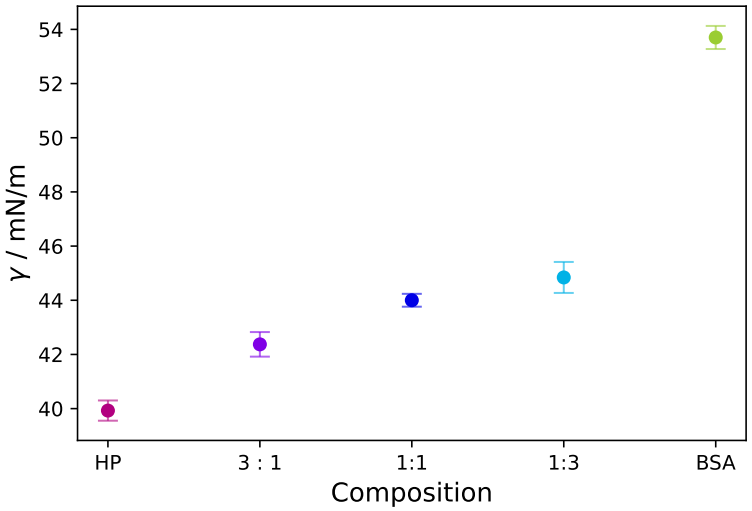

Figure 4.8.: Surface tension of HP and BSA solutions as well as mixtures thereof. From left to right the solutions contain 4 wt% HP, 3 wt% HP + 1 wt% BSA, 2 wt% HP + 2 wt% BSA, 1 wt% HP + 3 wt% BSA and 4 wt% BSA.

for lowering the surface tension, the presence of hydrophobin is more relevant than its concentration.
Surface tension and bubble radius determine the Laplace pressure, which is the driving force in disproportionation and coalescence leading to foam decay [107, 112, 354]. Since the Laplace pressure is proportional to the surface tension [112], a lower surface tension reduces the Laplace pressure and leads to a more stable foam.
The effect of surface tension is also reflected in the shape of a droplet of the protein solution. In general, droplets of liquids with a low surface tension tend to deviate more from a sphere than droplets of liquids with a high surface tension [92]. Figure 4.9 shows photos of 50 µL droplets on a hydrophobic surface (Parafilm covered glass slide, cf. [178]) at the beginning, after 30 min, 3 h and 7 h. The droplet of the HP solution looks more flat (lower curvature) and has a smaller contact angle than the droplet of the BSA solution. This is in accordance with a lower surface tension of the HP solution. The mixtures of HP and BSA show droplet shapes in between the shapes of the droplets of pure HP or BSA solutions and reflect the behavior measured for the surface tension. Over time all droplets become flatter, however, the different behavior remains consistent. In the frame of this thesis, the droplet shape was investigated qualitatively to illustrate the differences in surface tension. Macroscopic differences in the droplet shape are clearly visible. For a quantitative analysis of contact angles, the resolution of the presented images is insufficient, because the vertices need to be defined with high accuracy. This could be done in future investigations. However, the contact angle is primarily used to describe the wettability of solid surfaces, which is of minor relevance to the formation and stability of foams. Since the quantitative information on surface tension was obtained from measuring surface tension with the

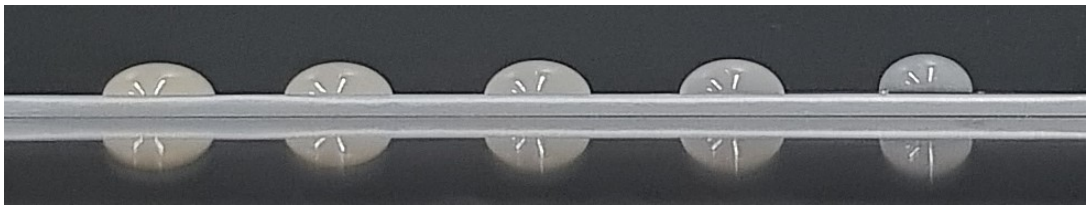

(a) 0 min

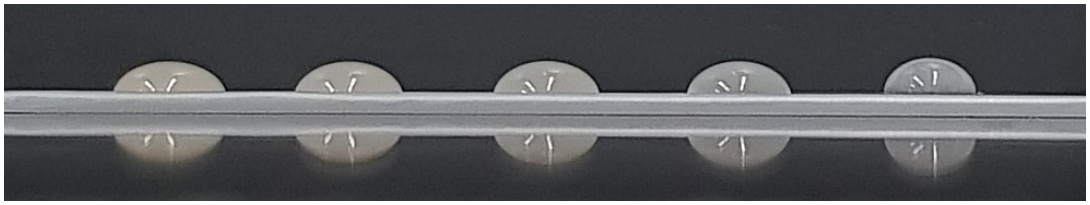

(b) 30 min

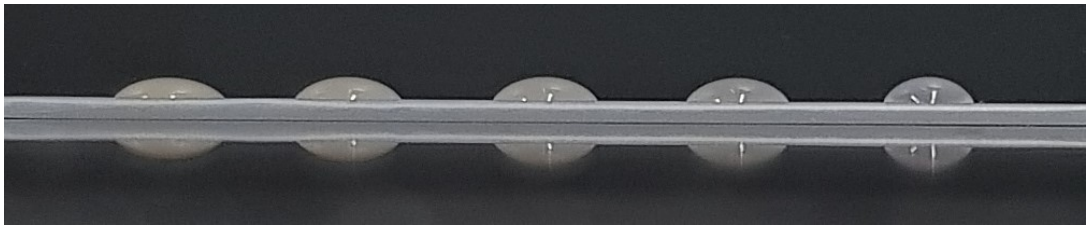

(c) 3 h

(d) 7 h

Figure 4.9.: Shape of droplets of HP and BSA solutions as well as mixtures thereof. From left to right the solutions contain 4 wt% HP, 3 wt% HP + 1 wt% BSA, 2 wt% HP + 2 wt% BSA, 1 wt% HP + 3 wt% BSA and 4 wt% BSA.

Wilhelmy plate method, the qualitative consideration of the droplet shape is sufficient here.
Figure 4.10 shows the same droplets from above. The base area of the droplets varies, especially after 7 h. The droplet of the BSA solution shows the smallest base area, which also reflects the higher surface tension.

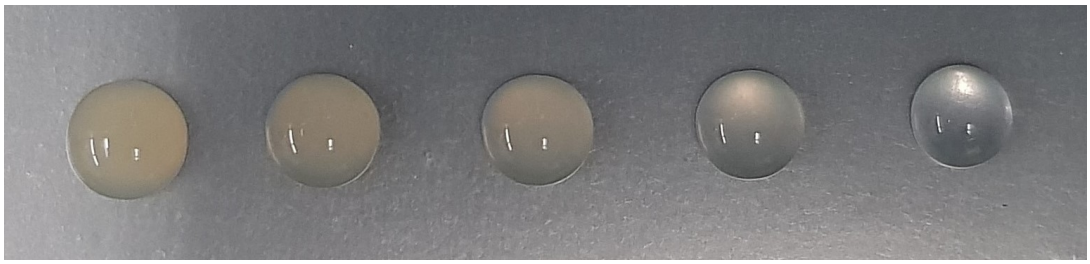

(a) 0 min

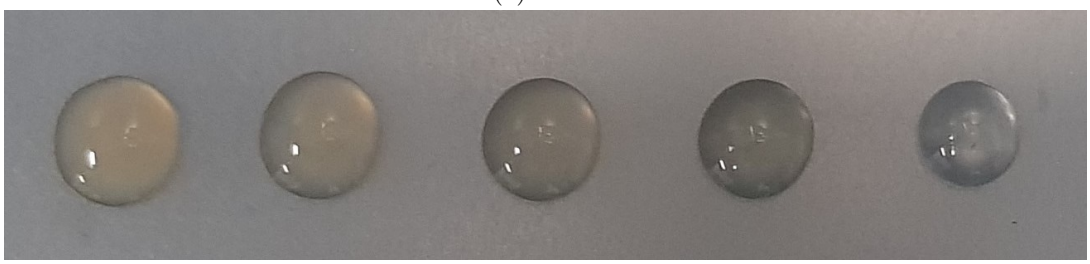

(b) 3 h

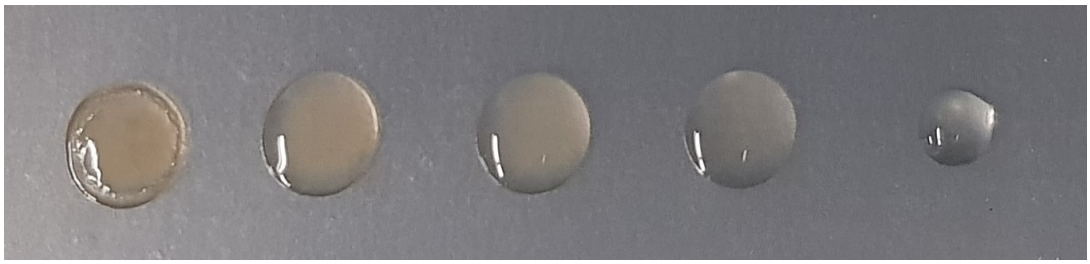

(c) 7 h

Figure 4.10.: Droplets of HP and BSA solutions as well as mixtures thereof viewed from above. From left to right the solutions contain 4 wt% HP, 3 wt% HP + 1 wt% BSA, 2 wt% HP + 2 wt% BSA, 1 wt% HP + 3 wt% BSA and 4 wt% BSA.

4.3.5. Brewster angle microscopy

Brewster angle microscopy was chosen as a method to investigate the arrangement of HP and BSA at the air-water interface, because with this method a direct imaging of hydrated interfaces is possible [249]. Figure 4.11 shows BAM images of the air-water interface with HP, HP + BSA, and BSA films, respectively.

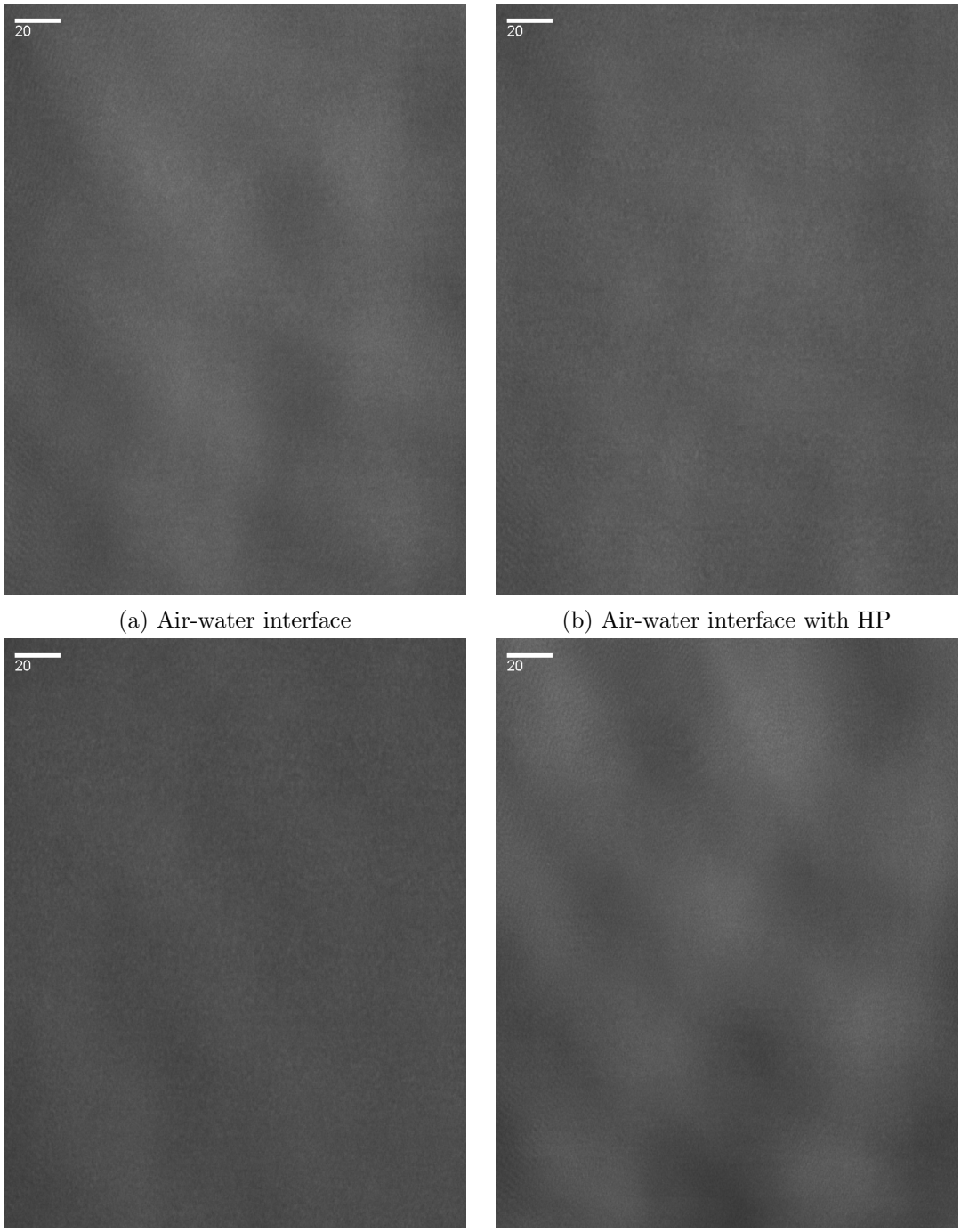

(a) Air-water interface

(b) Air-water interface with HP

(c) Air-water interface with HP + BSA

(d) Air-water interface with BSA

Figure 4.11.: BAM of HP, BSA and a 1:1-mixture thereof each at the air-water interface. The scale bar represents 20 µm.

In these images, background reflexes from the trough bottom are seen as well as a very fine, rigid structure, which looks exactly the same in all images. It is therefore concluded that the contrast and magnification of this method are not sufficient to visualize the tiny structures formed by HP and BSA. For this reason, AFM was used as another imaging technique on smaller scales to investigate the arrangement of the proteins at the hydrophobic-hydrophilic interface.

4.3.6. Atomic force microscopy

Overview AFM was performed to investigate the arrangement of HP and BSA at the air-water interface. The surface of a protein solution was transferred to a hydrophobic substrate (highly-oriented pyrolytic graphite – HOPG) and the surface structure of the dried sample was then imaged using AFM.
First, sample solutions with a concentration of 4 wt% protein were investigated, which is the concentration used for foam formation. Figure 4.12 shows overviews of 3 µm scan size of such samples. The HP sample shows a quite even surface with some deep spherical holes, which can be considered nanobubbles, also referred to as ultrafine bubbles. Surface nanobubbles are gas-filled pockets in the shape of truncated spheres with heights of 10 nm to 100 nm and radii of 50 nm to 500 nm [355]. These form spontaneously at water-solid interfaces of hydrophobic surfaces from gas dissolved in the liquid [356–359]. The mixture of HP and BSA shows smaller nanobubbles and a more uneven surface. The BSA sample, on the other hand, does not show nanobubbles and its surface is quite even (consider the scalebar on the right of each image). Surface nanobubbles form spontaneously at hydrophobic interfaces, also for BSA solutions [356, 357]. The current AFM investigations show more nanobubbles for HP-containing samples than for pure BSA solution samples. This observation leads to the conclusion that the nanobubbles are held better by HP, which means that HP stabilizes the bubbles better. This in turn also suggests an improved foam stability, which was indeed observed mesoscopically for HP (see Subsection 3.6.3 and Figures 3.16 and 3.17).
For the pure HP and the pure BSA solution, the surface roughness was determined using the software *Gwyddion*. The mean square roughness σ of height irregularities is calculated from the second central moment μ_2 of the data values z_n:

$$\mu_i = \frac{1}{N}\sum_{n=1}^{N}(z_n - \bar{z})^i \tag{4.1}$$

where $\bar{z}$ is the mean value. The mean square roughness is then given by

$$\sigma = \mu_2^{1/2} \tag{4.2}$$

[360]. For the images shown in Figure 4.12, determination of the roughness of the whole image leads to 14.8 nm for the HP sample and 0.38 nm for the BSA sample. The roughness is markedly higher for HP, however, the interfacial arrangement of

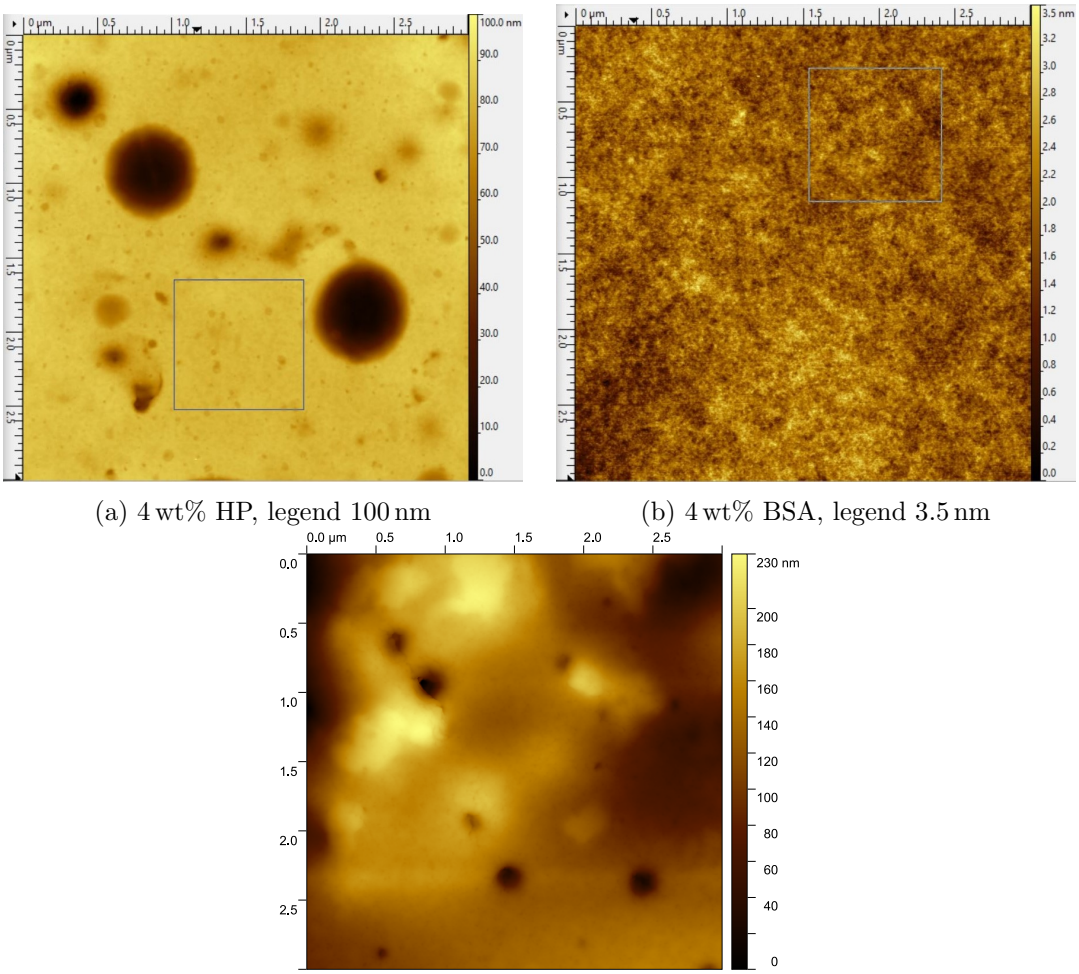

(a) 4 wt% HP, legend 100 nm

(b) 4 wt% BSA, legend 3.5 nm

(c) 2 wt% HP + 2 wt% BSA, legend 230 nm

Figure 4.12.: AFM overviews with a scan size of 3 µm of surfaces of solutions containing 4 wt% protein transferred to HOPG. HP shows more and larger nanobubbles than the mixture, whereas BSA does not show nanobubbles. The gray squares (edge length 150 pixel) mark areas, where the surface roughness was determined.

HP contains large holes from the nanobubbles. Therefore, also the surface roughness within a square without nanobubbles was evaluated to obtain better comparability with the BSA sample. In this case, the mean square roughness for the HP sample is 1.8 nm and for BSA it is 0.35 nm. This indicates, that the roughness of the BSA surface is only about 1/5 of the roughness of the HP sample surface, which suggests that the surface produced by BSA is much smoother. The formation of indentations such as small holes and ruptures is a sign for the high affinity of HP molecules to find other HPs and form aggregates, which is caused by the high surface hydrophobicity of these molecules. In addition, the elevations observed for the mixture of HP and BSA also suggest the formation of aggregates.

To have a closer look on the structures formed by HP and BSA, Figure 4.13 shows AFM scans of 0.5 µm size of HP, BSA and mixtures thereof at HP:BSA-ratios of 3:1, 1:1, and 1:3. For HP samples a structure with some holes is found. These holes are generally not spherical and much smaller than the nanobubbles observed in Figure 4.12, which suggests that these cannot be considered nanobubbles. The observed structures rather arise from the arrangement of HP molecules and their attraction to each other, which is caused by their strong hydrophobicity. For BSA, the random structure looks as smooth and uniform as the large section shown above in Figure 4.12. The mixture with more BSA (1:3-mixture) shows a similar surface structure as the pure BSA sample. It is still quite smooth, but contains some more and deeper indentations as shown by the legend, the range of which is about twice as high as the legend of pure BSA. The roughness of the mixture is 0.62 nm (entire image) and of pure BSA it is 0.34 nm (entire image). These results show, that the roughness increases by about a factor 2 when adding HP to BSA in a 1:3 weight fraction ratio. For the 1:1-mixture of HP and BSA, the structure of the protein layer changes. The image indicates, that the protein arrangement contains fiber-like or rod-like structures, which suggests some interaction of HP and BSA. From the DSC measurements (shown in Subsection 4.3.3), it is known that HP and BSA interact with each other and that their interaction depends on the HP:BSA-ratio as discussed there. These interactions influence the arrangement of the different proteins as observed. The 3:1-blend of HP and BSA shows a structure in between that of the pure HP sample and the 1:1-mixture. Similarly to the structure of the 1:1-mixture, the arrangement contains some rod-like structures, however it looks denser. Also in this case, the HP and BSA molecules seem to interact with each other.

However, the shown scans taken at a protein concentration of 4 wt% protein show multilayers of proteins. Otherwise the observed holes would not be as deep. For this reason, HP and BSA arrangements at the interface were investigated for various protein concentrations.

Hydrophobin Figures 4.14, 4.15 and 4.16 show AFM scans of transferred surfaces of HP-solutions at different concentrations. The images reveal various structures, which are not concentration dependent, but rather different structures are found at different spots on the sample respectively different identically prepared samples. The structures

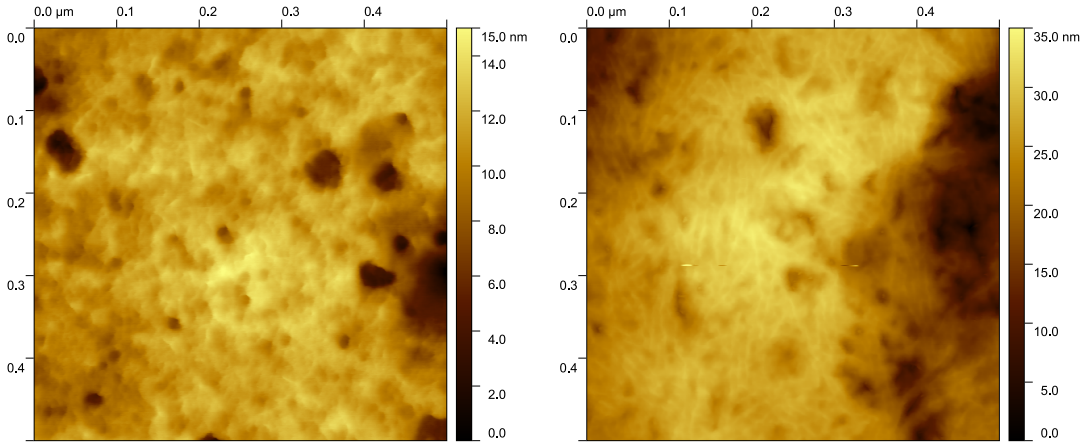

(a) 4 wt% HP, legend 15 nm

(b) 3 wt% HP + 1 wt% BSA, legend 35 nm

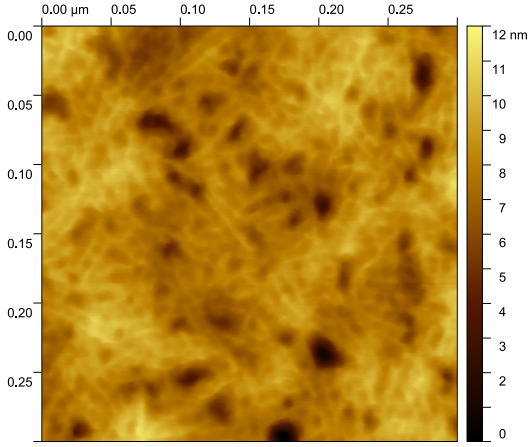

(c) 2 wt% HP + 2 wt% BSA, legend 12 nm

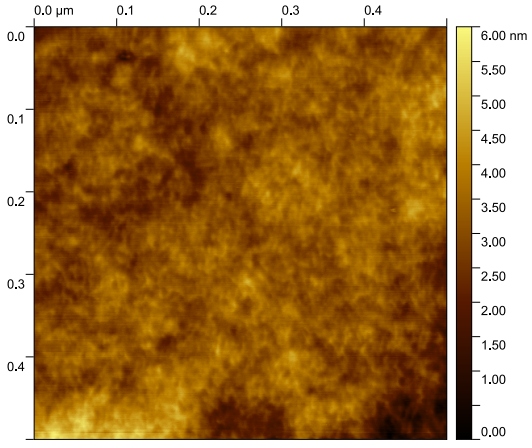

(d) 1 wt% HP + 3 wt% BSA, legend 6 nm

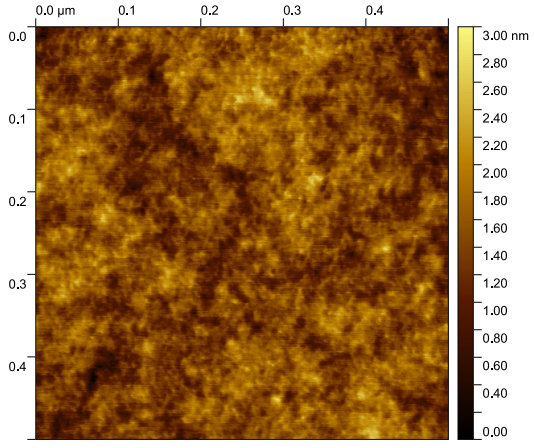

(e) 4 wt% BSA, legend 3 nm

Figure 4.13.: AFM scans with a size of 0.5 µm of transferred surfaces of solutions containing 4 wt% protein.

show holes of different shapes from almost spherical to irregular and rupture-like. These structures demonstrate that the HP proteins exhibit a robust mutual attraction. Hydrophobins have large hydrophobic surface patches [16, 71, 160, 162], which attract each other and lead to the formation of aggregates [106, 159, 341, 361]. The strong hydrophobicity facilitates the attraction between HPs in close proximity. This in turn leads to structures containing areas with a high protein density as well as holes. Furthermore, hydrophobins are small molecules with a compact barrel structure, which allows hydrophobins to pack very densely [16].

Literature on natural class I hydrophobins reports the spontaneous formation of so-called rodlet-structures [71, 72, 159, 362–366]. The rodlet structures are further characterized as rod-like structures [71, 341] and laterally associated fibrillar structures [341, 363]. The precise arrangement of these rodlets may vary depending on the type of hydrophobin and environmental conditions [365, 367, 368]. For the formation condition of rodlets different descriptions are used such as hydrophobins "spontaneously" self-assemble [72, 106, 178, 363], "rodlets appear to be formed" [160], "hydrophobins have the capacity to assemble" [99] or "ability to self-assemble" [106] into nanorods or "tendency to form fibrillar or rod-like aggregates at interfaces" [341]. In addition, rodlet formation was observed during compression of the interface [71, 160, 369] and upon drying of a hydrophobin solution at a solid surface [103, 160, 370]. Furthermore, it was reported that the formation of rodlets occurs after a few hours [178, 371]. These formulations show that the conditions for rodlet formation are not precisely predictable, respectively not thoroughly enough investigated yet.

More detailed investigations approved, that rodlet formation may need several compression cycles and may also involve several intermediate steps, which include several rearrangements of the hydrophobins [160, 369, 371, 372]. These intermediate steps in the arrangement of hydrophobins at the air-water interface were explored by De Vocht et al. [370, 371], who investigated the self-assembly of the hydrophobin SC3 and suggested that the rodlet formation takes place via intermediate steps, which include changes in the secondary structure of the protein. The monomeric state of the hydrophobin SC3 is soluble in water. At air-water interfaces, it spontaneously forms an α-helical state. Minutes later, a spontaneous transition into β-sheet1 state occurs and a stable amorphous protein film is build at the interface. The transition into β-sheet2 state, which forms stable rodlet films, happens spontaneously and takes hours. [371] The transition from amorphous hydrophobin layers to rodets was also described by Takahashi et al. [367] for the hydrophobin RolA and by Valsecchi et al. [368] for RodA. All together these findings suggest that these transitions occur for various species of class I hydrophobins. On the way to a saturated surface covered with rodlets, two phases can be distinguished: the first phase contains sparsely distributed rodlets, whereas in the second phase rodlets are densely packed. This happens via two processes: formation of new rodlets and elongation of existing rodlets. [367] The formation of different structures at intermediate steps may explain a large variety of regular structures formed by hydrophobins as was observed in the AFM images shown in this thesis for the H*B hydrophobin (HP). The influence of compression of the interfacial layer on the molecular arrangement was studied by Yu et al. [369]. These authors

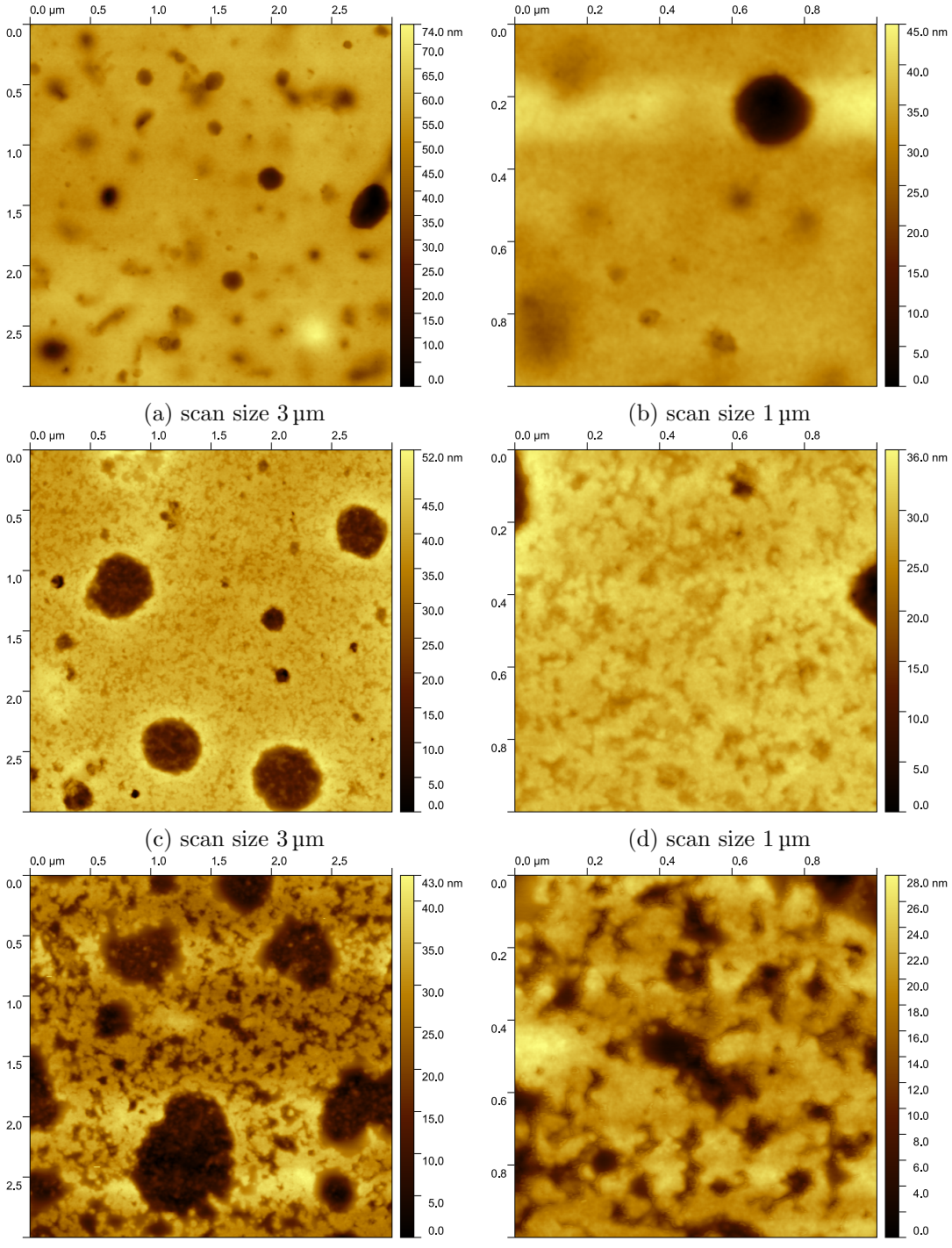

(a) scan size 3 µm (b) scan size 1 µm

(c) scan size 3 µm (d) scan size 1 µm

(e) scan size 3 µm (f) scan size 1 µm

Figure 4.14.: AFM scans of transferred surfaces of solutions containing 4 wt% HP.

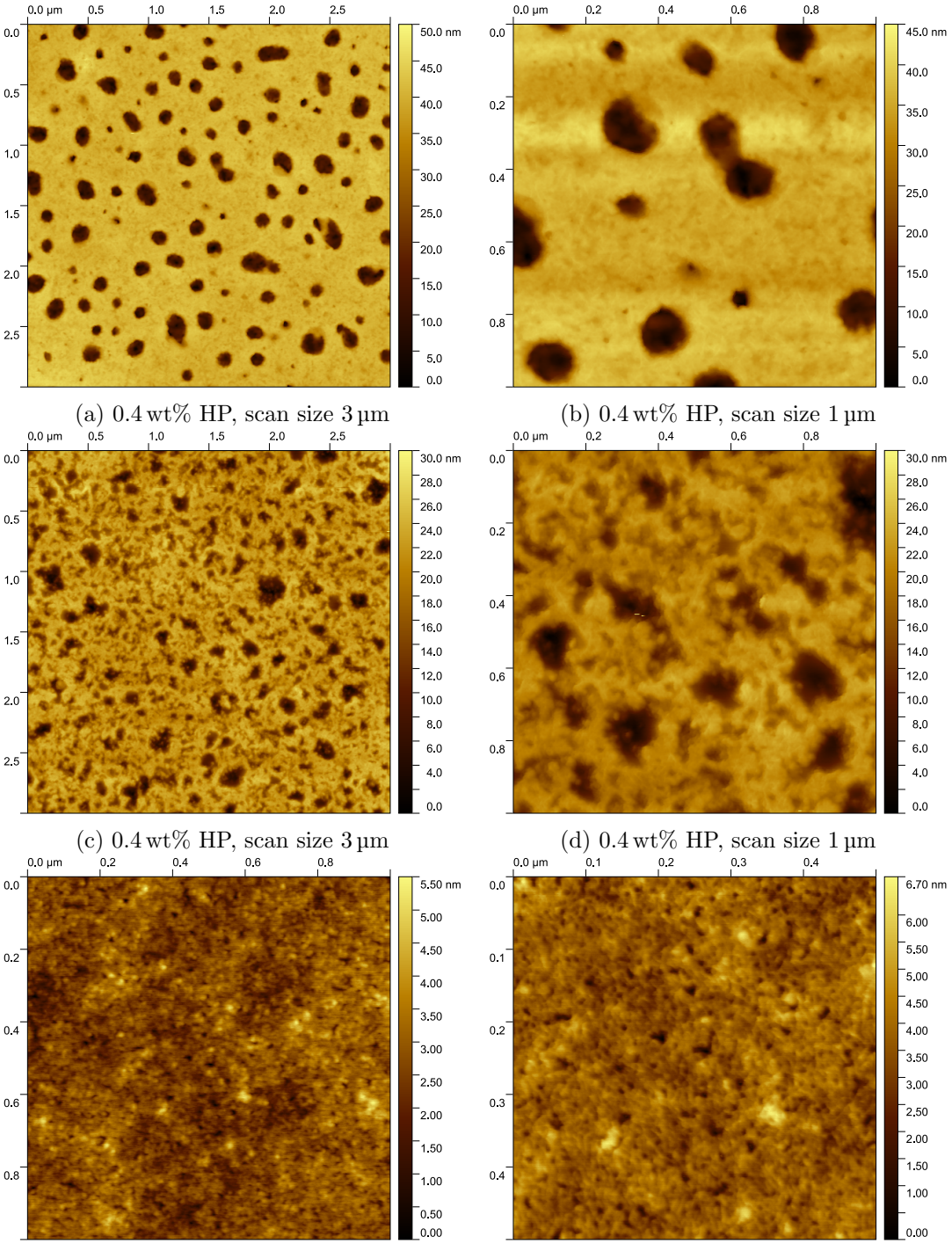

(a) 0.4 wt% HP, scan size 3 µm

(b) 0.4 wt% HP, scan size 1 µm

(c) 0.4 wt% HP, scan size 3 µm

(d) 0.4 wt% HP, scan size 1 µm

(e) 0.04 wt% HP, scan size 1 µm

(f) 0.04 wt% HP, scan size 0.5 µm

Figure 4.15.: AFM scans of transferred surfaces of HP-solutions with varying concentrations.

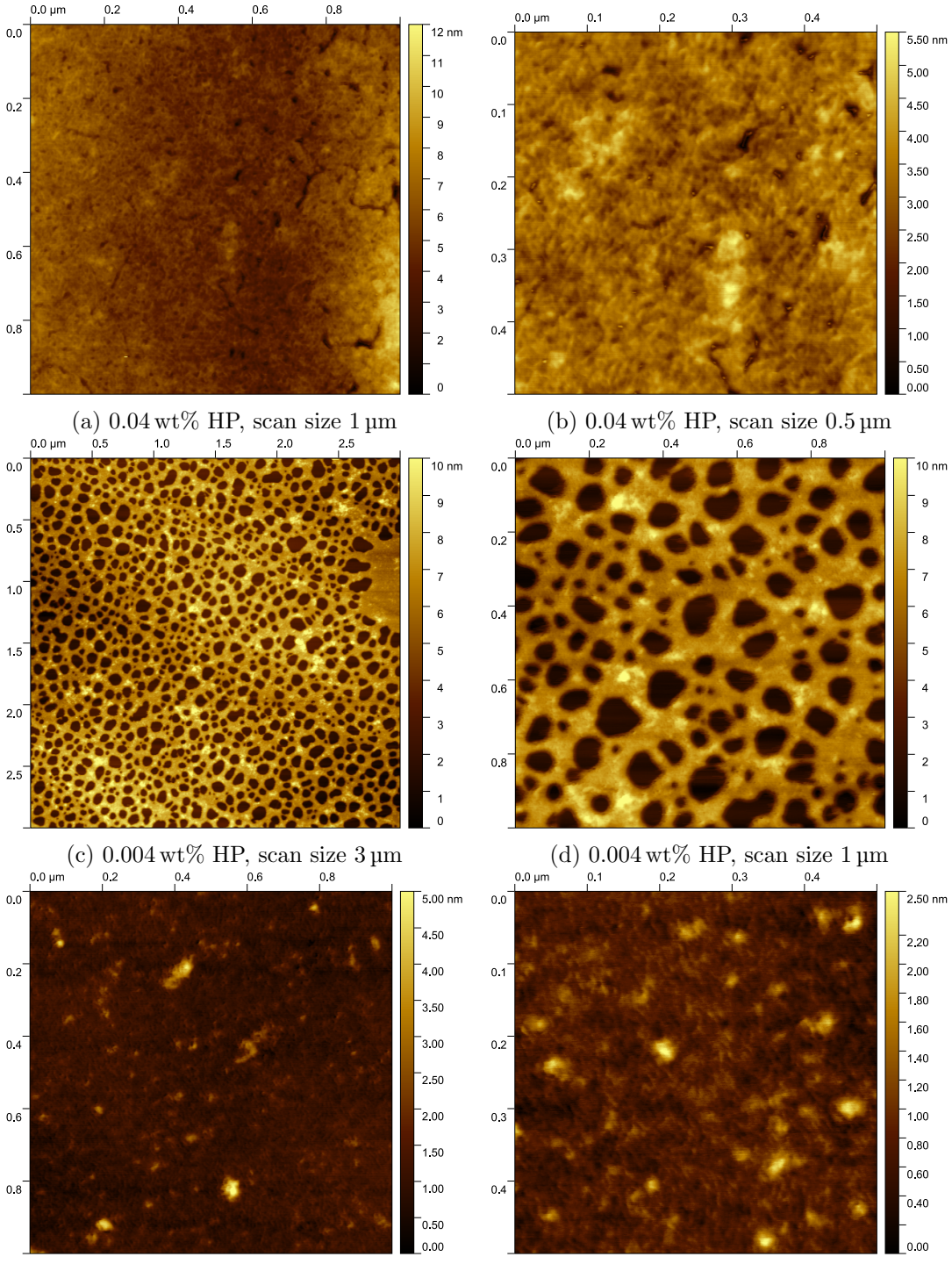

(a) 0.04 wt% HP, scan size 1 µm

(b) 0.04 wt% HP, scan size 0.5 µm

(c) 0.004 wt% HP, scan size 3 µm

(d) 0.004 wt% HP, scan size 1 µm

(e) 0.004 wt% HP, scan size 1 µm

(f) 0.004 wt% HP, scan size 0.5 µm

Figure 4.16.: AFM scans of transferred surfaces of HP-solutions with varying concentrations.

investigated the assembly of the hydrophobin HGFI and observed that compression causes a reorganization of the film with local rodlet rearrangements. Furthermore, they found out that multiple compression leads to more aligned rodlets [369]. In this thesis, the samples investigated with AFM were not compressed. However, in a foam compression of the interfaces occurs during ripening of the foam as bubbles grow at the expense of others that shrink as a result (Ostwald-ripening). The air-water interfaces in foams are permanently changing their sizes, which causes relocation of the hydrophobins and facilitates the formation of rodlets. This leads to a high stability of the hydrophobin films at the interfaces and consequently a high foam stability.
An important factor in hydrophobin assembly into rodlets at the air-water interface is their amphipathic character [362, 368]. The amphiphilic nature allows for an arrangement at the interface. However, the formation of highly ordered films involves also lateral protein interactions [178]. Class I hydrophobins contain a β-barrel core, which is stabilized by four disulfide bridges. From this core inter-cystein loops extend, which have hydrophobic surfaces. [71, 105, 170, 367, 368] These hydrophobic patches are important for the formation of rodlets [105, 173, 362], since more localized hydrophobic patches facilitate a more efficient hydrophobin assembly [362]. During rodlet formation, hydrophobins interact via the hydrophobic Cys-Cys loops, which butt against each other [367]. The interaction involves stacking of β-sheets [106]. Furthermore, electrostatic interactions are involved in hydrophobin interaction and may influence the adsorption characteristics and rodlet formation [106, 367, 373]. However, Takahashi et al. [367] concluded that these are not the driving force in the formation of rodlets, but might inhibit their elongation. In addition, also hydrophobins carrying a net charge form rodlets [106]. This suggests, that hydrophobic interactions are more relevant in rodlet formation than electrostatic interactions. Also Wösten et al. [374] concluded that "self-assembly must be driven by an increase in entropy, probably by hydrophobic interactions since changes in the pH or the presence of salt hardly affected self-assembly" [374].
The formation of such rodlets was indeed observed in a dried droplet of a 0.04 wt% HP solution. AFM scans are shown in Figure 4.17. The height is shown on the left and the phase on the right, because the rodlets were more clearly detected in the phase images. The observed rodlet structures show similarity with those reported in the literature for various types [72, 106, 362, 364, 367, 368, 373] of class I hydrophobins. The precise HP rodlet arrangement varies for different hydrophobins and also between variants within one species [368].
To investigate the rodlet structures in more detail, a height profile was measured in the AFM height image. Figure 4.18 shows how the height profile of HP rodlets was extracted. The software *Gwyddion* allows to measure height profiles in AFM images. Therefore, a line is drawn by hand on the AFM image, along which the height profile shall be shown (4.18 (a)). Subfigure (b) shows the obtained height profile. Local minima between the peaks are marked with gray dots. To subtract the uneven background the first five minima were fitted with a linear function using *Python* (cf. subfigure (c)). The finally obtained profile is shown in Subfigure (d). The peaks show a width of about 8.5 nm and a height of (1.13 ± 0.10) nm. Rodlet

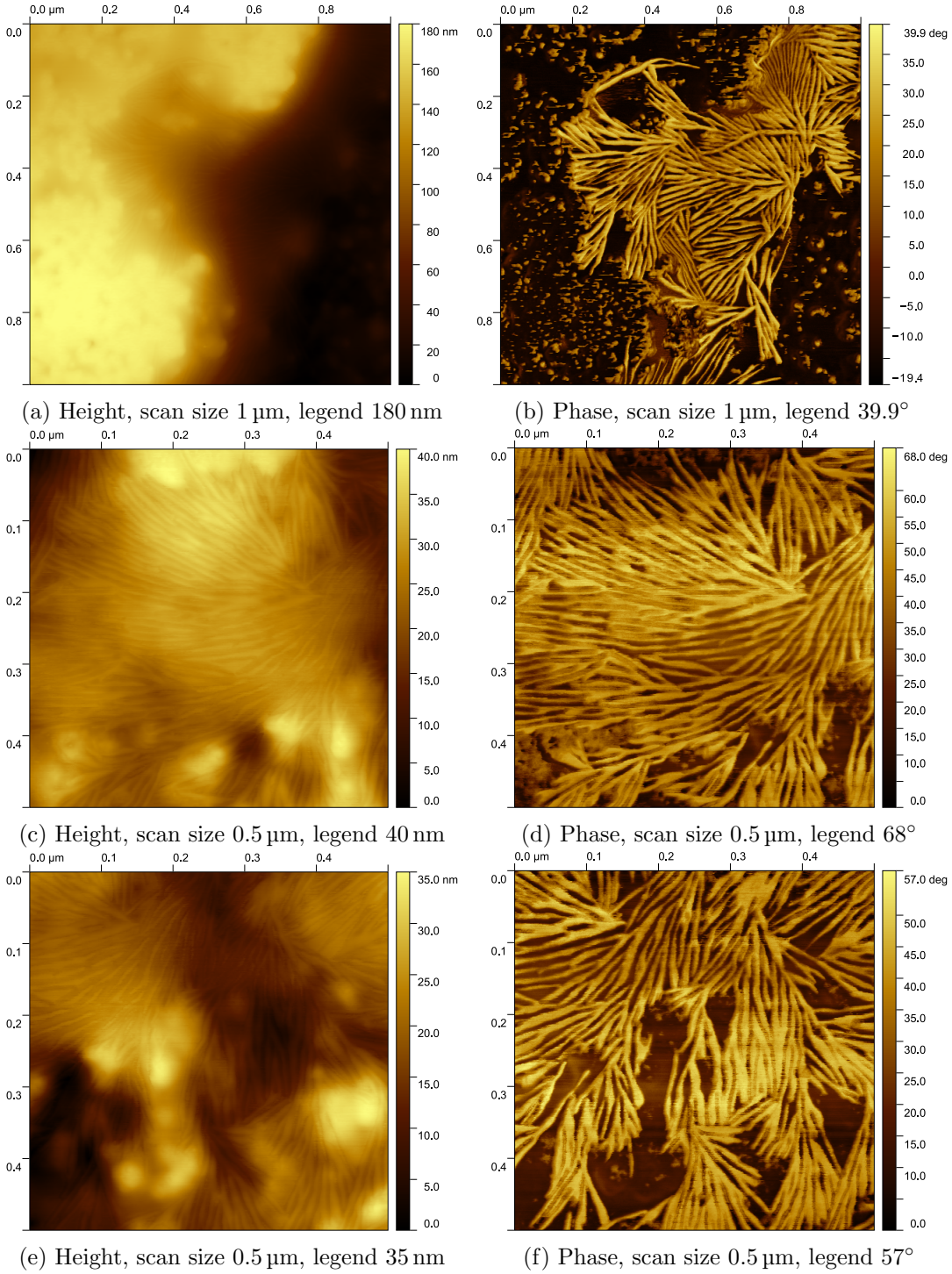

(a) Height, scan size 1 µm, legend 180 nm

(b) Phase, scan size 1 µm, legend 39.9°

(c) Height, scan size 0.5 µm, legend 40 nm

(d) Phase, scan size 0.5 µm, legend 68°

(e) Height, scan size 0.5 µm, legend 35 nm

(f) Phase, scan size 0.5 µm, legend 57°

Figure 4.17.: AFM height profiles and phases of a rodlet structure observed on a dried droplet of a 0.04 wt% HP solution.

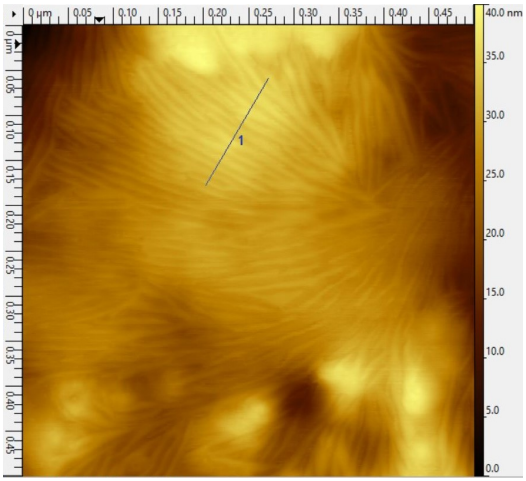

(a) AFM image with HP rodlet structure. The line labeled with 1 marks the location along which the height profile is analyzed.

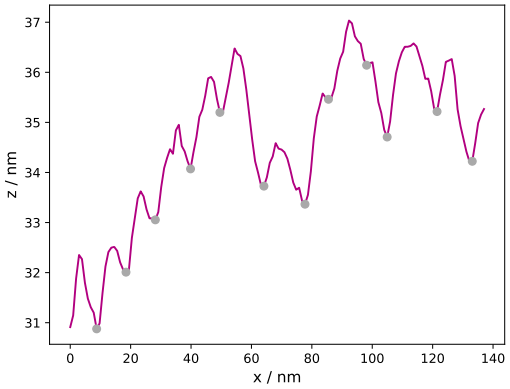

(b) Height profile along line 1.

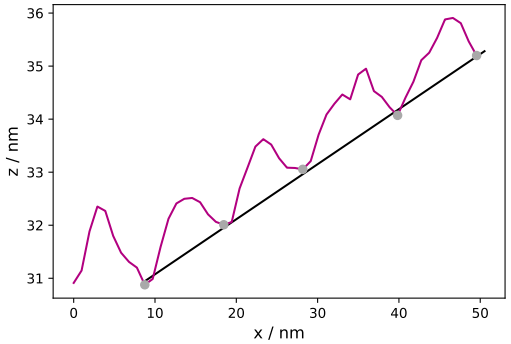

(c) Fitting of the first five local minima with a linear function.

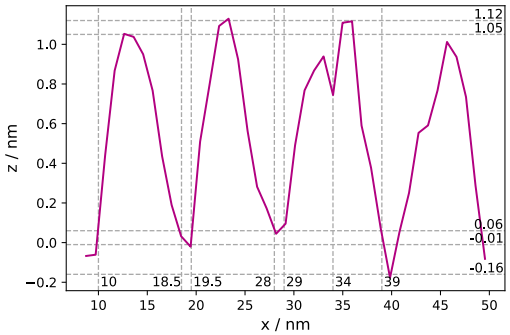

(d) Corrected height profile. The width of the peaks is about 8.5 nm and their height about 1 nm.

Figure 4.18.: Evaluation of an AFM height profile of a rodlet structure observed on a dried droplet of a 0.04 wt% HP solution.

sizes of about 2.5 nm height and 6 nm to 15 nm width were reported for different class I hydrophobins [70, 72, 366, 368, 370]. This means that the reported rodlet height is about twice as high as for the H*B hydrophobin used in the current study. The difference is probably caused in a slightly different size or structure of these hydrophobins or different environmental conditions. However, the sizes of the formed rodlets are in the same order of magnitude ensuring that the observed structures indeed show hydrophobin rodlets.
According to literature, the regular structures formed by hydrophobins lead to very strong and robust interfacial films [16, 105, 170, 172]. These are relevant for a high foam stability, as was observed mesoscopically (cf. Section 3.6.3).

BSA For BSA, similar, smooth surfaces are observed at different concentrations as shown in Figure 4.19. The arrangement of the BSA molecules looks random. For the lowest concentration the structures seem a little bit coarser. Since the protein concentration is lower, the BSA layer may be thinner and its surface looks coarser, because the intermolecular distance becomes larger.
BSA molecules contain many surface charges and some surface hydrophobic amino acids, which are spread along their surface. Both interactions have to be considered when the molecules arrange towards each other at the air-water interface. Hydrophobic amino acids attract each other as well as oppositely charged amino acids whereas like-charged amino acids repel each other. However, the hydrophobic amino acids are rather spread across the protein surface than forming a concentrated hydrophobic patch. Therefore, the electrostatic interaction is considered to have a stronger influence on the arrangement of these molecules. The BSAs orient in such a way that the electrostatic energy is minimized. This leads to an irregular arrangement of the molecules as observed in the AFM images.

HP-BSA mixtures Figure 4.20 shows AFM scans of structures formed by mixtures of HP and BSA. These structures have in common that they contain some irregularly shaped holes, which indicate the interaction of some molecules. The formed structures vary depending on the HP:BSA ratio.
For pure HP samples some very regular structures were observed, which were not noticed to the same extent for samples of HP-BSA mixtures. Therefore, it can be concluded that the formation of such very regular patterns is impeded by the presence of a relevant quantity of BSA. Although hydrophobins generally have less surface charges [146], these still can interact with the charged surface amino acids of BSA. Therefore, electrostatic interaction between HP and BSA is conceivable. Indeed, Wang et al. [375] report electrostatic interaction between BSA and surface-bound hydrophobins HGFI and HFBI. Hydrophobic interaction dominates between the strongly hydrophobic surface patches of hydrophobins and causes them to aggregate. However, some hydrophobic interaction can also be imagined between HP and BSA, although less relevant than between HPs, because BSA does not contain a similarly distinct hydrophobic patch as does HP. The precise orientation of intermolecular forces depends

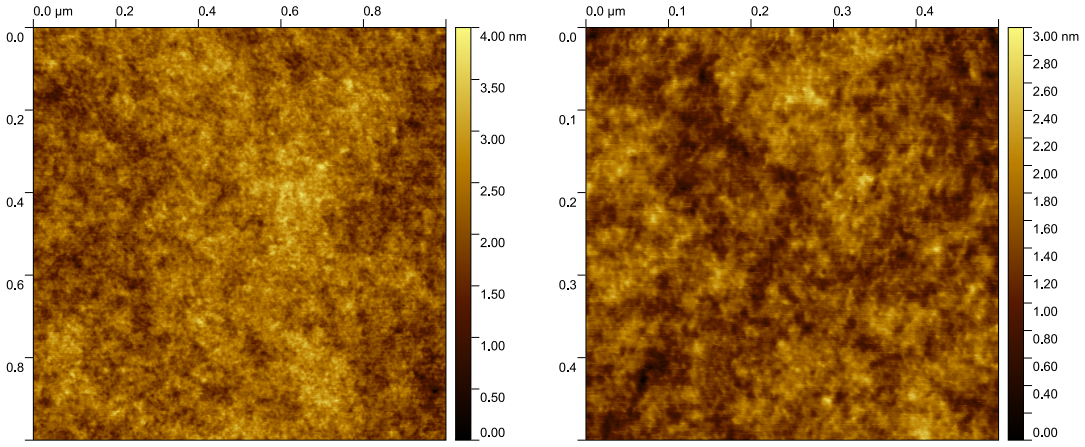

(a) 4 wt% BSA, scan size 1 µm

(b) 4 wt% BSA, scan size 0.5 µm

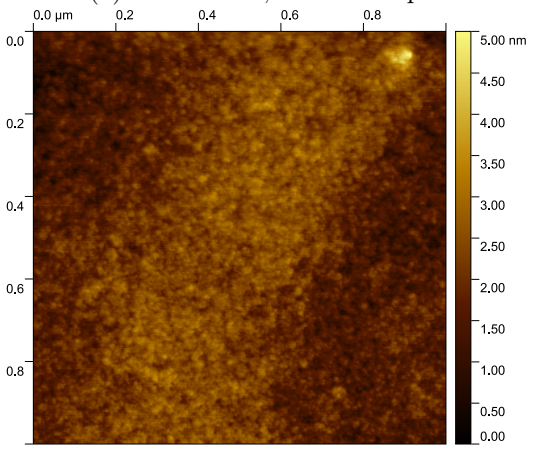

(c) 0.4 wt% BSA, scan size 1 µm

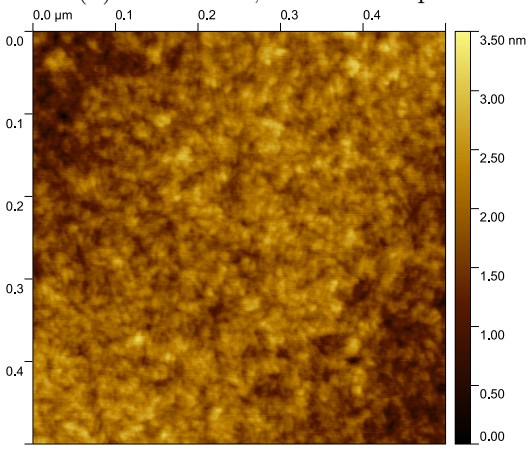

(d) 0.4 wt% BSA, scan size 0.5 µm

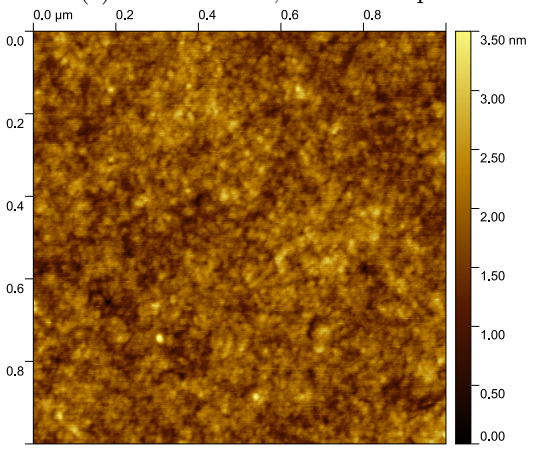

(e) 0.04 wt% BSA, scan size 1 µm

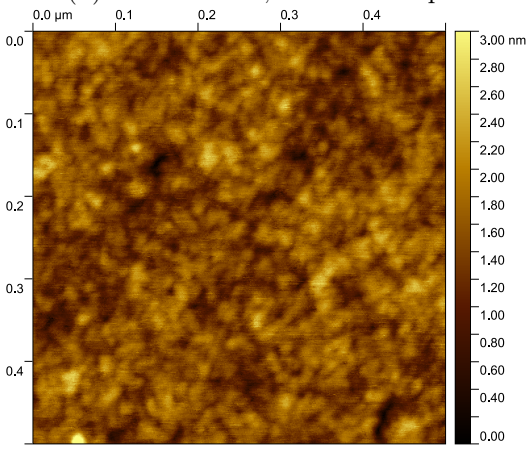

(f) 0.04 wt% BSA, scan size 0.5 µm

Figure 4.19.: AFM scans of transferred surfaces of BSA-solutions with varying concentrations.

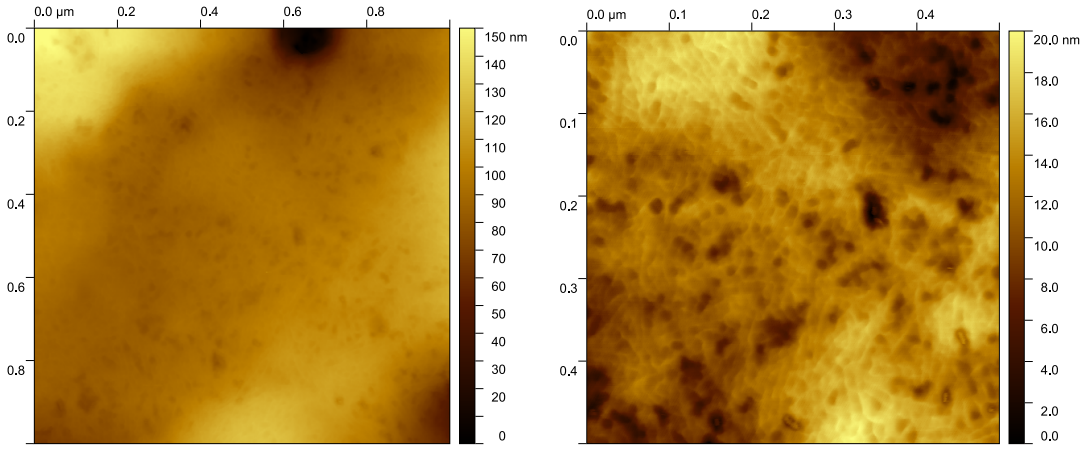

(a) 3 wt% HP + 1 wt% BSA, scan size 1 µm

(b) 3 wt% HP + 1 wt% BSA, scan size 0.5 µm

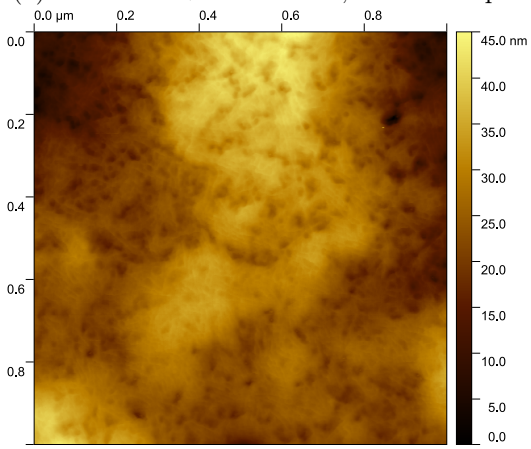

(c) 2 wt% HP + 2 wt% BSA, scan size 1 µm

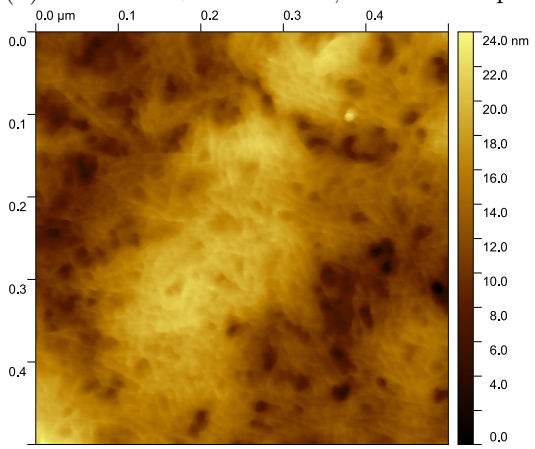

(d) 2 wt% HP + 2 wt% BSA, scan size 0.5 µm

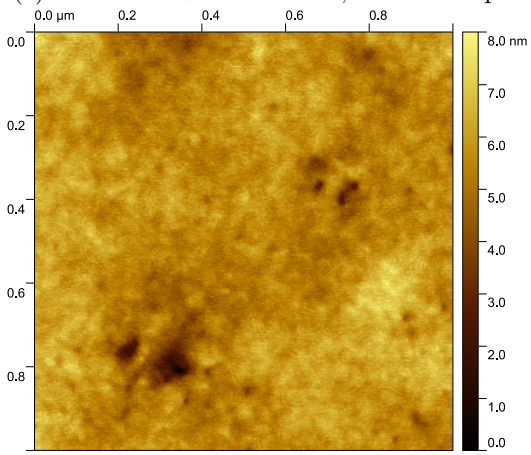

(e) 1 wt% HP + 3 wt% BSA, scan size 1 µm

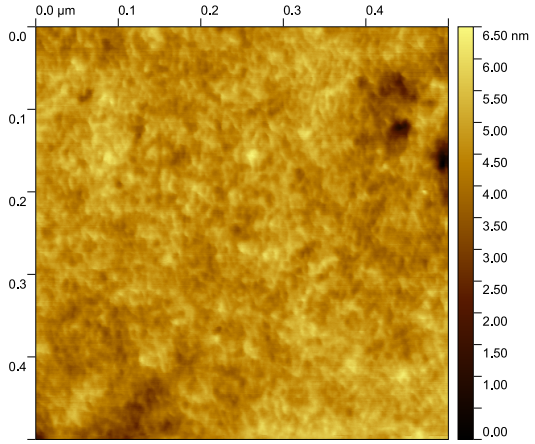

(f) 1 wt% HP + 3 wt% BSA, scan size 0.5 µm

Figure 4.20.: AFM scans of transferred surfaces of solutions containing mixtures of HP and BSA with varying HP:BSA ratios.

on the specific arrangement of charged and hydrophobic amino acid residues at the protein surfaces.

In addition, the arrangement of the two protein species towards each other depends on their molecular size and their surface-to-volume ratio. HP is a small protein with about 100 amino acids [156, 162] and a molecular weight of about 10 kDa [159], which has a compact barrel structure and may contain extended hydrophobic inter-cystein loops [146, 162, 367]. BSA, on the other hand, is a much larger molecule containing 583 amino acids [146] and having a molecular weight of about 66.5 kDa [143–145]. BSA has a heart-like triangular shape. Therefore, the size of BSA will roughly be about six times larger than that of HP, which could lead to the assumption that several HPs arrange around one BSA. However, the strong hydrophobic attraction between different hydrophobins might also lead to large aggregates of hydrophobins, which may have a similar or even larger size than a BSA molecule and probably a different shape. Hydrophobins aggregate by orienting the hydrophobic surface patches towards each other and the hydrophilic part to the outside (water) [367]. Surface charges are then oriented to the water and can interact with BSA molecules. The network-like structures observed for HP:BSA ratios of 3:1 and 1:1 may involve rodlet formation. However, these rodlets are not as parallel oriented as observed for pure HP, since their alignment is disturbed by the presence of BSA. Pham et al. [72] discovered that the presence of the class II hydrophobin MHPI can suppress the rodlet formation of the class I hydrophobin MPG1. This may suggest, that also other proteins like BSA can hinder the formation and alignment of rodlets.

For 3:1 and 1:1 HP:BSA-ratios a quite rough surface with network-like structures is observed by AFM (cf. Figure 4.20). Furthermore, the formation of more elevations is detected, which suggests that some attractive interaction is present between the molecules leading to some kind of clustering. At these ratios, many more HP molecules are present than BSAs (cf. Table 4.2). The interactions relevant for the formation of the network-like structures and elevations may involve HP-HP interactions as well as HP-BSA interactions. A relatively strong interaction between BSA and HP molecules was observed in the DSC measurements, which is relevant in the formation of the observed interfacial structures.

At the 1:3 ratio the surface looks more homogeneous with a few holes. In this case, due to the higher BSA concentration, the contribution of BSA-BSA interactions might be more relevant. These lead to the more even height looking similar to the structure formed by pure BSA, but a bit rougher. However, the increased roughness detected by AFM and the second peak in the DSC thermogram suggest that also HP-BSA interactions play a role, although maybe less relevant than at the HP:BSA mass fraction ratios of 1:1 and 3:1. The holes indicate the presence of HP, which, due to their amphiphilic nature, allow for the formation of such structures.

4.4. Conclusions

Additionally to the investigations of the stability of HP-BSA foams shown in Section 3.6.3, the protein interactions and their interfacial arrangement were investigated here. These results help understand how the different molecular properties and the resulting protein interactions influence the interfacial arrangement and the generated foam properties. Due to their strongly amphipathic nature, hydrophobin molecules interact strongly with one another. This leads to the formation of regular structures including network-like structures, holes, and rodlets in the interfacial films. These regularly structured films significantly lower the surface tension and lead to a high foam stability. The regularity of the arrangements and the stability of the interfacial layers may even be enhanced during foam ripening: the gas diffusion between bubbles leads to changes in the bubble sizes, which are accompanied by compression of the air-water interfaces. These compressions in turn may lead to rearrangements of the proteins at the interfaces and in case of hydrophobins to formation of rodlets.
For BSA very smooth interfacial arrangements are observed. The arrangement of BSA is most probably driven by minimization of the electrostatic energy.
HP-BSA mixtures show, that with increasing HP content the denaturation temperature of BSA is lifted as observed from DSC measurements. This suggests that HP and BSA interact and stabilize each other. Furthermore, the surface tension is lower for HP solutions than for BSA solutions and for HP-BSA blends is decreased with increasing HP content. Investigations of the interfacial protein arrangements using AFM showed, that these are less regular for the mixtures than for pure HP solutions. This suggests that the presence of BSA impedes the very regular HP arrangements. The less regular arrangements stabilize the bubble surfaces less efficiently against coarsening and rupture. As a consequence, the most stable foams are found for pure HP solutions, which exhibit the most regular patterns of protein arrangements.

5. Foam stabilization by addition of hydrocolloids

5.1. Introduction

Hydrocolloids are used in the food and beverage industry as gelling agents, emulsifiers, thickeners and stabilizers to control the textural properties, microstructure, shelf-life and flavor of a food product [211, 215]. In foams food thickening agents can be applied to enhance the viscosity of the solution and by this improve the foam stability [208, 376]. A high viscosity of the continuous phase of a foam slows down drainage and the mobility of bubbles, which are relevant processes for the destabilization of a foam [90, 107, 210, 238, 239].
In this chapter, three different food-grade hydrocolloids are added to BSA solutions and their influence on solution viscosity and stability of BSA-stabilized foams is investigated and compared. These hydrocolloids are xanthan gum (XG), guar gum (GG) and iota-carrageenan (IC), all non-starch polysaccharides. Their structure and properties are described in Section 2.3. The reason for this choice lies in their distinct and different physical properties. XG is a highly negatively charged rigid rod [233]. IC is less negatively charged, but more flexible [217]. The electrostatic repulsion of the negative charges exerts a force on the self-avoiding walk of the chain. Consequently, the polymer chain elongates and arranges into a string of independent blobs with each blob containing a self-avoiding chain (chain under traction) [377]. GG is uncharged and very flexible and can therefore be regarded as a polymer which performs a self-avoiding walk (self-avoiding coil) [217]. These simple models are sketched in Figure 5.1. These fundamental differences influence their interaction with other molecules.

Figure 5.1.: Very simplified models of the three polysaccharides xanthan gum (XG), iota-carrageenan (IC) and guar gum (GG). Sketches not drawn to scale.

Furthermore, charge as well as shape of a molecule influence the viscosity of the so-

lution [91, 230, 231, 233, 235]. For this reason, these polysaccharides are used as thickening agents and to enhance the stability of a foam as is demonstrated in the following.

5.2. Materials and Methods

5.2.1. Sample preparation

For all measurements BSA (A7030, heat shock fraction, protease free, fatty acid free, essentially globulin free, pH 7, $\geq$ 98 %) from Sigma-Aldrich (Saint Louis, MO, USA) was used as-received.
The polysaccharides guar gum (Unipektin Ingredients AG, Eschenz, Switzerland) and xanthan gum (Jungbunzlauer Suisse AG, Basel, Switzerland) were dissolved in ultrapure water (18.2 MΩ cm) by stirring over night. The next morning, guar gum was centrifuged at 15 090 ×g for 20 min at 20 °C to remove cell material. Iota-carrageenan (Carl Roth GmbH + Co.KG, Karlsruhe, Germany) was dissolved in ultrapure water and heated to 70 °C for 20 min to complete solution. After preparing the polysaccharide solution, BSA was added to it and dissolved by further stirring. The final solutions contained 4 wt% BSA and 0.4 wt% polysaccharide in ultrapure water.

5.2.2. Measurement of solution viscosity

XG, GG and IC form shear-thinning solutions when dissolved in water [378–380]. To measure solution viscosity flow sweeps were performed in a couette geometry (DIN concentric cylinders with smooth surfaces, bob diameter 28 mm, bob length 42 mm, cup diameter 30.4 mm, gap 5921 µm and loading gap 90 mm) at 25 °C with a DHR3 rheometer from TA Instruments (New Castle, DE, USA). After filling the measuring cup, samples were allowed to rest for 300 s. Measurements were performed in rotation and the shear rate was varied every 30 s. The shear rate was raised from 0.01 s^{-1} to 1000 s^{-1}, and subsequently it was decreased again from 1000 s^{-1} to 0.01 s^{-1}.

5.2.3. Foam formation

For foam formation a T 25 easy clean control ULTRA-TURRAX (IKA-Werke GmbH & Co. KG, Staufen, Germany) equipped with dispersion tool S 25 N - 10 G was used. 2 g of protein solution were dispersed at a speed of 20 000 rpm for 1 min in a custom-built glass cylinder with overflow protection as described in 3.6.2.

5.2.4. Imaging of the foam

The temporal evolution of the samples was observed using an Axio Scope.A1 light microscope from Carl Zeiss (Oberkochen, Germany) with a magnification of 10 × and simultaneously with a Canon EOS 7D camera equipped with objective Canon Macro Lens EF 100mm 1:2.8 L IS USM and a Canon TC-80N36D remote release with timer function (Canon Inc. Headquarters, Tokyo, Japan) for 30 min or 60 min, respectively.

The camera was mounted to a repro stand RS 2 XA from Kaiser Fototechnik (Kaiser Fototechnik GmbH & Co. KG, Buchen, Germany) and samples monitored by the camera were placed on top of a luminous plate LED Slimlite plano (Kaiser Fototechnik GmbH & Co. KG, Buchen, Germany). Directly after foam formation a sample of the foam was transferred to a microscope slide and covered with a cover slip. For microscope images 0.005 g foam were transferred using a microspoon whereas for camera images 0.01 g were used.

5.2.5. Analysis of the mean bubble size

For more reliable statistics the camera images were taken for bubble size analysis. The image was cropped to have a size of 3000×3000 pixels and to show only the bubbles of the foam, not the area surrounding the sample. Subsequently, the contrast of the image was enhanced (2-fold). Afterwards, the image was converted to a binary image. A python script (cf. Appendix A.1) counted all connected same-color pixels as one bubble. The number of pixels of one bubble was converted into micrometer and provides the area of the bubble. From the area the equivalent diameter was calculated, which is the diameter of a circle of the same area as the measured bubble. Having computed the equivalent bubble diameter of each bubble in the image, the mean equivalent bubble diameter of all bubbles in this image was calculated.
All measurements were repeated for three identical samples and means and standard deviations were calculated.

5.3. Results and discussion

5.3.1. Foam images

Figure 5.2 shows a microscope image and a camera image of a BSA-stabilized foam. For analysis of the temporal evolution of the mean bubble size, the camera images were used, because these show a larger number of bubbles and therefore provide more reliable statistics.
For visualization of the properties of foams with different polysaccharide composition, microscope images of BSA-stabilized foams without and with GG, IC or XG are shown in Figure 5.3. All foams containing one of the polysaccharides appear wetter compared to those stabilized only by BSA. The higher liquid content of the foam arises from the enhanced water holding capacity of the hydrocolloids [216], which retains larger amounts of water in the lamellae between the bubbles. According to the microscope images, the foams containing XG or IC retain a higher liquid fraction for a longer time than the foams containing GG. The increased viscosity slows down drainage, which contributes to retaining a higher liquid fraction. A high liquid fraction reduces the rate of coalescence, because bubble surfaces are separated by sufficient liquid. Lower coalescence rates in turn, contribute to a slower increase of the mean bubble size and a more stable foam. [90, 107, 238] As can be seen from the microscope images, the ripening of the wet foams containing IC or XG is dominated by Ostwald-ripening.

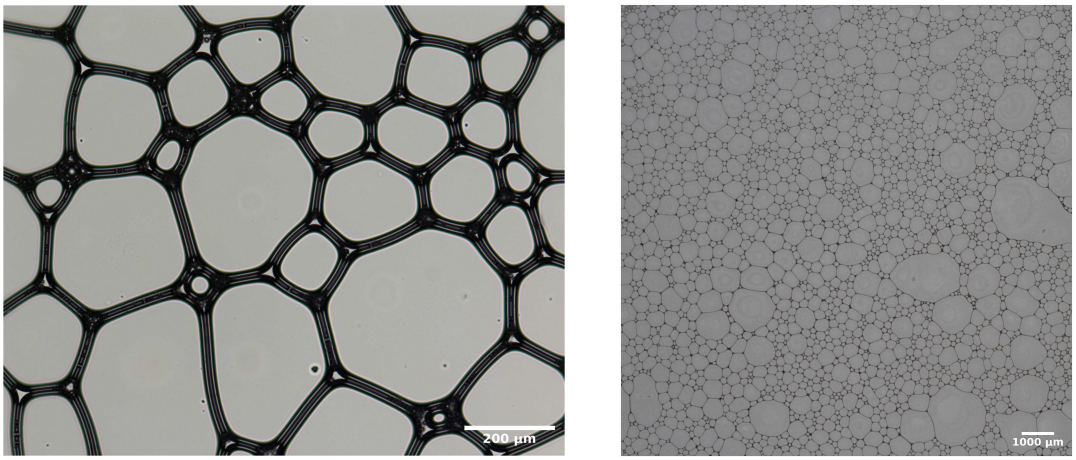

(a) Microscope (b) Camera

Figure 5.2.: Microscope and camera image of a foam stabilized by 4 wt% BSA after 10 min. Microscopy performed in bright field transmission mode with a magnification of 10 ×.

5.3.2. Solution viscosity

Figure 5.4 shows the results of the flow sweeps performed for solutions of BSA with added polysaccharides: XG, IC and GG, respectively. The dynamic viscosity η is displayed in dependence of the shear rate $\dot{\gamma}$. Shown are the flow sweeps for decreasing shear rates. The viscosity of the pure BSA solution was too low to be measured properly (cf. Appendix C.1). All three solution types show shear thinning behavior. The shear thinning behavior is most pronounced for the solutions containing XG and least pronounced for the solutions containing GG. At low shear rates, the solutions containing XG show the highest viscosity, followed by IC and the lowest viscosity is observed for solutions containing GG. However, since XG shows the steepest slope (most pronounced shear thinning behavior), the graphs cross. At shear rates above about $20\,s^{-1}$ the viscosity of the XG containing solutions becomes lower than that of the solutions containing IC. At shear rates above about $200\,s^{-1}$, the viscosity of the solutions containing XG even slightly undercuts the viscosity of the solutions containing GG.

The viscosity of a dispersion is determined by the shape and charge of its components [91, 230, 231, 233, 235]. Of the selected polysaccharides, XG is the most negatively charged and also exhibits the highest stiffness. The high charge and the elongated, stiff molecule both enhance the viscosity of the solution (see Equations 2.23 and 2.22). This results in the highest viscosity being observed at low shear rates. Nevertheless, at elevated shear rates, the rods adopt an orientation parallel to the flow direction, facilitating sliding between them [381, 382], which explains the pronounced shear-thinning behavior. Contrarily, GG is uncharged and flexible. Therefore, there is no viscosity increase due to electroviscous effects. Also, the molecule, which behaves as

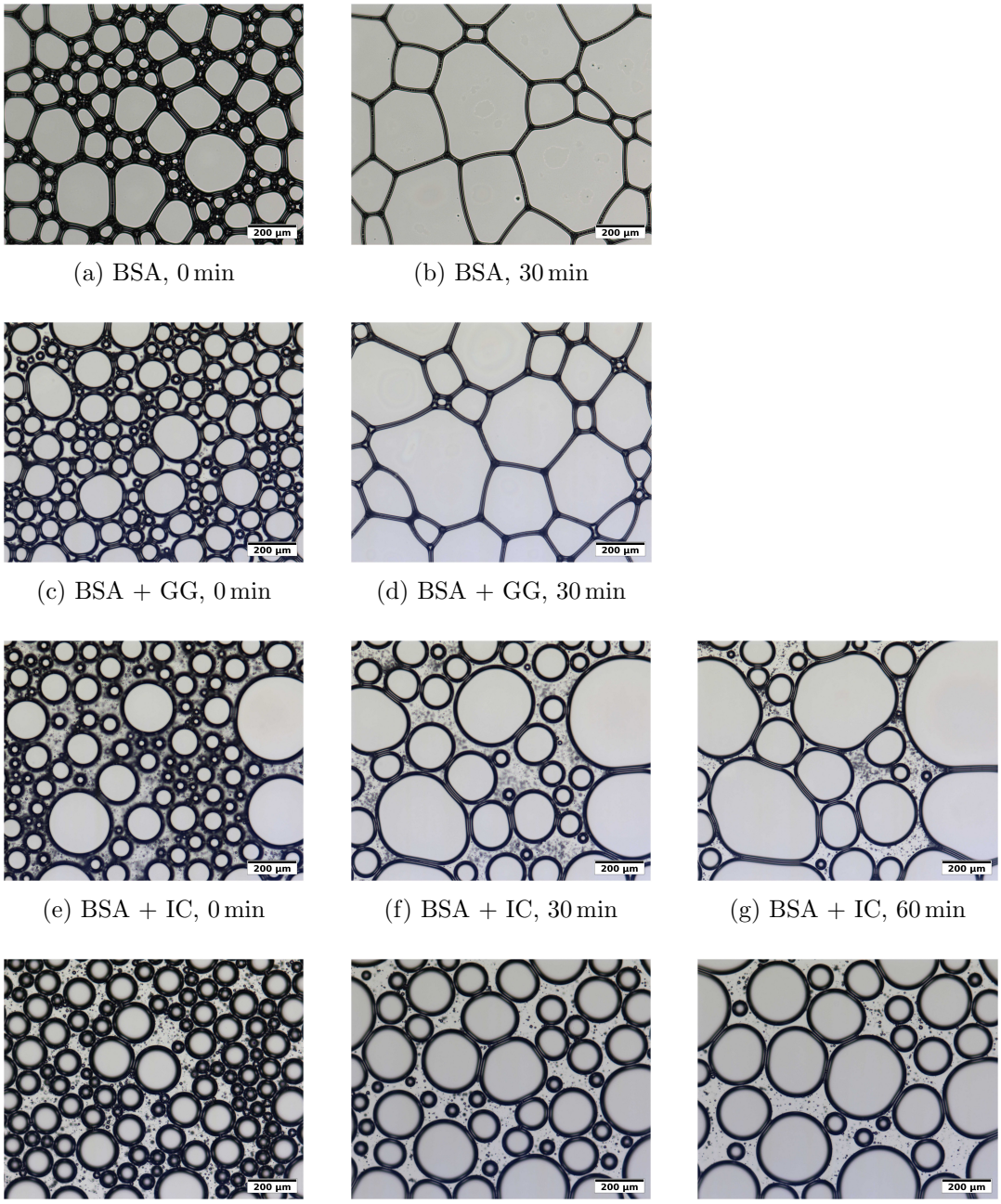

(a) BSA, 0 min (b) BSA, 30 min

(c) BSA + GG, 0 min (d) BSA + GG, 30 min

(e) BSA + IC, 0 min (f) BSA + IC, 30 min (g) BSA + IC, 60 min

(h) BSA + XG, 0 min (i) BSA + XG, 30 min (j) BSA + XG, 60 min

Figure 5.3.: Microscope images of 4 wt% BSA without (first row) and with addition of 0.4 wt% polysaccharide: GG (second row), IC (third row) and XG (forth row).

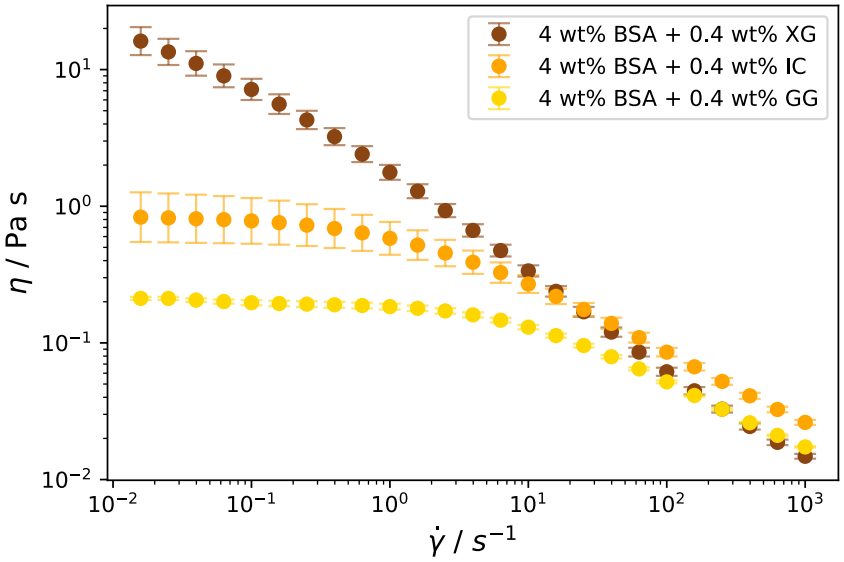

Figure 5.4.: Shear rate dependent dynamic viscosity of BSA solutions with added polysaccharides: comparison of XG, GG and IC.

a self-avoiding coil, is less extended, which leads to a lower exponent in Equation 2.22 and a lower viscosity increase. IC is negatively charged, but flexible on certain scales. The shape of the molecule is that of a string of electrostatic blobs. Its exponent in Equation 2.22 is expected to be between that for a self-avoiding coil and a rigid rod. Due to its less strong negative charge, the electroviscous effect is less pronounced than for XG. It can thus be concluded that the viscosity of IC is intermediate between those of XG and GG, as was measured for shear rates below about $20\,s^{-1}$.

5.3.3. Temporal evolution of the mean bubble size

The temporal evolution of the mean equivalent bubble diameters d_{equ} for BSA-stabilized foams without additives and with XG, IC and GG added, respectively, is shown in Figure 5.5.
The initial mean bubble size is decreased for samples containing a polysaccharide and deviates slightly among samples containing XG, IC or GG. During foam formation very high shear rates are applied by the ultra turrax T 25 (cf. Appendix C.2). At such shear rates, the viscosity of XG is lower than that of IC and GG due to its stronger shear thinning behavior. The viscosity during foam formation influences the incorporation of air bubbles into the foam and their initial size: the initial bubble size decreases with increasing viscosity [383, 384]. These effects explain the larger initial mean equivalent bubble diameter of the pure BSA-stabilized foams ($(101.8 \pm 11.4)\,\mu m$) as compared to systems with added polysaccaride and the slightly smaller initial bubble size of the foams with added IC ($(76.9 \pm 3.3)\,\mu m$) compared to the foams containing XG ($(82.3 \pm 2.0)\,\mu m$) or GG ($(83.6 \pm 9.1)\,\mu m$).

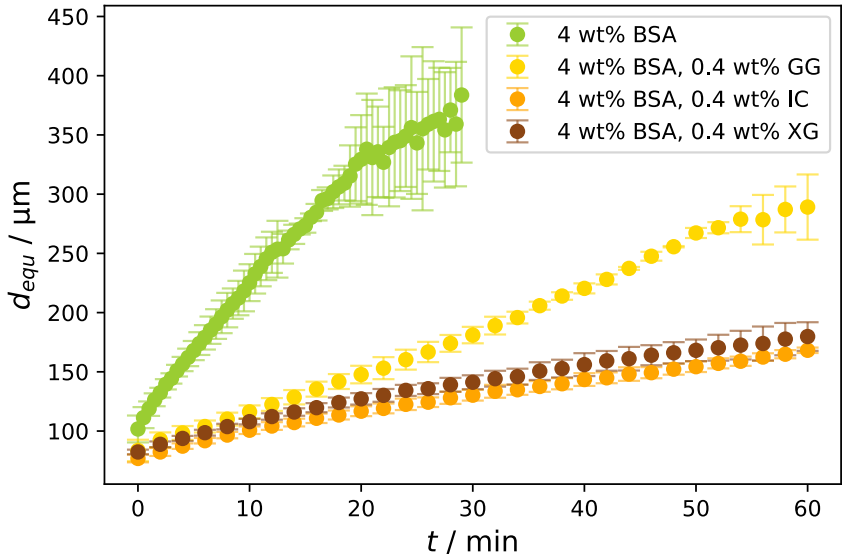

Figure 5.5.: Temporal evolution of the mean bubble size of BSA solutions without and with added polysaccharides: comparison of XG, GG and IC.

Over the whole measurement time the mean bubble size is significantly lower for samples containing a polysaccharide than for the samples without a stabilizer. This observation indicates that the foam stability is significantly increased by the addition of polysaccharides. By adding polysaccharides, the viscosity of the sample solution is significantly enhanced, which prevents fast drainage as well as creaming of bubbles [90, 107, 239, 376]. Both of these effects play a pivotal role in foam stability. They impact the thickness of the lamellae, which in turn affects the rate of coalescence [90, 238]. This explains the increased foam stability observed for foams containing polysaccharides.

At $t = 0$, the mean bubble sizes of the samples containing a polysaccharide deviate only by a few µm. At later times, the samples containing GG develop a significantly increased mean bubble size as compared to the samples containing XG or IC, respectively. This observation indicates that the foams containing XG or IC are more stable than those with GG. While monitoring the foam under the microscope, the foam rests, coarsening of the foam is considered sufficiently slow, and the foam can be considered as being close to mechanical equilibrium [112]. It is therefore evident that the viscosities pertinent to drainage are those measured for exceedingly low shear rates. Due to the relatively high viscosities of XG and IC solutions, these foams retain a higher liquid fraction (cf. microscope images in Figure 5.3) and show a slow increase of the mean bubble size. The lower viscosity of GG solutions yields a faster increase in the mean equivalent bubble diameter. Although XG shows a higher solution viscosity at low shear rates than IC, the evolutions of their mean bubble sizes exhibit similar courses and proceed quite close to each other. To explain these similarly evolving

mean equivalent bubble diameters of foams containing XG or IC it is thus insufficient to discuss only the viscosity differences. The bubble size results indicate that additionally a destabilizing mechanism is present in the foams containing XG. For this reason, the structural differences between the stiff, negatively charged XG rods and the IC strings of independent blobs have to be taken into account.
In addition to the influence of the polysaccharide structure also their interaction with BSA may influence foam stability [238]. To visualize the inter-polysaccharide interactions determined by their stiffness and electrical charge as well as their interaction with interfacially adsorbed BSA in thinning lamellae, models are shown in Figures 5.6 and 5.7. Each subfigure shows a bubble surface with adsorbed BSA on both the left and right side defining the edges of the lamella of varying thickness. The case without added polysaccharide is shown in Subfigures 5.6 (a) to (d). Over time, the lamella thins due to drainage of liquid from the foam and the bubbles eventually coalesce (Subfigures (c) and (d)).
The flexible GG polymers (Subfigures 5.6 (e) to (g)) show weak mutual interaction and take a random distribution within the lamella to maximize entropy. Over time, some GG polymers drain with the liquid. Due to its polarity, GG interacts weaker with BSA than the charged polymers XG or IC do. To maximize entropy, GG will therefore mostly be dissolved in the water and have a minor influence on the interfacial stability of wet foams (other than enhancing solution viscosity). Due to excluded volume effects, van der Waals interactions and hydrogen bonding GG polymers interact with each other or BSA when coming into close proximity. The stability of thin lamellae in dry foams (Subfigure 5.6 (g)) is increased via bridging the two interfaces by adsorbed flexible GG chains [385].
Flocculation and creaming of oil-in-water emulsions and model food systems provoked by XG were observed by Gunning et al. [386] and Koczo et al. [240]. These authors explain their observation by a depletion mechanism causing an isotropic/anisotropic phase separation according to Flory's theory of rod-like particles [241–243]. However, the XG rods are strongly negatively charged, which makes a purely entropy-driven parallel alignment unlikely. To minimize the electrostatic energy, these negatively charged rods take random orientations. Such arrangements consume a large space due to the associated large excluded volume effects. As the lamellae thin, the space available to such configurations is constricted. More configurations for minimization of the electrostatic energy are available in the liquid phase of already drained liquid. For this reason, the rigid nature and strong negative charge of XG might contribute to phase separation into a bubble-rich phase at the top and a liquid phase at the bottom. Such effects destabilize the foam as they contribute to drainage and for this reason counteract the stabilizing effects caused by a higher solution viscosity. In addition, electrostatic interaction of XG with BSA is relevant, because its negative net charge interacts with local surface charges of BSA (Subfigure 5.7 (a)). Thus, electrostatic attraction between BSA and XG can lead to an increased steric interaction within the lamellae (Subfigures 5.7 (b) and (c)). Steric interaction of adsorbed polymers increases the stability of lamellae against coalescence and therefore enhances bubble stability [19, 385]. For XG molecules attracted by interfacially adsorbed BSAs, the combination

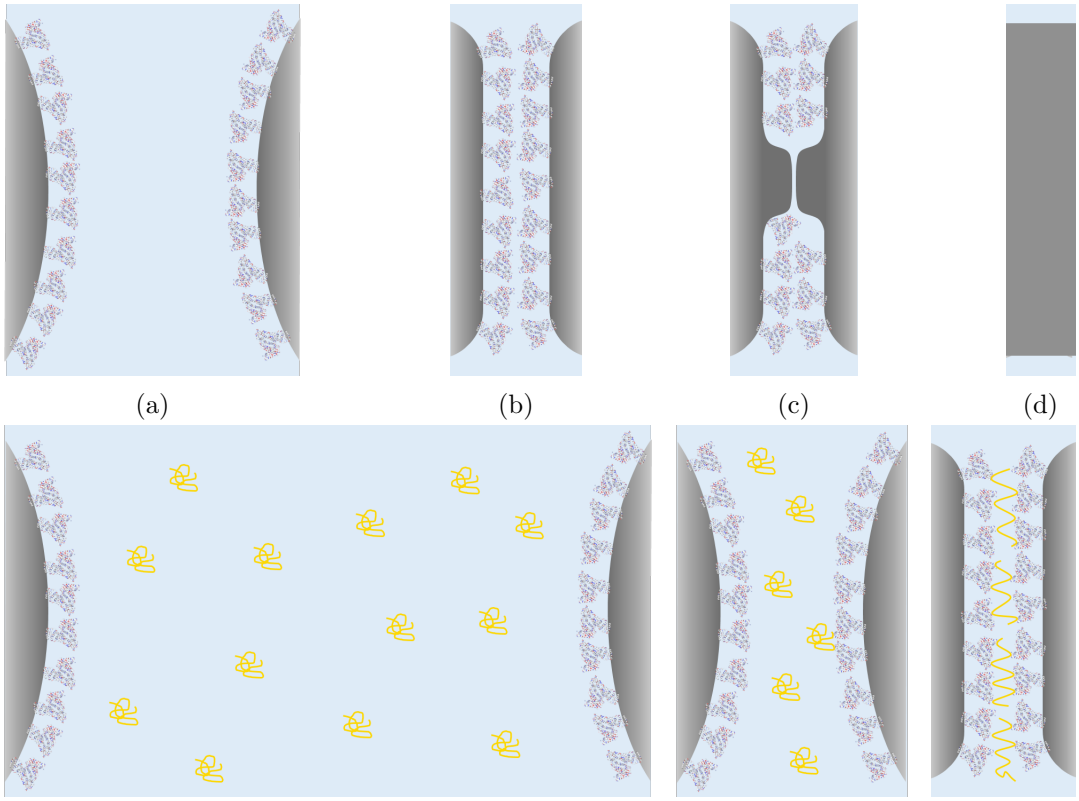

Figure 5.6.: Thinning lamellae without polysaccharide (Subfigures (a) to (d)) and with GG (Subfigures (e) to (g)). Schematic not drawn to scale.

of their high stiffness and strong negative charge leads to large excluded volumes and a strong steric repulsion between approaching air-water interfaces. Such interactions counteract lamella thinning and therefore support retaining a high liquid fraction in the foam, thereby stabilizing the lamellae against coalescence. Consequently, such steric interactions within the lamellae may increase the foam stability additionally to the high viscosity of XG solutions. However, as described above the strong mutual repulsion and high stiffness of XG molecules also cause a destabilizing mechanism, because more orientations are available to such highly charged rigid rods in the liquid phase of drained liquid. At decreasing liquid content due to drainage, free XG molecules such as the ones shown in Subfigure 5.7 (a) in the middle are pushed out of the foam and drain with the liquid. Since XG is highly negatively charged and BSA shows only local surface charges, the electrostatic repulsion between XG molecules is stronger than their electrostatic interaction with BSA. For this reason, the steric stabilization by XG breaks at further decreasing liquid content of the foam (Subfigure 5.7 (c) and (d)).
For IC more configurations are possible in the confined space of the lamellae, because these molecules are less negatively charged and the strings of independent blobs are more flexible, which leads to smaller excluded volumes. For this reason, phase separating effects caused by the molecular charge and stiffness are much less pronounced. Since IC is less negatively charged and more flexible, it bends more easily. Due to its negative charge, it is still attracted by positive surface charges of BSA, but repulsion by negative surfaces charges is less strong. Also their mutual repulsion is less strong than for XG molecules. Therefore, more configurations are available to IC molecules in the thinning lamellae. As the lamellae thin, the strings of independent blobs bend due to the electrostatic repulsion and still provide for a steric stabilization of the lamellae. The higher polymer flexibility also allows for attaching to both BSA coated interfaces and bridging approaching bubble surfaces [385] as shown in Subfigure 5.7 (g). For this reason, also thin lamellae are well stabilized by IC. As a consequence of the strong mutual XG repulsion and large excluded volume effects, the foams containing XG show similar stabilities as the foams containing IC, although a lower viscosity was measured for IC solutions at low shear rates.

5.4. Conclusions

Addition of polysaccharides to BSA-stabilized solutions increases their dynamic viscosity and enhances foam stability. Foams containing XG or IC are more stable than foams containing GG. It can be concluded that higher viscosities lead to smaller bubble sizes and more stable foams. Although solutions containing XG show a higher viscosity at low shear rates, the evolution of the mean bubble size of their foams is comparable to that of foams containing IC. This implies that also the structural differences of the polysaccharides affect their interaction with other polysaccharide molecules and BSA, which in turn impact foam stability. The stiff and highly negatively charged XG rods aim for random orientations due to their strong mutual electrostatic repulsion

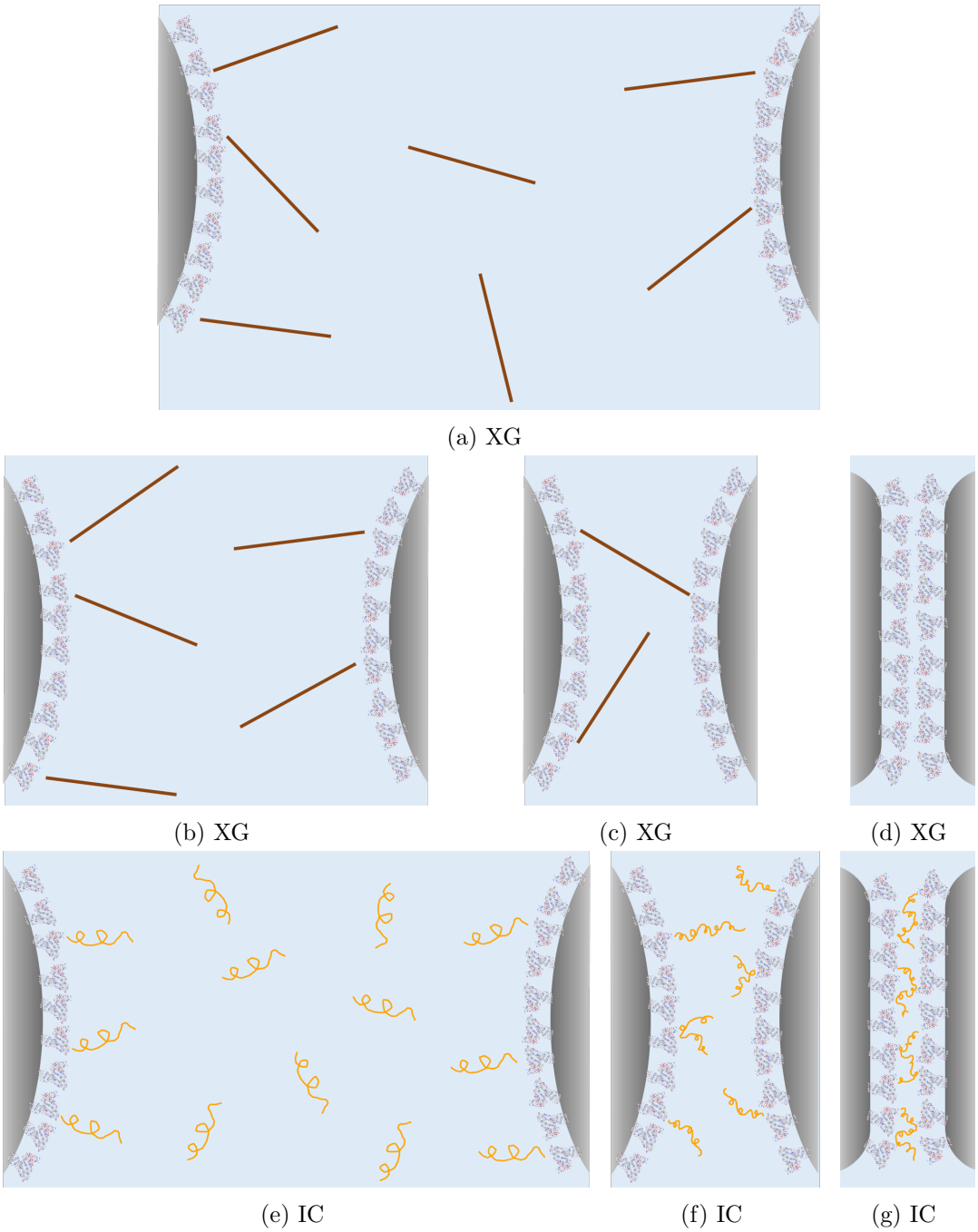

(a) XG

(b) XG

(c) XG

(d) XG

(e) IC

(f) IC

(g) IC

Figure 5.7.: Steric stabilization of thinning lamellae by XG (Subfigures (a) to (d)) and IC (Subfigures (e) to (g)). Schematic not drawn to scale.

and large excluded volume effects. These properties on the one hand increase solution viscosity, on the other hand also support phase separation into a bubble rich phase and a liquid phase, which promotes foam decay. Attraction to interfacially adsorbed BSA facilitates lamellae stabilization via steric repulsion of the approaching interfaces. However, the strong negative charge and high stiffness of XG cause the steric stabilization by XG rods to collapse under confinement of the space of the lamellae. The higher flexibility and lower negative charge of IC allows for steric stabilization of approaching bubble surfaces also for thin lamellae and bridging stabilization of even thinner lamellae. Bridging stabilization of thin lamellae is also facilitated by the flexible polymer GG.

6. Influence of the pH value on BSA-stabilized foams

6.1. Introduction

In this chapter a model foam system consisting of BSA in water and incorporated air bubbles is investigated and different pH values of the solution are considered.
According to literature [40, 42, 89], the foam stability varies depending on solution pH for BSA-stabilized foams. It was therefore assumed that this system would be an appropriate subject for testing the developed method for bubble size analysis. However, subsequent investigation of BSA-stabilized foams at different pH values revealed that this was a more complex and intriguing topic than had been anticipated.
BSA has the advantage of being well-characterized [65, 78–86]. The structure of BSA has been elucidated and structural, pH-depending changes have been reported in more details [65, 147, 148]. However, foam properties were mostly investigated for gas sparging at low concentrations (0.1 % [40], $\leq 3\,\mu mol\,L^{-1}$ [89], $15\,\mu mol\,L^{-1}$ [42]). In the current study, the protein concentration of 4 wt% BSA is much higher, because whipping requires protein concentrations of 3 % to 40 % [35]. Applying this concentration resulted in the formation of smooth foams.
Engelhardt et al. [42] report a strong pH-dependence of the foam stability for BSA solutions with a concentration of $15\,\mu mol\,L^{-1}$. The highest foam stability of about 80 % is found at the IEP. From there it decreases to about 30 % at pH 3 as well as pH 9. Moreover, the authors employed ellipsometry to quantify the thickness of the adsorbed protein layer at the air-water interface. Their results suggest the formation of a multilayer structure at the IEP and a protein monolayer at both high and low pH. Kim and Kinsella [40] considered drainage rates of foams made of 0.1 % BSA solutions and report a maximum foam stability at pH 5 to 6, which is close to the IEP. Foam height was considered by Zawala et al. [89], who found that foams formed by solutions of concentrations of $0.9\,\mu mol\,L^{-1}$ to $3\,\mu mol\,L^{-1}$ BSA were most stable at a pH between 4.8 and 5.8, which is around the IEP of BSA. At pH 3.9 and 10, the foam stability was significantly reduced.
In protein-based foams, the proteins must align along the air-water interfaces according to hydrophilic and hydrophobic regions [139–141]. Therefore, the pH-dependence of foam stability can be attributed to the molecular properties of BSA, which undergoes a conformational change in response to changes in solution pH.
When varying the pH value, the charge and conformation of the protein change, which influence not only the interfacial arrangement but also the solution viscosity [91, 236]. It has been demonstrated that at the concentration employed, the pH-

dependent viscosity alterations resulting from electroviscous effects are markedly more pronounced than at low protein concentrations. The viscosity exerts an influence on the flow behavior of the solution, which in turn affects the drainage of liquid from the foam. Moreover, the coalescence and ascent of bubbles are impeded. Consequently, alterations in solution viscosity exert an influence on the stability of the foam. [90, 107, 210, 238, 239] In the considered system, the effects of pH-dependent conformational changes and molecular arrangements at the air-water interface on the foam stability are largely compensated by the effects that pH-dependent viscosity changes have on foam stability. Therefore, a much less pronounced pH-dependence is observed than that reported by Engelhardt et al. [42], Zawala et al. [89] and Kim et al. [40] for foams containing low BSA concentrations.
Nevertheless, the effects of the molecular arrangements are still very important especially at later time scales, when the foam becomes dryer. Foams at the IEP show comparable drainage and bubble size growth rates as foams at pH 3, although having a much lower dynamic viscosity of the protein solution. This indicates that the multilayer formation of proteins at the air-water interface indeed slows down bubble growth and drainage. In addition, the foam height decreases slower at the IEP than at the other pH values. Consequently, the formation of a protein multilayer leads to an improved foam stability, especially at later times.
The following chapter presents models developed based on the results presented in the literature. Changes in pH cause a variation of the protein surface charge and an unfolding of the globular conformation of BSA. These pH-dependent structural changes affect the functionality and consequently the arrangement of BSA molecules at the air-water interface. By considering these structural changes on a microscopic scale and relating them to the macroscopic foam stability, structure-function relationships are derived. The models elucidate the manner by which the pH-dependent conformational alterations of BSA impact their disposition at air-water interfaces, and the extent to which these effects influence the foam stability.
In a second part of the chapter, results at a concentration of 4 wt% BSA are presented, where the pH-dependence of the foam stability is less pronounced. Measurements of the dynamic viscosities and particle sizes are combined with a detailed analysis of the foam stability considering the temporal evolution of foam heights, drainage, mean bubble diameters and circularities. The interplay of molecular arrangement and viscosity are discussed here to understand the distinct behavior observed in the different experiments.

6.2. Modeling structure-function relationships

6.2.1. Molecular properties of BSA

As already mentioned in Subsection 2.2.1, the structure of BSA can be divided into three domains, commonly referred to as domains I, II and III. The general structure of each domain is comprised of two large double loops and one small double loop, which are formed by disulfide bonds. The initial large and small double loops are linked by

a short peptide sequence, while the latter is connected to the second large double loop by a more substantial segment. A further peptide connects the second large double loop to the subsequent domain. Domain I encompasses amino acids 1-190, domain II consists of amino acids 191-382, and domain III comprises amino acids 383-583. In comparison to domains II and III, domain I is devoid of one disulfide bond (between positions 8 and 54), resulting in the presence of a single loop instead of the initial large double loop.[147]
In three dimensions, the native globular shape of BSA is arranged in a heart-like shape, also known as the Normal (N) form. Domains I and II form one half of the N-form, while domain III forms the other half. [146, 148–150]
The primary and secondary structure provide more detailed information about the structural and functional properties of the protein. The properties of the amino acids in the protein, such as their electrical charge and hydrophobicity, the helical content of the protein and the number of cysteins present, are particularly relevant to the interface activity of the protein, and therefore relevant for the foam stability.
These considerations result in a sketch for domain III as shown in Figure 6.1. The model is based on information provided by J. R. Brown in [147] (p. 36) about the structure of BSA and information from swissmodel.expacy.org [146] entry with UniProtKB P02769. Details are provided in Appendix D.2, see Figures D.1, D.2, and D.3.
The model in Figure 6.1 includes the amino acid sequence (primary structure) as well as relevant physical properties of the amino acids. Positively and negatively charged amino acids are colored green and red, respectively. Hydrophobic amino acids are marked in blue and polar amino acids are shown in black. In particular, at the end of domain III (lower part in Figure 6.1) several hydrophobic amino acids are spatially close to each other. This part is located at the protein surface when regarding the 3D model provided by swiss-model [146] (cf. Figure 2.3d), and is thus beneficial for the surface activity of BSA.
The 11 helices in domain III cause a certain rigidity of these parts of the molecule. The locations of the helices are indicated by the configuration of the amino acids in the model and a white helix superimposed on the primary structure. Furthermore, disulfide bonds are indicated by a yellow line, and the primary structure is bent to form double loops.
It is important to note that the N-form corresponds to the shape at the IEP. In this compact shape the two parts of the heart-like shape are held together by electrostatic attraction of oppositely charged amino acids and hydrophobic interactions [148, 149]. Hydrophobic amino acids and the charges of hydrophilic amino acids at the interface of the two parts of the heart-like shape are illustrated in Figure 6.2. A more detailed examination reveals the presence of hydrophobic interactions and the electrostatic attraction between oppositely charged amino acids, as illustrated on the right part of Figure 6.2.
The charge of the amino acids depends on the pH of the solution. When lowering the pH below the IEP of BSA, some of the previously negatively charged amino acids become neutral or positively charged. The exact charge changes depend on whether the pH is lower than the IEP of the amino acid. In BSA, the overall number of

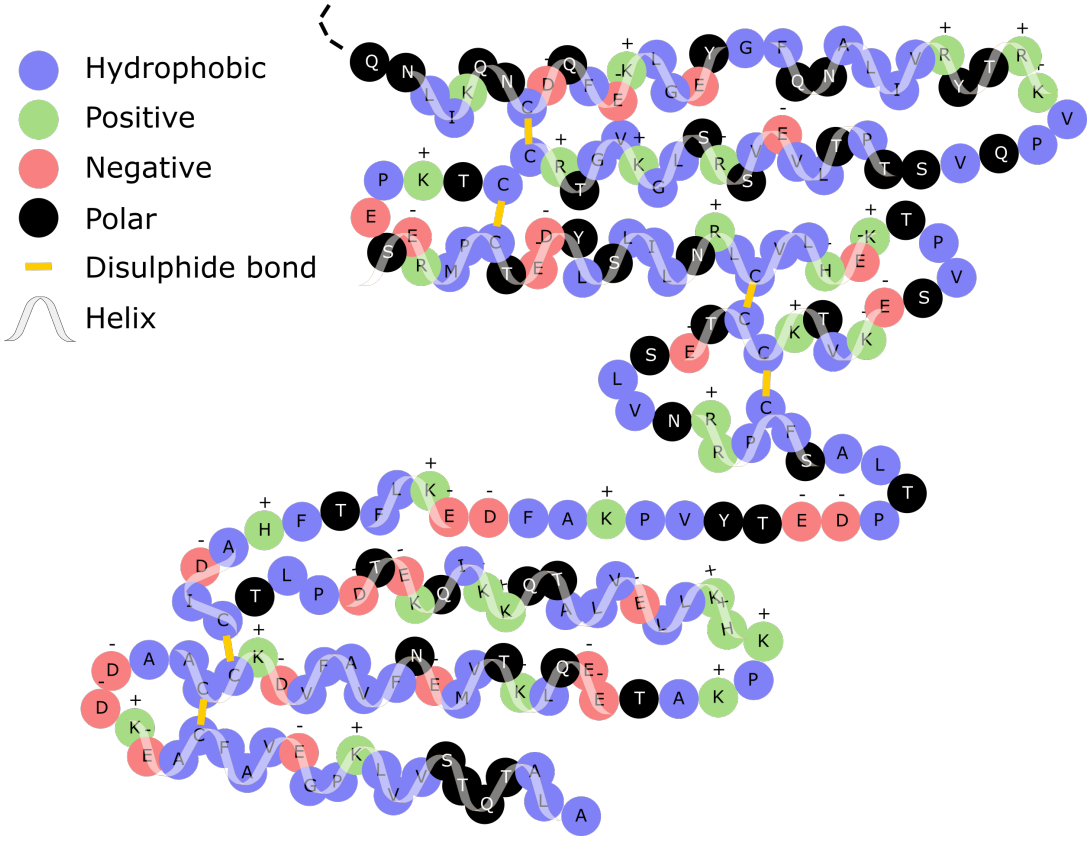

Figure 6.1.: Model of domain III including charge and hydrophobicity of the amino acids, disulfide bonds, and helices. The dashed line at the top implies the connection to domain II.

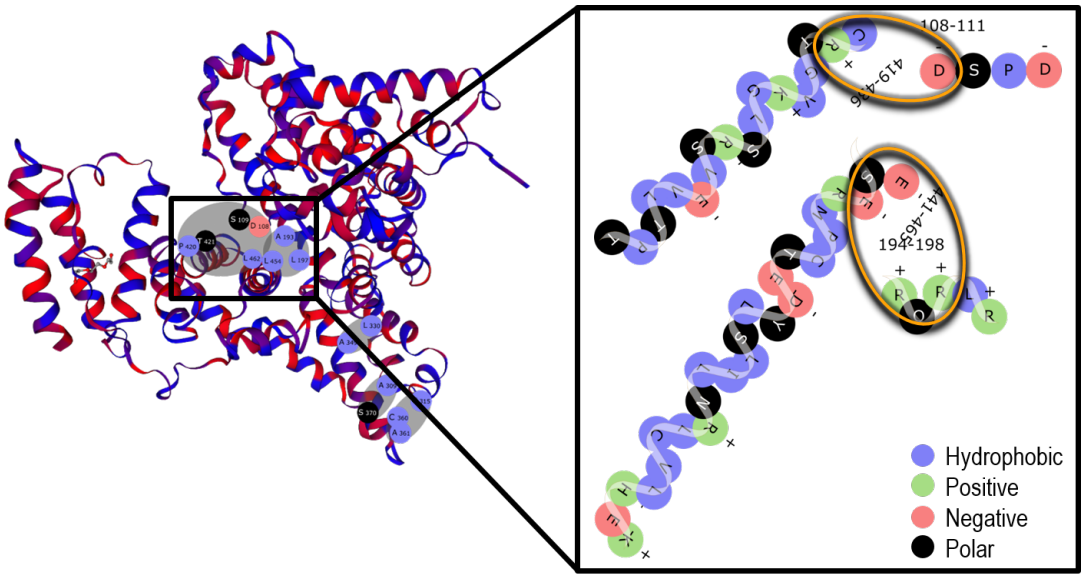

Figure 6.2.: Electrostatic interactions (highlighted by yellow ellipses) of amino acids at the interface of the two parts of the heart-like globular shape of BSA.

positively charged amino acids increases, which implies a stronger repulsive interaction within the protein conformation. As a consequence, the BSA molecule unfolds between domain II and domain III [65, 148–150].

The resulting conformation is called Fast (F) form and occurs at pH values below pH 4 [149]/ pH 4.5 [79]. The charge changes and unfolding of the N-form into the F-form of BSA was confirmed by Baler et al. [150] using molecular dynamics simulations. The simulation indicates the change from a total net charge of -9 at pH 7.4 to a highly positively net charge of +100 at pH 3.5. This publication provides an excellent illustration of the opening of the heart-like shape between domain II and domain III. At even lower pH values, the shape of BSA continues to expand, reaching the Expanded (E) form below pH 3.5 [149]. These conformational changes are associated with a loss of helical content.

When increasing the pH to alkaline conditions, some of the positively charged amino acids become neutral or negatively charged (depending on the IEP of the amino acid). This leads to more negative charges in the protein, which repel each other and cause a conformational change. As a result, the volume of the BSA molecule increases and there is a loss of helical content. The Basic (B) form is typically found between pH 7 and pH 9 [65] / above pH 8 [149].

Figure 6.3 illustrates the relevant unfolding of domain III without disulfide bond disruption. Possible sites where the molecule can unfold under these constraints are marked with gray arrows. As the molecule unfolds, it becomes more flexible. In addition, otherwise hidden hydrophobic parts can be exposed. For these reasons, the protein gains more possibilities to arrange itself at the air-water interface, as illustrated

in Figure 6.4.

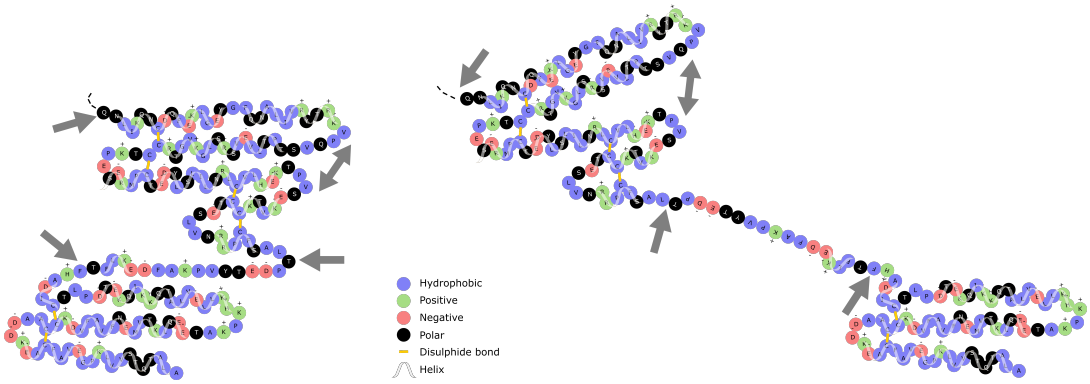

Figure 6.3.: Unfolding of domain III under the restriction that disulfide bonds stay intact. Spots of unfolding are marked with gray arrows. Left: domain III in globular shape, right: domain III in unfolded form.

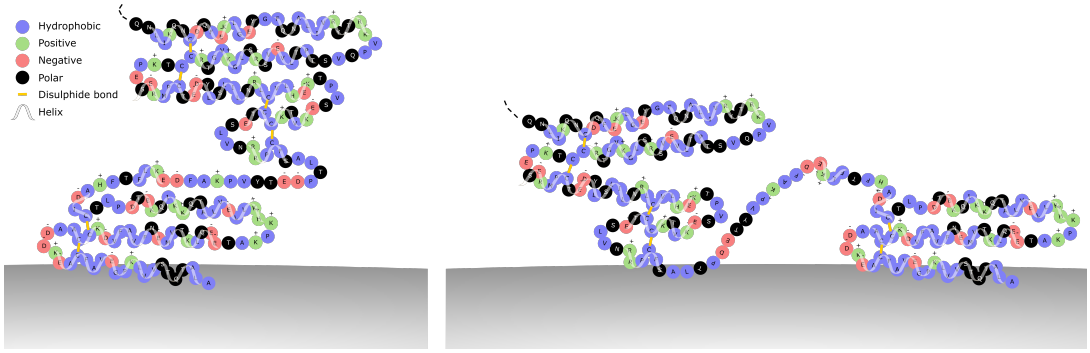

Figure 6.4.: Resulting arrangement at the air-water interface of domain III in globular shape (left) and unfolded shape (right).

6.2.2. BSA at air-water interfaces: Structure and function

Since proteins align along air-water interfaces according to hydrophilic and hydrophobic regions, the exact structure of the protein has a major influence on the stability of the foam. Not only the hydrophobicity of the proteins but also their flexibility play a key role in foam formation and stability [32, 387].
Furthermore, a multilayer of surface-active proteins provides higher foam stability than a monolayer. However, multilayer formation depends on the interaction of the proteins with each other, where the charge of the protein is particularly important. Engelhardt et al. [42] have reported that at the IEP of BSA solutions, multilayers of proteins form at an air-water interface, whereas at both alkaline and acidic pH, monolayers of proteins are found at the air-water interface.

In order to develop a descriptive model of this multilayer arrangement of several proteins at the air-water interface, energetically favorable interactions of BSA in its globular form with each other are considered. To do this, the charge and hydrophobicity of the amino acids on the protein surface are taken into account. The corresponding arrangement of two BSAs is shown in Figure 6.5.

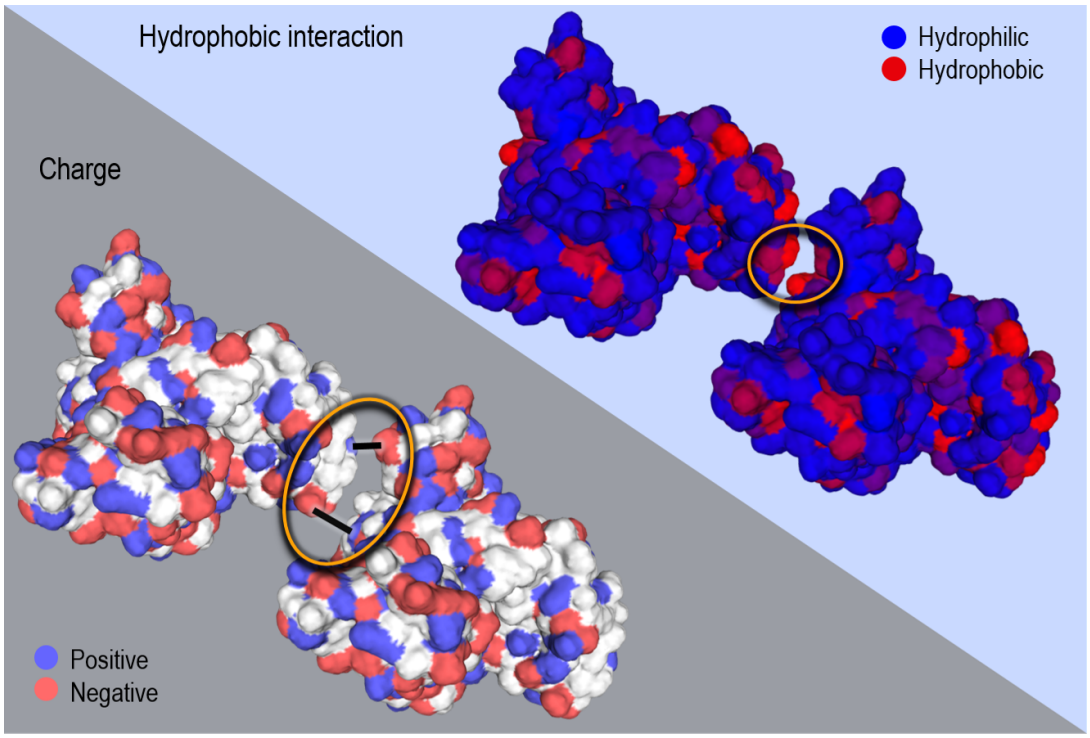

Figure 6.5.: Electrostatic and hydrophobic interactions of two BSAs and resulting energetically favorable arrangement by matching oppositely charged regions and hydrophobic interactions simultaneously.

In the N-form, the majority of surface amino acids are hydrophilic, which ensures water solubility. These hydrophilic amino acids can carry an electrical charge. [388] An examination of the charges on the surface amino acids reveals the presence of both positively and negatively charged amino acids. These amino acids not only interact with water, but can also interact with surface amino acids of other BSAs if they come into close proximity. At the IEP, when the total charge of the molecule is zero, two BSA can come into close proximity, and charged surface amino acids can interact locally. The oppositely charged amino acids of two BSAs attract each other. One potential example of electrostatic interaction is illustrated in Figure 6.5 on the left.
As mentioned earlier, the thermodynamic properties of the amino acids require the protein to arrange itself at the interface. A closer look at the conformation of the BSA protein at different pH values allows a better understanding of the interfacial properties and foam stability. In particular, in domain III there is a part with several hydrophobic

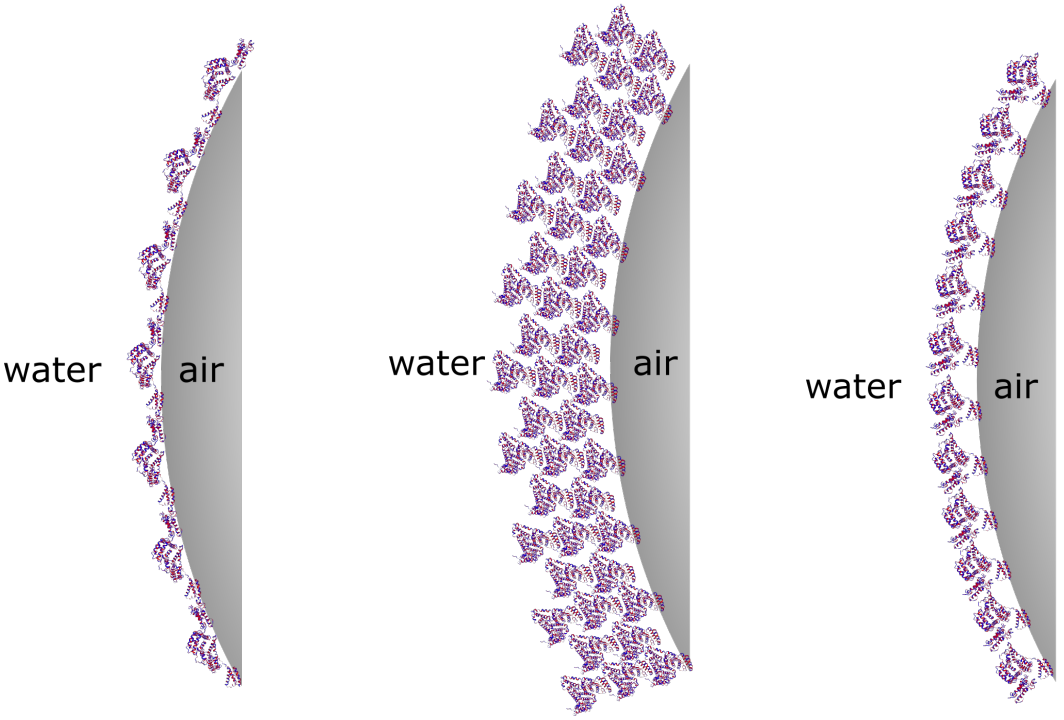

Figure 6.6.: Arrangement of BSA molecules at the air-water interface at different pH conditions: (a) Acidic environment, (b) IEP and (c) alkaline environment.

amino acids. In a foam, this part is likely to be exposed to the hydrophobic air [139, 141], turning BSA into a surface-active molecule [140, 389]. However, in the case of multilayer formation, there are more opportunities to hide hydrophobic parts of the protein from contact with water. This is because there are several parts of the BSA surface with hydrophobic amino acids. A possible arrangement of the hydrophobic interaction between two BSA molecules is shown in Figure 6.5 on the right.

Figure 6.6 shows a model of the arrangement of a number of BSA molecules at the air-water interface at an acidic pH, at the IEP and in an alkaline environment.

In acidic environments, BSA unfolds into the F-form and expands into the E-form [65]. The protein becomes more flexible and finds more possibilities to arrange its hydrophilic and hydrophobic amino acids at the air-water interface. However, due to the overall positive charge at acidic pH values below the IEP, BSA molecules repel each other. Therefore, some proteins are pushed into the liquid and contribute no longer to the surface activity. Consequently, a monolayer of BSA is formed around the air bubble. Figure 6.6a shows a model for such an arrangement.

As mentioned already, BSA proteins are shaped in the N-form at their IEP. Because of their neutral net charge, several BSA proteins interact with each other to form a

multilayer on the surface of the bubble, as local charges and hydrophobic interactions allow stacking, as shown in Figure 6.5. A model of the layers around bubbles in this arrangement is shown in Figure 6.6b.
An increase in pH above the IEP results in more negatively charged amino acids and a net negative charge on the BSA molecule. The negatively charged amino acids repel each other and cause the volume of a BSA molecule to increase, resulting in the B-form of BSA. The overall negative charge causes repulsion between the proteins. A monolayer is formed at the air-water interface, as shown in Figure 6.6c.
The multilayers surrounding the air bubbles are more resilient than the monolayers. Consequently, the interfacial film of BSA at the IEP is capable of stabilizing the bubbles in a superior way, thereby significantly reducing the coalescence rate and drainage. In addition, the formation of aggregates inside the lamellae can block drainage [390]. This results in an increased foam stability at the IEP compared to foams at high or low pH as reported by Engelhardt et al. [42], Zawala et al. [89] and Kim et al. [40].

6.3. Materials and methods

6.3.1. Sample preparation

BSA (A7030, heat shock fraction, protease free, fatty acid free, essentially globulin free, pH 7, $\geq 98\,\%$) was purchased from Sigma-Aldrich (Saint Louis, MO, USA) and was used as-received. If not indicated differently, solutions of 4 wt% BSA in ultrapure water (18.2 MΩ cm) were prepared. This protein concentration was chosen, because whipping requires a protein concentration of 3 % to 40 % [35] and because it resulted in smooth foams.
The pH was adjusted by adding either HCl or NaOH and pH values were measured with a SevenExcellence pH meter S400 with pH electrode InLab Micro Pro-ISM (Mettler-Toledo International Inc., Greifensee, Switzerland). Typical examples showing the pH range of food products are natural lemon juice (pH 2.39 reported by Yapo [391]) and albumen of henn eggs (Silversides et al. report pH values between 7.78 and 9.26 [392]). Based on these literature values and on the determination of the IEP, measurements were performed for BSA solutions at pH 3 (acidic), pH 5.1 (IEP), pH 7 (neutral) and pH 9 (basic).

6.3.2. Determination of the isoelectric point

To determine the isoelectric point (IEP) of BSA, the zeta potential of BSA solutions at pH 3, 4, 5, 6, 7, 8 and 9 was measured using a Malvern Zetasizer Nano-Z (Malvern Panalytical GmbH, Kassel, Germany).
For each of the pH values three identical samples were prepared and for every sample the zeta potential was measured five times. All measurements were performed at a temperature of 25 °C. Afterwards, mean values and standard deviations of the measured zeta potentials were calculated and plotted against pH. From the plot the point of zero zeta potential, i. e. the isoelectric point, was determined.

6.3.3. Measurement of solution viscosity

Solutions of concentrations of 0.1 wt% BSA and 4 wt% BSA at pH values of 3, 5.1, 7, and 9, respectively, were prepared as described in 6.3.1. For each concentration and each pH value three identical samples were prepared. The viscosity of each sample was measured at a temperature of 25 °C using a Lovis 2000 M microviscometer from Anton Paar (Anton Paar GmbH, Graz, Austria). These measurements were performed by a trained service technician inhouse.

6.3.4. Dynamic light scattering

Light scattering measurements have been performed on an ALV spectrometer consisting of a goniometer and an ALV-5004 multiple-tau full-digital correlator with 320 channels (ALV-Laser Vertriebsgesellschaft mbH, Langen, Germany), which allows measurements over an angular range of 30° to 150°. A He-Ne laser (wavelength of 632.8 nm) is used as the light source. For temperature controlled measurements, the light scattering instrument is equipped with a thermostat from Julabo (JULABO GmbH, Seelbach, Germany). Measurements were performed in triplicate at 20 °C at 9 angles ranging from 30° to 150°. DLS measurements were performed by a trained service technician inhouse. The raw data contains the lag time and the correlation, which contains the information about the intensity fluctuations. For analysis, a CONTIN fit [265–267] (regularized fit) was performed using the ALV-correlator software (version V.3.0.2.5) to fit the autocorrelation function and extract the hydrodynamic radii. As a result, the intensity over radius is obtained. The location of the peak represents the hydrodynamic radius of the particles and the width of the peak is a measure for the polydispersity. The (main) peak of the hydrodynamic radius was fitted with a logarithmic normal distribution using the programming language *Python* (Python Software Foundation, version 3.8.8). This procedure was performed for each angle. By plotting the obtained hydrodynamic radii over the angles and fitting with a linear function the hydrodynamic radius at 0° was extrapolated.

6.3.5. Foam formation

For foam formation a T 25 easy clean control ULTRA-TURRAX (IKA-Werke GmbH & Co. KG, Staufen, Germany) equipped with dispersion tool S 25 N - 10 G was used. 2 g of protein solution were dispersed at a speed of 20 000 rpm for 1 min. The glass vessel used for foaming the protein solution was a custom-built glass cylinder with overflow protection in the upper part as shown in Figure 6.7 (a). The inner diameter of the glass cylinder was 13.6 mm, the height of the cylinder without overflow protection was 65 mm and the total height of the glass vessel was 90 mm.

6.3.6. Foam stability and drainage

After preparing and foaming the protein solution, the glass vessel with the foam was placed in front of a LED Slimlite plano luminous plate (Kaiser Fototechnik, Buchen,

(a) (b) (c)

Figure 6.7.: (a) Glass vessel for foam formation. (b) Foam initially after foam formation. (c) Foam and liquid drainage after 30 min.

Germany), so that images could be taken of foams illuminated in transmission. A Canon EOS 7D camera with objective Canon Macro Lens EF 100mm 1:2.8 L IS USM and a Canon TC-80N36D remote release with timer function (Canon Inc. Headquarters, Tokyo, Japan) were used to take photos every 1 min for 30 min. Foam heights and liquid heights were measured from the images using ImageJ software (ImageJ 1.53v / Java 1.8.0_172 (64bit)). The foam height in the middle of the glass vessel is lower than at the outside. To find the bottom of the meniscus, the foam height was read where more light was transmitted by the foam. The measurement procedure was repeated for three identical samples and means were calculated. To provide uncertainties, standard deviations and a reading error of 2 mm for foam heights or 0.5 mm for liquid heights were combined.
An established method to characterize the stability of a foam is to measure the foam height immediately after foaming and after a certain time. The foam stability s_f is then calculated as follows [42, 44–48, 137]:

$$s_f = \frac{V_{f,t}}{V_{f,0}} \tag{6.1}$$

where $V_{f,t}$ is the foam volume at time t and $V_{f,0}$ is the foam volume at $t = 0$. Typical time intervals used are 5 min [42], 30 min [44–47] and 60 min [48]. Since the diameter of the glass vessel stayed constant, here the foam height is used instead of the foam volume to characterize the foam stability:

$$s_f = \frac{h_{f,t}}{h_{f,0}} \tag{6.2}$$

where $h_{f,t}$ is the mean height of the foam at time t and $h_{f,0}$ is the mean height of the foam at $t = 0$. This method to characterize foam stability was applied for better

comparison with literature. $t = 5\,\text{min}$ was chosen as described by Engelhardt et al. [42]. Additionally, the foam stability was calculated for $t = 30\,\text{min}$.
For a more detailed investigation of the foam stability, the temporal evolution of foam height and drainage was monitored over 30 min in 1 min intervals as described above. The measured heights were plotted on logarithmic and double logarithmic scales. For the foam heights, fitting with a linear function could be applied to the data plotted on double logarithmic scale. Therefore, foam heights on linear scales were fitted with power laws.

6.3.7. Bubble size

Samples were prepared and foamed as described in 6.3.1 and 6.3.5. Immediately after preparation 0.01 g of foam were transferred to a microscope slide using a microspoon and then covered with a cover slip. Three little pieces of teflon film with a thickness of 50 µm served as spacer between microscope slide and cover slip. Bright field light microscopy was performed in transmission using a Leica MS5 stereomicroscope (Leica Microsystems GmbH, Wetzlar, Germany) with 1.6-fold magnification. Microscope images were taken every 1 min for 30 min. Microscopy was performed for three identical samples. The obtained images were pre-processed in *Python* by applying gaussian blur filter (cv2.GaussianBlur, cv2 version 4.6.0), image subtraction (cv2.subtract (2 times)), kuwahara filter (pykuwahara 0.3.2), background subtraction (skimage.restoration.rolling_ball, skimage.restoration.ellipsoid_kernel, skimage version 0.18.1) and contrast enhancement (PIL.ImageEnhance.Contrast, PIL version 8.2.0). Subsequently, the images were segmented using *Cellpose* [299, 300] and the obtained masks were analyzed in *Python*. The temporal evolution of the mean equivalent bubble diameter and the mean bubble circularity were analyzed. Further information about this method are provided in Section 3.6.

6.4. Results and discussion

6.4.1. Isoelectric point

Figure 6.8 shows the measured zeta potentials of BSA solutions at different pH values. From the plot the isoelectric point (IEP) was determined as the point of zero zeta potential. This approach resulted in an IEP of 5.1, which is in agreement with literature values. Reported values for the IEP of BSA solutions are in the range of pH 4.2 to pH 5.5 [42, 83, 151–155].

6.4.2. Macroscopic foam stability – comparison with literature

Figure 6.9a displays the measured foam stabilities for solution concentrations of 4 wt% BSA at pH 3, 5.1, 7 and 9 calculated with equation 6.2. Foam stabilities were calculated for $t = 5\,\text{min}$ (filled circles) as described by Engelhardt et al. [42]. The foam

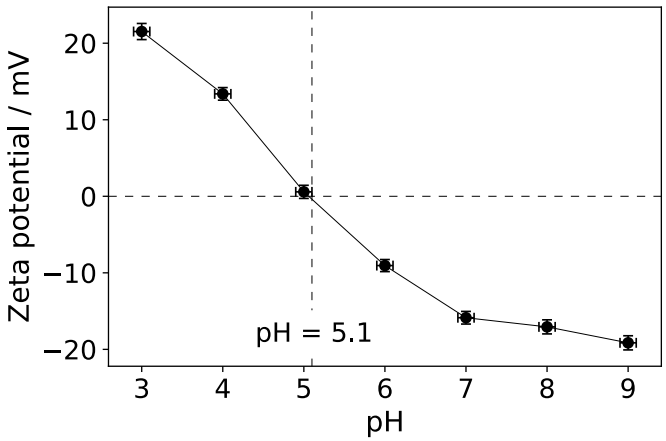

Figure 6.8.: Zeta potential of BSA solutions at different pH for determination of the IEP. Lines are a guide to the eye.

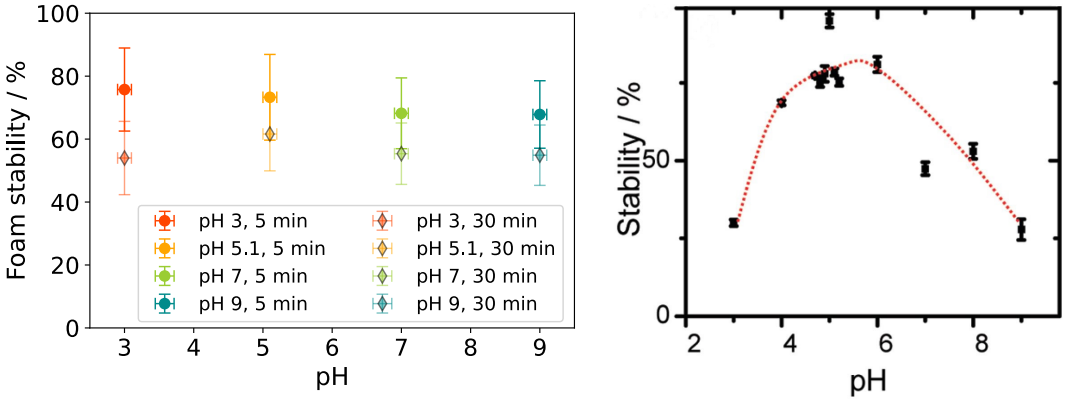

(a) This study.

(b) Determined by Engelhardt et al. Reprinted with permission from [42]. Copyright 2012 American Chemical Society.

Figure 6.9.: Macroscopic stability of BSA-stabilized foams at varying pH.

stability is slightly enhanced at low pH compared to higher pH values. However, the foam stabilities at the different pH values differ only by about 10 % from one another. Additionally, the foam stability was calculated by using the foam height after 30 min and relating it to the initial foam height (black diamond shape filled with color). This time range has been used in other publications for the calculation of the foam stability [44–47]. Here, the foam stability is slightly enhanced at the IEP and therefore the foam stabilities follow the expected trend of a most stable foam at the IEP. However, also the values obtained in this case show only small pH-dependent variations in the range of about 10 %.
In any case, the observed pH-dependence of the foam stability is considerably less pronounced than that described in the literature [40, 42, 89]. For comparison Figure 6.9b shows the result of Engelhardt et al. [42], where the foam stabilities vary by about 50 % and show a strong pH-dependence. It can thus be surmised that additional interactions must play a role. In order to gain further insight, the bulk was characterized by measuring the hydrodynamic radius of the molecules / aggregates in solution as well as the dynamic viscosity of the solution.

6.4.3. Dynamic light scattering

The hydrodynamic radii of polymers in solution or particles in suspension can be determined from dynamic light scattering experiments. The hydrodynamic radius, designated as R_h, is distributed according to a log-normal probability distribution. The median μ^* and the mode m_{mode} of this distribution were determined as shown in Figure 6.10. As can be seen from the figure, the hydrodynamic radius is about 6 to 9 times larger at the IEP than at the other pH values (depending on whether median or mode are considered). This indicates that the BSA molecules are aggregated at the IEP. Aggregates typically exhibit a more extensive size distribution (greater polydispersity) than that observed for single molecules, due to the potential for variation in the number of molecules present within the aggregate. As a measure for the width of the distribution the interval of confidence $[\mu^*/\sigma^*, \mu^* \cdot \sigma^*]$ is used, which is shown by the colored error bars in Figure 6.10. This interval is significantly larger at the IEP than at lower or higher pH values, which underlines the assumption of aggregate formation at the IEP. More information about the extraction of the presented quantities are provided in Appendix D.9. Given the zero net charge of the proteins at the IEP and the possibilities for interactions between two BSA molecules (cf. Figure 6.5) it can be concluded that aggregates are formed at the IEP in the bulk. Engelhardt et al. [42] have reported multilayer formation at the air-water interface for BSA at its IEP. These findings lead to the assumption that the molecules attract each other and a multilayer formation as discussed in Section 6.2 is likely. At pH values lower or higher than the IEP the measured hydrodynamic radii are much smaller and the interval of confidence is quite narrow. Therefore, it can be concluded that monomers are present at low or high pH. As discussed in Section 6.2, BSA carries a net charge at pH values different from the IEP and therefore these molecules repel each other. For these reasons, monolayer formation is expected at the air-water interface as was

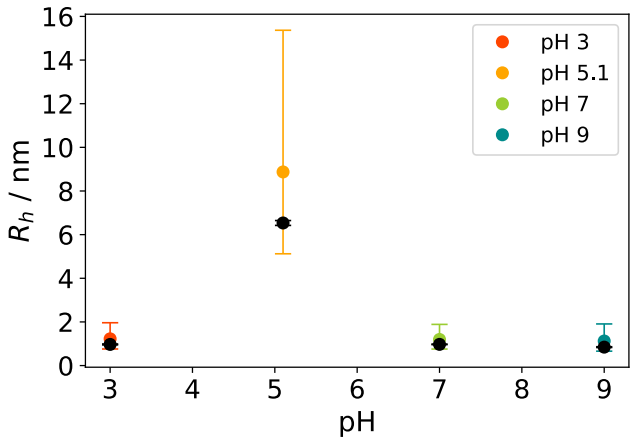

Figure 6.10.: Hydrodynamic radius R_h of BSA at different pH. Colored circles show the median $\bar{\mu}^*$ and black circles the mode $\bar{m}_{mode}$. The large error bars signify the interval of confidence (68.3 %).

also reported by Engelhardt et al. [42].

6.4.4. Solution viscosity

In light of the crucial role played by solution viscosity in the context of liquid foams, it is evident that this parameter exerts a profound influence on the flow behavior of the liquid phase, which in turn affects the mobility and rising of bubbles, the coalescence, and the drainage of liquid from the foam. These processes affect the stability of the foam. [90, 107, 210, 238, 239, 390]

The dynamic viscosities of solutions at concentrations of 0.1 wt% BSA and 4 wt% BSA, respectively, at pH 3, pH 5.1, pH 7, and pH 9 are displayed in Figure 6.11. For all pH values the dynamic viscosities of samples of 4 wt% BSA are higher than the dynamic viscosities of samples of 0.1 wt% BSA. It is also noteworthy that the dynamic viscosity of the solution in question is subject to alteration in accordance with the pH level. At pH 3, the highest dynamic viscosity is recorded. Conversely, the lowest dynamic viscosity is observed at the IEP. At pH levels above the IEP, the dynamic viscosity increases as the pH of the solution rises. This effect, although present at both concentrations, is much more pronounced at 4 wt% BSA.

Since the charge of the BSA molecule changes with varying pH, the behavior of the viscosity at different pH values can be explained by electroviscous effects [91, 236], which are caused by electrical charges on the molecule surface. The diffuse double layer of charges around the molecule causes a resistance to the flow of the liquid (primary effect). Furthermore, the intermolecular repulsion between double layers (secondary effect) and interparticle repulsions which affect the shape of the molecule (tertiary effect) contribute to the flow resistance.[91] The additional flow resistance caused by the electroviscous effect increases the viscosity.

Because of the molecular net charge of BSA, the viscosity of the solution increases at pH values different from the IEP [233]. When considering how the viscosity rises from the IEP to pH 7 to pH 9, the charge dependence of the dynamic viscosity is effectively demonstrated by the measurement. Furthermore, also the volume increase of the BSA molecule when undergoing conformational changes at low or high pH values contributes to an increase in solution viscosity [65, 236] (see also Subsection 2.4.2). Unfortunately, the crystal structure for high pH was not reported in the literature. However, the significant viscosity differences suggest that the conformation of BSA at high pH has a less extended shape than the E-form at low pH. In addition, the absolute value of the zeta potential is slightly larger at pH 3 than at pH 9 (cf. Figure 6.8), which denotes a higher absolute value of the net charge at pH 3 than at high pH and explains, together with size differences for different conformations, the viscosity differences between pH 3 on the one hand and pH 7 and 9 on the other hand.

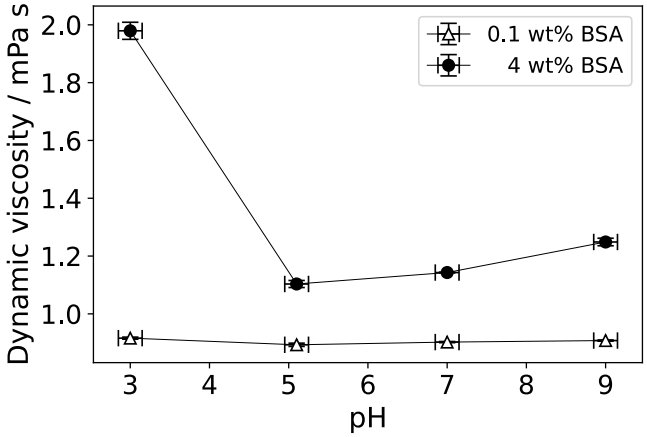

Figure 6.11.: pH-dependent viscosity of BSA solutions at concentrations of 0.1 wt% BSA and 4 wt% BSA. Lines are a guide to the eye.

This finding is in accordance with literature, since Yadav et al. [91] found the same course of the pH-dependency for the relative viscosity of BSA solutions with a concentration of $40\,\mathrm{g\,L^{-1}}$ (which is about the same concentration as used in the current study).

6.4.5. Foam height

To investigate the foam stability in more detail the temporal evolution of the foam height was monitored. In order to ascertain the formula that best describes the decay of the foam, the measured data was plotted in both logarithmic and double logarithmic forms. An exponential decay function can be represented by a linear function, if the ordinate is plotted logarithmically. Conversely, a power law decay is represented by a linear function, if both the ordinate and abscissa are plotted logarithmically. For this reason, decadic logarithms of the measured heights and the time were calculated

and plotted. Afterwards, the data in double logarithmic plots was fitted with a linear function

$$y = mx + n \tag{6.3}$$

where m is the slope of the linear function and n is the intersection with the y-axis. Furthermore, $y = \log_{10}(h_f/\mathrm{mm})$ represents the decadic logarithm of the foam height and $x = \log_{10}(t'/\mathrm{min})$ represents the decadic logarithm of the time $t' = t + 1\,\mathrm{min}$. Figure 6.12 shows the logarithmic as well as double logarithmic representation of the measured foam height over time for foams with 4 wt% BSA at different pH. The diagrams show that the measurement data is better represented by a linear fit in double logarithmic representation, which suggests a power law decay of the foam.
For pH 7 and 9, a slight inflection is observed after about 5 min. This inflection may be attributed to a general pattern of short- and long-term behavior. At the beginning, the foam is still wet, the lamellae are still of considerable thickness, and liquid drains at a faster rate from the foam. This results in a faster reduction of the foam height (a steeper slope). This effect is more pronounced at pH 7 and 9, because on the one hand the liquid has a lower dynamic viscosity in these cases than at pH 3 and on the other hand the interface is stabilized by a protein monolayer instead of the multilayer formed at pH 5.1.
The first value deviates most from the linear fit. This value might contain a higher uncertainty, since the foam is denser at the beginning and therefore appears darker. Furthermore, at the first data point a small amount of foam might still flow down from the walls of the glass vessel, which would mean that the first value should actually be higher than measured. However, at later times the meniscus is lower and the foam becomes less dense, which makes reading the meniscus more difficult and therefore also influences the accuracy of foam height determination. To enhance the accuracy of the measurements, these could be repeated with a considerably larger sample volume (if available) in a wider vessel and with a brighter light source.
Additionally, foam heights were plotted in a linear plot. To minimize the errors on the fit parameters the normalized foam height $h_{f,t'}/h_{f,0}$ was plotted over time, where $h_{f,t'}$ is the foam height at time t' and $h_{f,0}$ is the foam height at time $t = 0$ ($t' = 1\,\mathrm{min}$). In this case the measured data can be fitted by a power law function with only one fit parameter which is the exponent c

$$\frac{h_{f,t'}}{h_{f,0}} = t'^{-c} \tag{6.4}$$

where t' is the time shifted by 1 min ($t' = t + 1\,\mathrm{min}$).
Figure 6.13 shows the normalized foam heights of BSA foams at pH 3, pH 5.1, pH 7 and pH 9. Only small differences in the normalized foam heights are observed. The foam at the IEP retains the highest normalized height after 30 min which indicates a slightly higher foam stability at the isoelectric point. This behavior is also reflected in the decay constant c. At pH 5.1 it is with $c_{pH5.1} = 0.151 \pm 0.002$ lower, whereas the decay constants at pH 3, pH 7 and pH 9 vary between 0.173 and 0.185.
The enhanced foam stability at the IEP is strongly associated with the molecular

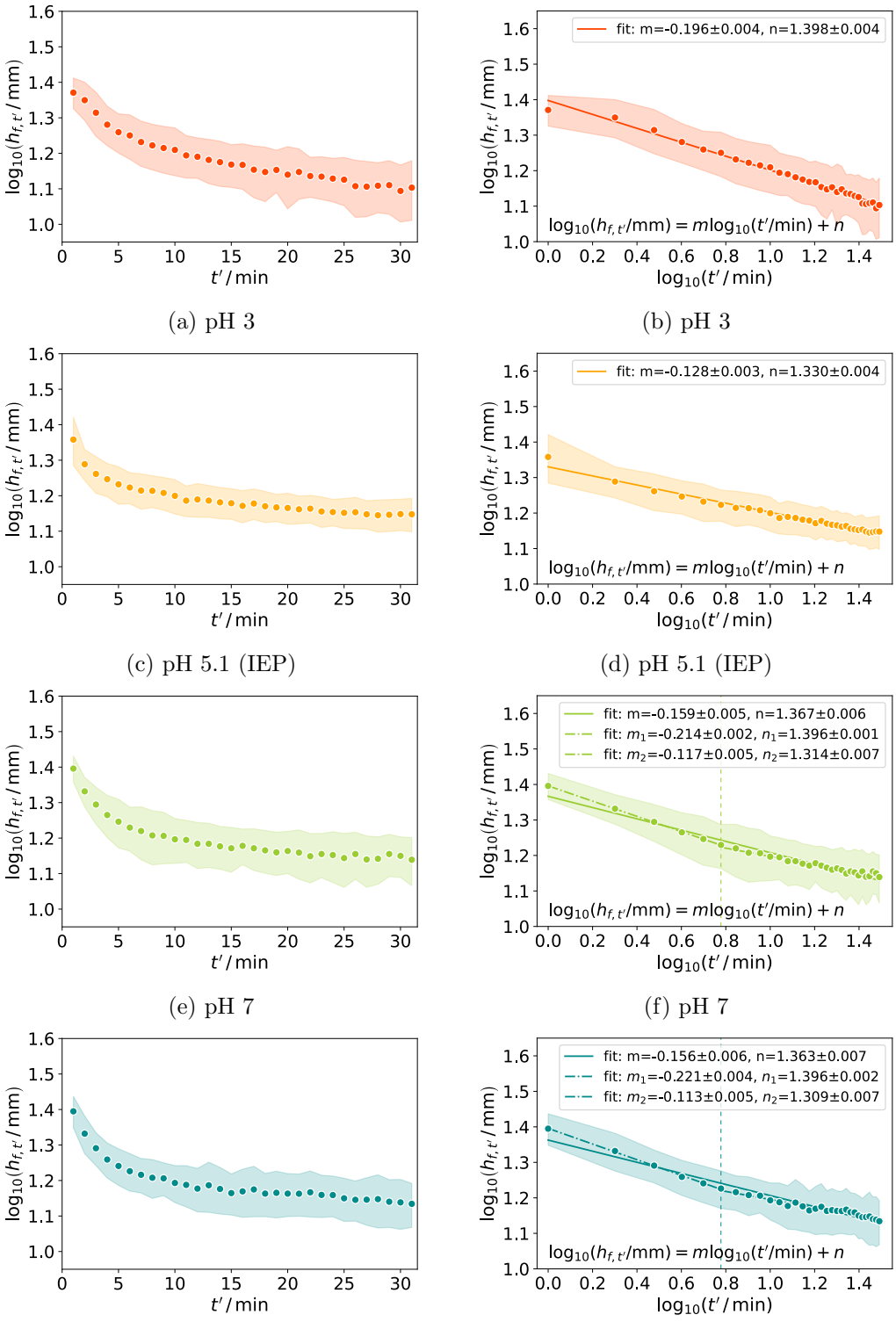

(a) pH 3 (b) pH 3

(c) pH 5.1 (IEP) (d) pH 5.1 (IEP)

(e) pH 7 (f) pH 7

(g) pH 9 (h) pH 9

Figure 6.12.: Logarithmic (left) and double logarithmic (right) representation of the foam height over time of BSA-stabilized foams (4 wt%) at different pH.

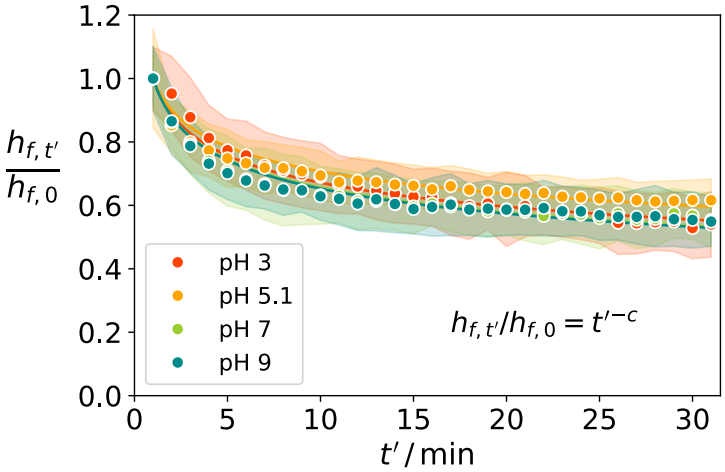

(a) Normalized foam height.

pH	c
3	0.173 ± 0.002
5.1	0.151 ± 0.002
7	0.183 ± 0.002
9	0.185 ± 0.003

(b) Fit parameters.

Figure 6.13.: Normalized foam height over time for BSA foams at pH 3, pH 5.1, pH 7 and pH 9.

arrangement of BSA at the air-water interfaces. At the IEP, multilayers are formed, which stabilize the interfaces leading to more stable foams, especially at longer times. On the other hand, also the viscosity influences the foam stability [390]. Since the dynamic viscosity at low and high pH values is enhanced due to electroviscous effects, these foams show only slightly lower normalized foam heights. At pH 3, the highest dynamic viscosity is found and the decay constant is higher than at the IEP but lower than at high pH. At pH 7 and 9, the dynamic viscosity is lower than at pH 3 (but higher than at the IEP) and the decay constants are larger than at pH 3 and 5.1, which means that the foams at high pH are less stable. While the viscosity increase significantly affects the foam stability at low and high pH, also under these conditions the molecular arrangement at the interface plays a central role in stabilizing the foam: although the solution viscosity at pH 9 is higher than at pH 7, the decay constants of the foam height are similar. The magnitude of the protein net charge is lower for BSA molecules at pH 7, which allows for a closer arrangement at the interface and an increased interfacial stability in comparison to that at pH 9. This demonstrates that regarding foam stability the different conformation and interfacial arrangement at pH 7 compensates for its lower dynamic viscosity in comparison to pH 9.

The foam ability or foaming capacity (shown in Figure 6.14) is given by the foam height at $t = 0$, immediately after foam formation [17, 42]. This value is slightly lower for foams at pH 5.1 than at higher or lower pH. The foaming capacity is dependent on the molecular properties of the protein such as its size, structure and charge [119]. The more flexible BSA conformations present at either a high or a low pH are capable of migrating and arranging themselves at the air-water interface with greater alacrity. This enables them to reduce the surface tension faster, thereby enhancing the foaming

capacity [393]. Higher viscosities on the other hand, yield smaller bubbles, where less

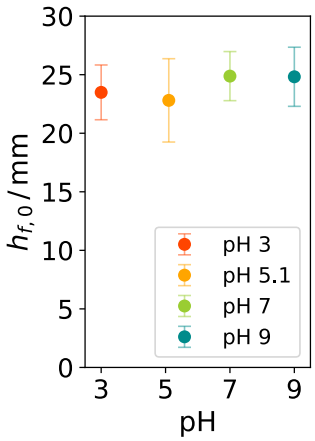

Figure 6.14.: Foaming capacity of BSA solutions at different pH.

air is incorporated in the foam [383–385]. This leads to a slightly lower foaming capacity at pH 3 than at pH 7 and pH 9.

6.4.6. Drainage

In examining the process of foam deterioration, consideration must be given not only to the change in foam height, but also to the amount of liquid drained from the foam [394]. The liquid drains through the Plateau borders due to gravity and capillary suction, which has significant influence on the foam stability [32, 112]. Proteins, which are not arranged at the bubble surfaces, flow with the draining liquid to the bottom, thereby decreasing the number of proteins available in the foam.
Figure 6.15 shows the temporal evolution of the liquid heights of the BSA foams at varying pH values. The liquid height rises over time as more and more liquid drains from the foam due to gravity. In the first about 5 min the rate of drainage is much higher than later on for all investigated foams. Two drainage regimes with a fast drainage in the beginning of their measurements and a slower drainage in the later course were also observed by Lamolinairie et al. [23], though for foams stabilized by surfactants. Directly after foam formation, the foams contain a high liquid content. These wet foams show thick lamellae. In this state, the drainage depends mostly on the solution viscosity and is therefore initially lowest for the foams at pH 3, where the bulk viscosity is highest.
Overall, the foams at pH 7 and pH 9 show an increased drainage as compared to foams at pH 3 and pH 5.1. In addition, more liquid drains from the foams at pH 7 than from the foams at pH 9 initially. The disparate liquid heights observed at pH values of 3, 7, and 9 can be attributed to the varying viscosities. The elevated viscosity at pH 3 results in reduced drainage. The lower viscosity observed at pH 9 results in enhanced drainage, while the even lower viscosity at pH 7 gives rise to significantly elevated

drainage.
At early times, the drainage of the foams at pH 5.1 is higher than that of the foams at pH 3. However, from about 6 min, these show almost identical liquid heights. At later times, there is less liquid in the foam. Consequently, the lamellae are thinner and the interfacial molecular arrangement, which is more resilient at the IEP, becomes more important. Proteins arranged at the bubble surfaces retain liquid in the foam, because proteins are able to bind water [395, 396]. For this reason, the formation of BSA multilayers not only increases the stability of the interfacial films, but also contributes to a lower drainage. This effect is relevant for the foam at the IEP especially at later times.

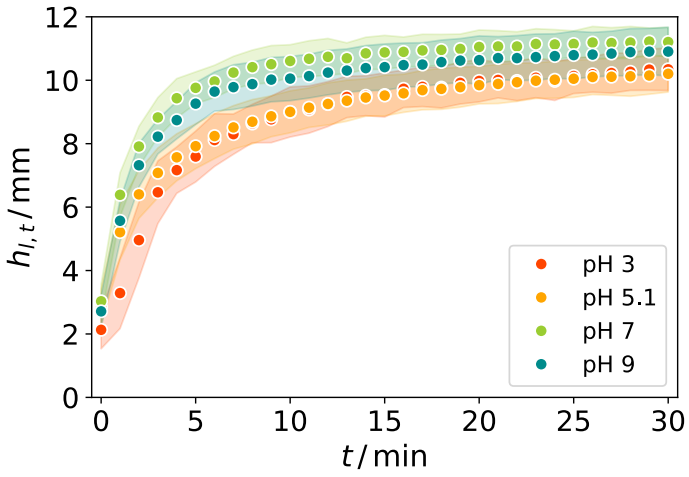

Figure 6.15.: Temporal evolution of the drainage (liquid height $h_{l,t}$) for BSA foams at pH 3, pH 5.1, pH 7 and pH 9.

6.4.7. Height of liquid in foam and height of gas in foam

The height of liquid in foam h_{lif} can be calculated from the height of liquid before foam formation h_b and the liquid height h_l (height of the liquid that is already drained) by

$$h_{lif} = h_b - h_l \tag{6.5}$$

The temporal evolution of the height of liquid in foam is shown in Figure 6.16.
The height of liquid in foam decreases with time as liquid drains from the foam. The decay follows a power law. The exponent c is lowest for foams at pH 5.1 for BSA, which means that the foams at the IEP retain more liquid than at different pH values. This observation is in agreement with the discussion above about the drainage. Upon multilayer formation at the IEP, the foam remains wetter, because more proteins remain in the foam and these attract and bind water molecules at their hydrophilic parts. The exponents of the power law decay are highest for foams at pH 7, followed by pH 9 and then pH 3. It can be concluded that the drainage of the solution is

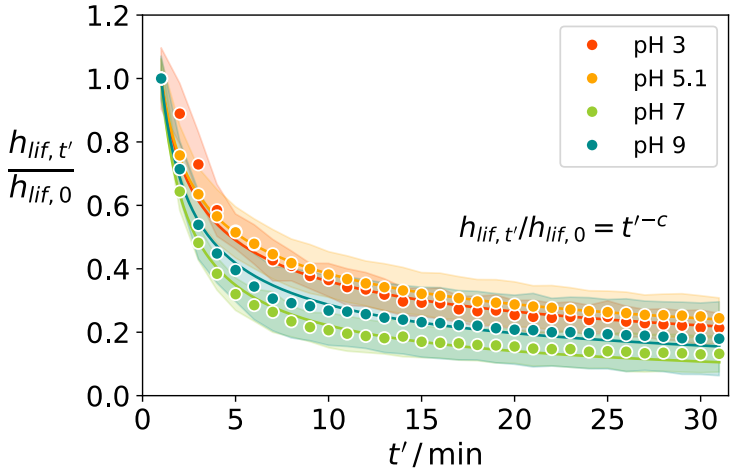

(a) Normalized height of liquid in foam.

pH	c
3	0.443 ± 0.005
5.1	0.415 ± 0.001
7	0.655 ± 0.007
9	0.542 ± 0.006

(b) Fit parameters.

Figure 6.16.: Normalized height of liquid in foam over time for BSA foams at pH 3, pH 5.1, pH 7 and pH 9.

dependent on the viscosity of the solution, which is highest for a pH of 3 and lowest for a pH of 7.
Additionally, the height of gas in foam h_{gif} can be determined from the foam height h_f and the height of liquid in foam h_{lif} by

$$h_{gif} = h_f - h_{lif} \tag{6.6}$$

The temporal evolution of the height of gas in foam is shown in Figure 6.17.
The capacity of the foam to incorporate gas is reflected in the initial height of gas in foam. It depends on several factors such as the solution viscosity, the protein structure and its diffusion rate to the interface, the protein film structure, elasticity and surface tension [13, 14, 384, 385]. This value is highest at pH 7 followed by pH 9. The foams at pH 3 and 5.1 show almost identical initial heights of gas in foam. For the foams different than the IEP this means, that solutions with higher viscosity can incorporate less air than solutions with lower viscosity. Indeed, a higher solution viscosity leads to smaller bubble sizes during foam formation and less incorporated air as was reported by De Preval et al. [383] and by Politova et al. [384]. The elongated BSA conformations at these pH values are more flexible and stabilize the interface faster but not as efficient on the long term as at the IEP. At the IEP however, the compact BSA globules are not as flexible and therefore do not stabilize the air-water interfaces as efficient during foam formation. The high shear forces during foam formation impede multilayer formation. As a result, less air is initially incorporated in the foam. This observation is in agreement with the observed lower initial foam height. The temporal evolution of the height of the gas in foam represents the capacity of the foam to retain gas in the foam. Once the multilayer has been formed, the interfacial arrangement of BSA

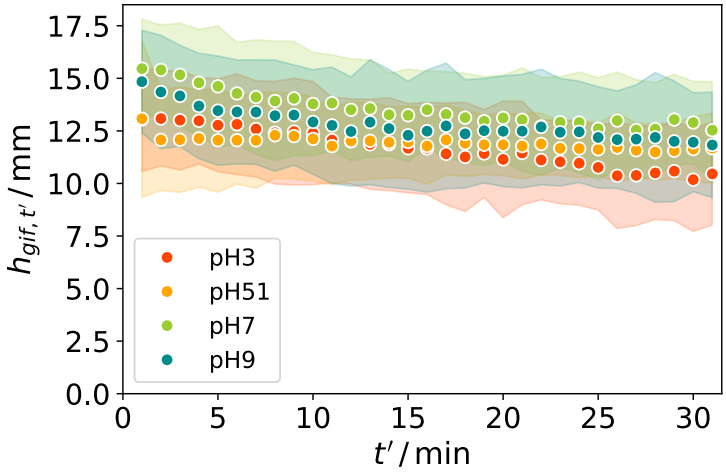

Figure 6.17.: Height of gas in foam over time for BSA foams at pH 3, pH 5.1, pH 7 and pH 9.

in foams at the IEP becomes more stable, which results in reduced bubble coarsening and a lower rate of air escape from the foam. This is reflected in the more constant height of gas in foam at the IEP.

6.4.8. Bubble size

On mesoscopic scales, foams are determined by their structure of air bubbles and liquid lamellae. Figure 6.18 shows microscope images of BSA-stabilized foams at varying pH. These microscope images demonstrate, that the BSA-stabilized foams at the IEP start with larger bubbles and show a more homogeneous bubble size distribution. Furthermore, the bubble shape is more polyhedral and starts earlier to be polyhedral than in case of the other foams. The lamellae between the bubbles are thicker at the IEP over the whole measurement range. The formation of protein multilayers at the air-water interfaces keeps the lamellae wet and stabilizes the bubbles.
The growth of the mean bubble diameter is a relevant measure of foam stability [25, 34, 55]. To gain inside into the foam stability at a mesoscopic level, bubble size growth over time was studied. Figure 6.19 shows the logarithmic and double logarithmic representation of the temporal evolution of the bubble size data. This data follows a linear trend on double logarithmic scales. A power law increase of the mean bubble size has also been reported for SDS (sodium dodecyl sulfate), soap and shaving foams [397–399]. Indeed, the BSA foam data is best represented by two linear fits, which means that a short-term and a long-term behavior is observed. The first term is defined by the first approximately 5 min. The short- and long-term behavior is more pronounced for the foams at pH 3, 7 and 9 than at the IEP. In the early time regime, the foams at pH 3 and 5.1 show similar slopes ((0.300 ± 0.006) and (0.299 ± 0.002)), whereas the slope at pH 9 is larger (0.352 ± 0.007) and for pH 7 even larger (0.403 ± 0.006). This

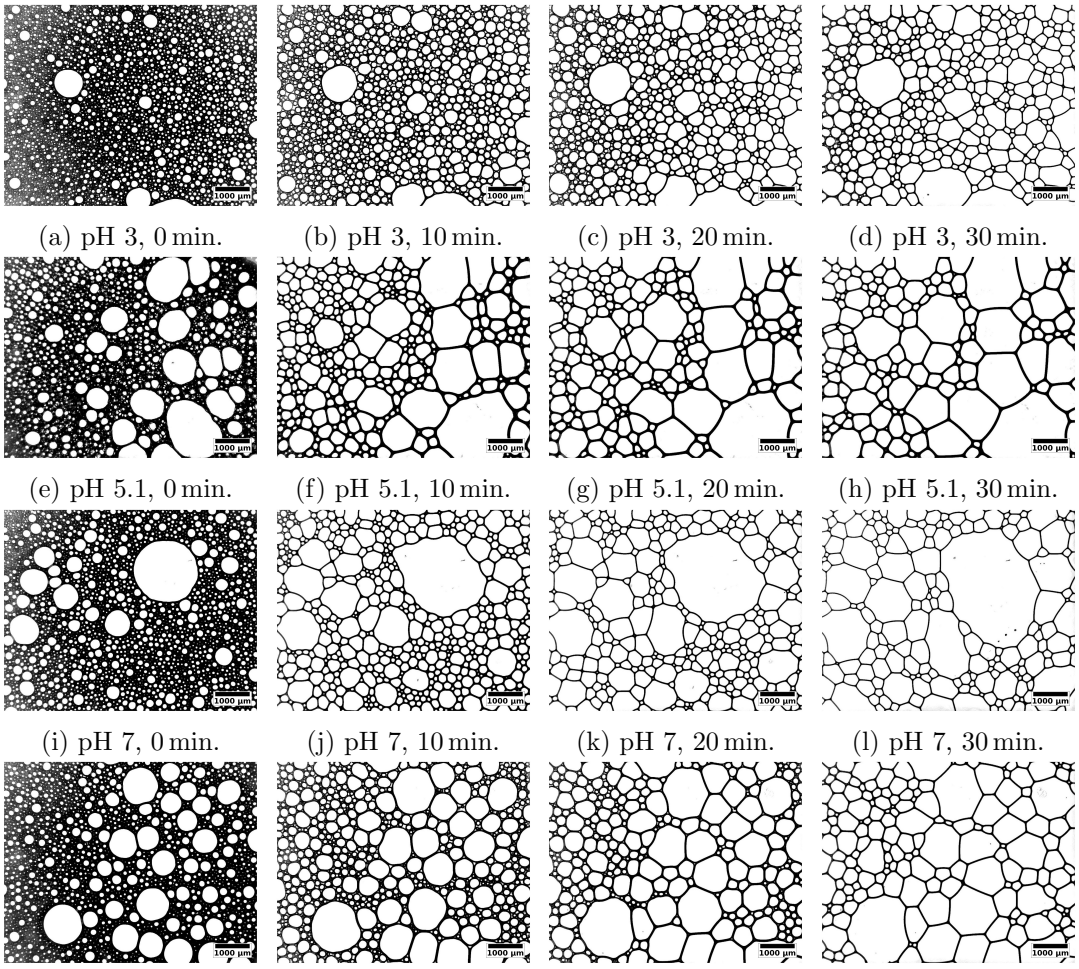

(a) pH 3, 0 min. (b) pH 3, 10 min. (c) pH 3, 20 min. (d) pH 3, 30 min.

(e) pH 5.1, 0 min. (f) pH 5.1, 10 min. (g) pH 5.1, 20 min. (h) pH 5.1, 30 min.

(i) pH 7, 0 min. (j) pH 7, 10 min. (k) pH 7, 20 min. (l) pH 7, 30 min.

(m) pH 9, 0 min. (n) pH 9, 10 min. (o) pH 9, 20 min. (p) pH 9, 30 min.

Figure 6.18.: Microscope images of BSA-stabilized foams at pH 3 (first row), pH 5.1 (second row), pH 7 (third row) and pH 9 (last row). Time proceeds from left to right.

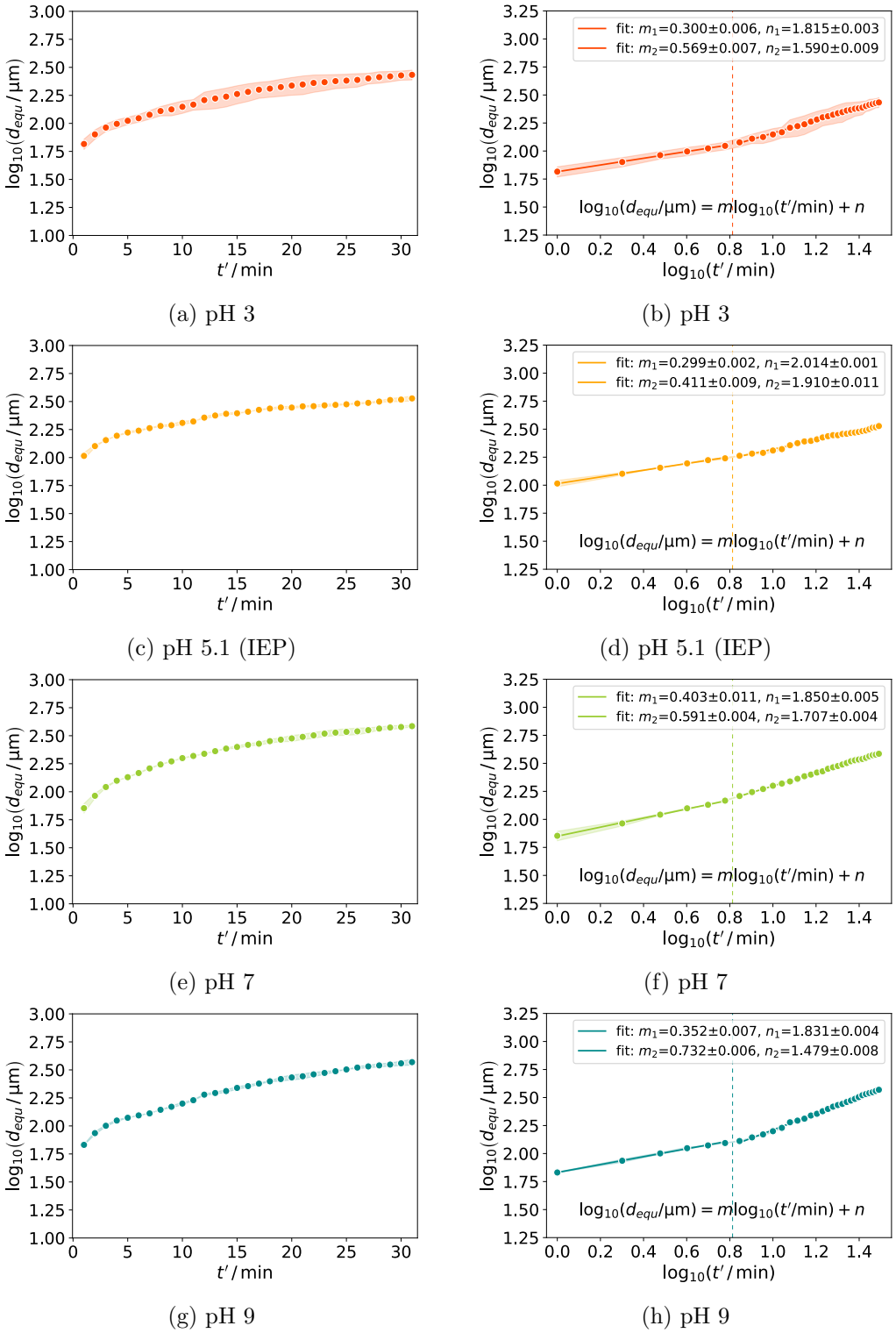

(a) pH 3 (b) pH 3

(c) pH 5.1 (IEP) (d) pH 5.1 (IEP)

(e) pH 7 (f) pH 7

(g) pH 9 (h) pH 9

Figure 6.19.: Logarithmic (left) and double logarithmic (right) representation of the mean equivalent bubble diameter over time of BSA-stabilized foams (4 wt%) at different pH.

means that the foam with the highest dynamic solution viscosity (pH 3) has a similar growth rate as the foam at the IEP. At a pH different than the IEP the bubbles grow faster for lower dynamic viscosities. In the second time regime, the bubble growth is slowest at the IEP and faster for pH 3, pH 7 and pH 9, which suggests that the foam at pH 5.1 is the most stable foam on the long term.
Figure 6.20 shows the temporal evolution of the mean equivalent bubble diameter. In

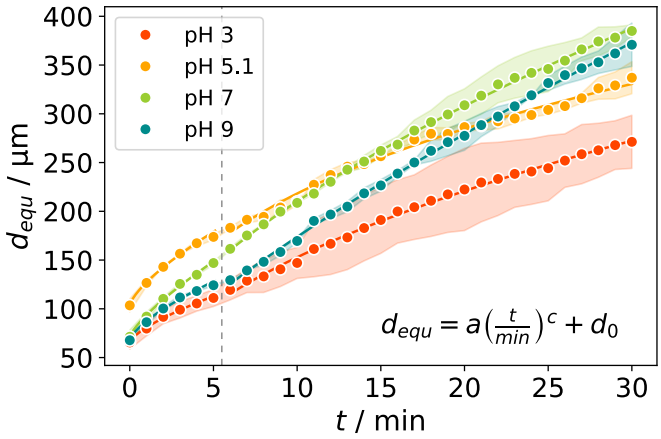

(a) Mean equivalent bubble diameter.

pH	a / µm	c	d_0 / µm
3	15.6 ± 1.6	0.69 ± 0.07	65.3 ± 1.3
	57.3 ± 14.8	0.48 ± 0.05	-19.8 ± 23.3
5.1	23.9 ± 1.0	0.72 ± 0.03	103.4 ± 0.9
	129.5 ± 74.1	0.32 ± 0.10	-50.7 ± 93.5
7	22.6 ± 2.6	0.77 ± 0.08	71.0 ± 2.2
	46.4 ± 6.8	0.61 ± 0.03	22.8 ± 13.2
9	19.9 ± 2.1	0.69 ± 0.07	67.6 ± 1.7
	24.3 ± 3.5	0.78 ± 0.04	27.1 ± 9.4

(b) Fit parameters.

Figure 6.20.: Temporal evolution of the mean equivalent bubble diameter for BSA-stabilized foams at pH 3, pH 5.1, pH 7 and pH 9. For each pH value the first line provides the fit parameters for the early time regime and the second line the fit parameters for the later time regime.

order to fit power laws to linear scales, an additional fit parameter, d_0, was employed for describing the initial bubble size. The data was fitted with two different power law exponents for each pH. At pH 5.1 the initial bubble size is largest with about 100 µm. In this case, the BSA conformation is less flexible and therefore has less options to arrange at the air-water interfaces. Multilayer formation is suppressed during foam

formation by the application of high shear rates. This leads to a less robust initial arrangement and larger initial bubble sizes. Also, at this pH the dynamic viscosity of the solution is lower, which supports the formation of larger bubbles during foam formation. However, multilayer formation stabilizes the bubbles well on the long term and therefore leads to a slower bubble growth, which is reflected in the lowest power law exponent in the second fit ($c = 0.32 \pm 0.10$).
The foams at pH 3, 7 and 9 start with significantly smaller bubble sizes of about 65 µm to 70 µm. Initially and especially after 5 min the bubble size is largest at pH 7, followed by pH 9 and smallest at pH 3. This means that the initial bubble size depends on the dynamic viscosity of the solution and also that bubbles grow faster in foams with lower solution viscosity. In this time regime the bubbles are still spherical (compare microscope images in Figure 6.18) and the foams are still wet. In this case, the foam stability is dominated by the drainage, which depends on the solution viscosity. In the second time regime ($t \geq 6$ min), the bubbles of foams at pH 7 and 9 grow faster than those at pH 3. At pH 7 and 9 more liquid drained from the foam (cf. Figure 6.15). Therefore, less proteins are available in the foam for providing interfacial stability. The steeper slope at pH 9 compared to pH 7 in the second time regime can be explained by the stronger net charge of the molecules, which complicates the arrangement at the interface due to mutual repulsion. At later time scales the molecular arrangement becomes more relevant, since less liquid is in the foam. The foam at pH 3 is still wetter (cf. Figure 6.15) and therefore the high solution viscosity still contributes to the foam stability more sognificantly. Furthermore, the viscosity also influences the surface tension [400–403] and therefore the bubble stability. Overall, the foams at pH 3 retain the smallest bubble sizes over the whole measurement range, although the power law exponent of the second time regime is higher at pH 3 than at pH 5.1. This indicates that the bubbles in the foam at the IEP exhibit the slowest growth over time in the second time regime, which suggests the formation of a more stable foam at the IEP. This conclusion aligns with the findings of the previous investigation of the foam height measurements (cf. Figure 6.13).

6.4.9. Circularity

Figure 6.21 shows the circularity of the investigated foams. The curve of the circularity is least steep for the foams at the IEP and these foams start with significantly lower circularity than the foams at higher or lower pH. This corresponds to the more polyhedral shape and the fact that bubbles start to look polyhedral earlier in time, as was observed in the microscope images shown in Figure 6.18. The foams at pH 5.1 showed larger bubbles from the beginning. In general, larger bubbles are more likely to exhibit shapes that deviate from a sphere. The gradual decline in bubble circularity over time indicates that the shape of the bubble remains relatively stable. At the IEP, the air-water interfaces in the foam are well-stabilized by the protein multilayer. This results in a reduction in shape changes over time.
At pH values that differ from the IEP, the initial bubble shape is spherical. Over time, the highest circularity is found for foams at pH 3, which also exhibit a rounder

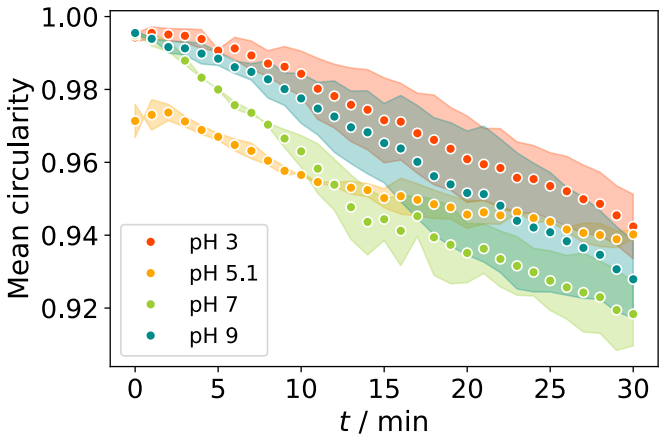

Figure 6.21.: Temporal evolution of the mean circularity

shape in the microscope images. With decreasing viscosity the bubble shape becomes increasingly non-spherical over time. In general, it can be stated that the interfacial molecular configuration and the dynamic viscosity of the solution both exert an influence on the evolution of the bubble shape.

6.5. Conclusions

Investigating the stability of BSA-stabilized foams with a concentration of 4 wt% at varying pH revealed the presence of an additional mechanism, since these did not show the strongly pH-dependent behavior to the same extent as expected on basis of examinations described in literature [40, 42, 89]. Due to its pH-dependent conformational changes, a more effective arrangement of BSA is assumed at the IEP, where the formation of multilayers has been reported [42]. Indeed, DLS data reveals the formation of aggregates at the IEP, which supports the presence of multilayers. In addition, the slower bubble size growth at a lower bubble circularity indicates an improved molecular stabilization of the air bubbles in the foam at the IEP. Nevertheless, foams at pH 3 demonstrate analogous drainage and diminutive bubble sizes. This can be attributed to the markedly elevated dynamic viscosity observed in solutions at pH 3 in comparison to the IEP. The substantial viscosity of the liquid impedes drainage and suppresses bubble growth, thereby reinforcing the stability of the foam.

At low protein concentrations comparable to those used by Engelhardt et al. [42], Zawala et al. [89] and Kim et al. [40], the pH-dependent changes of the dynamic viscosity are visible but their effects on foam stability are negligible compared to the differences caused by the formation of multilayers (IEP) versus monolayers (high and low pH). At such low BSA concentrations the foam stability is dominated by conformational changes of BSA. At pH values different than the IEP, the molecules become more flexible and exhibit a net charge, which leads to inter-protein repulsion.

The surface tension is higher than at the IEP [56]. The less effective arrangement of BSA molecules at the air-water interfaces results in a reduction of the stabilization of the bubbles. At the IEP, the net charge of BSA is neutral and the formation of a multilayer of proteins at the air-water interface stabilizes the bubbles in the foam.
At higher BSA concentrations, the influence of electroviscous effects increases and reaches a significant contribution. The strong repulsion between charged BSA enhances the viscosity of the solution, which visibly influences the foam stability. Since the dynamic solution viscosity is lowest at the IEP and increases at higher or lower pH values, it influences the foam stability in an opposite way compared to the effects caused by conformational changes and molecular arrangements of BSA. For this reason, the foam stability becomes less pH-dependent.
Two time regimes are observed: for the foam heights and even more clearly for the temporal evolution of the mean equivalent bubble diameter. The early time regime is dominated by the solution viscosity, since the foams are wet and the drainage is strong (cf. Figure 6.15). At later times, molecular arrangements at the air-water interfaces become more important and dominate the foam stability. The two time regimes seem to be more pronounced for foams at a pH value different than the IEP. At later times, the bubbles grow faster in foams at a pH value different from the IEP than at the IEP. This suggests that the multilayer arrangement at the IEP is indeed more stable and leads to an increased foam stability at the IEP.
The investigated model system effectively demonstrates that foam stability is a function of the interplay between protein interactions and their arrangement at the air-water interface, as well as the dynamic viscosity of the solution. Although the dynamic viscosity is lowest at the IEP, the foams are still most stable, because the efficient molecular multilayer arrangement stabilizes the interfaces well and impedes coarsening. The resulting slower bubble size growth leads to a slower decay of the foam.

7. Systematic oat drink formulations and their foam stability

This chapter explores an application of a protein-stabized foam in an everyday food system: oat drink foam. Two master theses were involved in the topic: Jana Reeh focused on developing a formulation of an organic barista oat drink [404], whereas Antonia-Louisa Schlichting investigated the foam properties of this oat drink [405]. The project idea was developed and most measurements were performed by the students, who were supervised by Prof. Thomas A. Vilgis and myself. The analysis and visualization of the data presented here was performed by myself. In addition, two articles published in industry journals originate from this project [406, 407].

Contributions
Judith Krom: Data curation, formal analysis, investigation, project administration, software, supervision, visualization, writing - original draft, writing - review & editing. **Jana Reeh:** Conceptualization, data curation, investigation, methodology, project administration, validation. **Antonia-Louisa Schlichting:** Conceptualization, data curation, investigation, methodology, project administration, validation. **Thomas A. Vilgis:** Conceptualization, methodology, project administration, resources, supervision, writing - review & editing.

7.1. Introduction

In recent years, many consumers have become more aware of their ecological footprint and this has increased the demand for plant-based foods and drinks. At the same time, oat drink has become a popular milk alternative and consumption of oat beverages is expected to continue to increase in the coming years [408]. From a sustainability perspective, the regional cultivation of oats contributes to the trend-setting success of oat drinks [409]. Lower climate impacts compared to cow's milk also make dairy-free alternatives attractive [410, 411]. In addition, oats contain a unique nutritional composition of amino acids, fatty acids, vitamins and minerals as well as a high fiber content and are suitable for most people with gluten-free diets [200, 201, 412–414].
This chapter aims for a more profound physical understanding of purely oat-based pasteurized drinks. The physical function of proteins, starch, and other polymers like β-glucans [415] define most of the textural and sensory properties [416]. Depending on the variety, oats contain 9.70 - 17.30 % protein, 27.30 - 50.01 % starch, and about 13.66 - 30.17 % fiber [198]. Compared to other cereals, the fiber content in oats is high and in particular it contains 2.70 - 3.50 % [198] / 3.9 - 5.7 % β-glucan [417]. In

general, oats do not store enough fat (5.20 - 12.40 % [198]) to produce a fullbodied mouthfeel comparable to that of cow's milk when mixed with water. So it is beneficial, if vegetable oils are added.
Technological aspects involve two main points: First, the oat drink requires pasteurization to meet food safety standards, which leads to gelatinization of the starch [418] and denaturation of some protein components [200, 419, 420]. Both of these provide for a strong increase in viscosity. Second, soaking ground oats in water produces a mucilaginous mouthfeel, mainly due to the presence of β-glucan and other non-starch polysaccharides [421]. In addition to these structural aspects, plant-based drinks usually show a slightly bitter taste, are astringent and have, compared to cow's milk, too little sweetness.
Many popular coffee specialties such as cappuccino, latte macchiato or flat white require a creamy, smooth and stable milk foam. A direct comparison of the foam properties of plant-based drinks with those of cow's milk shows that the foaming capacity (initial foam volume) was lower for milk than for plant-based products (oat and pea drink). However, the foams of the plant-based milk alternatives are less stable and show more coarsening than milk foams. [2] Specially produced "oat drink barista editions" convince with good foam properties. However, they often contain additives such as acidity regulators, thickeners, or other emulsifying proteins (e.g. soy protein). Macroscopic foam properties such as foaming capacity and foam stability are based on the interfacial activity of the emulsifiers at the air-water interfaces and the viscosity of the aqueous phase within the foam lamellae. In oats, mainly interfacially active proteins are suitable emulsifiers, while starch and polysaccharides determine the viscosity. Compared to proteins found in cow's milk or in other cereals, nuts or legumes such as soy, oat proteins show poorer foaming properties [422, 423]. The proteins in oats consist of 50 - 80 % [200] / 70 - 80 % of globulins, 4 - 14 % of prolamins, 1 - 12 % of albumins, and < 10 % of glutelins [201]. Predominant storage proteins are 12S globulins [200]. Relevant for foamability are primarily albumins and avenins (prolamins in oats), which may contribute to interfacial stability due to their structure [419].
The present study investigated how it is possible to formulate a purely oat-based pasteurized beverage with acceptable foaming properties, adjusting the palatability with canola oil. From a physical point of view, it is necessary to understand the individual process steps on a macroscopic and molecular level.
Achieving these goals requires enzymatic treatments at several levels. α-amylase counteracts starch gelatinization during pasteurization and thereby lowers the viscosity of the oat drink, because it cleaves the α-1,4 glycosidic bonds of starch molecules [424]. Also Deswal et al. [416, 425] used α-amylase to liquefy oat starch and reduce viscosity during heat treatment. In a second step, we used glucoamylase for further reduction of the viscosity and saccharification of the oat starch leading to a certain sweetness of the oat drink. Additionally to α-1,4 glycosidic bonds glucoamylase hydrolyzes also the α-1,6 glycosidic bonds at the branching points of amylopectin [426]. Furthermore, the enzymatic treatment with β-glucanase, cellulase and pentosanase prevents an unpleasant slimy mouthfeel triggered by water-soluble fibers β-glucan, cellulose and pentosan. Also Patra et al. [427] used β-glucanase to lower the viscosity of oat

drinks.
The second applied enzyme preparation contained also a protease. Proteases hydrolyze peptide bonds in proteins [428]. Since oat proteins are the relevant surface-active molecules in the regarded system, proteases significantly impact the foam properties. Treatment with the protease trypsin reduces the foam stability, but may improve foaming capacity [429, 430].
Furthermore, also heat treatment (pasteurization) may cause a denaturation of proteins and therefore is considered in this regard. Moreover, the impact of the addition of canola oil on foaming capacity and foam stability was investigated.
The described approach defines the roadmap of this chapter which is illustrated in Figure 7.1.

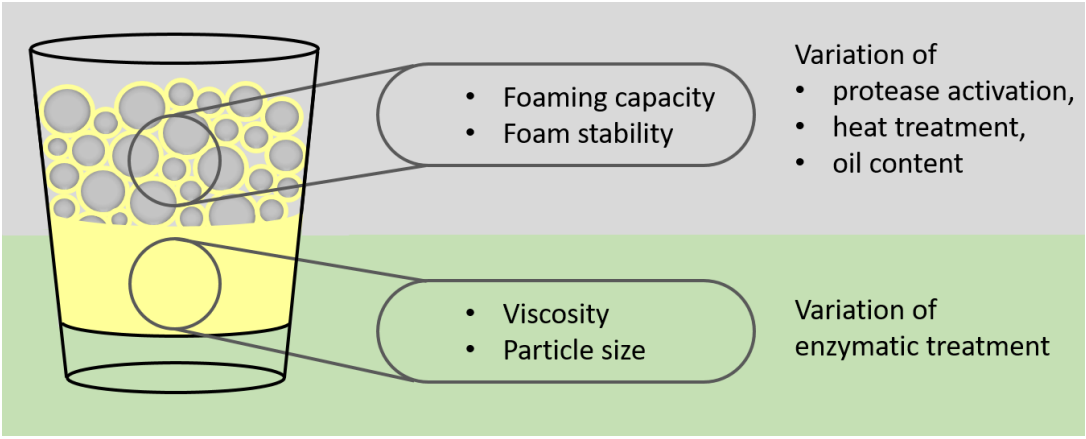

Figure 7.1.: Visualization of the chapter outline.

Table 7.1 summarizes the abbreviations used in this chapter. Details of the sample preparations are given in the following.

7.2. Materials and methods

7.2.1. Materials

Dehusked oats from Davert (Midsona Deutschland GmbH, Ascheberg, Germany) were purchased from a local organic grocery store. These oats originate from German, controlled organic cultivation. For all samples tap water (18-20 °dH, hardness range "hard", 3.21 mmol L^{-1} to 3.57 mmol L^{-1} calcium carbonate, 2.1 mg L^{-1} nitrate) was used.
Three different enzyme preparations (C. Schliessmann Kellerei-Chemie GmbH & Co.KG, Schwäbisch Hall, Germany) were applied. Enzyme preparation 1 (EP1) facilitates the liquefaction of the gelatinized starch and reduces the viscosity of the sample significantly. According to the manufacturer, it was obtained from *Bacillus subtilis* and contains an α-amylase, which is optimally effective at temperatures be-

Abbreviation/ Sample name	Explanation
EP1	Enzyme preparation 1 (α-amylase)
EP2	Enzyme preparation 2 (glucoamylase, α-amylase, protease)
EP3	Enzyme preparation 3 (β-glucanase, cellulase, pentosanase)
S1	Treatment with EP1 only
S2	Treatment with EP1 and EP2
S3	Treatment with EP1, EP2, and EP3
S3Oi	Treatment with EP1, EP2, and EP3, addition of canola oil and salt*
Pa	Protease active
Pap	Protease active, pasteurization
Pi	Protease inactive
Pip	Protease inactive, pasteurization*
Oi0	No addition of canola oil
Oi1	1 % canola oil
Oi2	2 % canola oil*
Oi3	3 % canola oil

*Standard sample

Table 7.1.: Abbreviations.

tween 65 °C and 75 °C. Enzyme preparation 2 (EP2) is derived from *Aspergillus niger* and serves the enzymatic saccharification of the previously liquefied starch. It contains glucoamylase, α-amylase, and proteases. The glucoamylase of microbial origin, which dominates the enzymatic activity, is optimally effective at temperatures between 35 °C and 55 °C. Enzyme preparation 3 (EP3) counteracts the formation of mucilage caused by heating due to the high fiber content in oats. It contains β-glucanase, hemicellulases and pentosanases from *Trichoderma ssp.* as its main enzymatic activity as well as xylanase and arabanase acting as secondary activity. EP3 acts most effectively at a temperature range of 40 °C to 70 °C. The concentrations of each enzyme preparation used in the investigations were selected on the basis of preliminary tests and were guided by the manufacturer's specifications.
In the end, Rapso gently pressed canola oil (VOG AG, Linz, Austria) and Erntesegen natural untreated rock salt without anti-caking agent or iodine addition (Hügli Nahrungsmittel GmbH, Radolfzell, Germany) were added to the oat drink.

7.2.2. Sample preparation – oat drink formulation

Starch gelatinization

60 g of oats were finely ground with 490 mL of tap water in a Thermomix (Vorwerk Deutschland Stiftung & Co. KG, Wuppertal, Germany) at speed level 9 for 2.5 min. The duration was chosen to ensure that the sample temperature did not increase too

much. Subsequently, the mixture was filtered through a 50 µm analytical sieve and stored in a refrigerator at 6 °C until measurement.

Enzymatic liquefaction of the starch

60 g of oats were finely ground with 490 mL of tap water in a Thermomix at speed level 9 for 10 min. On a magnetic stirrer the sample was heated to 70 °C while constantly stirring at a speed of 1200 rpm. 10 µL of EP1 were added and allowed to act at constant temperature (70 °C) for 90 min. Afterwards, the heating plate was turned off and the sample was stirred for another 10 min. The sample was then filtered through a 50 µm analytical sieve and subsequently heated to 95-105 °C for 10 s to deactivate the enzymes. To compensate for the evaporated water, tap water was added until a sample weight of 450 g was reached. The sample was then divided into two 225 g samples and each of these samples was homogenized with a T 25 easy clean control ULTRA-TURRAX equipped with S25 EC - T - C - 18G ST dispersion tool (IKA-Werke GmbH & Co. KG, Staufen, Germany) at 20 000 rpm for 8 min. The mixture was stored in a refrigerator at 6 °C until measurement.

Enzymatic saccharification of the starch

To study the influence of starch saccharificaton, samples were prepared as described above for starch liquefaction. In addition, 45 min after EP1 was added, 50 µL of EP2 were added and allowed to act for another 45 min at maximum 70 °C before switching off heating.

Enzymatic cleavage of non-starch polysaccharides

To study the influence of the cleavage of β-glucan, cellulose and pentosans, samples were prepared as described above for starch saccharification. In addition, after treatment with EP1 and EP2 and after heating was switched off for 5 min, 10 µL of EP3 were added and allowed to react for another 5 min before filtration.

Addition of oil and salt

Samples were prepared as described above. Additionally, before homogenization 2 % canola oil and 0.1 g salt were added. By homogenization the canola oil was finely dispersed. During experimentation, processing and application no creaming of the canola oil was observed.

7.2.3. Sample preparation – investigation of foam properties

Standard samples were prepared with all three enzymatic treatments as well as addition of 2 % canola oil and 0.1 g salt. In the figures showing measurement results, the standard sample is always marked in red. To investigate the impact of the proteases contained in EP2, the pasteurization, and the canola oil content, the following variations were performed.

Variations in the preparation of oat drink

Influence of protease and heat treatment: Here, the temperature during treatment with EP2 was varied to either activate or inactivate the proteases. Additionally, samples with (sample Pa) and without (sample Pi) protease treatment were each investigated with (samples Pap, Pip) and without (samples Pa, Pi) pasteurization (heating to 95 - 105 °C for 10 s). Proteases are active at 35 °C to 60 °C [431]. To activate the proteases, sample Pa was held at 50 °C during treatment with EP2. In sample Pi, the proteases were inactivated by heating the sample to 70 °C during treatment with EP2.
Influence of oil addition: Additionally to the standard sample described above, which contains 2 % of canola oil, oat drink samples containing no canola oil, 1 % of canola oil and 3 % of canola oil were prepared. For these samples the particular percentage of oil was added instead of the 2 % canola oil mentioned in 7.2.2.

Frothing of oat drink

For foam formation, a commercial milk frother MMF-234-V2 (Dirk Rossmann GmbH, Burgwedel, Germany) was used. Therein, the oat drink sample was simultaneously heated and foamed with the aid of a rotating pin. For all foaming tests a 85 g sample was foamed. Before foam formation, the oat drink samples had an average temperature of 13.6 °C. The foaming process took approximately 1 min and the samples were on average heated to 72.9 °C.

7.2.4. Particle size analysis

Sample preparation – starch gelatinization

Samples were prepared as described in Subsection 7.2.2 for starch gelatinization. After mixing, the temperature of the sample was maximum 35 °C. In contrast to the description in 7.2.2 only 50 g of the mixture were filtered through a 50 µm analytical sieve and stored in the refrigerator until measurement. The remaining 500 g were heated under constant stirring at a speed of 1200 rpm. At a temperature of 70 °C, 50 g were taken, filtered through a 50 µm test sieve and stored in the refrigerator until measurement. At a temperature of 90 °C, the remaining sample was filtered through a 50 µm test sieve and stored in the refrigerator until measurement.

Sample preparation – enzymatic treatment

All residual samples subjected to enzymatic treatment were prepared as described above in Subsection 7.2.2 for enzymatic liquefaction of the starch, enzymatic saccharification of the starch, enzymatic cleavage of the β-glucan, and addition of oil and salt.

Procedure

A Laser Diffraction Particle Size Analyzer LS 13 320 (Beckman Coulter, Inc., Brea, California) was used to determine the sizes of the particles in the samples. With this method it is possible to measure particle sizes in a range of 0.040 µm to 2000 µm. The refractive indices used for particle size calculation were 1.332 for the continuous phase and 1.4 for the disperse phase. Before each measurement, a calibration was performed, which included degassing, background measurement, equalization, and sample chamber adjustment. Each measurement itself consisted of three runs at 10 % obscuration. Nevertheless, each sample was measured three times. Afterwards, mean values as well as the corresponding standard deviations were calculated and plotted using the programming language *Python* (Python Software Foundation, version 3.8.8). Each measurement showed several peaks at different size classes of particle sizes representing different ingredients of the multi-component system of the oat drink. In order to obtain the width of each peak of the particle size distribution, the peaks were fitted using a superposition of probability density functions of the log-normal distribution, and geometrical standard deviations were calculated. More information on the fitting are provided in the supplementary information E.1

7.2.5. Viscosity measurement

A Discovery HR-3 rheometer (TA Instruments, New Castle, Delaware) was used for all rheological measurements.

Starch gelatinization

The sample was prepared as described in 7.2.2. For measuring starch gelatinization a cup-vane geometry was chosen and the measurement was performed in rotation. The vane length was 42 mm and the vane rotor had a diameter of 28 mm while the measuring cup had a diameter of 30.4 mm. A temperature ramp at a shear rate of $200\,\mathrm{s}^{-1}$ was measured [432]. Here, the temperature first increased from 25 °C to 90 °C and then decreased again to 25 °C with a rate of $3\,\mathrm{K\,min}^{-1}$. The dynamic viscosity was measured every 30 s. The temperature ramp was measured only once to visualize the effect of gelatinization.

Measurements of the samples after enzymatic treatment

Samples were prepared as described in Subsection 7.2.2 for enzymatic starch liquefaction, starch saccharification, β-glucan cleavage, and addition of oil and salt. For measuring the dynamic viscosity after each step of enzymatic treatment, flow sweeps were performed using a concentric cylinder geometry as measuring system. The DIN rotor had a diameter of 28 mm and a length of 42 mm whereas the measuring cup had a diameter of 30.4 mm. The temperature during the measurements was 25 °C. After filling the measuring cup, the samples were allowed to rest for 300 s. Measurements were performed in rotation, with the shear rate increasing from $0.01\,\mathrm{s}^{-1}$ to

631 s^{-1} and then decreasing again to 0.01 s^{-1}. The shear rate increased respectively decreased every 30 s. For analysis the values measured for decreasing shear rates were used as they showed less fluctuations. The flow sweep measurements were performed in triplicate. Afterwards, mean values as well as the corresponding standard deviation were calculated and plotted.

7.2.6. Optical microscopy

Sample preparation

Optical microscopy of the oat drink was performed for samples of the final formulation to check the emulsification of the canola oil. Therefore, samples were prepared as described above (cf. Subsection 7.2.2) one day and microscopy was performed the next day. Furthermore, to characterize the microstructure of oat drink foams, optical microscopy was performed of foamed samples prepared according to Subsection 7.2.3 and viewed directly after frothing.

Procedure

A droplet of oat drink sample or a spatula tip of foam sample was placed on a microscope slide and covered with a cover slip. Subsequently, the sample was viewed using an Axio Scope.A1 light microscope (Carl Zeiss AG, Oberkochen, Germany) in transmission bright field mode and images were taken using objectives with 10-, 20-, 40-, or 100-fold magnification, respectively.

7.2.7. Camera photos of foam

To investigate a larger section of the foam structures, images were taken with a Canon EOS 7D (Canon Inc., Tokio, Japan) digital camera. The camera was mounted on a repro stand RS 2 XA (Kaiser Fototechnik, Buchen, Germany) and had the same distance to the specimen for all exposures. The specimens were placed on a LED Slimlite plano luminous plate (Kaiser Fototechnik, Buchen, Germany), so that images could be taken of foams illuminated in transmission and the foam structures were clearly visible.

7.2.8. Foam height measurement

The foaming capacity as well as the foam stability were measured with the same method based on the "cylinder pour test" by Vundla and Torline ([41] as cited in [5]), who investigated the foam decay rate and stability of beer foams. The experiments were performed in a measuring cylinder with a nominal volume of 250:2 mL. The tall design according to DIN EN ISO 4788 has a height of 31.1 cm and a diameter of 3.5 cm. The foamed sample was filled into the measuring cylinder directly after foam formation. The total height of foam and drained liquid (total height) as well as the height of drained liquid (liquid height) were measured. Subsequently, the foam height,

which results from the difference between the total height and the liquid height, was calculated. Height measurements were performed after 0 min, 1 min, 3 min, 5 min, 7 min, 10 min and 15 min. The foam heights at time $t = 0$ determine the foaming capacity. The time-dependent foam heights were used to determine the foam stability. The heights were measured for three identical samples and then mean values and standard deviations were calculated.
To investigate the foam stability, the measured foam heights were plotted over time. To find out whether an exponential or a power law decay was shown by the sample, the foam heights were plotted logarithmically as well as double logarithmically. These plots are provided in the supplementary information E.2. Afterwards, the different samples of one series were plotted in one plot with linear axis in order to compare the samples with each other. Furthermore, the data were fitted with power law functions:

$$h_{f,t'}/h_{f,0} = t'^{-c} \tag{7.1}$$

where $h_{f,t'}$ is the foam height at time t', $h_{f,0}$ is the initial foam height at $t = 0$, t' represents the time shifted by 1 min, and c corresponds to the exponent of the power law. Note, that for fitting the data with a power law function, the time was shifted by 1 min, thus $t' = t + 1$.

7.2.9. Sensory tests

After each processing step, the taste, texture and mouthfeel of the oat drink were examined and described by sensory tests. Furthermore, for the foamed samples of different oil contents (no addition of oil, 1 %, 2 % and 3 % canola oil added) the taste of the canola oil as well as the texture respectively mouthfeel of the foam were tested. The in-house testing was carried out by Jana Reeh and Antonia Schlichting, both certified sensory managers. For this purpose, a simple descriptive test was carried out and no statistical evaluation was performed.

7.2.10. Overview

Figure 7.2 summarizes the applied treatments during oat drink preparation and the main methods of measurement.

7.3. Results and discussion

7.3.1. Application of enzymatic treatment

Viscosity of the oat drink

Before enzymatic treatment the flavor of the oat drink is perceived as green, herbal and raw and the texture is inhomogeneous, watery and sandy. Furthermore, the consistency of the oat drink after pasteurization is rather pudding-like and therefore the viscosity is too high for an oat drink.

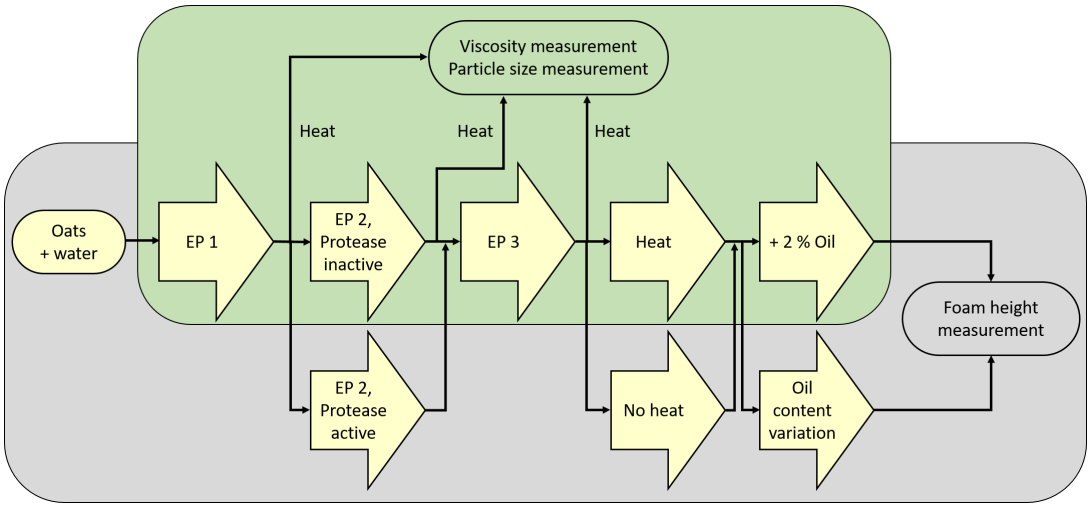

Figure 7.2.: Visualization of applied treatment steps and investigations.

The effects of oat starch gelatinization are known from various studies. Gelatinization temperatures of native oat starch have been reported to be in the range of 53 °C to 63 °C ([433–437] as cited in [438]) and onset gelatinization temperatures of different oat cultivars have been reported in the range of 44.7 °C to 47.3 °C [435]. Therefore, here only a single rheological measurement for verification was performed. Figure 7.3 shows the measured viscosity increase of the sample of ground oats in water at rising temperature due to starch gelatinization. From 25 °C to a temperature of 55.5 °C, the

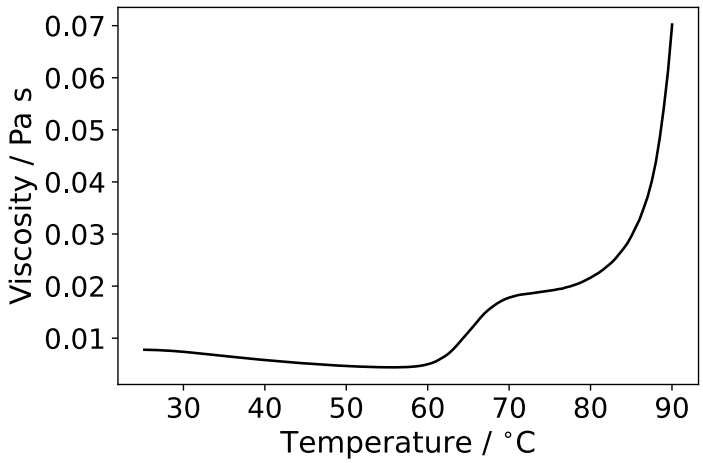

Figure 7.3.: Dynamic viscosity of an oat drink preparation without enzymatic treatment as a function of temperature. Single measurement.

dynamic viscosity decreased slightly from 0.0078 Pa s to 0.0044 Pa s. At temperatures above 55.5 °C, the dynamic viscosity significantly increased up to about 70 °C and

then leveled off up to about 80 °C. Subsequently, the dynamic viscosity rose steeply again until it reached 0.0702 Pa s at the final temperature of 90 °C. The increase of the viscosity in steps corresponds to the melting and swelling of oat starch known from literature: Depending on the cultivar and breeds, oat starches show two (or three) gelatinization temperatures [439]. The relatively diluted oat drink preparations do not form pastes in the usual sense. The concentration of amylose and amylopectins are lower than their overlap concentrations and the increase of viscosity needs to be adressed to the water uptake of starch granules due to the conformational changes of amylose and amylopectin [440].
After treatment with EP1 samples heated to 100 °C for pasteurization show lower viscosity but still remain relatively viscous and the oat drink has a mushy, slimy consistency. The flavor of the oat drink is green and herbal. The texture is inhomogeneous, gelatinous and pasty.
To investigate the viscosity changes caused by the different enzyme preparations, flow sweep measurements were performed after each step of enzymatic treatment. The results of the flow sweeps are represented in Figure 7.4.
All measured samples showed a shear-thinning behavior, as the measured dynamic viscosity decreased with increasing shear rate. The shear-thinning effect was most pronounced in the sample treated with EP1 only. This can be explained by the orientation of proteins, amyloses and non-starch polysaccharides in the shear direction. Topological constraints such as entanglements are less to be expected [441–443].
This shear-thinning effect shows to be reversible, because when the shear rate decreased, the flow resistance increased again. This means that no destructive structural changes are evoked by the shearing and supports the aforementioned interpretation.
Subfigure 7.4a shows the viscosities in dependence of the shear rate in double logarithmic representation. When comparing the viscosities of the samples it stands out that the sample treated with EP1 shows the highest viscosity among enzymatically treated samples. Its viscosity at low shear rates ((5.816 ± 1.321) Pa s at $0.1\,\mathrm{s}^{-1}$) is two orders of magnitude higher than for the samples with further enzymatic treatment (sample S2 (0.051 ± 0.002) Pa s, S3 (0.027 ± 0.002) Pa s and S3Oi (0.028 ± 0.004) Pa s at $0.1\,\mathrm{s}^{-1}$). Accordingly, the application particularly of EP2 significantly lowered the viscosity.
At high shear rates the viscosities of the samples differed less. At a shear rate of $631\,\mathrm{s}^{-1}$ sample S1 showed a viscosity of (0.068 ± 0.007) Pa s, whereas sample S2 had a viscosity of (0.0219 ± 0.0007) Pa s and samples S3 and S3Oi showed viscosities of (0.0081 ± 0.0005) Pa s and (0.0076 ± 0.0005) Pa s, respectively.
The viscosity before any enzymatic treatment was significantly higher than after treatment with EP1. No flow sweep of the sample without enzymatic treatment was performed, because its viscosity was too high to be measured in cup-vane geometry in the whole shear rate range. However, the sample cooled to 25 °C after measuring the temperature ramp (cf. Figure 7.3) had a viscosity of about 0.8 Pa s. This is significantly higher than the viscosity of sample S1 at a shear rate of $200\,\mathrm{s}^{-1}$, which is about 0.1 Pa s.
It is well-known that the enzyme α-amylase (contained in EP1) cleaves the α-1,4

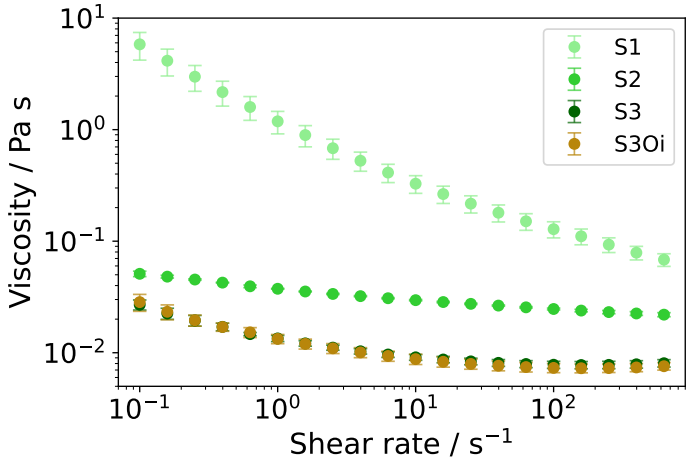

(a) Flow sweeps after each step of enzymatic treatment as well as after addition of oil and salt.

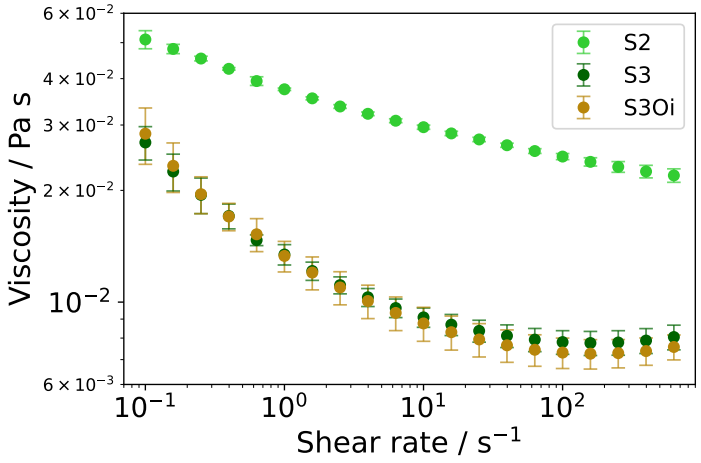

(b) Flow sweeps after step 2 and 3 of enzymatic treatment as well as after addition of oil and salt.

Figure 7.4.: Flow sweeps after each step of enzymatic treatment as well as after the addition of oil and salt.

glycosidic bonds of starch molecules [424]. Thus, smaller oligosaccharide fragments with different numbers of glucose units as well as isolated single glucose molecules are formed from the large polysaccharides by hydrolytic cleavage. However, the α-1,6 glycosidic bonds present in amylopectin as branching points cannot be cleaved by α-amylase.

After EP2 treatment, the oat drink remains liquid after cooling and shows an improved mouthfeel. The viscosity of the oat drink is already much closer to that of cow's milk which is in the order of magnitude of $10^{-3}\,\mathrm{Pa\,s}$ [444]. Due to the saccharification of the starch, the flavor of the oat drink is noticeably sweeter, but a mucilaginous and viscid texture persists.

The glucoamylase contained in EP2 is able to hydrolyze the α-1,4 bonds of the saccharides from the non-reducing end and additionally the α-1,6 bonds at the branching points of the amylopectin. Thus, the remaining branched glucose saccharides are further cleaved by glucoamylase. Cleavage of the α-1,6 glycosidic bonds thus produces more and shorter glucose chains whose molecular weights are determined by the branched parts of the amylopectin. These can then in turn be split into shorter oligosaccharides or mono-, di- and trisaccharides by α-amylase or by the glucoamylase itself. Consequently, the oat drink tastes sweeter compared to the previous step.

As can be seen from the pronounced shear thinning behavior shown in the viscosity measurements displayed in Figures 7.4a and 7.4b, the oligosaccharides formed by the enzymatic treatment are still large and long enough to form entanglements in the concentrated solutions [445, 446]. The presence of α-1,6 glycosidic bonds further enhances these effects, since not only long chains are present that became entangled with one another, but also branched molecules with linked branches of glucose chains that cause the molecules to become entangled with one another. Additionally, the β-glucans with molecular weights up to $105\,\mathrm{g\,mol^{-1}}$ to $108\,\mathrm{g\,mol^{-1}}$ yielding root-mean-square radii from 20 nm to 140 nm in good solvent, contribute to the overall shear thinning for the starch sensitive enzymatic treatments with EP1 and with EP1+EP2 [447].

After treatment with EP3 the flavor of the resulting oat drink is sweet and cereal-like. The texture is now perceived as homogeneous and of sufficiently low viscosity.

The high proportion of non-starch-polysaccharides contained in oats causes mucilage formation. Among these especially β-glucan is worthwhile to mention, because oats contain the highest content of β-glucan among cereals. Oats exhibit an average content of 3.9 % to 5.7 % β-glucan, which has, on average, about 30 % β-1,3 and 40 % β-1,4 glycosidic branching [417]. Furthermore, cellulose (15.9 % in husked oats, 4.1 % in naked oats [417]) and pentosans are non-starch polysaccharides present in oats.

Treatment with EP3 reduces the remaining irritating, mucous mouthfeel. Cellulase, β-glucanase and pentosanase enable the cleavage of β-glucans by attacking the β-1,3 and β-1,4 bonds of the glucose chains and hydrolysis of cellulose and pentosan. Shorter glucose chains reduce viscosity and slightly increase sweetness. Hydrolyzed celluloses, β-glucans and pentosans reduce the viscosity significantly (cf. Figures 7.4a, 7.4b) and consequently improve the mouthfeel.

In the whole shear rate range the flow sweep measurements revealed lower viscosities

after treatment with EP3 than before (cf. Figure 7.4b), which indicates that smaller amounts of branched polymers or glucose chains were left.
After adding oil and salt, the oat drink appears milky, balanced and sweet with an appealing cereal-like flavor. The salt concentration at the limit of the perception threshold underlines the sweetness of the drink. The neutral taste of the canola oil has no influence on the sensory perception, but the emulsified oil droplets lead to a rich mouthfeel.
The flow sweep of sample S3Oi appears similar to that of sample S3. Obviously, the addition of canola oil and salt only causes little variations in the viscosity which are mainly in the range of uncertainties.

Particle size of oat drink constituents

To obtain more information, particle size measurements were performed for samples heated to 35 °C and 70 °C, respectively. Figure 7.5 shows the particle sizes of the sam-

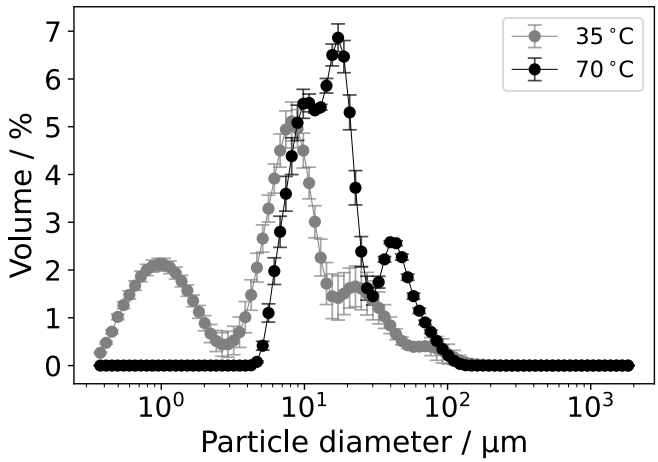

Figure 7.5.: Particle size distributions for oat drink samples without enzymatic treatment heated to 35 °C and 70 °C, respectively.

ples at a temperature of 35 °C and 70 °C. At 35 °C, three peaks occurred, whereby the highest volume share was represented by particles of a size of 7.9 µm with a geometric standard deviation of 1.5 µm. The samples heated to 70 °C showed a different particle size distribution with a shift to larger particle sizes. Here, the highest volume share was given by particles with a size of 18.1 µm with a geometric standard deviation of 0.8 µm. The reason for this shift towards larger particle sizes at 70 °C is the swelling of the starch granules.
According to literature the length range of native oat starch granules is 5.85 µm to 6.9 µm, their width ranges from 3.0 µm to 7.5 µm and their mean granule width is in the range of 1.5 µm to 9.75 µm [448]. These ranges correspond to the experimentally determined sizes shown in Figure 7.5.

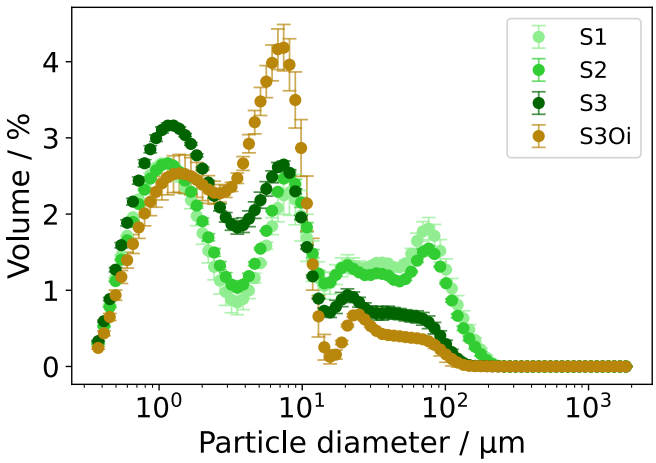

Figure 7.6.: Results of the particle size measurements after each of the three enzyme treatments and after addition of oil and salt.

The results of the particle size measurements, which indicate swelling of the starch granules, also confirm the interpretation of the rheological measurement (Figure 7.3). At low temperatures the starch granules still absorb little water and remain in their crystalline form as initially an amorphous hydration of the starch granules occurs. The rotation and heating of the sample in the rheometer cause the starch particles to separate from each other and thus float more freely in the suspension. Consequently, the viscosity initially decreases slightly. At temperatures above 55.5 °C however, the starch granules begin to swell. Consequently, the granule size increases and the viscosity rises as the larger particles restrain each other's motion.

Figure 7.6 shows the measured particle size distributions in the samples after each of the enzymatic treatments, and after addition of oil and salt. Looking at the particle size distributions after the individual process steps, it is noticeable that mainly particles can be distinguished in three size ranges. The first peak has a mean value of about 1.2 µm and the second one at about 8 µm. Larger particles are present in the range of about 15 µm to 100 µm.

Comparing the measurements with each other shows that after each enzymatic treatment the volume fraction (peak height) of the larger particles decreases, while the volume fraction of the smaller particles increases. This can be explained by the enzymatic cleavage of the long glucose chains of starch and non-starch polysaccharides β-glucan and cellulose into smaller fragments, as this reduces the size of the particles. Besides β-glucanase and cellulase, EP3 also contained pentosanase and xylanase, which cleave non-starch polysaccharides originating from cell wall material explaining the strong decrease of particles in the size range of about 15 µm to 100 µm.

After addition and homogenization of the canola oil (sample S3Oi), a clear increase of particles with a size in the range of 2.7 µm to 13.0 µm can be seen. These particles

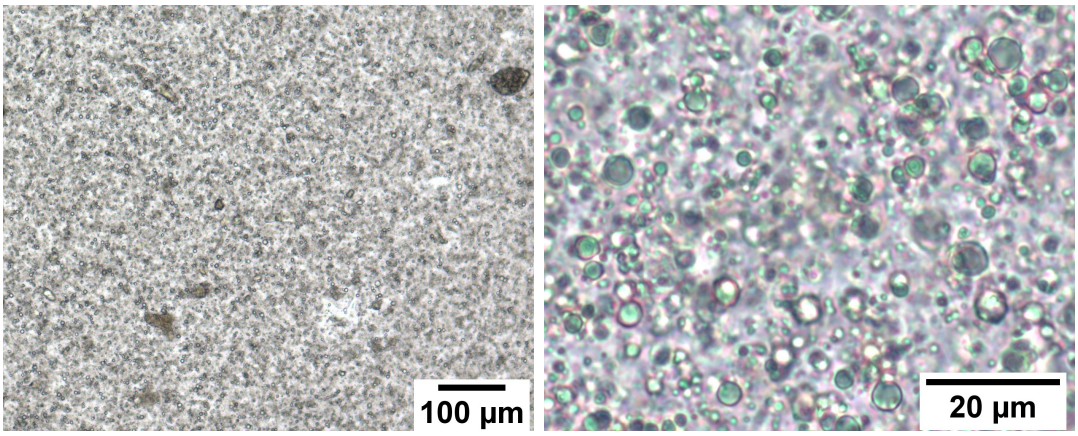

Figure 7.7.: Bright field optical microscopy of the oat drink at 10-fold magnification (left) and 100-fold magnification (right). The larger brownish particles with irregular shape represent polysaccharides from the cell wall material of the oat grain whereas the greenish and white (depending on the focus) spheres represent oil droplets.

represent the oil droplets, as could be verified by means of light microscopy images (cf. Figure 7.7). The oil droplets are visible as greenish-white circles with a size between 1 µm and 13 µm, as well as remaining cell wall material as brownish, irregularly shaped particles with a size in the range of 10 µm to 100 µm.

7.3.2. Investigation of foam properties

Protease and heat treatment

The macroscopic foam properties are mainly determined by the given molecular interactions of the proteins at the air-water interfaces. These in turn depend on the protein structure, the electric charges, and the sequence of hydrophilic and hydrophobic amino acids at the protein surface. Hydrophobicity plays a special role in foam formation, because it determines how proteins arrange themselves along the air-water interface. This arrangement lowers the surface energy and stabilizes the air bubble. The stability of the foam thus depends strongly on the primary and secondary structure of the proteins. In addition, also their tertiary and quaternary structures are relevant for foaming, because these influence which amino acids are exposed to the protein surface.

Storage proteins in oats are dominated by 12S globulins, which are very dense and mostly occur in hexa-6-mers [146, 205, 449]. This means six identical proteins with over 500 amino acids pack together into dense globules via physical interactions. Another fraction of storage proteins are avenins (prolamins) which are considerably smaller with a maximum of 214 amino acids [146, 449]. The collective term albumins covers a whole range of water-soluble proteins and enzymes [200]. Typical representatives of these different groups are shown in Figure 7.8. The coloring of the protein structures indicates their interfacial activity. Sequences and amino acids in red are hydrophobic, whereas blue ones are hydrophilic. 12S globulins are extremely stable, so they can only participate indirectly in foam formation via electrostatic complexes, especially since only a few sequences at their surface can turn towards the hydrophobic air. Avenins and albumins, on the other hand, can align much better at the air-water interfaces. They have a strongly hydrophobic part that can project into the air and stabilize the interfaces, as exemplified for the native state of tryptophanin in Figure 7.9. Indeed, Kaukonen et al. [38] investigated the foaming properties of differently processed oats and found that tryptophanin is a major foam-active oat protein. Also Ma et al. [419] found that oat albumins induce a high foaming capacity, whereas globulins and prolamins show similar foam stability as albumins.

Treatment with EP2 is recommended at a temperature of 50 °C. The protease contained therein can be deactivated by setting the temperature to 70 °C during enzyme treatment. However, at the same time α-amylase and glucoamylase remain active and cleave the starch. Furthermore, each of these samples was examined once with and once without pasteurization.

Figure 7.10 shows the foaming capacity of the four samples. Sample Pi shows a slightly lower foaming capacity compared to the other three samples. In this sample the proteins are in their native form.

The protease contained in EP2 changes the interfacial activity of the proteins in two ways. On the one hand, the resulting peptide interfaces can be active. Secondly, the structure of these peptides becomes more heterogeneous. As a result, the foaming capacity increases while the foam stability decreases, e. g. when a rearrangement of

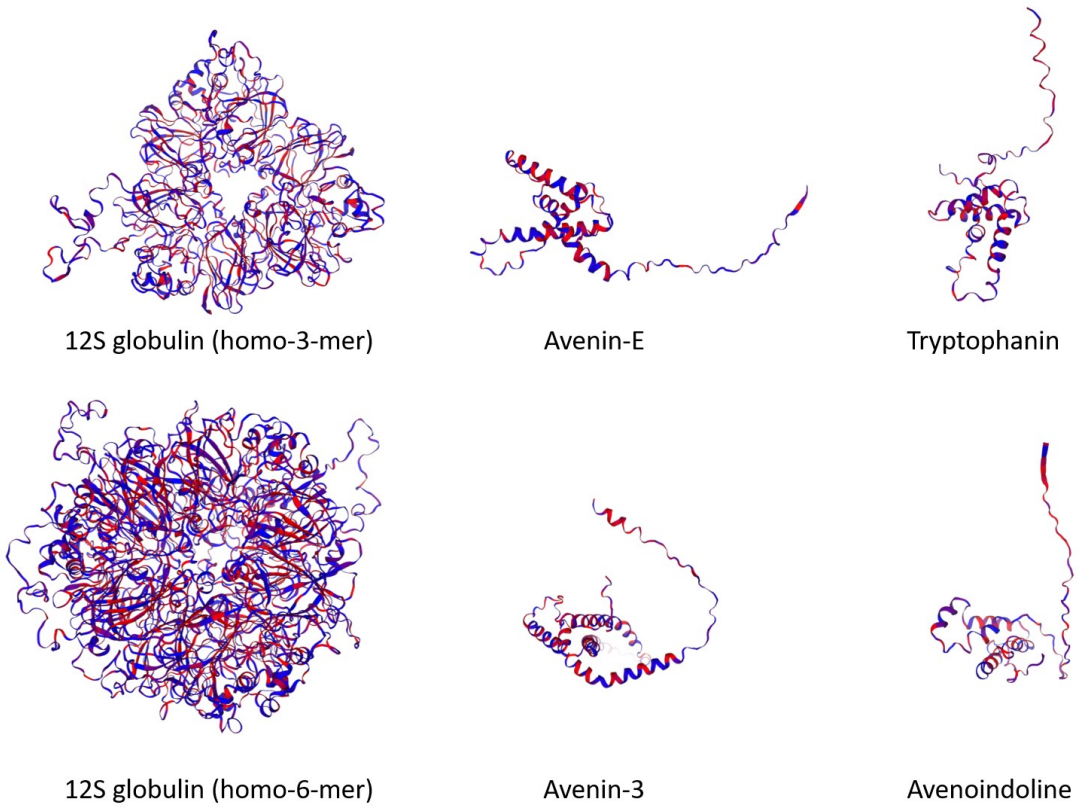

Figure 7.8.: Selection of oat proteins: The 12S globulin (UP-ID: O49258) homo-3-mer and homo-6-mer, the prolamins avenin-3 (UP-ID: P80356) and avenin E (UP-ID Q09114), and the albumins tryptophanin (UP-ID: A7U439) and avenoindoline (UP-ID: Q9M4E2) [146]. Hydrophobic amino acids are colored in red and hydrophilic ones in blue. The surfaces of these proteins are shown in Figure 2.12.

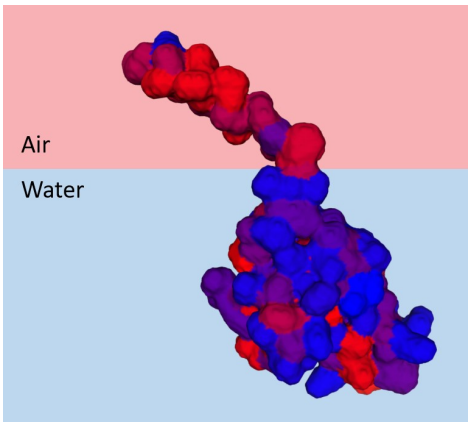

Figure 7.9.: Native tryptophanin in protein surface representation at the air-water interface. The single hydophilic amino acid at the end of the distinct hydrophobic part is thermodynamically tolerated because of the strong free energy gain.

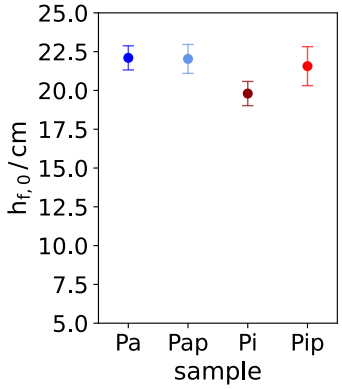

Figure 7.10.: Influence of protease treatment and pasteurization on foaming capacity.

the emulsifiers takes place at the interfaces.
Moreover, some oat proteins denature during pasteurization, and the denaturation temperature is protein-specific. Globulins in oats denature at a temperature of ≈110 °C (peak), whereas albumins in oats denature at temperatures as low as ≈87 °C (peak) [419]. The prolamins in oats (avenins) show a denaturation temperature of ≈102.8 °C [450]. During the preparation of the oat drink, the samples were heated to 95 – 105 °C for 10 s.
The thermal denaturation of the albumins during pasteurization also alters foam formation and stability. The distribution of the proteins at the interfaces becomes more space-consuming, new competing interactions occur and the interfacial activity decreases further. Furthermore, cysteine present in the proteins can be re-crosslinked upon heating, which in turn changes the arrangement and decreases the interfacial activity.
After pasteurization albumins are denatured, since they denature at a temperature of ≈87 °C (peak) [419]. The heat-denatured albumins as well as the peptides in the protease treated samples seem to be more flexible due to their structural changes, so that they can migrate faster to the air-water interface, accumulate there and reduce the surface tension. This results in more foam during frothing, thus a higher foaming capacity.
In Figure 7.11a the measured foam heights for samples Pa, Pap, Pi, and Pip are displayed over time. The data are fitted with power law decays. The time-dependent behavior of the foams shows that sample Pi has the highest normalized foam height after 15 min and thus the highest foam stability.
This indicates that the native proteins arrange themselves compactly at the bubble surface and stabilize the foam. Avenins and albumins in their native conformation show an elongated, strongly hydrophobic part which makes them arrange at the interface and stabilize the air bubble in the foam. The peptides after protease treatment as well as the partially heat-denatured proteins loose this property and consequently arrange themselves less stably. In these cases, the air bubbles grow and escape more easily and the foam collapses faster.

Sample name	Exponent
Pa	$c = 0.071 \pm 0.006$
Pap	$c = 0.172 \pm 0.006$
Pi	$c = 0.048 \pm 0.001$
Pip	$c = 0.151 \pm 0.008$

Table 7.2.: Influence of protease treatment and pasteurization on foam stability: Fit parameters.

Common processes observed in foams are Ostwald ripening and coalescence of bubbles. Ostwald ripening describes the growth of larger bubbles at the expense of small bubbles caused by a gas transfer from the small to the large bubble [19, 329]. Consequently the

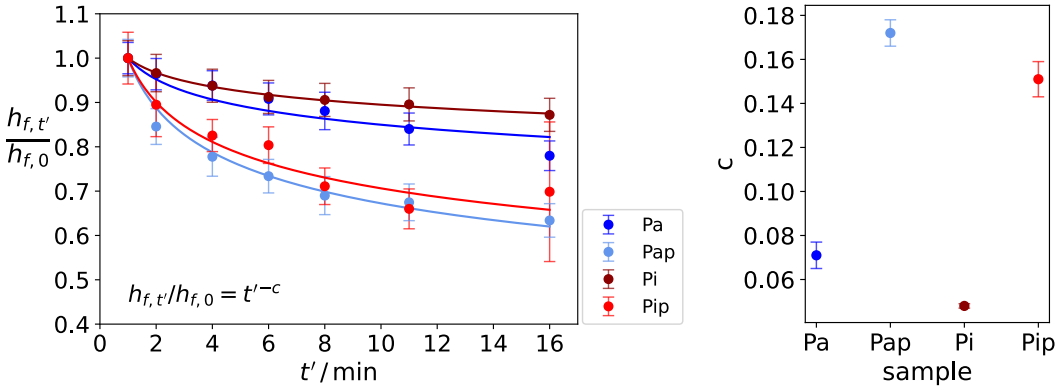

(a) Normalized foam heights.

(b) Exponents of power law fits.

Figure 7.11.: Influence of protease treatment and pasteurization on foam stability.

mean bubble size increases, which determines the foam stability. The rate of Ostwald ripening depends also on the surfactant type [329]. Coalescence, on the other hand, means that the film between two bubbles ruptures and the two bubbles unite into one large bubble [330]. To observe the bubble growth, photographs of the foam were taken, as shown in Figure 7.12. The photographs show the four samples at the beginning and after 15 min, respectively. These images confirm the observations made for the foam heights. It can be clearly seen here that sample Pi has the smallest bubbles during the entire observation period. The bubble diameter hardly grows. Consequently, the foam height decreases more slowly, which indicates a high foam stability. The other samples, but especially sample Pap, show a clear increase in bubble size over the measurement period. In addition to the shrinkage of smaller bubbles and growth of larger bubbles (Ostwald ripening), it can also be observed that bubbles grow together (coalescence). Large bubbles move to the top of the foam and eventually escape from the foam. This results in a reduced foam height and consequently a lower foam stability.
As mentioned already, sample Pi exhibits the highest foam stability. However, for comparison with marketable products, which have to be pasteurized, sample Pip was chosen as the standard sample.

Addition of canola oil

The influence of the oil content on the foam stability is also of functional importance. Therefore, samples with a canola oil content of 1 %, 2 % and 3 % canola oil were investigated and compared to samples without addition of canola oil. Their foaming capacity is shown in Figure 7.13. The highest foaming capacity was measured for sample Oi1. For higher canola oil contents the foaming capacity decreases with increasing canola oil content. However, the sample without canola oil shows a lower foaming capacity. This behaviour can be explained by the interplay of different effects. On the one hand, the viscosity of the sample changes with oil addition. During foam forma-

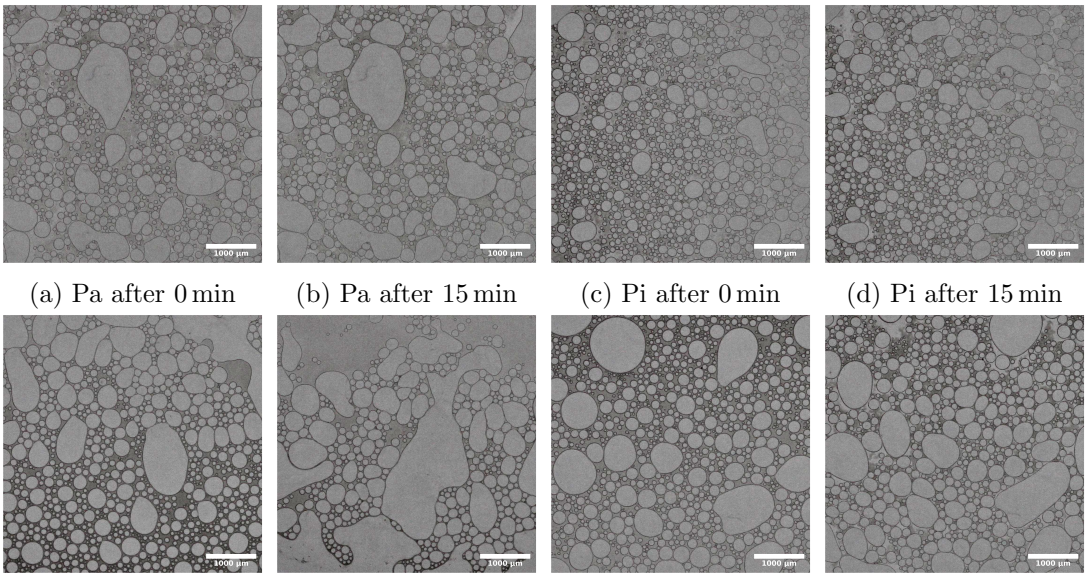

(a) Pa after 0 min (b) Pa after 15 min (c) Pi after 0 min (d) Pi after 15 min

(e) Pap after 0 min (f) Pap after 15 min (g) Pip after 0 min (h) Pip after 15 min

Figure 7.12.: Camera photos of the foam of samples Pa, Pap, Pi, and Pip after 0 min and 15 min each. Contrast of the images was enhanced by factor 2. Scale bars are 1000 µm.

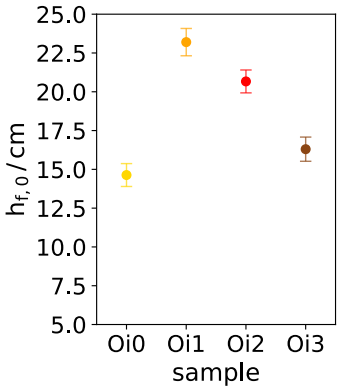

Figure 7.13.: Influence of canola oil content on foaming capacity.

tion high shear rates are applied. At high shear rates, the viscosity of samples with oil is lower than that of sample Oi0 (cf. Figure 7.4b). Samples of lower viscosity can incorporate more air during foam formation and therefore show an increased foaming capacity [384]. In addition, initially the finely dispersed oil droplets may cause a Pickering effect: small solid or soft particles can stabilize the hydrophobic-hydrophilic interfaces in emulsions and foams [451–454]. Indeed, an accumulation of oil droplets at the air-water interfaces is observed as shown in Figure 7.15. Such Pickering effect would also contribute to the increased foaming capacity of samples containing oil. However, when the foam films become thinner, oil can also act as defoamer [455]. For this reason, a stabilizing effect of added oil is not observed on the long term (cf. foam stability shown in Figure 7.14). On the other hand, the addition of canola oil results in more hydophobic:hydrophilic interfaces. Therefore, less emulsifyers stabilize the air-water interfaces. This effect becomes more relevant with increasing canola oil content.

Figure 7.14a shows the measured foam heights for samples Oi0, Oi1, Oi2, and Oi3 over time. Each data set is fitted with a power law decay (cf. 7.2.8 and Figure E.9). Although the differences are small, the investigation of the time-dependent foam heights shows that the foam stability decreases with increasing oil content. The decrease of the foaming capacity and stability with increasing oil concentration can be explained by a competitive situation: the oil-water interface of the droplets now competes with the air-water interface of the bubbles for the hydrophobic parts of the surface-active proteins. An increased oil content therefore leads to more proteins attaching to the oil droplet surfaces. The fewer proteins left on the air bubble surface cannot stabilize the air bubbles as well as at lower oil contents. Consequently, the air escapes faster, resulting in lower foam stability. The microscope images in Figure 7.15 show clearly how oil droplets accumulate at the air bubble surface and also agglomerate. Additionally, oil can act as antifoam. This means, that oil droplets induce foam film rupture by bridging the two surfaces of a foam film [455]. This effect becomes more relevant as the foam becomes drier. Furthermore, during foam ripening the shear forces are very low. At low shear rates the viscosities of samples with and without oil are similar respectively slightly increased for samples with oil. The slightly higher viscosity retards drainage and enhances foam stability for canola oil containing samples. However, this effect is smaller than the destabilizing effects of the added canola oil.

Sample name	Exponent
Oi0	$c = 0.151 \pm 0.002$
Oi1	$c = 0.157 \pm 0.004$
Oi2	$c = 0.178 \pm 0.005$
Oi3	$c = 0.186 \pm 0.005$

Table 7.3.: Influence of canola oil content on foam stability: Fit parameters.

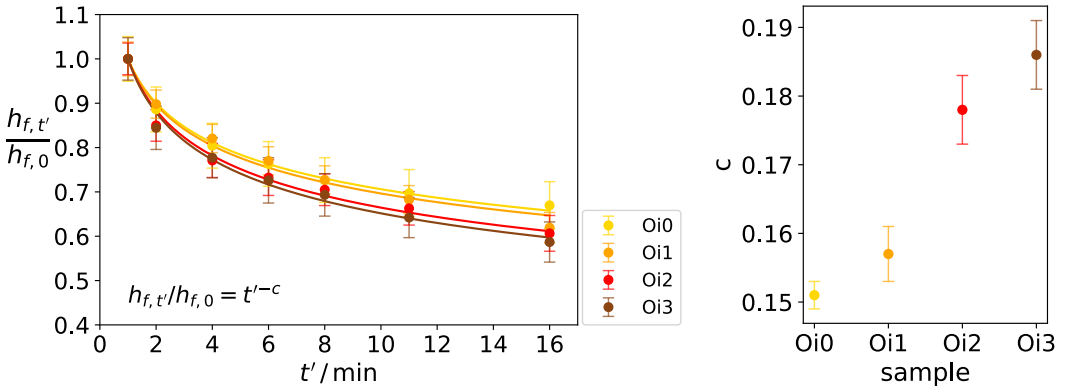

(a) Normalized foam heights.

(b) Exponents of power law fits.

Figure 7.14.: Influence of canola oil content on foam stability. With increasing oil content, the foam stability decreases.

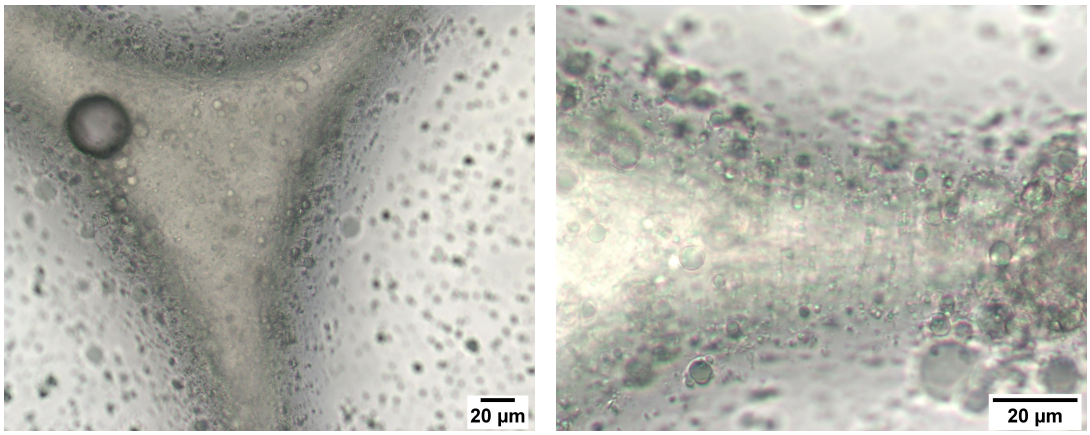

Figure 7.15.: Bright field optical microscopy of an oat drink foam containing 2 % canola oil. Left: Plateau border at 40-fold magnification. Right: Lamella and adjoined air bubbles at 100-fold magnification. An accumulation of oil droplets at the air-water interface is observed.

Although the foam stability decreases with increasing oil content, an addition of 2 % canola oil was chosen for the standard sample. The reason is to allow comparison with products available on the market which also aim for a pleasant mouthfeel.

7.4. Conclusions

This chapter shows how an oat drink with excellent drinkability and good foaming properties can be produced without resorting to additives such as foam stabilizers, emulsifiers, sweeteners and texturizing hydrocolloids. Instead, by systematically and selectively comparing the different temperature and enzymatic treatments, the sensory and physical effects of the native oat components protein and starch can be attributed to the physical properties. It was shown that conformational changes of the proteins caused by enzymatic cleavage or heat-induced denaturation slightly increase the foaming capacity, but significantly reduce the foam stability of the oat drink. Furthermore, the addition of canola oil improves the mouthfeel of the oat drink, while the foam stability decreases slightly with increasing oil content. From this, further insights can be derived for the production of oat and other plant-based drinks.

8. General conclusions and outlook

8.1. General conclusions

Investigating model systems of liquid foams stabilized by H*B hydrophobin or BSA showed that large hydrophobic patches at the protein surface and a low molecular net charge promote a more resilient assembly at air-water interfaces, which increases the macroscopic stability of the foam. In addition, increasing the dynamic viscosity of the solution, either by a high protein charge or by addition of a hydrocolloid, enhances the stability of wet foams by retarding drainage. The influence of polysaccharide addition on foam stability is mainly driven by viscosity enhancement, however also the stiffness and charge of the polysaccharide need to be considered to explain differences in foam stability.
Furthermore, the investigations show that for each system of interest the precise molecular properties of all involved components and their possible interactions need to be considered in order to understand and predict foam stability.
More detailed conclusions regarding each investigated system are provided at the end of each chapter.

8.2. Outlook

To further characterize the surface-active properties of the proteins and the interfacial arrangement, surface-specific techniques such as sum frequency generation and ellipsometry could be applied. With these methods information about orientation of the protein towards the interface, the vibrational state of the molecule and the thickness of the interfacial protein layer could be obtained.
Using a Langmuir-through the arrangement and rearrangement under compression could be studied for HP and BSA at the air-water interface. With the help of a barrier the air-water interface can be compressed. For this reason, the investigated interfacial behavior would better mimic the conditions in a foam, where interfaces are not static. Langmuir troughs can be combined with techniques such as Brewster angle microscopy to obtain information about domain formation. However, the use of a Langmuir-trough was not possible at the time of the measurements for this thesis, because there was no Langmuir-trough at the institute in operation.
In addition, to better characterize the film thinning and mechanisms of destabilization of foam films, the thickness of thin films could be studied via interferometry [57]. On a thin film pressure balance the disjoining pressure can be measured for changing film thicknesses and the structure of the films and changes in their thickness can be

monitored visually [56, 57, 456]. A foam film located between two coalescing bubbles could be studied by applying the laser extinction method [57, 457].
Drop shape analysis of sessile drops or pendant drops and the measurement of contact angles of sessile drops could deepen the insight into changes of the surface tension at varying conditions such as the addition of another protein or a hydrocolloid to the system. These methods would complement the surface tension measurements obtained from applying the Wilhelmy plate method and could confirm these results.
Furthermore, small angle neutron scattering (SANS) or X-ray scattering (SAXS) could be applied to non-invasively investigate the structure formation in thin films and foams [458]. With SAXS the shape of the stabilizers and aggregate formation in the bulk or in thin films could be studied [58, 458], whereas SANS would provide an ensemble average of the three-dimensional foam structure [458]. Lamolinairie et al. succeeded to combine a foam analyzer with a SANS experiment. With this setup a foam and its aging can be investigated on different length scales within one experiment [23]. Characteristics such as the liquid fraction, the foam film thickness and the disjoining pressure of the films could be monitored simultaneously in a draining foam [23].
To deepen the insights into oat drink foam formation, model systems stabilized by pure oat proteins could be investigated. However, pure oat globulins, albumins and prolamins (avenins) are not readily commercially available. For this reason, oat protein concentrates or isolates would need to be purified by different chemical methods. With the pure proteins more precise studies on which proteins are essential for the foam formation of oat drinks could be performed. With this, the role of the albumin fraction of oats in foam stability could be clarified. Other oat drink components such as β-glucan or starch could then be added step-by-step and their influence investigated.

A. Supplementary information: Method development

This is supplementary information to Chapter 3.

A.1. Python script of threshold-based approach for image analysis

This *Python* script (Python Software Foundation, version 3.8.8) contains a function *bubblesize* to analyze the mean bubble size of all bubbles in one image using a threshold-based approach. First, the image is converted into a binary image by thresholding. The background color is black (0) and the bubbles (foreground) are white (255). Subsequently, the area and equivalent diameter of each bubble are determined by using measure.regionprops from the skimage library [459] (skimage version 0.18.1). This function counts all connected foreground pixels. From the bubble area the equivalent diameter is calculated, which is the diameter of a sphere with same area as the bubble. Subsequently, the mean equivalent bubble diameter of all bubbles in the image is calculated.

[1]:
```
import cv2 #Import OpenCV library for image processing
import matplotlib.pyplot as plt #Import Matplotlib library for␣
 ↪plotting
import numpy as np #Import NumPy library for numerical operations
from scipy import ndimage #Import ndimage for multidimensional image␣
 ↪processing
from skimage import io, color, measure #Import specific functions␣
 ↪and submodules from skimage library

from statistics import mean, stdev #Mean and standard deviation

import os #Import os module for operating system functions
import glob #Import glob module for pathname pattern expansion
```

[2]:
```
print('Please choose the pixel_to_um conversion.')
print('For camera with reprostativ please crop the image(s) before.')
#pixel_to_um = 0.455193 #Conversion of units for 10x magnification␣
 ↪(microscope)
```

```
pixel_to_um = 4.6904637 #Conversion of units for camera with␣
↪reprostativ
```

[3]:
```
print('Calculation of the mean bubble diameter of all bubbles in one␣
↪image.')

def bubblesize(img, pixel_to_um):
    """Calculation of the mean bubble diameter for bubbles in a␣
↪given image.
    The image is converted into a binary (black-white) image. The␣
↪bubble size (area of a bubble) is calculated by
    counting all connected pixels of same color. From the area of␣
↪the bubble the equivalent diameter of a sphere
    with same area is calculated. Subsequently, the mean bubble␣
↪diameter of all bubbles in the image is calculated.
    parameters:
    img ... image
    pixel_to_um ... constant for conversion of pixels into um"""

    #Conversion to binary image and measurement of bubble size␣
↪(regionprops):
    ret, thresh = cv2.threshold(img, 0, 255, cv2.THRESH_BINARY_INV +␣
↪cv2.THRESH_OTSU)
    mask  = thresh == 0
    s = [[1,1,1], [1,1,1], [1,1,1]] #Structuring element
    labeled_mask, num_labels = ndimage.label(mask, structure=s) #␣
↪ndimage.label: non-zero = feature, 0 = background
    bubbles = measure.regionprops(labeled_mask, img)

    #Save the properties: (cf. [460])
    propList = ['Area', 'equivalent_diameter']
    output_file = open ('bubble_sizes.txt', 'w')
    output_file.write((',' + ','.join(propList) + '\n'))
    for bubble_props in bubbles:
        output_file.write(str(bubble_props['Label']))
        for i, prop in enumerate(propList):
            if(prop == 'Area'): #Convert pixels into um for bubble␣
↪area
                to_print = bubble_props[prop]*pixel_to_um**2
            else: #Convert pixels into um for equivalent diameter
                to_print = bubble_props[prop]*pixel_to_um
            output_file.write(',' + str(to_print))
```

```
        output_file.write('\n')
    #Repetition, otherwise error with number of lines in textfile
    propList = ['Area', 'equivalent_diameter']
    output_file = open ('bubble_sizes.txt', 'w')
    output_file.write((',' + ','.join(propList) + '\n'))
    for bubble_props in bubbles:
        output_file.write(str(bubble_props['Label']))
        for i, prop in enumerate(propList):
            if(prop == 'Area'):
                to_print = bubble_props[prop]*pixel_to_um**2
            else:
                to_print = bubble_props[prop]*pixel_to_um##
            output_file.write(',' + str(to_print))
        output_file.write('\n')

    #Calculate mean bubble diameter (for bubbles with diameter␣
↪>50um):
    data = np.loadtxt('bubble_sizes.txt', unpack=True,␣
↪delimiter=',', skiprows=1)
    x = data[0]
    y = data[2]
    equ_diam = data[2]
    bubble_diameter = list()
    for j in equ_diam:
        if j>50:
            bubble_diameter.append(j)
    mbs = mean(bubble_diameter)

    #Return the mean bubble diameter of all bubbles in the image:
    return mbs
```

[4]:
```
print('Saving of mean bubble diameters of several images.')
print('Please copy the images of one measurement in the current␣
↪folder (same directory as python file). Save values in␣
↪mean_values_M1 and diagrams as M1. (Also, change the name of the␣
↪file: image_measurements). Repeat this step for measurement two␣
↪and three (M2 and M3).')
#Save mean bubble diameters for several images in one file:
img_dir = '' #Current directory -> images to analyse have to be in␣
↪the same directory as program
data_path = os.path.join(img_dir,'*jpg')
files = glob.glob(data_path)
```

```
mean_values = [] #Empty list for mean values

for f in files: #For each file (image)
    img = cv2.imread(f, 0) #Read the image
    plot = bubblesize(img, pixel_to_um) #Apply bubble size function
    mean_values.append(plot) #Append mean bubble size to list
    plt.clf() #Close file
```

A.2. Python script of machine learning-based approach for image analysis

This subsection is based on the code published in the supporting information of manuscript

Simple method to assess foam structure and stability using hydrophobin and BSA as model systems
Judith Krom, Konrad Meister, Thomas A. Vilgis
ChemPhysChem (2024)
DOI: 10.1002/cphc.202400050.[302]

The following is quoted from the supporting information of [302]. The typesetting (including the capitalization of captions) was adjusted to the style of the thesis.

Python script: Image pre-processing This script is used to pre-process images by applying Gaussian blur filter (cv2.GaussianBlur), image subtraction (cv2.subtract), Kuwahara filter (pykuwahara 0.3.2), background subtraction (skimage.restoration.rolling_ball, skimage.restoration.ellipsoid_kernel) and contrast enhancement (PIL.ImageEnhance.Contrast). It was written in *Python* version 3.8.8 (Python Software Foundation) using the platform *Anaconda* and the web application *Jupyter Notebook*.
In the second cell several folders are created to store the different stages of the pre-processing and allow control over the various steps involved. After running this cell, the microscope images are manually transferred into the folder '00_OriginalImages' and the rest of the script is run subsequently. The resulting pre-processed images can be found in the folder '06_EnhancedContrast'. The parameters 'k1', 'k2', 'k_radius', 'ellips_kernel_1', 'ellips_kernel_2', 'ellips_kernel_3', and 'factor' influence the filter effects (see corresponding comments in the script). They can be varied according to the content of the images to improve the results.

[1]:
```
import cv2 #Import OpenCV library for image processing
import matplotlib.pyplot as plt #Import Matplotlib library for␣
 ↪plotting
```

```
import numpy as np #Import NumPy library for numerical operations

import os #Import os module for operating system functions

#Import kuwahara function from pykuwahara module:
from pykuwahara import kuwahara
#Import specific functions and submodules from skimage library:
from skimage import data, io, filters, restoration, util, color
#Import specific functions from the restoration submodule of skimage:
from skimage.restoration import rolling_ball, ellipsoid_kernel

#Import the Image and ImageEnhance modules from PIL library:
from PIL import Image, ImageEnhance
```

[2]:
```
#Create directories

#Folders to create:
directory_list = ['00_OriginalImages', '01_BlurImages',␣
↪'02_SubtractedImages',
    '03_KuwaharaFilter', '04_Background', '05_SubtractedBackground',
    '06_EnhancedContrast']

#Set current working directory as parent directory path:
parent_dir = os.getcwd()

for i in directory_list: #Iterate over each item in the␣
↪directory_list
    #Create the full path by joining parent_dir and i:
    path = os.path.join(parent_dir, i)
    os.mkdir(path) #Create a directory at the specified path
```

[3]:
```
#Gaussian blur, image subtraction, Kuwahara filter

#Image directory:
data_path = '00_OriginalImages/'

#Parameters:
k1 = 9 #Kernel size for Gaussian blur, has to be positive and odd
k2 = k1 #Kernel size for Gaussian blur, symmetric kernel
k_radius = 4 #Radius for Kuwahara filter

for f1 in os.listdir(data_path): #Images in file directory
    f1_name = os.path.splitext(f1)[0]
```

```
    img = cv2.imread(data_path + f1)
    blur_img = cv2.GaussianBlur(img, (k1, k2), 0) #Gaussian blur␣
↪filter
    cv2.imwrite('01_BlurImages\Gaussianblur-'+f1, blur_img)
    subtracted = cv2.subtract(img, blur_img) #Image subtraction
    subtracted_subtracted = cv2.subtract(img, subtracted) #Image␣
↪subtraction
    cv2.imwrite('02_SubtractedImages\Subtracted-'+f1,␣
↪subtracted_subtracted)
    filt2_2 = kuwahara(subtracted_subtracted, method='gaussian',
        radius=k_radius) #Kuwahara filter, default sigma: computed␣
↪by OpenCV
    cv2.imwrite('03_KuwaharaFilter\KuwaharaGauss-'+f1, filt2_2)
    plt.clf()
```

[4]:
```
#Background subtraction - rolling ball algorithm

#Image directory:
data_path_get_2 = '03_KuwaharaFilter/'
data_path_save_2 = '04_Background/'
data_path_save_3 = '05_SubtractedBackground/'

#Parameters:
ellips_kernel_1 = 130 #Length of the principal axis of the ellipsoid
ellips_kernel_2 = ellips_kernel_1 #Symmetric ellipsoidal kernel
ellips_kernel_3 = 0.2 #Length of the intensity axis of the ellipsoid

for f2 in os.listdir(data_path_get_2):
    f2_name = os.path.splitext(f2)[0]
    f2_name_repl = f2_name.replace('KuwaharaGauss-','')
    #Conversion to 8-bit grayscale:
    image = io.imread(data_path_get_2 + f2, as_gray=True)
    plt.imshow(image)
    #Background subtraction:
    #Invert the image - needed for white background:
    image_inverted = util.invert(image)
    kernel = restoration.ellipsoid_kernel((ellips_kernel_1,␣
↪ellips_kernel_2),
        ellips_kernel_3) #Create an ellipsoid kernel
    #Use rolling ball algorithm for estimating background intensity␣
↪with the
    #ellipsoid kernel:
```

```
    background_inverted = restoration.rolling_ball(image_inverted,␣
↪kernel=kernel)
    #Subtract the background:
    filtered_image_inverted = image_inverted - background_inverted
    filtered_image = util.invert(filtered_image_inverted)
    #Invert the image (white background):
    background = util.invert(background_inverted)

    io.imsave(data_path_save_2 + 'Background-'+f2_name_repl+'.jpg',␣
↪background)
    result = image-background
    io.imsave(data_path_save_3 +␣
↪'SubtractedBackground-'+f2_name_repl+'.jpg',
    result)
```

[5]:
```
#Contrast enhancement

#Image directory:
data_path_get = '05_SubtractedBackground/'
data_path_save = '06_EnhancedContrast/'

for f3 in os.listdir(data_path_get):
    f3_name = os.path.splitext(f3)[0]
    f3_name_repl = f3_name.replace('SubtractedBackground-','')
    im = Image.open(data_path_get+f3) #Read the image
    enhancer = ImageEnhance.Contrast(im) #Image brightness enhancer
    factor = 2.0 #Factor for increasing the contrast
    im_output = enhancer.enhance(factor) #Increase the contrast
    im_output.save(data_path_save + 'EnhancedContrast-' +␣
↪f3_name_repl + '.jpg')
    im_output.save(data_path_save + 'EnhancedContrast-' +␣
↪f3_name_repl + '.tif')
    plt.clf()
```

Python script: Bubble analysis After processing the pre-processed microscope images in the *Cellpose* [299, 300] GUI, *Cellpose* will provide a '_seg.npy'-file containing the information of the bubble masks. The script provided below is run to analyze different properties of the foam.
The second cell creates several folders to store information obtained from the analysis of the microscope images. After running this cell, the '_seg.npy'-files obtained from *Cellpose* are put manually in the data folders 'data_sb' and 'data_lb', respectively: If there is only one set of masks for a sample, it should be in the folder 'data_sb'. In case of two sets of masks, the file containing masks of small bubbles is placed into 'data_sb' and the file containing the masks of large bubbles into the folder 'data_lb'.
To analyze images with two sets of masks, cells 3 and 4 are run. If all masks detected in one image are contained in one '_seg.npy'-file, cells 5 and 6 are run. In the cells 4 and 6, respectively, the samples have to be specified by providing their sample name ('sample1' is replaced by the name of the sample) and the labels of the time series (in the example: ['0000', '0005', '0010', '0015', '0020', '0025', '0030']). Furthermore, the pixel-to-µm ratio of the applied magnification of the used micrsocope has to be provided (*pixeltoum*).
To collect the time-dependent data of each sample in a txt.file, cell 7 is run after checking the provided parameters. The list *time* contains the time steps of the measurement in minutes. In *sample_list* multiple sample names can be provided (['sample1', 'sample2']). *number_list* contains the labels of the time series as provided in the sample names (as before). Moreover, a limit can be supplied. Only bubbles with a larger equivalent diameter than this limit will be considered when calculating the mean circularity. After running cell 7, txt-files containing the mean bubble properties for each time step can be found in the folder 'results' for each sample. These data can be used to plot the temporary evolution of bubble size, circularity, and dispersity of the samples.
Additionally provided info:

File	Info
result_areas_sample1_0000.txt	Total areas
result_bubble-properties_sample1_0000.txt	Properties of each bubble in one image
dat_masks_sample1_0000.txt	Labelled bubble masks
dat_masks_edgebubblesremoved_sample1_0000.txt	Labelled bubble masks
sample1_0000_masks.jpg	Image of bubble masks
sample1_0000_outlines_overlay.jpg	Image of outlines of bubble masks overlayed with microscope image
mean_values_sample1.txt	Mean bubble properties for each time step

[1]:
```
import os
#Set the environment variable KMP_DUPLICATE_LIB_OK to True:
os.environ['KMP_DUPLICATE_LIB_OK']='True'

#Import cellpose functions for plotting masks / outlines:
from cellpose import plot, utils

import numpy as np
import matplotlib.pyplot as plt
import matplotlib.cm as cm #colormaps

from skimage.measure import label, regionprops, regionprops_table
```

[2]:
```
#Create directories

#Folders to create:
directory_list = ['bubble-properties', 'combined-masks',
'combined-masks_edge-bubbles-removed', 'data_lb', 'data_sb',
'result-images', 'results']

#Set current working directory as parent directory path:
parent_dir = os.getcwd()

for i in directory_list:
    path = os.path.join(parent_dir, i)
    os.mkdir(path)
```

[3]:
```
#Two sets of masks
def two_bubblemasks(dats, datl, sample, number, pixeltoum):
    """Function that adds the two sets of masks of small and large␣
 ↪bubbles into
    one array, remove edge bubbles and display the results.
    Parameters:
    dats ... masks of small bubbles
    datl ... masks of large bubbles
    sample ... sample name
    number ... number of the sample which refers to a timestep
    pixeltoum ... pixel-to-um ratio"""

    dats_masks = dats['masks'] #Masks of small bubbles
    datl_masks = datl['masks'] #Masks of large bubbles

    lens = len(dats['colors']) #Number of colors of small bubbles
```

```
                            #-> number of small bubbles

    #Correct labels of large bubble masks:
    shape = datl_masks.shape #Shape of the array of large bubble␣
↪masks
    datl_masks_02 = datl_masks #Copy the array
    for x in range(shape[0]):
        for y in range(shape[1]):
            if datl_masks[x, y] != 0: #All non-zero values in the␣
↪array
                #Add number of small bubbles
                #-> numbering of large bubbles starts at len1+1
                datl_masks_02[x, y] = datl_masks[x, y]+lens

    #Delete bubbles drawn in both (dats_masks and datl_masks) in␣
↪datl_masks:

    #Iterate over each element in the array:
    for x in range(shape[0]):
        for y in range(shape[1]):
            #Check if the mask exists in both arrays:
            if dats_masks[x, y] != 0 and datl_masks_02[x, y] != 0:
                #Store the value of the current element:
                value = datl_masks_02[x, y]
                #Iterate over each element again to find and update␣
↪matching
                #values
                for x in range(shape[0]):
                    for y in range(shape[1]):
                        #If the value matches the stored value, set␣
↪it to zero
                        if datl_masks_02[x, y] == value:
                            datl_masks_02[x, y] = 0


    #Add masks of small and large bubbles into one array:
    dat_masks = dats_masks + datl_masks_02

    #Crop:
    dat_masks = dat_masks[10:shape[0]-30, 10:shape[1]-30]
    reshape = dat_masks.shape

    #Save data:
```

```
    np.savetxt('combined-masks\\dat_masks_' + sample + '_' + number␣
↪+'.txt', dat_masks, fmt='%i')

    #Total bubble area, total lamella area, total area - with edge␣
↪bubbles
    bubble_area = np.count_nonzero(dat_masks!=0)
    lamella_area = np.count_nonzero(dat_masks==0)
    total_area = bubble_area + lamella_area

    #Calculate area and equivalent diameter of each bubble:
    lens = len(dats['colors']) #Number of small bubbles
    lenl = len(datl['colors']) #Number of large bubbles
    lenmask = lens + lenl #Total number of bubbles

    s = (3,lenmask+1) #Define tuple with dimensions 3 and lenmask+1
    c = np.zeros(s) #Array of shape s filled with zeros

    #Iterate over number of bubbles:
    for i in range(lenmask+1):
        first = c[0]
        first[i] = i+1 #Insert bubble labels
        second = c[1]
        second[i] = np.count_nonzero(dat_masks == i+1) #Insert␣
↪bubble areas
        third = c[2]
        #Calculate equivalent diameters from bubble areas and insert␣
↪them:
        third[i] = 2*np.sqrt(second[i]/np.pi)
    diameter = c[2] #Equivalent diameter


    #Select first row, first column, last row and last column
    fr = dat_masks[0] #first_row
    lr = dat_masks[-1] #last_row
    fc = dat_masks[:,0] #first_column
    lc = dat_masks[:,-1] #last_column

    #Create lists for labels different from 0:
    list_fr = list() #fr - first row
    list_fc = list() #fc - first column
    list_lr = list() #lr - last row
    list_lc = list() #lc - last column
```

```
    #Create lists for number of labels:
    number_of_labels_fr = list() #first row
    number_of_labels_fc = list() #first column
    number_of_labels_lr = list() #last row
    number_of_labels_lc = list() #last column

    #Create lists for labels (each label occurs once):
    value_list_fr = list()
    value_list_fc = list()
    value_list_lr = list()
    value_list_lc = list()

    #Create lists for equivalent diameters:
    diameter_fr = list()
    diameter_fc = list()
    diameter_lr = list()
    diameter_lc = list()

    #Array containing relevant data for edge bubbles:
    edges = [[fr, list_fr, number_of_labels_fr, value_list_fr,␣
↪diameter_fr],
             [fc, list_fc, number_of_labels_fc, value_list_fc,␣
↪diameter_fc],
             [lr, list_lr, number_of_labels_lr, value_list_lr,␣
↪diameter_lr],
             [lc, list_lc, number_of_labels_lc, value_list_lc,␣
↪diameter_lc]]

    for i in edges:
        for k in i[0]: #Select labels different from 0 for fr, fc,␣
↪lr, lc
            if k!= 0:
                i[1].append(k)

        for s in range(lenmask+1):
            if s in i[1]:
                i[2].append(i[1].count(s)) #Number of labels
                i[3].append(s) #Labels

        for n in i[3]:
            i[4].append(diameter[n-1]) #Equivalent diameter

        a=dat_masks #Copy array with all masks
```

```
        t = i[3] #Labels
        l = i[2] #Numbers of edge pixels l
        d = i[4] #Equivalent diameter of edge bubbles d
        for z in range(len(i[3])): #Remove edge bubbles
            if l[z] > 1/4*d[z]:
                a[a == t[z]] = 0

    #Save data:
    np.savetxt('combined-masks_edge-bubbles-removed\\dat_masks_edge
    bubblesremoved_' + sample + '_' + number +'.txt', a, fmt='%i')

    #Number of edge bubbles:
    lenedge = len(value_list_fr) + len(value_list_fc) +␣
↪len(value_list_lr) + len(value_list_lc)
    #Number of bubbles:
    bubnum = len(np.unique(a))-1
    #Save data:
    with open('bubble-properties\\result_areas_' + sample + '_' +␣
↪number +'.txt', 'w') as t:
        t.write('total bubble area,total lamella area,total area,␣
↪total number of bubbles, number of edge bubbles\n')
        t.write(str(bubble_area) + ',' + str(lamella_area) + ',' +␣
↪str(total_area) + ',' + str(bubnum) + ',' + str(lenedge) + '\n')

    #Show masks:
    image = dats['img']
    image2 = image[10:shape[0]-30, 10:shape[1]-30]
    mask_RGB = plot.mask_overlay(image2, dat_masks)
    plt.imshow(dat_masks, cmap='Blues')#'flag')
    plt.axis('off')
    plt.savefig('result-images\\' + sample + '_' + number +'_masks.
↪jpg', dpi=400, bbox_inches='tight', pad_inches = 0)

    #Plot image with outlines of all bubbles overlaid in blue
    outlines = utils.outlines_list(dat_masks) #Outlines of the masks
    image = dats['img'] #Microscope image
    plt.imshow(image[10:shape[0]-30, 10:shape[1]-30], cmap='gray')
    plt.axis('off')
    #Draw outlines:
    for o in outlines:
        plt.plot(o[:,0], o[:,1], color='b')
    #Save image:
```

```
    plt.savefig('result-images\\' + sample + '_' + number␣
↪+'_outlines_overlay.jpg', dpi=400, bbox_inches='tight', pad_inches␣
↪= 0)


    #Bubble properties:
    props = regionprops_table(dat_masks,
                              properties=['label', 'area',
                                      'equivalent_diameter',␣
↪'feret_diameter_max', 'perimeter', 'perimeter_crofton'])

    #Calculate circularity
    circ = 4.*np.pi*props['area']/(props['perimeter_crofton']**2.)␣
↪#circularity

    #Conversion of pixel into um:
    label = props['label']
    area = pixeltoum * pixeltoum * props['area']
    equ_diam = pixeltoum * props['equivalent_diameter']
    feret = pixeltoum * props['feret_diameter_max']
    perimeter = pixeltoum * props['perimeter']
    perimeter_crofton = pixeltoum * props['perimeter_crofton']

    #Save data:
    with open('bubble-properties\\result_bubble-properties_' +␣
↪sample + '_' + number +'.txt', 'w') as t:
        t.write('label,area,equivalent_diameter,feret_diameter_max,
        perimeter,perimeter_crofton,circularity\n')
        for index_t in range(len(label)):
            t.write(str(label[index_t]) + ',' + str(area[index_t]) +␣
↪',' + str(equ_diam[index_t]) + ',' + str(feret[index_t]) + ',' +␣
↪str(perimeter[index_t]) + ',' + str(perimeter_crofton[index_t]) +␣
↪',' + str(circ[index_t]) + '\n')

    plt.clf()
    plt.close('all') #Close all the figure windows
```

[4]:
```
sample = 'sample1' #Sample name
number_list = ['0000', '0005', '0010', '0015', '0020', '0025',␣
 ↪'0030']
#Time steps
data_path_sb = 'data_sb\\' #Directory of masks of small bubbles
```

```
data_path_lb = 'data_lb\\' #Directory of masks of large bubbles
pixeltoum = 5.94460 #Pixel-to-um ratio

for file in number_list:
    dat1 = np.load(data_path_sb + 'EnhancedContrast-' + sample + '_'␣
 ↪+ file +
                '_seg.npy', allow_pickle=True).item()
    dat2 = np.load(data_path_lb + 'EnhancedContrast-' + sample + '_'␣
 ↪+ file +
        '_seg.npy', allow_pickle=True).item()
    r = two_bubblemasks(dat1, dat2, sample, file, pixeltoum)
```

[5]:
```
#Only one set of masks
def one_bubblemasks(dat, sample, number, pixeltoum):
    """Function that removes edge bubbles and displays the results.
    Parameters:
    dat ... bubble masks
    sample ... sample name
    number ... number of the sample which refers to a timestep
    pixeltoum ... pixel-to-um ratio"""

    dat_masks = dat['masks'] #Bubbles masks

    #Crop
    shape = dat_masks.shape #Shape of masks array
    dat_masks = dat_masks[10:shape[0]-30, 10:shape[1]-30]
    reshape = dat_masks.shape

    #Save data:
    np.savetxt('combined-masks\\dat_masks_' + sample + '_' + number␣
 ↪+'.txt', dat_masks, fmt='%i')

    #Total bubble area, total lamella area, total area - with edge␣
 ↪bubbles
    bubble_area = np.count_nonzero(dat_masks!=0)
    lamella_area = np.count_nonzero(dat_masks==0)
    total_area = bubble_area + lamella_area


    #Calculate area and equivalent diameter of each bubble:
    lenmask = len(dat['colors']) #Number of bubbles

    s = (3,lenmask+1) #Define tuple with dimensions 3 and lenmask+1
```

```
    c = np.zeros(s) #Array of shape s filled with zeros

    #Iterate over number of bubbles:
    for i in range(lenmask+1):
        first = c[0]
        first[i] = i+1 #Insert bubble labels
        second = c[1]
        second[i] = np.count_nonzero(dat_masks == i+1) #Insert␣
↪bubble areas
        third = c[2]
        #Calculate equivalent diameters from bubble areas and insert␣
↪them:
        third[i] = 2*np.sqrt(second[i]/np.pi)
    diameter = c[2] #Equivalent diameter

    #Select first row, first column, last row and last column
    fr = dat_masks[0] #first_row
    lr = dat_masks[-1] #last_row
    fc = dat_masks[:,0] #first_column
    lc = dat_masks[:,-1] #last_column

    #Create lists for labels different from 0:
    list_fr = list() #fr - first row
    list_fc = list() #fc - first column
    list_lr = list() #lr - last row
    list_lc = list() #lc - last column

    #Create lists for number of labels:
    number_of_labels_fr = list() #first row
    number_of_labels_fc = list() #first column
    number_of_labels_lr = list() #last row
    number_of_labels_lc = list() #last column

    #Create lists for labels (each label occurs once):
    value_list_fr = list()
    value_list_fc = list()
    value_list_lr = list()
    value_list_lc = list()

    #Create lists for equivalent diameters:
    diameter_fr = list()
    diameter_fc = list()
    diameter_lr = list()
```

```
    diameter_lc = list()

    #Array containing relevant data for edge bubbles:
    edges = [[fr, list_fr, number_of_labels_fr, value_list_fr,␣
↪diameter_fr],
             [fc, list_fc, number_of_labels_fc, value_list_fc,␣
↪diameter_fc],
             [lr, list_lr, number_of_labels_lr, value_list_lr,␣
↪diameter_lr],
             [lc, list_lc, number_of_labels_lc, value_list_lc,␣
↪diameter_lc]]

    for i in edges:
        for k in i[0]: #Select labels different from 0 for fr, fc,␣
↪lr, lc
            if k!= 0:
                i[1].append(k)

        for s in range(lenmask+1):
            if s in i[1]:
                i[2].append(i[1].count(s)) #Number of labels
                i[3].append(s) #Labels

        for n in i[3]:
            i[4].append(diameter[n-1]) #Equivalent diameter

        a=dat_masks #Copy array with all masks
        t = i[3] #Labels
        l = i[2] #Numbers of edge pixels l
        d = i[4] #Equivalent diameter of edge bubbles d
        for z in range(len(i[3])): #Remove edge bubbles
            if l[z] > 1/4*d[z]:
                a[a == t[z]] = 0

    #Save data:
    np.savetxt('combined-masks_edge-bubbles-removed\\dat_masks_edge
    bubblesremoved_' + sample + '_' + number +'.txt', a, fmt='%i')

    #Number of edge bubbles:
    lenedge = len(value_list_fr) + len(value_list_fc) +␣
↪len(value_list_lr) + len(value_list_lc)
    #Number of bubbles:
```

```
    bubnum = len(np.unique(a))-1
    #Save data:
    with open('bubble-properties\\result_areas_' + sample + '_' +␣
↪number +'.txt', 'w') as t:
        t.write('total bubble area,total lamella area,total area,␣
↪total number of bubbles, number of edge bubbles\n')
        t.write(str(bubble_area) + ',' + str(lamella_area) + ',' +␣
↪str(total_area) + ',' + str(bubnum) + ',' + str(lenedge) + '\n')

    #Show masks:
    image = dat['img']
    image2 = image[10:shape[0]-30, 10:shape[1]-30]
    mask_RGB = plot.mask_overlay(image2, dat_masks,
                        colors=np.array(dat['colors']))
    plt.imshow(dat_masks, cmap='Blues')
    plt.axis('off')
    plt.savefig('result-images\\' + sample + '_' + number +'_masks.
↪jpg', dpi=400, bbox_inches='tight', pad_inches = 0)

    #Plot image with outlines of all bubbles overlaid in blue:
    outlines = utils.outlines_list(dat_masks) #Outlines of the masks
    image = dat['img'] #Microscope image
    plt.imshow(image[10:shape[0]-30, 10:shape[1]-30], cmap='gray')
    #Draw outlines:
    for o in outlines:
        plt.plot(o[:,0], o[:,1], color='b')
    #Save image:
    plt.savefig('result-images\\' + sample + '_' + number␣
↪+'_outlines_overlay.jpg', dpi=400, bbox_inches='tight', pad_inches␣
↪= 0)

    #Bubble properties:
    props = regionprops_table(dat_masks,
                              properties=['label', 'area',
                                          'equivalent_diameter',␣
↪'feret_diameter_max', 'perimeter', 'perimeter_crofton'])

    #Calculate circularity:
    circ = 4.*np.pi*props['area']/(props['perimeter_crofton']**2.)␣
↪#circularity

    #Conversion of pixel into um:
```

```
    label = props['label']
    area = pixeltoum * pixeltoum * props['area']
    equ_diam = pixeltoum * props['equivalent_diameter']
    feret = pixeltoum * props['feret_diameter_max']
    perimeter = pixeltoum * props['perimeter']
    perimeter_crofton = pixeltoum * props['perimeter_crofton']

    #Save data:
    with open('bubble-properties\\result_bubble-properties_' +␣
↪sample + '_' + number +'.txt', 'w') as t:
        t.write('label,area,equivalent_diameter,feret_diameter_max,
        perimeter,perimeter_ crofton,circularity\n')
        for index_t in range(len(label)):
            t.write(str(label[index_t]) + ',' + str(area[index_t]) +␣
↪',' + str(equ_diam[index_t]) + ',' + str(feret[index_t]) + ',' +␣
↪str(perimeter[index_t]) + ',' + str(perimeter_crofton[index_t]) +␣
↪',' + str(circ[index_t]) + '\n')

    plt.clf()
    plt.close('all') #Close all the figure windows
```

[6]:
```
sample = 'sample1' #Sample name
number_list = ['0000', '0005', '0010', '0015', '0020', '0025',␣
↪'0030']
#Time steps
data_path_sb = 'data_sb\\' #Directory of bubble masks
pixeltoum = 1/0.16822 #Pixel-to-um ratio

for file in number_list:
    dat = np.load(data_path_sb + 'EnhancedContrast-' + sample + '_'␣
↪+ file + '_seg.npy', allow_pickle=True).item()
    r = one_bubblemasks(dat, sample, file, pixeltoum)
```

[7]:
```
#Time steps:
time = [0, 5, 10, 15, 20, 25, 30]

sample_list = ['sample1'] #List with sample names
#List with numbers of the sample (time steps):
number_list = ['0000', '0005', '0010', '0015', '0020', '0025',␣
↪'0030']

limit = 60 #60 um - 10 pixels
```

```
for sample in sample_list:
    mean_bubble_diameter = list()
    std_bubble_diameter = list()

    with open('results\\mean_values_' + sample + '.txt', 'w') as t:
        t.write('label,mean area/ um^2,std area,mean␣
↪equivalent_diameter/ um,std equivalent_diameter,smallest␣
↪equivalent_diameter/ um,largest equivalent_diameter/ um,median␣
↪equivalent_diameter/ um,total perimeter/ um,mean␣
↪circularity,dispersity\n')
    for number in number_list:
        bubble_dat_num = np.
↪loadtxt('bubble-properties\\result_bubble-properties_' + sample +␣
↪'_' + number +'.txt', unpack=True, delimiter=',', skiprows=1)
        area = bubble_dat_num[1] #Bubble area
        area_mean = np.mean(area) #Mean of bubble area
        area_std = np.std(area) #Standard deviation of bubble area
        equ_diam = bubble_dat_num[2] #Equivalent diameter
        equ_diam_mean = np.mean(equ_diam)
        mean_bubble_diameter.append(equ_diam_mean)
        equ_diam_std = np.std(equ_diam)
        std_bubble_diameter.append(equ_diam_std)
        smallest_diam = np.min(equ_diam) #Smallest equivalent␣
↪diameter
        largest_diam = np.max(equ_diam) #Largest equivalent diameter
        equ_diam_median = np.median(equ_diam) #Median of equivalent␣
↪diameter
        croftonp = bubble_dat_num[5] #Crofton perimeter
        perim_sum = np.sum(croftonp) #Total perimeter of all bubbles
        circularity = bubble_dat_num[6] #Circularity
        circ_arr=np.zeros(len(circularity))
        for i in range(len(equ_diam)):
            if equ_diam[i]>limit: #Only bubbles > limit considered
                circ_arr[i] = circularity[i]
        circ_arr2=circ_arr[circ_arr != 0] #Remove zero elements
        circ_mean = np.mean(circ_arr2)
        area_average_weighted = np.average(area, weights=area) #Area␣
↪weighted average of area
        disp = area_average_weighted/area_mean #Dispersity
        with open('results\\mean_values_' + sample + '.txt', 'a') as␣
↪t:
```

```
            t.write(number + ',' + str(area_mean) + ',' +␣
↪str(area_std) + ',' + str(equ_diam_mean) + ',' + str(equ_diam_std)␣
↪+ ',' + str(smallest_diam) + ',' + str(largest_diam) + ',' +␣
↪str(equ_diam_median) + ',' + str(perim_sum) + ',' + str(circ_mean)␣
↪+ ',' + str(disp) + '\n')
```

Here the quotation from the supporting information of [302] ends.

A.3. Versions of libraries used in Python

Library	Version
cellpose	2.0.5
cv2	4.6.0
glob2	0.7
matplotlib	3.3.4
numpy	1.20.1
PIL	8.2.0
pykuwahara	8.2.0
scipy	0.3.2
skimage	0.18.1

B. Supplementary information: HP-BSA interactions

This supplementary information refers to Chapter 4.

B.1. Sodium dodecyl sulfate-polyacrylamid gel electrophoresis

Figure B.1 shows the results of a SDS-PAGE of aqueous solutions of HP, BSA and mixtures of HP and BSA with and without reducing agent each. The wells with pure

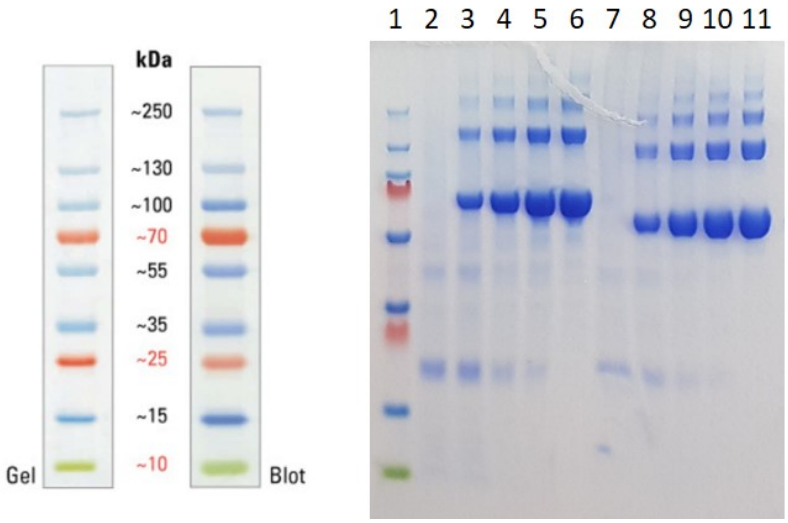

Figure B.1.: SDS-PAGE of aqueous solutions (0.1 wt%) of HP, BSA and their mixtures. (1) Marker, (2) HP, (3) HP-BSA 3:1, (4) HP-BSA 1:1 (5) HP-BSA 1:3 and (6) BSA with reducing agent each, (7) HP, (8) HP-BSA 3:1, (9) HP-BSA 1:1 and (10) HP-BSA 1:3 and (11) BSA each without reducing agent.

HP and pure BSA solutions show the characteristic pattern as observed in Figure 4.2. The SDS-PAGE of the mixtures of BSA and HP show the addition of BSA and HP with intensities according to the ratio of the mixture. However, no signs of interaction of BSA and HP are seen. The samples without reducing agent show the same patterns as the ones with reducing agents, which are shifted to lower molecular weights. These

shifts can be explained by not completely unfolded polypeptides, which lead to a faster migration through the gel than that related purely to the molecular mass [277]. Also in the case without reducing agent, no signs of interaction of HP and BSA are detected.

B.2. Surface coverage for BAM experiments

The amount of protein needed for film formation at the air-water interface was roughly estimated as a starting point of BAM experimets. The radius of BSA is $R_{BSA} = 3.4\,\mathrm{nm}$ and its molecular weight is $M = 66.430\,\mathrm{Da}$ [461]. In this approximation BSA is assumed a sphere with radius R_{BSA}. The maximum packing density of circles in 2D (air-water interface) is $\eta = \frac{\pi}{2\sqrt{3}} = 0.9069$. This value determines how much of the air-water interface is covered by circles (BSA molecules). The area that one BSA molecule takes is given by $A_{BSA} = \pi R_{BSA}^2$ and the area of the air-water interface is $A_I = \frac{\pi}{4} d_t^2 = 1963.5\,\mathrm{mm}^2$ with the trough diameter $d_t = 50\,\mathrm{mm}$. Hereof results the number of BSAs at the interface

$$N = \frac{\eta A_I}{A_{BSA}} = \frac{\eta d_t^2}{4R_{BSA}^2} = 4.9 \times 10^{13}$$

These surface molecules have a total weight of $m_{sm} = NM = 5.40 \times 10^{-9}\,\mathrm{kg}$. If a density of $\rho = 1\,\mathrm{kg\,L^{-1}}$ is assumed, the required volume of a 0.4 wt% BSA solution to cover the air-water interface is therefore

$$V = \frac{m_{sm}}{c\rho} = \frac{5.40 \times 10^{-9}\,\mathrm{L}}{0.004} = 1.35\,\mu\mathrm{L}$$

.

B.3. Influence of AFM substrate

Figure B.2 shows AFM images of an empty HOPG substrate. The substrate appears very flat and clearly looks different than the investigated samples. Therefore, even though the BSA samples look quite flat, it can be concluded, that these indeed show the sample.

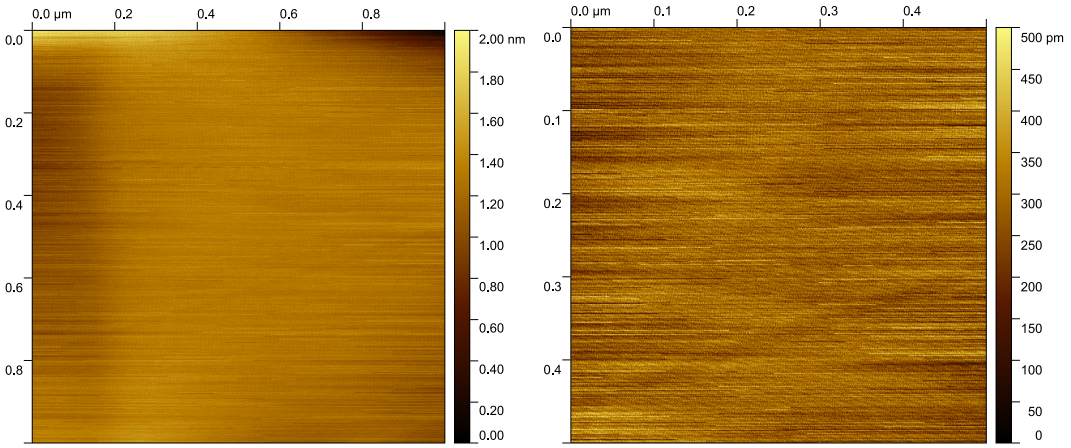

(a) scan size 1 µm, legend 2 nm (b) scan size 0.5 µm, legend 500 pm

Figure B.2.: AFM of empty HOPG.

Figure B.3 shows dried droplets of 4 wt% BSA solutions on different substrates commonly used for AFM: HOPG, mica and silicium. When comparing the images no significant differences in the arrangement of BSA molecules are detected. It can therefore be concluded that the substrate does not influence the observed BSA arrangement.

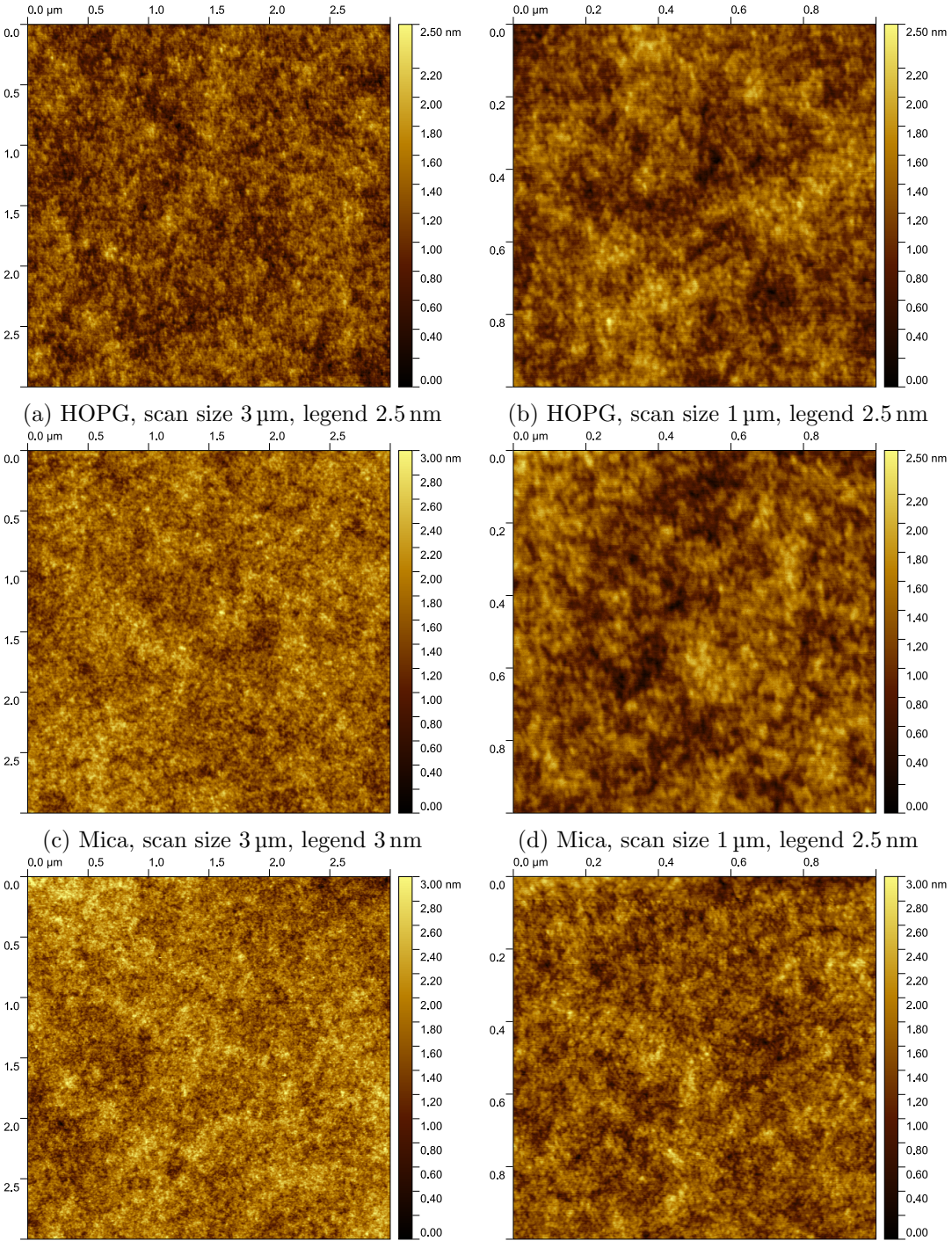

(a) HOPG, scan size 3 µm, legend 2.5 nm

(b) HOPG, scan size 1 µm, legend 2.5 nm

(c) Mica, scan size 3 µm, legend 3 nm

(d) Mica, scan size 1 µm, legend 2.5 nm

(e) Silicium, scan size 3 µm, legend 3 nm

(f) Silicium, scan size 1 µm, legend 3 nm

Figure B.3.: AFM of dried droplets of 4 wt% BSA solutions on different substrates.

B.4. Additional AFM images of HP rodlets

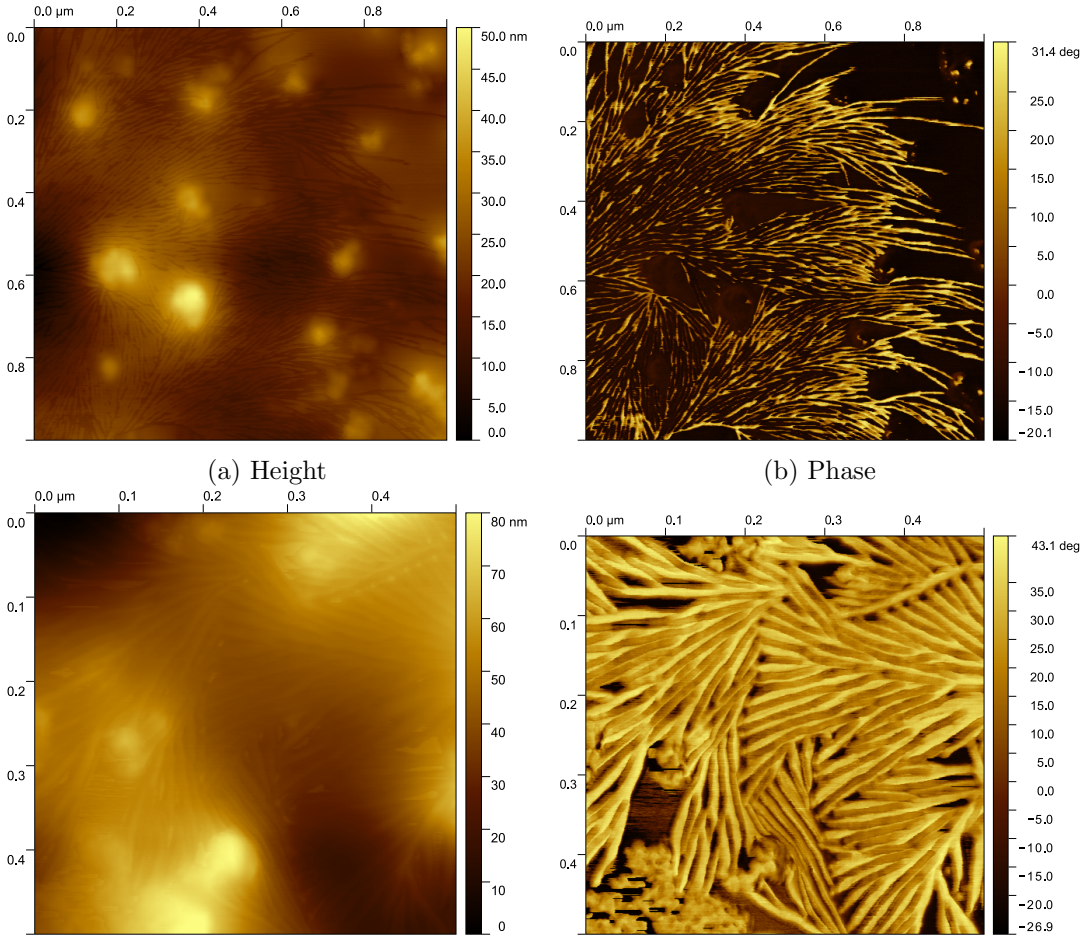

(a) Height (b) Phase

(c) Height (d) Phase

Figure B.4.: AFM height profiles and phases of a rodlet structure observed on a dried droplet of a 0.04 wt% HP solution.

C. Supplementary information: Addition of hydrocolloids

This is supplementary information referring to Chapter 5.

C.1. Viscosity of a BSA solution

Figure C.1 shows the viscosity measured for a pure BSA solution as well as the low-torque limit and the secondary flow limit, which are shown by dashed lines. For

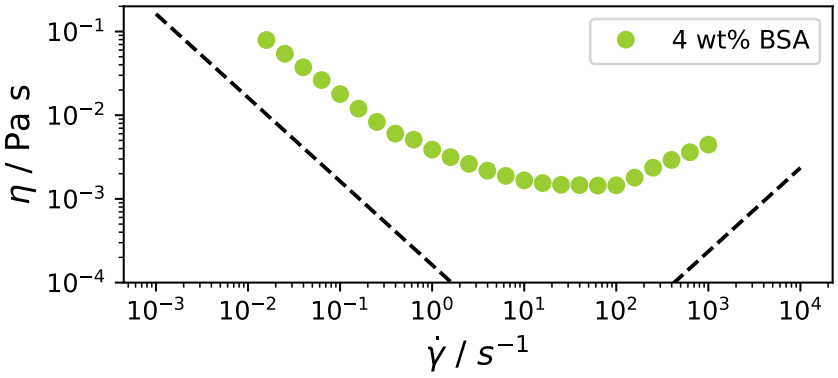

Figure C.1.: Dynamic viscosity of a pure BSA solution (4 wt%).

samples with a low viscosity, misinterpretation of results is likely, if experimental windows are not attended and measurements are performed at non-ideal conditions. In this case, for an actually Newtonian fluid apparent shear thinning and shear thickening behavior can be observed. Ostensible shear thinning behavior at low shear rates can be measured due to low-torque limit effects. At high shear rates an apparent, but not real, shear thickening effect can be observed due to secondary flow effects. [462] The low-torque limit and secondary flow limit were estimated by considering parameters of the geometry and the rheometer as described by Ewoldt et al. [462]. Although the calculated technical limits are not reached in this case, they seem to approximate asymptotically, from which it can be concluded that the course of the measurement is influenced by these effects.
Therefore, the results of measuring the viscosity of BSA-solutions without any additives cannot be interpreted safely. However, it is certain, that the viscosity is much lower than that of solutions with added polysaccharides.

C.2. Estimation of the shear rate during application of the ultra turrax T 25

For convenience and readability Figure C.2 shows the photos of the ultra turrax T 25 tool already depicted in Figure 3.3 again. It consists of a stator on the outside, which

(a) (b)

Figure C.2.: Ultra turrax T 25 tool S 25 N - 10 G as viewed (a) from the side and (b) from below.

has the shape of a cylinder wall with some slots in the lower part. Inside there is a rotor, which consists of two blades. During application of the tool, the rotor moves with high speed. Due to this rotation the sample is automatically drawn axially into the tool and then forced radially through the slots (cf. Subfigure C.3c).

Figure C.3 shows sketches of the setup of the ultra turrax T 25 tool and its working principle.

A rough estimation of the shear rate in the gap between rotor and stator is given in the following for a rotational frequency of 20 000 rpm.

Calculation of radius r and distance h (dimensions of the tool as shown in Figure C.3):

$$r = \frac{7.4\,\text{mm}}{2} = 3.7\,\text{mm}$$

$$h = \frac{(8.2 - 7.4)\,\text{mm}}{2} = 0.4\,\text{mm}$$

Time for one revolution (at a rotational frequency of 20 000 rpm):

$$T = \frac{1}{20000}\,\text{min} = \frac{60}{20000}\,\text{s} = 0.003\,\text{s}$$

Shear rate:

$$\dot{\gamma} = \frac{v}{h} = \frac{2\pi r}{Th} \approx 19\,373\,\text{s}^{-1}$$

where v is the velocity at the outside of the moving plate and all other variables are as given above and in Figure C.3. Therefore, the highest shear rate applied during foam formation is of the order of $10^4\,\text{s}^{-1}$.

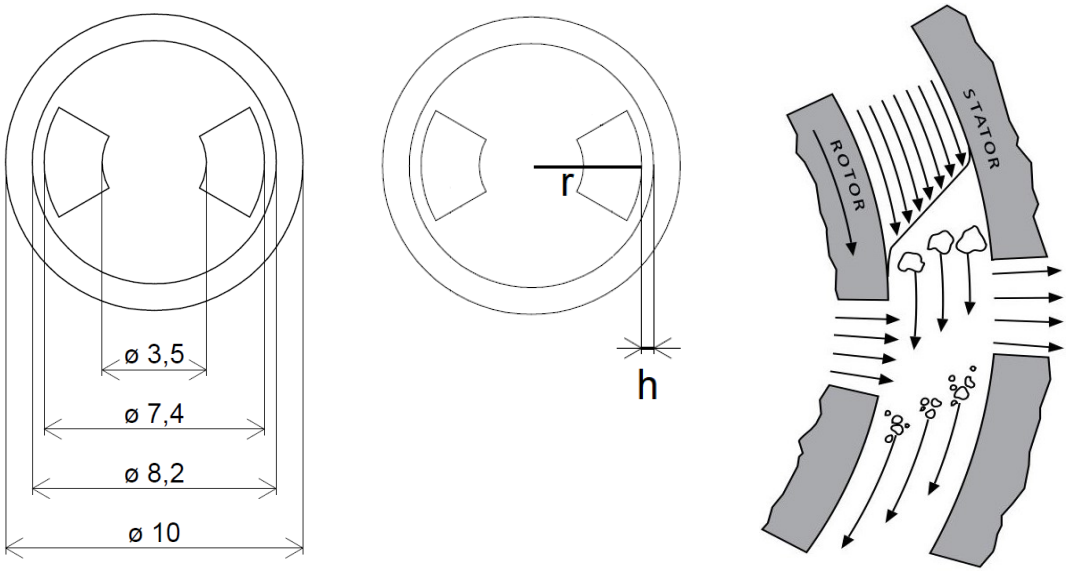

(a) (b) (c)

Figure C.3.: Setup and working principle of the ultra turrax T 25 tool S 25 N - 10 G. (a) Dimensions of the tool as viewed from below. (b) Definition of the gap size h (distance between rotor and stator) and the radius of the rotor r. (c) Rotor/stator working principle as described in the manual from IKA [305]. All dimensions are given in mm. Subfigure (c) reproduced from [305] with permission of IKA-Werke GmbH & Co. KG, Staufen, Germany.

C.3. Test of the threshold-based method to determine the mean equivalent bubble size

In the threshold-based method used, connected white pixels were counted as a bubble and its area determined by counting the number of all connected white pixels. It could potentially happen that parts of lamellae are represented by white pixels and were therefore counted as a bubble. Additionally, if a black pixel in the lamellae was missing, two bubbles could be counted as one bubble of a larger size. These effects cannot be controlled by the current method. For this reason, in one image the white lamellae were colored black manually. To test the method, then the results of this image were compared with the one without manual correction of the binary image. The images with and without pixel correction are shown in Figure C.4

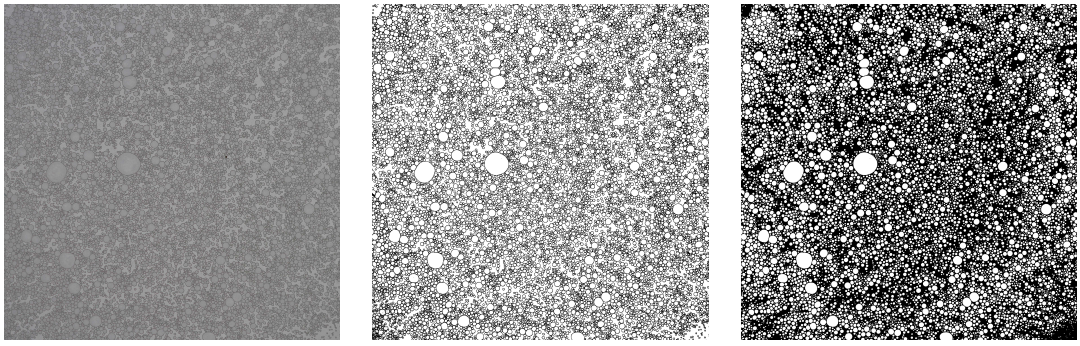

(a) (b) (c)

Figure C.4.: Test of the preliminary approach to measure mean bubble size. (a) Original image of a foam formed of an aqueous solution of 4 wt% BSA + 0.4 wt% guar gum. (b) Binary image (thresholded) without manual pixel corrections. (c) Binary image of the same image with lamellae colored black manually.

The mean equivalent bubble diameter determined for the image in Figure C.4b is 102.1 µm and for the image in Figure C.4c it is 96.3 µm. The mean value of the mean equivalent diameter determined with this method for the images of three independent identical samples is (95.9 ± 7.4) µm. Therefore, the deviation between the corrected and uncorrected images was considered as being within the range of the uncertainty of the measurement.

D. Supplementary information: Influence of pH variation

This appendix provides supplementary information to Chapter 6.

D.1. Estimation of the overlap concentration of BSA solutions

The overlap concentration c^* for random coils in good solvent can be estimated by

$$\frac{M}{N_A R_g^3} \simeq c^* \simeq \frac{3M}{4\pi N_A R_g^3} \tag{D.1}$$

where N_A denotes Avogadro's number, $M = M_W N_A$ is the polymer molar mass (M_W is the molecular weight) and R_g is the radius of gyration [463, 464]. Using literature data for R_g and M_W, the overlap concentration can be estimated as shown in Table D.1.

	Smilgies and Folta-Stogniew [143]	Mylonas and Svergun [144]	Akiyama [145]
M_W / kDa	67.1	66.0	66.4
R_g / nm	2.76	2.99	2.93
$\frac{M}{N_A R_g^3}$ / $\mathrm{g\,mL^{-1}}$	5.30	4.10	4.38
$\frac{3M}{4\pi N_A R_g^3}$ / $\mathrm{g\,mL^{-1}}$	1.27	0.98	1.05

Table D.1.: Estimation of the overlap concentration of BSA solutions.

From table D.1 it can be concluded that $c^* \gtrsim 1\,\mathrm{g\,mL^{-1}}$. Measurements in this study were performed for protein concentrations of 4 wt% or lower. For this concentration holds $c = 4\,\mathrm{wt\%} \approx 0.04\,\mathrm{g\,mL^{-1}} < c^*$. Therefore, it can be concluded that the experiments were performed at concentrations below the overlap concentration.

D.2. Swissmodel data

Figures D.1, D.2 and D.3 show information provided by swissmodel.expacy.org [146] about the charge and hydrophobicity of the amino acids in the primary structure, the helical content of BSA and the location of cysteine bonds.

D. Supplementary information: Influence of pH variation

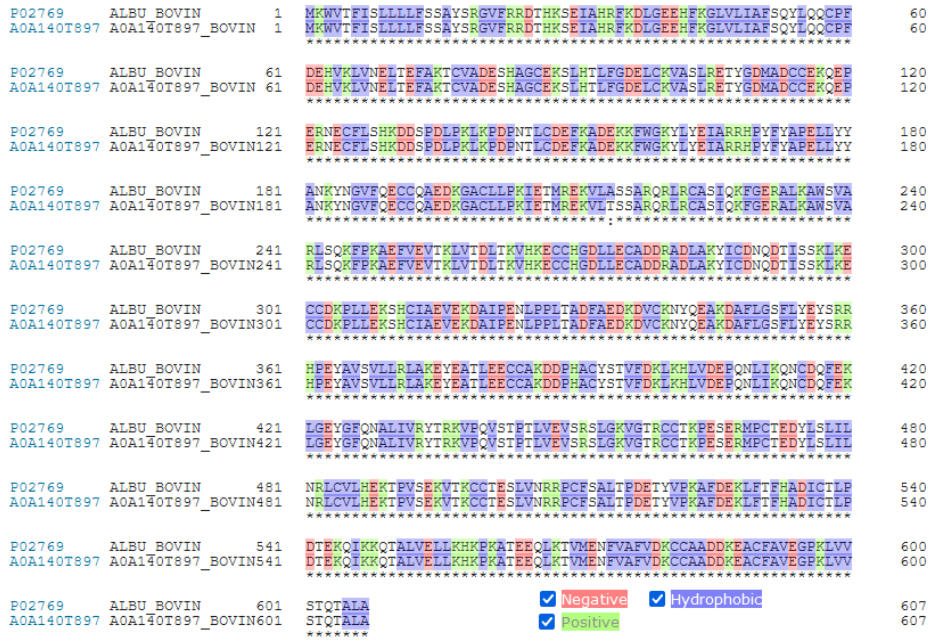

Figure D.1.: Primary structure of BSA where electrostatic and hydrophobic properties of the amino acids are highlighted. Reproduced from `https://swissmodel.expasy.org/` [146], licensed under CC BY-SA 4.0 license. For more information, visit `https://swissmodel.expasy.org/docs/terms_of_use`.

Figure D.2.: Information about the secondary structure of BSA. Reproduced from `https://swissmodel.expasy.org/` [146], licensed under CC BY-SA 4.0 license. For more information, visit `https://swissmodel.expasy.org/docs/terms_of_use`.

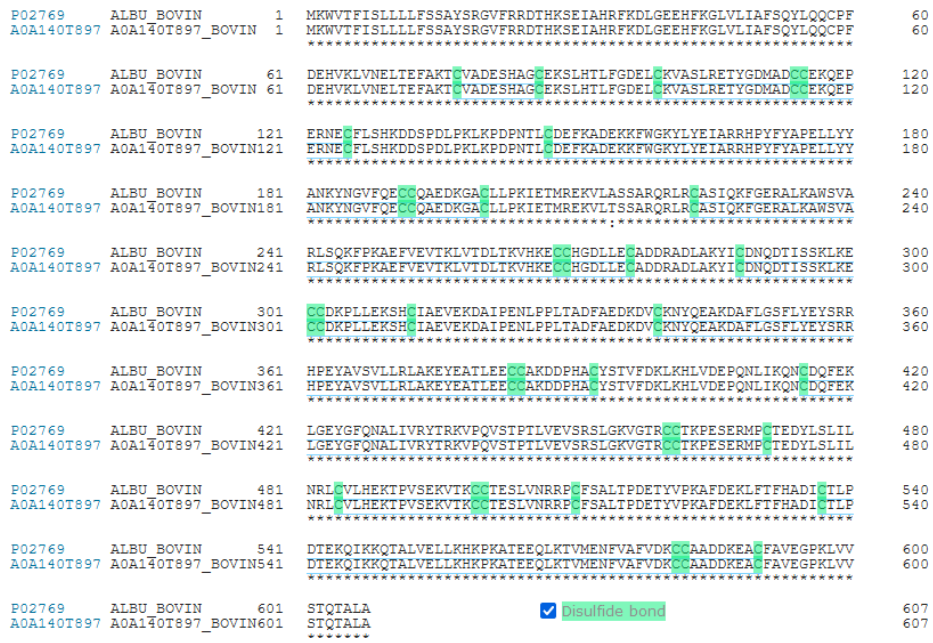

Figure D.3.: Location of disulfide bonds in the primary structure of BSA . Reproduced from `https://swissmodel.expasy.org/` [146], licensed under CC BY-SA 4.0 license. For more information, visit `https://swissmodel.expasy.org/docs/terms_of_use`.

D.3. Discussion on the determination of the isoelectric point of BSA

The isoelectric point (IEP, in literature also pI) of a component of a mixture, for example charged particles in an aqueous solution, is the "pH at which there is no net motion in an electric field" [465]. At this pH value, "the zeta potential (or surface potential), equivalent to the net charge of the molecule including bound ions, is zero" [154]. It has to be distinguished from the isoionic point (IIP), which describes the pH value at which the number of positive and negative charges of a zwitterionic molecule is equal [154]. A common method to determine the isoelectric point experimentally, is to put an aqueous solution of the charged particle of interest into an electric field and to measure the electrophoretic velocity of the charged particles of the solution using dynamic light scattering. From the electrophoretic velocity and the applied electric field strength then the zeta potential is calculated. [151–153] Commonly, determination of the zeta potential is performed using devices such as the Zetasizer Nano ZS (Malvern Panalytical Ltd, UK) used in this study [83, 151–154]. Subsequently, the measured zeta potentials are plotted over pH. Since the IEP is the pH value where the zeta potential equals zero, it can then directly be read from the plot [42]. Since proteins carry a net charge depending on the solution pH, this method can be applied to determine the IEP of a protein. Alternatively, IEPs of proteins can also be calculated from the amino acid sequence of the protein and taking into account the pK values of

Zeta potential	Method	Protein concentration	Temperature °C	Buffer/ Salt concentration	Ref.
5.2 ± 0.1	exp	$150\,\mu mol\,L^{-1}$	24	–	[42]
5.1 (independently of ionic strength) 5.1 (MES buffer) 4.7 (MES-TRIS buffer) 5.5	exp theo	500 ppm to 8000 ppm	20 ± 0.1	Mes, Tris, Mes-Tris buffers, 10^{-3}, $5 \cdot 10^{-3}$, 10^{-2}, $0.15\,mol\,L^{-1}$ NaCl	[153]
4.2-4.7 5.27 zero salt	exp	$1\,g\,L^{-1}$	25	0.01, 0.10, 0.25, $0.50\,mol\,L^{-1}$ NaCl	[154]
4.7	exp	$15.0\,g\,L^{-1}$	25.0 ± 0.5		[83]
4.7	exp	$0.044\,mmol\,L^{-1}$	20		[151]
5.4 5.4	exp theo				[152]
5.4	theo				[155]

exp ... measured experimentally with Zetasizer Nano ZS (Malvern Panalytical Ltd, UK)
theo ... calculated from amino acid composition of protein

Table D.2.: Literature overview: IEP of BSA.

the side chains [153, 155].

An overview of IEP values of BSA found in the literature is provided in Table D.2.

Different values have been reported in the literature for the IEP of BSA varying from pH 4.2 to 5.5 [42, 83, 151–155]. Here, calculated IEPs (5.4-5.5 [152, 153, 155]) were mostly slightly higher than experimentally measured IEPs of BSA (4.2-5.4 [42, 83, 151–154]). Depending on the model used for calculating the IEP these differences can be explained by the assumptions made. These include the assumption of the theoretical model that all ionizable amino acid groups were accessible to the water; however, in reality a small part is not accessible to the water [153]. Other reasons are given by the shape of the BSA molecule, which was approximated with a sphere, however using an ellipsoid of revolution may be more appropriate. Furthermore, the dipole moment of BSA may cause additional effects. In addition, the surface charge of the BSA molecule is distributed inhomogeneously across the surface and may cause an electric field that is not spherically symmetric. [154]

Furthermore, it was found that the exact determination of points of zero charge / potential of proteins depends not only on the solution pH but also on the measurement conditions. In this regard it is worthwhile to mention, that the measured IEP of a protein depends also on the type of background salt solution used in the measurement as well as on the concentration of the background salt solution. It was found, that an increase of ionic strength (i.e. salt concentration) shifts the IEP values to lower pH, since a lower BSA zeta potential was obtained as the salt concentration increased [151, 154]. The effect, that (counter)ions adhered to the particle surface weaken the surface potential, is called *surface potential dampening* [152]. On the other hand, it has been

claimed that the IEP of BSA was independent of the ionic strength of the solution, but dependent on the buffer used [153]. In this thesis no buffer or background salt solution were used.
The variation of the temperature of the sample showed that temperature has a much smaller impact on the zeta potential than pH. However, the most significant increase of the zeta potential was observed in the temperature range of 15-30°C where the zeta potential increased with rising temperature [151].
Typically, with increasing pH the zeta potential decreases. Consequently, positive zeta potential values are found at a pH below the IEP and negative zeta potentials at pH values above the IEP [152]. Due largely to the lack of interparticle electrostatic repulsion, proteins commonly aggregate near their IEP [152, 154].

D.4. Evaporation during foam height measurement

To test for evaporation during the foam height measurement, a sample of 4 wt% BSA in ultrapure water was weighted directly after foam formation and after 30 min. The humidity in the room was 39.7 % and the room temperature was 24.0 °C during this measurement. The weight at the beginning was 1.559 g. After 30 min, which is the period of the foam height measurements, the sample weight was 1.552 g. These are 99.6 % of the initial weight. For this reason, the influence of evaporation on the foam height decay was considered negligible. Additionally, the sample weight was measured after 120 min, which amounted to 1.546 g. These are still 99.2 % of the initial weight. For comparison, the foam height reduces to about 55 % after 30 min. This means that drainage of liquid from the foam and escape of gas from the foam have a much stronger influence on the decay of the foam height than evaporation.

D.5. Logarithmic and double logarithmic plots of the liquid in the foam

Logarithmic and double logarithmic representations of the height of liquid in foam are shown in Figure D.4. The data shows a similar course as logarithmic and double logarithmic plots of the foam height (cf. Figure 6.12). The height of liquid in foam can be fitted with a linear function on double logarithmic scales, which suggests a power law decay. Similarly to the foam height plots, also here a slight inflection is observed for the foams at pH 7 and pH 9, which results from a stronger drainage at early times, when the foam is still wet.

D.6. Logarithmic and double logarithmic plots of the drainage

Figure D.5 shows the logarithmic and double logarithmic representations of the measured heights of drained liquid. In neither representation the data is well represented by linear fitting.
The liquid height h_l is related to the height of liquid in foam h_{lif} via

$$h_l = h_b - h_{lif} \tag{D.2}$$

where h_b is the height of liquid before foam formation. From this relation follows, that only h_l or h_{lif} can be represented by a linear function in double logarithmic representation. Since h_{lif} is represented by a power law (see Subsection D.5), h_l is not.

$$h_l = h_b - h_{lif} = h_b - h_{lif,0}t'^m \tag{D.3}$$

$$\log(h_l) = \log(h_b - h_{lif,0}t'^m) = \log(h_b(1 - \frac{h_{lif,0}}{h_b}t'^m)) = \log(h_b) + \log(1 - \frac{h_{lif,0}}{h_b}t'^m) \tag{D.4}$$

where $\log(h_b)$ is a constant and $\log(1 - \frac{h_{lif,0}}{h_b}t'^m) \neq m\log(t')$ and therefore does not show a linear relation in double logarithmic representation. For this reason, h_l is not assumed to follow a power law.

D.7. Logarithmic and double logarithmic plots of the gas in the foam

Figure D.6 shows the logarithmic and double logarithmic representations of the measured heights of gas in foam h_{gif}. These heights change less over time than the other determined heights (h_f, h_l and h_{lif}).

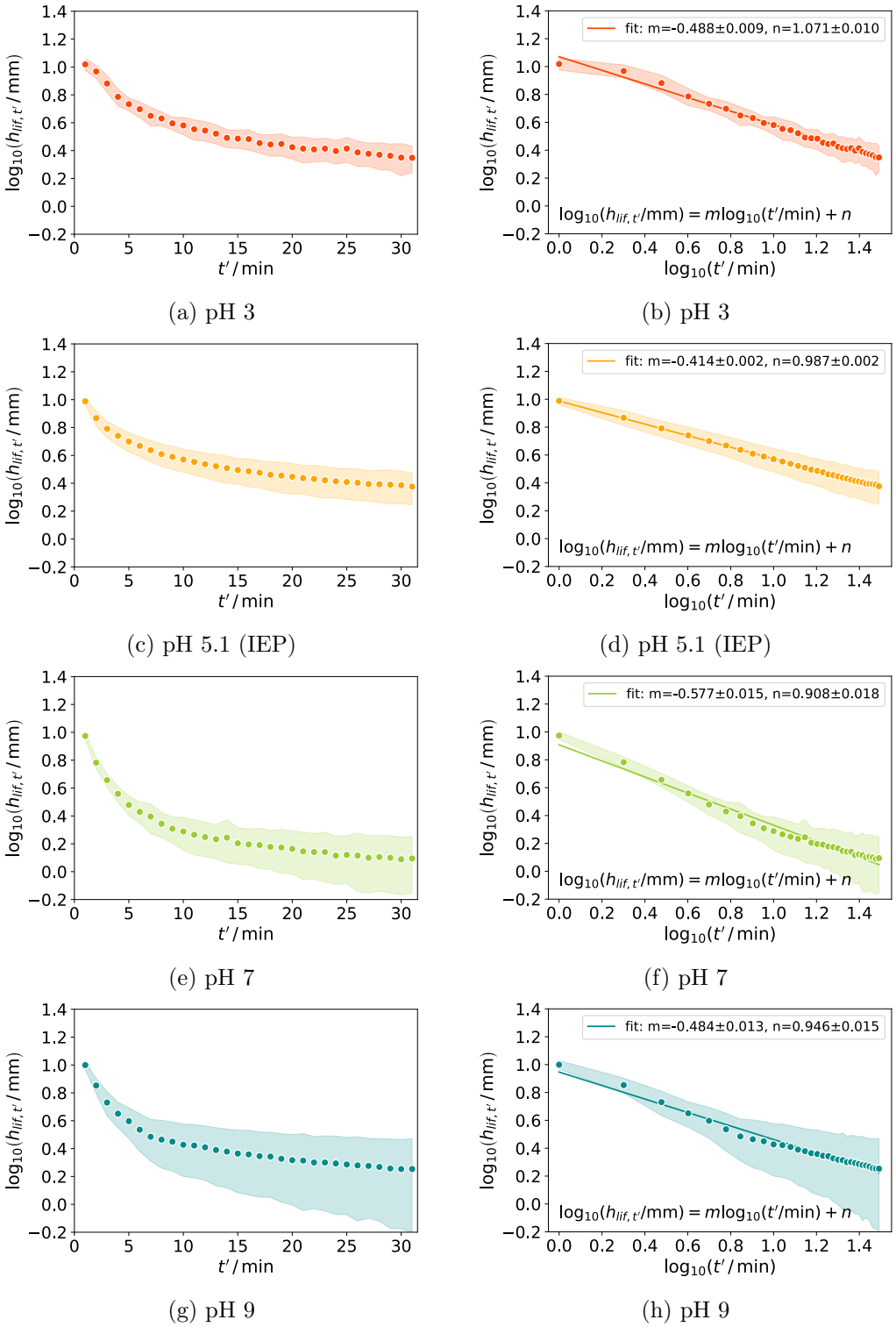

(a) pH 3 (b) pH 3

(c) pH 5.1 (IEP) (d) pH 5.1 (IEP)

(e) pH 7 (f) pH 7

(g) pH 9 (h) pH 9

Figure D.4.: Logarithmic (left) and double logarithmic (right) representation of the height of liquid in the foam over time of BSA-stabilized foams (4 wt%) at different pH values.

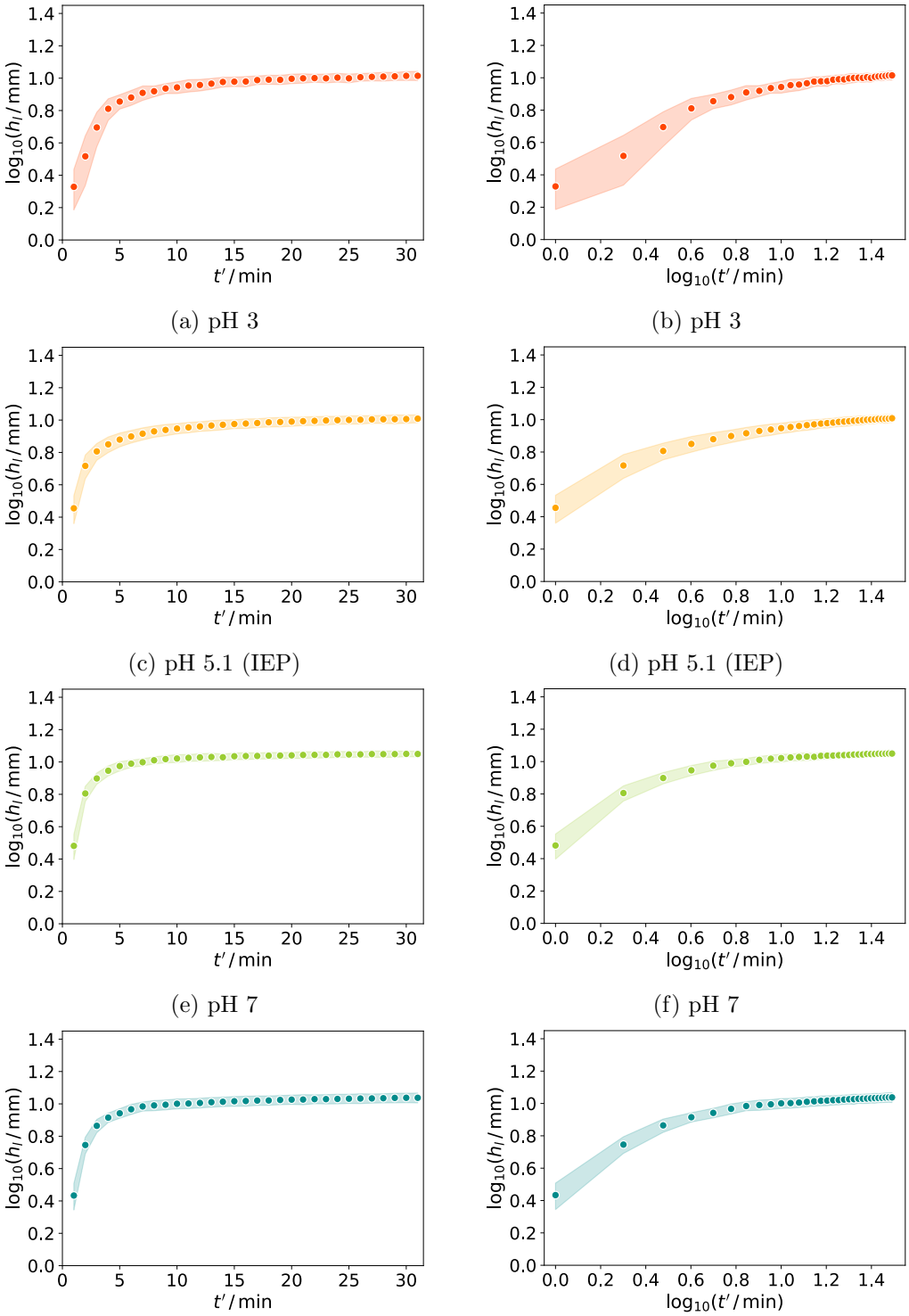

(a) pH 3 (b) pH 3

(c) pH 5.1 (IEP) (d) pH 5.1 (IEP)

(e) pH 7 (f) pH 7

(g) pH 9 (h) pH 9

Figure D.5.: Logarithmic (left) and double logarithmic (right) representation of the liquid height over time of BSA-stabilized foams (4 wt%) at different pH values.

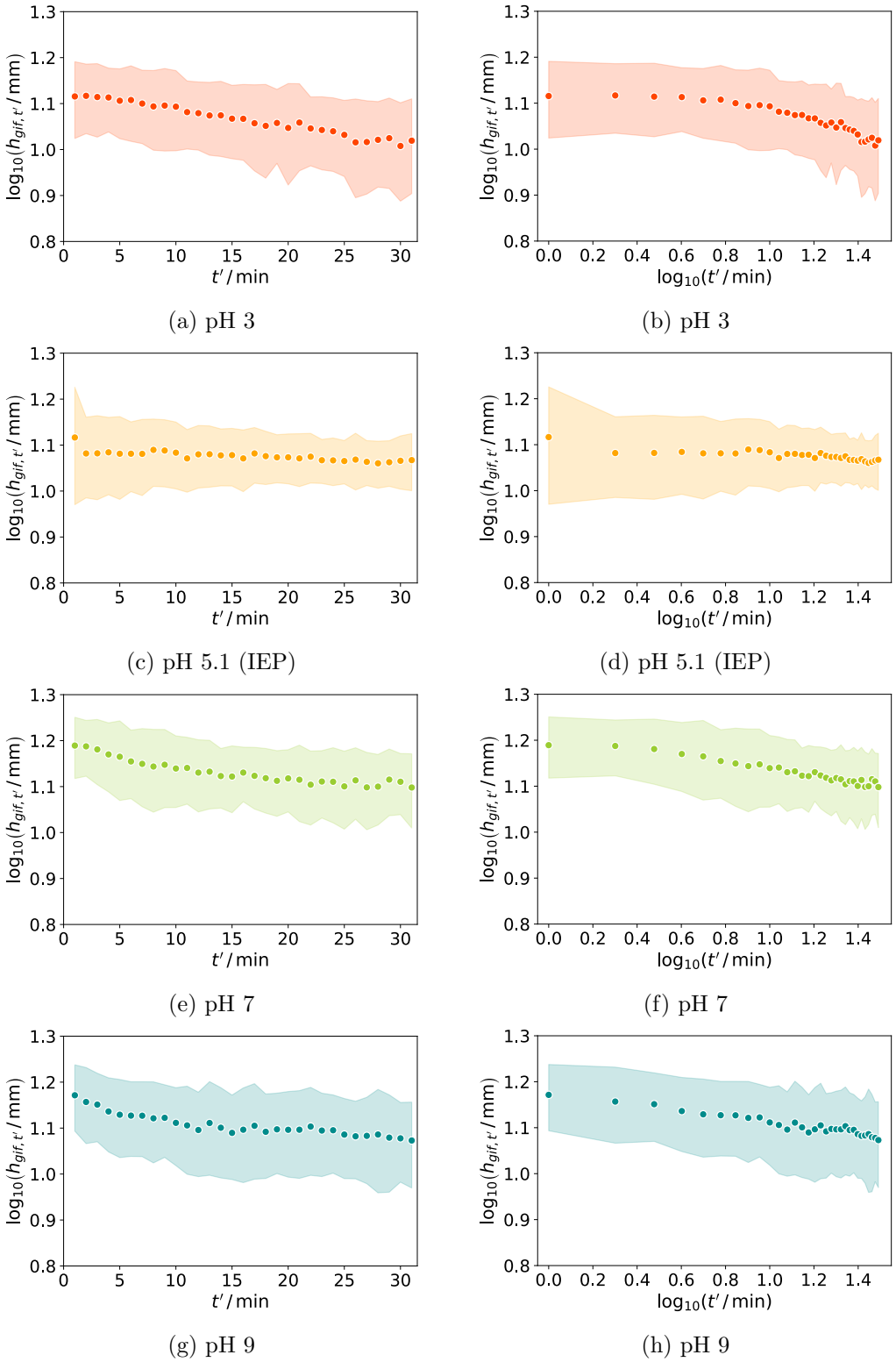

(a) pH 3

(b) pH 3

(c) pH 5.1 (IEP)

(d) pH 5.1 (IEP)

(e) pH 7

(f) pH 7

(g) pH 9

(h) pH 9

Figure D.6.: Logarithmic (left) and double logarithmic (right) representation of the height of gas in foam over time of BSA-stabilized foams (4 wt%) at different pH values.

D.8. Comparison of the bubble size analysis with and without manual correction

After segmentation with *Cellpose* some bubbles were not masked correctly. Especially, some tiny bubbles were not detected, but also for a few large bubbles the segmented mask did not exactly represent the shape of the bubble. Therefore, manual corrections were made in the *Cellpose* GUI. To check, how much these manual changes influence the evaluation of the data, analyses of measurements with and without manual corrections are compared.

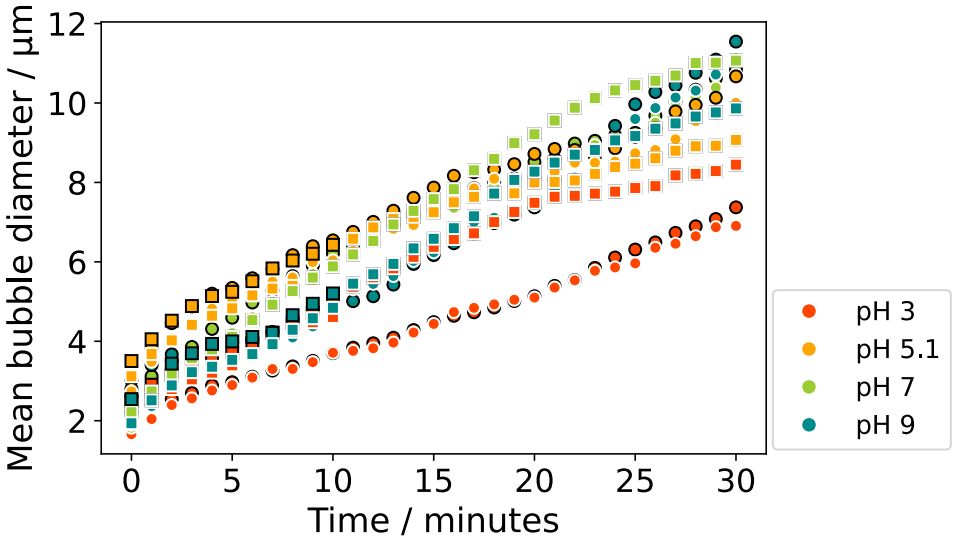

Figure D.7.: Effect of manual corrections on the mean equivalent bubble diameter. For each pH value two independent measurements of identically prepared samples are shown, which are marked with square and spherical symbols, respectively. For each sample manually corrected data is shown with white outline and uncorrected data with black outline.

Figure D.7 shows measurements of the mean equivalent bubble diameter. For the four different pH values, two measurements of identically prepared samples are shown each (square and spherical symbol). Furthermore, for each measurement the data without correction (black outlines) and with corrections (white outlines) are shown. The differences between uncorrected and manually corrected data are rather small. Slight deviations of the mean equivalent bubble diameters are detected, however the trends of the curves of corrected and uncorrected data are similar and the deviations are within the variations between two different measurements of identically prepared samples.
Figure D.8 shows the total perimeter of all bubbles in the image, i. e. the sum of the perimeters of all bubbles in the image. In this case, especially in the beginning the differences between uncorrected and manually corrected data are more significant.

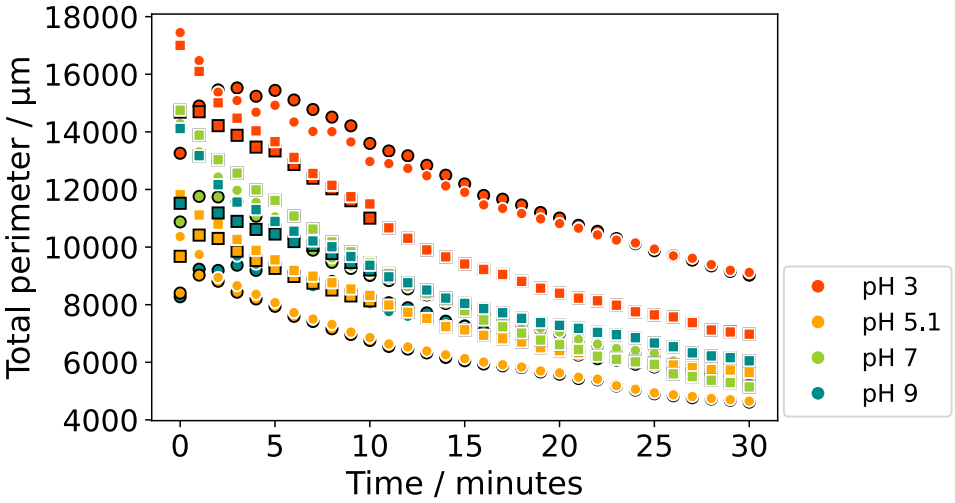

Figure D.8.: Effect of manual corrections on the total perimeter of all bubbles. For each pH value two independent measurements of identically prepared samples are shown, which are marked with square and spherical symbols, respectively. For each sample manually corrected data is shown with white outline and uncorrected data with black outline.

This deviation comes from the many tiny bubbles present at early times, which were not detected. Their perimeters add up to a large total perimeter. During ripening of the foam the mean equivalent bubble diameter increases due to coalescence and Ostwald ripening. Since many tiny bubbles have a larger total surface area than few large bubbles, the total perimeter decreases over time. On the other hand, spheres have the smallest surface in relation to their volume as compared to other shapes. Therefore, when the bubble shape changes to polyhedral, the surface area might increase, if the total gas volume would remain constant. However, some air escapes from the foam over time. For this reason, the shape changes make a minor contribution on the total perimeter. The main influence on the total bubble perimeter arises from the bubble size as is also seen when comparing the different pH values. The foams at pH 3 showed the smallest mean equivalent bubble diameters (cf. Figure 6.20) and the largest total perimeter. On the other hand, foams at the IEP start with the largest bubble sizes and the smallest total bubble perimeter.

D.9. Dynamic light scattering

From the DLS measurements the correlation function, which represents the intensity fluctuations of the particles in the solution, is obtained. The exponential decays of the correlation function were fitted by applying the CONTIN method [265–267] (regularized fit) using the ALV-correlator software. From this analysis the intensity over hydrodynamic radius was obtained. The main peak was fitted with a log-normal distribution function:

$$f(x) = \frac{A}{\sqrt{2\pi}\sigma x} \exp\left(-\frac{1}{2}\left(\frac{\log(x)-\mu}{\sigma}\right)^2\right) \tag{D.5}$$

where A is a constant factor, σ the standard deviation and μ the mean [466]. For log-normal distributions the median (also multiplicative or geometric expected value) is defined as $\mu^* := \mathrm{e}^{\mu}$ and the multiplicative (or geometric) standard deviation is given by $\sigma^* := \mathrm{e}^{\sigma}$. Furthermore, the interval of confidence, which contains 68.3 % of the values, is covered by the interval $[\mu^*/\sigma^*, \mu^* \cdot \sigma^*]$ for such distributions. [466] The most common value of the distribution is given by the mode $m_{mode} = \exp\left(\mu - \sigma^2\right)$ [467]. Figure D.9 shows exemplarily the peak fits at the 9 different scattering angles for a BSA solution at pH 3. From these fits the median μ^*, the multiplicative standard deviation σ^* and the interval of confidence $[\mu^*/\sigma^*, \mu^* \cdot \sigma^*]$ were obtained for each angle. Since each measurement was performed in triplicate, the mean values $\bar{\mu}^*$, $\bar{\sigma}^*$ and $\bar{m}_{mode}$ and the standard deviations $\Delta\mu$, $\Delta\sigma$ and Δm_{mode} of three identical samples were calculated for each angle. Subsequently, these values were plotted over the scattering angles as shown in Figures D.10, D.11, D.12 and D.13 for each pH value. To extrapolate these values to a scattering angle of 0°, each parameter was fitted with a linear function. The fit parameter n denotes the value extrapolated to 0° for each parameter ($\bar{\mu}^*$, $\bar{m}_{mode}$, $\bar{\mu}^*/\bar{\sigma}^*$ and $\bar{\mu}^* \cdot \bar{\sigma}^*$). $\bar{\mu}^*$ and $\bar{m}_{mode}$ serve as a measure of the hydrodynamic radius R_h and the confidence interval $[\bar{\mu}^*/\bar{\sigma}^*, \bar{\mu}^* \cdot \bar{\sigma}^*]$ as a measure of the width of the distribution. These values were used for the plot shown in Figure 6.10.

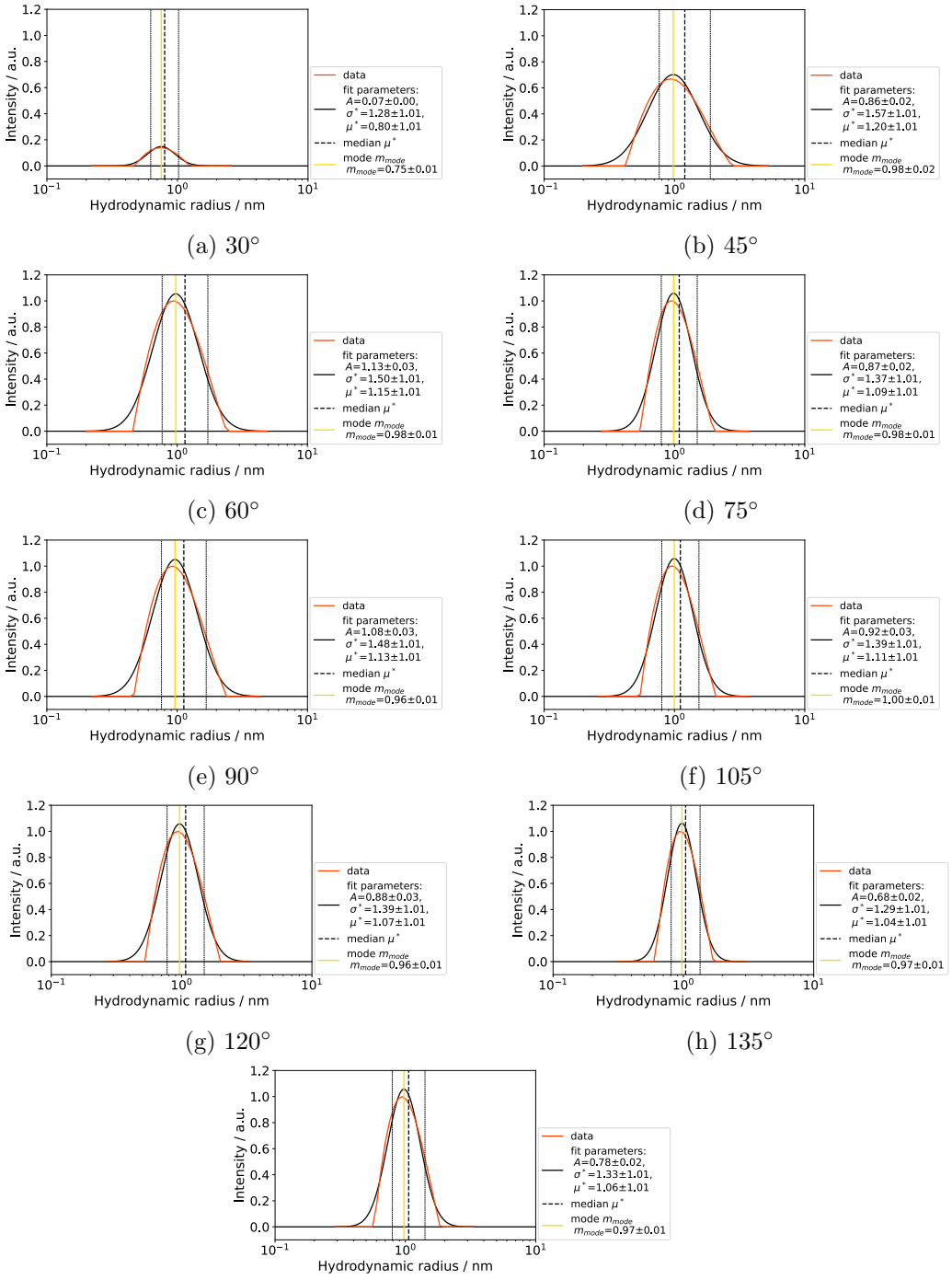

(a) 30° (b) 45°

(c) 60° (d) 75°

(e) 90° (f) 105°

(g) 120° (h) 135°

(i) 150°

Figure D.9.: Peak fitting with a log-normal distribution function as shown for a BSA solution at pH 3. From each fit the median μ^* (dashed line), the mode m_{mode} (yellow line) and the multiplicative standard deviation σ^* are obtained. The constant factor A serves as an additional fit parameter. The interval of confidence (68.3 %) is marked by the thin dashed lines.

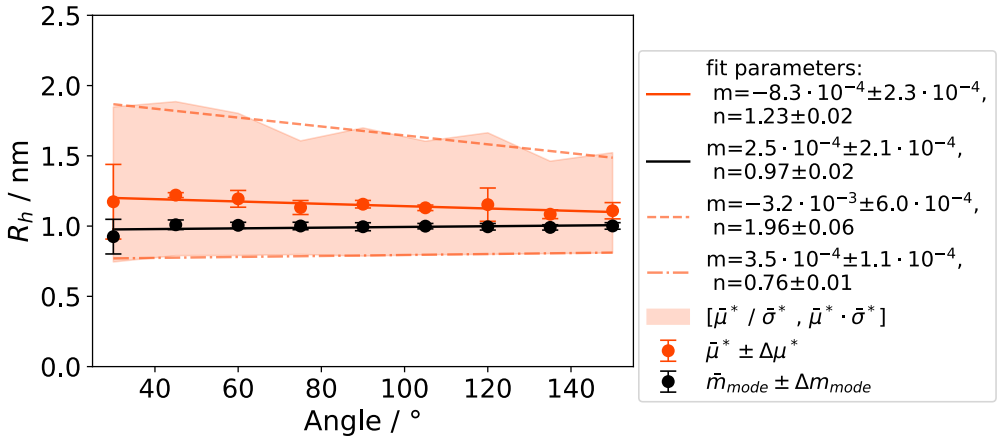

Figure D.10.: Angular dependency of the hydrodynamic radius as represented by the median $\bar{\mu}^*$, the mode $\bar{m}_{mode}$ and the interval of confidence $[\bar{\mu}^*/\bar{\sigma}^*, \bar{\mu}^* \cdot \bar{\sigma}^*]$ for BSA solutions at pH 3. For extrapolation to a scattering angle of 0° the parameters $\bar{\mu}^*$, $\bar{m}_{mode}$, $\bar{\mu}^*/\bar{\sigma}^*$ and $\bar{\mu}^* \cdot \bar{\sigma}^*$ are each fitted with a linear function.

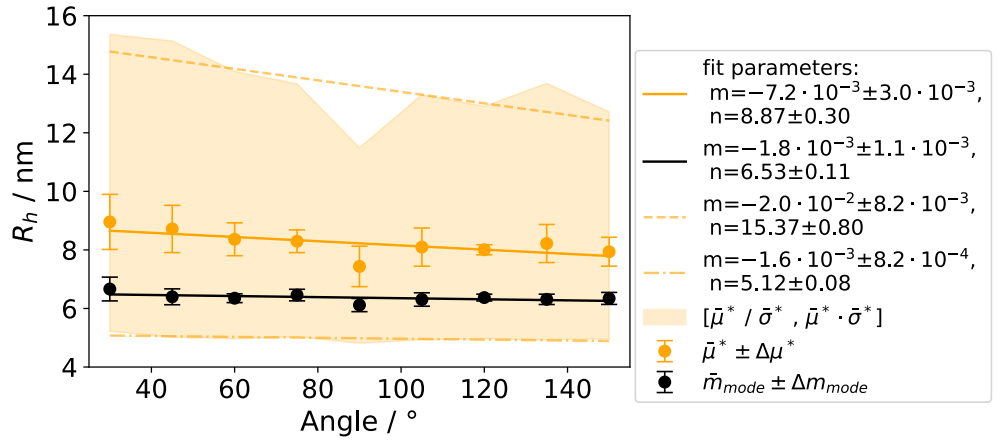

Figure D.11.: Angular dependency of the hydrodynamic radius as represented by the median $\bar{\mu}^*$, the mode $\bar{m}_{mode}$ and the interval of confidence $[\bar{\mu}^*/\bar{\sigma}^*, \bar{\mu}^* \cdot \bar{\sigma}^*]$ for BSA solutions at pH 5.1. For extrapolation to a scattering angle of 0° the parameters $\bar{\mu}^*$, $\bar{m}_{mode}$, $\bar{\mu}^*/\bar{\sigma}^*$ and $\bar{\mu}^* \cdot \bar{\sigma}^*$ are each fitted with a linear function.

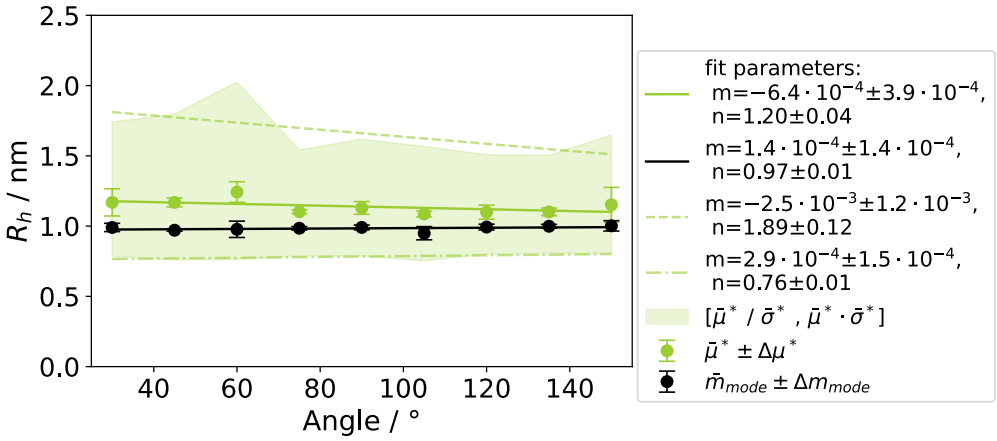

Figure D.12.: Angular dependency of the hydrodynamic radius as represented by the median $\bar{\mu}^*$, the mode $\bar{m}_{mode}$ and the interval of confidence $[\bar{\mu}^*/\bar{\sigma}^*, \bar{\mu}^* \cdot \bar{\sigma}^*]$ for BSA solutions at pH 7. For extrapolation to a scattering angle of 0° the parameters $\bar{\mu}^*$, $\bar{m}_{mode}$, $\bar{\mu}^*/\bar{\sigma}^*$ and $\bar{\mu}^* \cdot \bar{\sigma}^*$ are each fitted with a linear function.

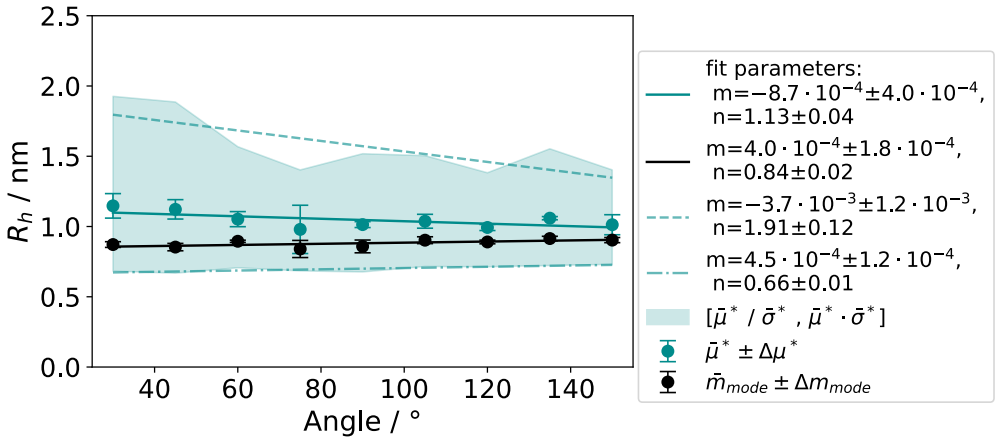

Figure D.13.: Angular dependency of the hydrodynamic radius as represented by the median $\bar{\mu}^*$, the mode $\bar{m}_{mode}$ and the interval of confidence $[\bar{\mu}^*/\bar{\sigma}^*, \bar{\mu}^* \cdot \bar{\sigma}^*]$ for BSA solutions at pH 9. For extrapolation to a scattering angle of 0° the parameters $\bar{\mu}^*$, $\bar{m}_{mode}$, $\bar{\mu}^*/\bar{\sigma}^*$ and $\bar{\mu}^* \cdot \bar{\sigma}^*$ are each fitted with a linear function.

E. Supplementary information: Oat drink

This supplementary information provides additional information on Chapter 7.

E.1. Curve fitting of particle sizes

For the measurements investigating the starch gelatinization, three main peaks of the particle size distribution were determined. These were fitted by the following function

$$f(x) = a_1 \mathrm{e}^{-\frac{1}{2}\left(\frac{\log_{10}(x)-\mu_1}{\sigma_1}\right)} + a_2 \mathrm{e}^{-\frac{1}{2}\left(\frac{\log_{10}(x)-\mu_2}{\sigma_2}\right)} + a_3 \mathrm{e}^{-\frac{1}{2}\left(\frac{\log_{10}(x)-\mu_3}{\sigma_3}\right)} \tag{E.1}$$

where x is the particle size, $a_i = \frac{1}{\sqrt{2\pi}\sigma_i x}$ are the prefactors, σ_i are the standard deviations of $\log_{10}(x)$, and μ_i are the expected values of $\log_{10}(x)$ with $i \in \{1, 2, 3\}$ representing the first, second, or third peak, respectively.
For the measurement of particle sizes after each step of enzymatic treatment, the first two peaks of the measurement were fitted using the function

$$g(x) = a_1 \mathrm{e}^{-\frac{1}{2}\left(\frac{\log_{10}(x)-\mu_1}{\sigma_1}\right)} + a_2 \mathrm{e}^{-\frac{1}{2}\left(\frac{\log_{10}(x)-\mu_2}{\sigma_2}\right)} \tag{E.2}$$

with parameters as above.
Curve fitting provided the fit parameters a_i, σ_i, and μ_i. To better describe the peaks in log-normal distribution the geometric (also multiplicative) standard deviations σ_i^* and geometric (also multiplicative) expected values (median) μ_i^* were calculated by $\sigma_i^* = 10^{\sigma_i}$ and $\mu_i^* = 10^{\mu_i}$, respectively. The errors on the fit parameters were obtained by taking the diagonal of the covariance matrix and calculating the square root. Subsequently, also the errors of σ and μ were exponentiated.
Figures E.1, E.2, E.3, E.4, E.5 and E.6 show the fitted particle size data and provide the obtained fit parameters.
When particle sizes are mentioned in the text, the geometric mean μ^* is provided as well as the geometric standard deviation σ^* demonstrating that 68 % of the particles of this size class were in the interval given by $[\mu^*/\sigma^*, \mu^* \cdot \sigma^*]$.
The larger particles detected in the measurements after each step of enzymatic treatment have not been fitted, because there are several smaller peaks that are hardly distinguishable or have large shoulders.

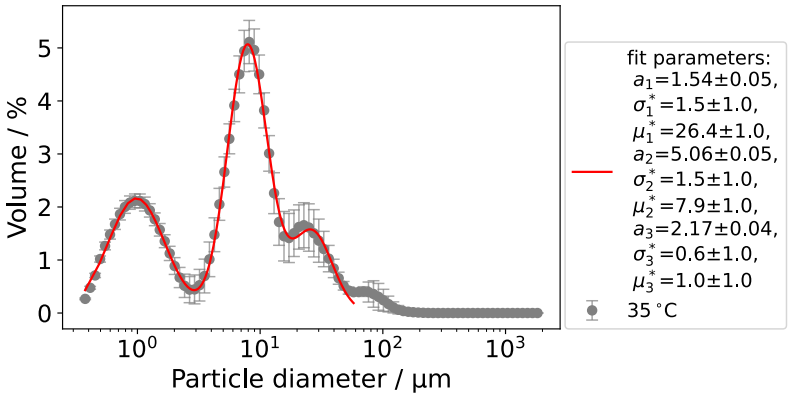

Figure E.1.: Fit of the particle size distribution of oat drink samples without enzymatic treatment heated to 35 °C.

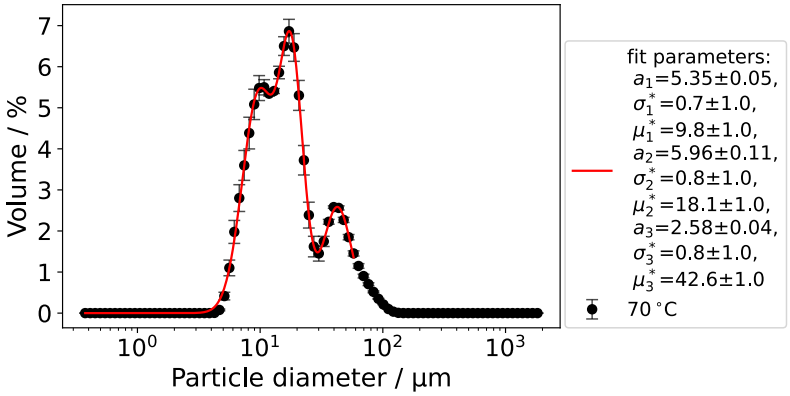

Figure E.2.: Fit of the particle size distribution of oat drink samples without enzymatic treatment heated to 70 °C.

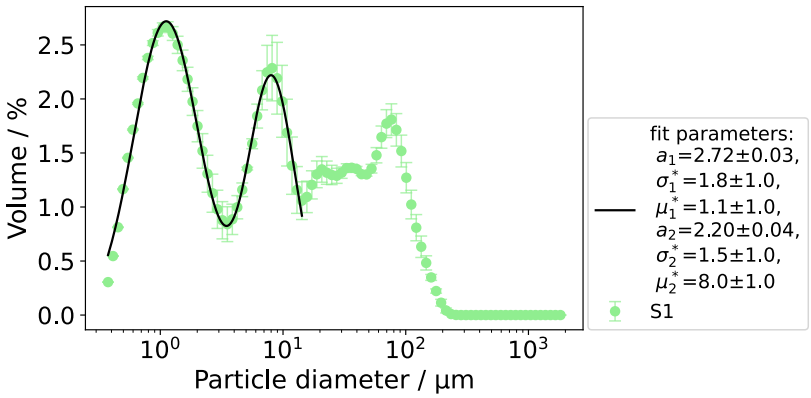

Figure E.3.: Fit of the first two peaks of the particle size distribution measured after treatment with EP1.

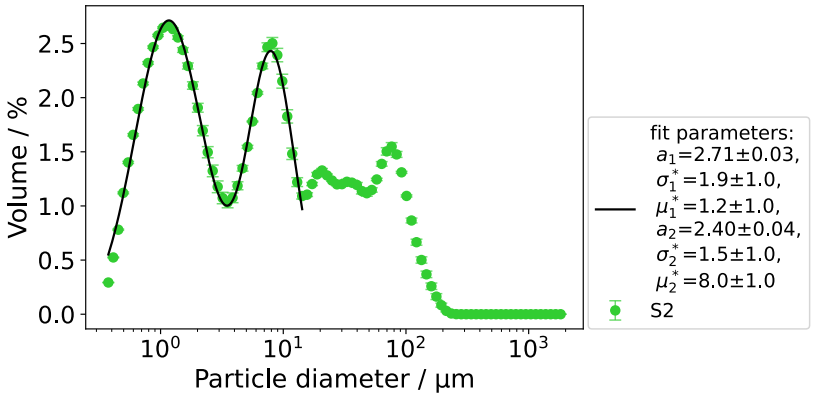

Figure E.4.: Fit of the first two peaks of the particle size distribution measured after treatment with EP2.

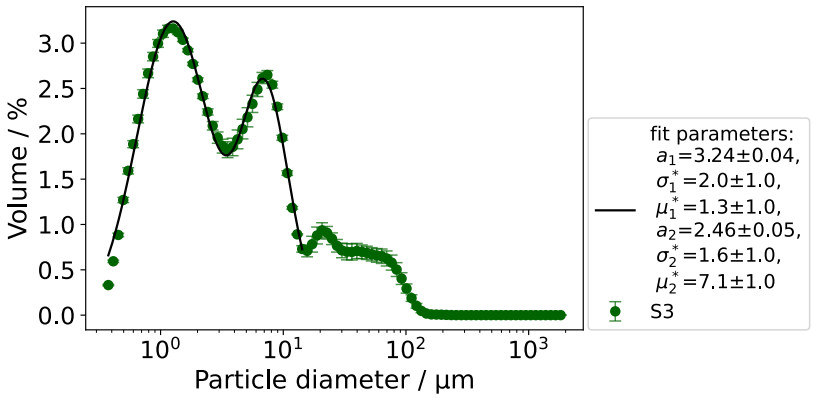

Figure E.5.: Fit of the first two peaks of the particle size distribution measured after treatment with EP3.

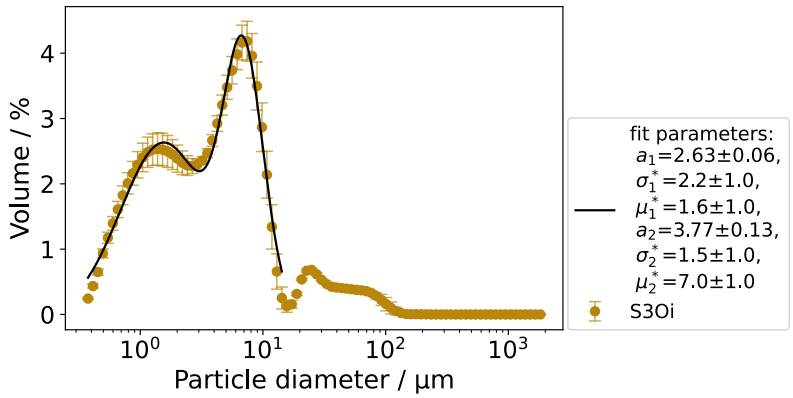

Figure E.6.: Fit of the first two peaks of the particle size distribution measured for the final formulation of the oat drink (standard sample).

E.2. Curve fitting of foam heights in logarithmic and double logarithmic representation

Logarithmic and double logarithmic representations of the measured foam heights of the different oat drink samples are shown in Figures E.7, E.8 and E.9.

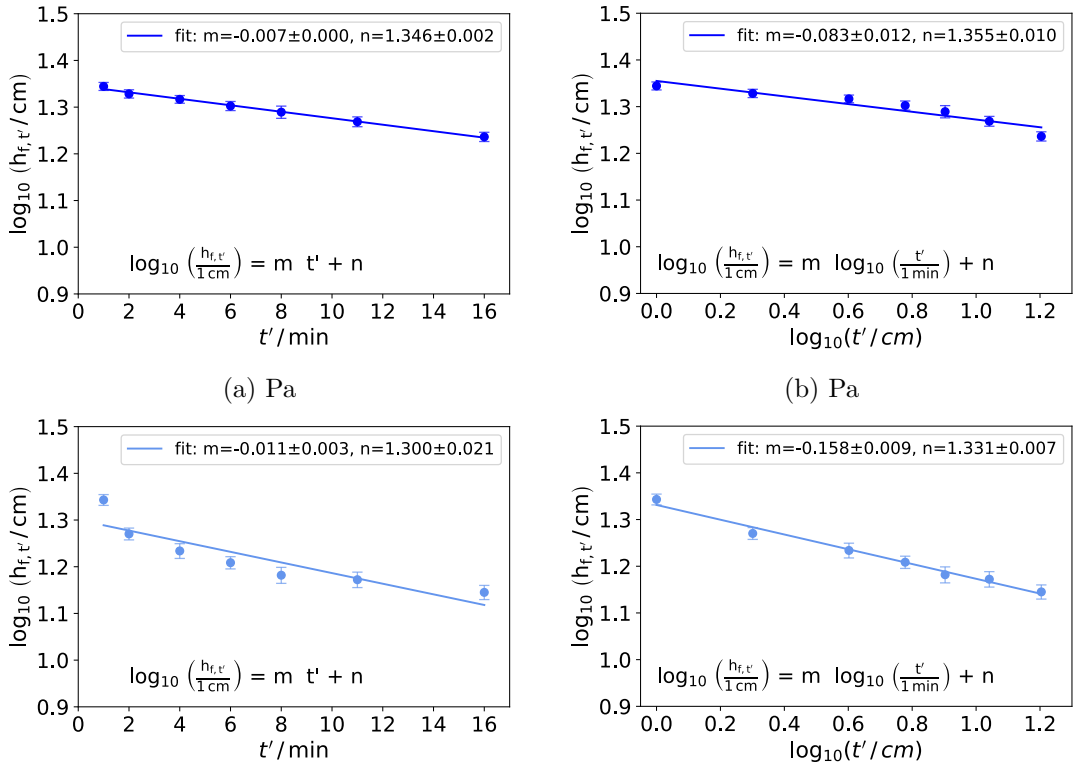

Figure E.7.: Logarithmic and double logarithmic representation of the foam height of samples Pa and Pap.

In most cases the data is better represented by a linear fit on double logarithmic scales, which suggests a power law decay of the foam height. Only for sample Pa the representation of the data on logarithmic scale is closer to a linear function than on double logarithmic scale. However, in this case also the data on double logarithmic scale does not deviate too much from a linear function. Because the deviations are quite small and because all other samples show linear correlations on double logarithmic scales (also the samples investigated in Chapter 6), the data of sample Pa was also fitted with a power law on linear scales. Furthermore, an exponential decay would suggest that a purely stochastic process causes the foam height decay. However, the reduction of the foam height depends on certain parameters like the drainage, initial bubble size and coarsening, which in turn are determined by factors like the solution viscosity and

the interfacial (re)arrangement of the surface active proteins.

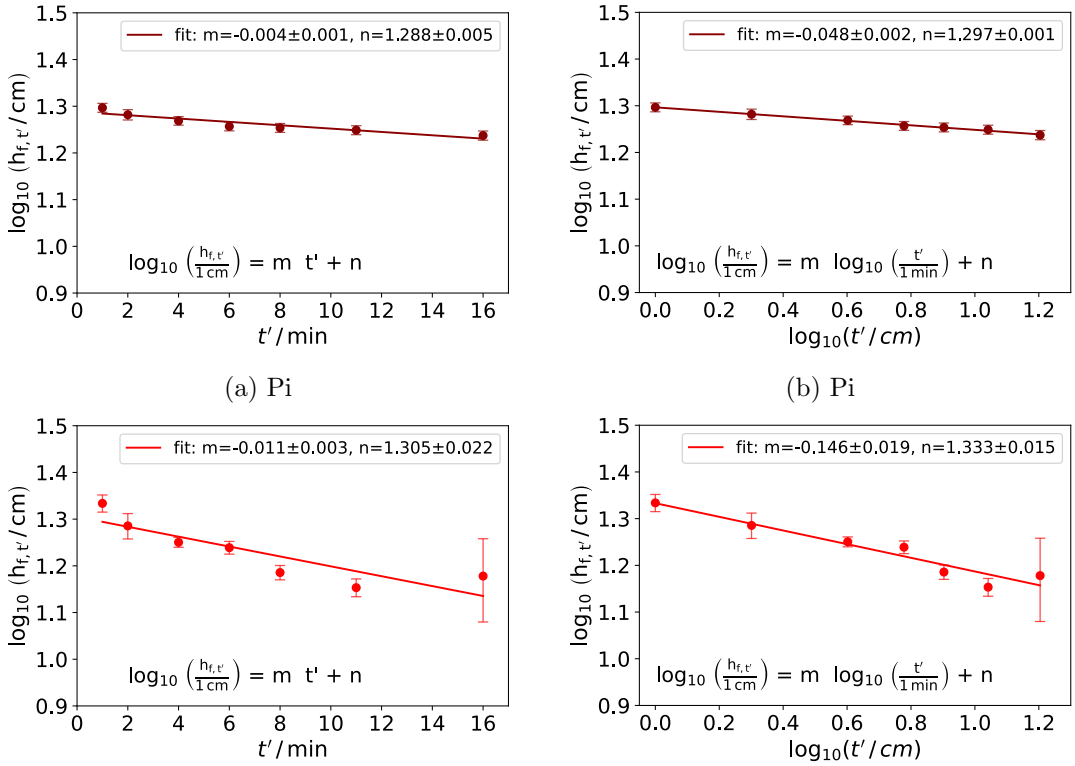

(a) Pi

(b) Pi

(c) Pip

(d) Pip

Figure E.8.: Logarithmic and double logarithmic representation of the foam height of samples Pi and Pip.

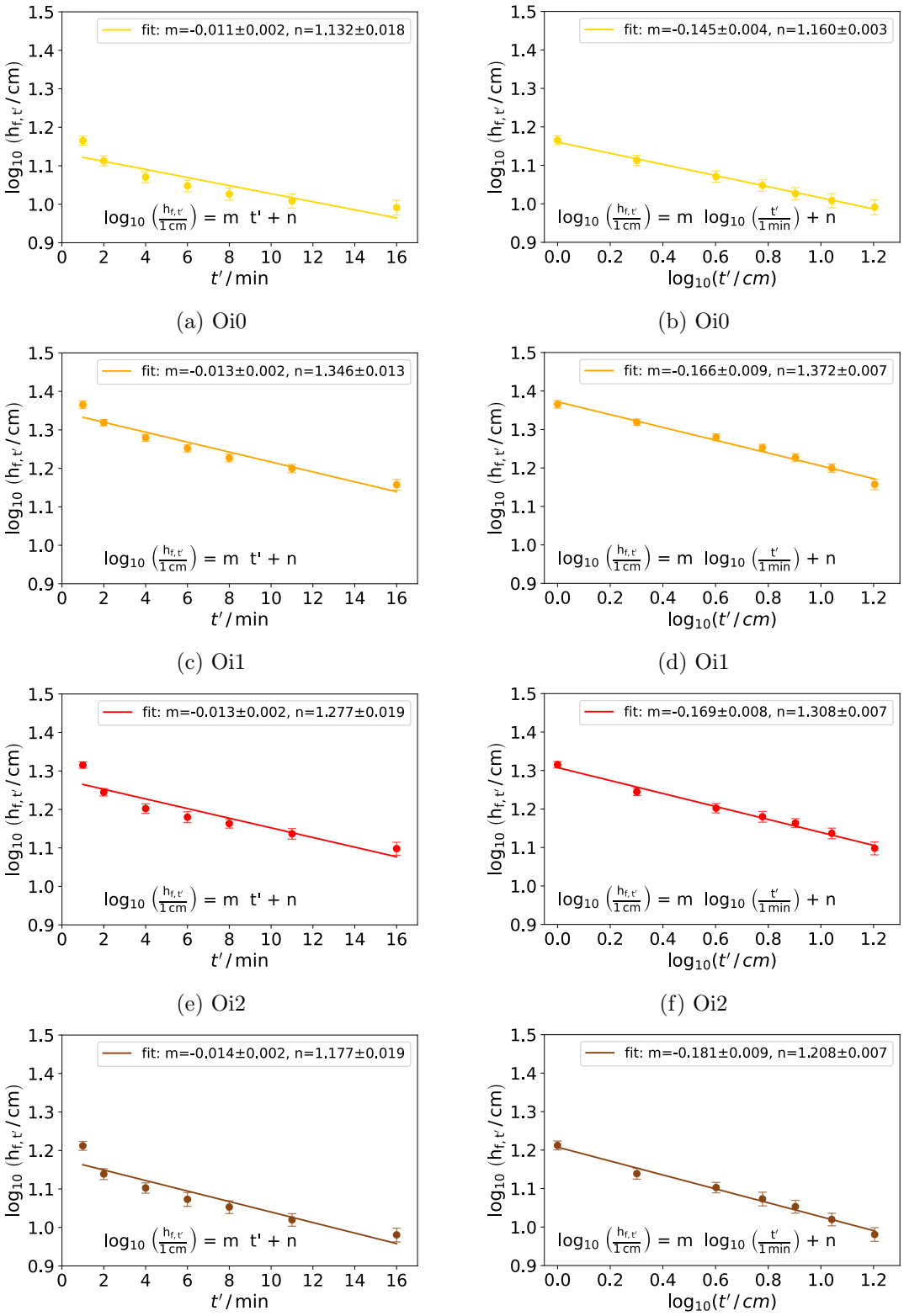

Figure E.9.: Logarithmic and double logarithmic representation of the foam height of samples Oi0, Oi1, Oi2 and Oi3.

Bibliography

[1] T. Huppertz. "Foaming properties of milk: A review of the influence of composition and processing". In: *International Journal of Dairy Technology* 63.4 (2010), pp. 477–488. DOI: 10.1111/j.1471-0307.2010.00629.x.

[2] D. Hummel, Z. Atamer, and J. Hinrichs. "New methodology for controlled testing of foaming properties of protein suspensions". In: *International Dairy Journal* 128 (2022), p. 105322. DOI: 10.1016/j.idairyj.2022.105322.

[3] T. F. Buhl, C. H. Christensen, and M. Hammershøj. "Aquafaba as an egg white substitute in food foams and emulsions: Protein composition and functional behavior". In: *Food Hydrocolloids* 96 (2019), pp. 354–364. DOI: 10.1016/j.foodhyd.2019.05.041.

[4] K. Lomakina and K. Míková. "A study of the factors affecting the foaming properties of egg white–a review". In: *Czech J. Food Sci* 24.3 (2006), pp. 110–118. DOI: 10.17221/3305-CJFS.

[5] C. W. Bamforth, ed. *Beer: A quality perspective*. Elsevier, 2009.

[6] N. Myhrvold, C. Young, and M. Bilet. "Volume 4: Incredients and preparations". In: *Modernist cuisine*. The Cooking Lab, 2011.

[7] N. Myhrvold, C. Young, and M. Bilet. "Volume 5: Plated-dish recipes". In: *Modernist cuisine*. The Cooking Lab, 2011.

[8] T. A. Vilgis. *Das Molekül-Menü: Molekulares Wissen für kreative Köche*. S. Hirzel Verlag, 2011. DOI: 10.3813/9783777621913.

[9] S. de Préval Eugénie, D. Fabrice, C. Gérard, and M. Samir. "Effect of bulk viscosity and surface tension kinetics on structure of foam generated at the pilot scale". In: *Food Hydrocolloids* 34 (2014), pp. 104–111. DOI: 10.1016/j.foodhyd.2012.12.001.

[10] S. N. Ashrafizadeh and A. Ganjizade. "Liquid foams: Properties, structures, prevailing phenomena and their applications in chemical/biochemical processes". In: *Advances in Colloid and Interface Science* 325 (2024), p. 103109. DOI: 10.1016/j.cis.2024.103109.

[11] S. Damodaran. "Protein-stabilized foams and emulsions". In: *Food proteins and their applications*. CRC Press, 2017, pp. 57–110.

[12] C. Balerin, P. Aymard, F. Ducept, S. Vaslin, and G. Cuvelier. "Effect of formulation and processing factors on the properties of liquid food foams". In: *Journal of Food Engineering* 78.3 (2007), pp. 802–809. DOI: 10.1016/j.jfoodeng.2005.11.021.

[13] J. M. Rodríguez Patino, C. Carrera Sánchez, and M. R. Rodríguez Niño. "Implications of interfacial characteristics of food foaming agents in foam formulations". In: *Advances in Colloid and Interface Science* 140.2 (2008), pp. 95–113. DOI: 10.1016/j.cis.2007.12.007.

[14] S. Rouimi, C. Schorsch, C. Valentini, and S. Vaslin. "Foam stability and interfacial properties of milk protein–surfactant systems". In: *Food Hydrocolloids* 19.3 (2005), pp. 467–478. DOI: 10.1016/j.foodhyd.2004.10.032.

[15] M. Krzan, H. Caps, and N. Vandewalle. "High stability of the bovine serum albumine foams evidenced in Hele–Shaw cell". In: *Colloids and Surfaces A: Physicochemical and Engineering Aspects* 438 (2013), pp. 112–118. DOI: 10.1016/j.colsurfa.2013.01.012.

[16] B. S. Murray. "Stabilization of bubbles and foams". In: *Current Opinion in Colloid & Interface Science* 12.4-5 (2007), pp. 232–241. DOI: 10.1016/j.cocis.2007.07.009.

[17] B. S. Murray. "Recent developments in food foams". In: *Current Opinion in Colloid & Interface Science* 50 (2020), p. 101394. DOI: 10.1016/j.cocis.2020.101394.

[18] E. Dickinson. "Food emulsions and foams: Stabilization by particles". In: *Current Opinion in Colloid & Interface Science* 15.1-2 (2010), pp. 40–49. DOI: 10.1016/j.cocis.2009.11.001.

[19] S. Damodaran. "Protein stabilization of emulsions and foams". In: *Journal of Food Science* 70.3 (2005), R54–R66. DOI: 10.1111/j.1365-2621.2005.tb07150.x.

[20] T. A. Vilgis. "Soft matter food physics—the physics of food and cooking". In: *Reports on Progress in Physics* 78.12 (2015), p. 124602. DOI: 10.1088/0034-4885/78/12/124602.

[21] J. Pu, B. Zhao, X. Liu, S. Li, B. Wang, D. Wu, J. Wang, and F. Geng. "Quantitative proteomic analysis of chicken egg white and its components". In: *Food Research International* 170 (2023), p. 113019. DOI: 10.1016/j.foodres.2023.113019.

[22] Y. Chen, L. Sheng, M. Gouda, and M. Ma. "Studies on foaming and physicochemical properties of egg white during cold storage". In: *Colloids and Surfaces A: Physicochemical and Engineering Aspects* 582 (2019), p. 123916. DOI: 10.1016/j.colsurfa.2019.123916.

[23] J. Lamolinairie, B. Dollet, J.-L. Bridot, P. Bauduin, O. Diat, and L. Chiappisi. "Probing foams from the nanometer to the millimeter scale by coupling small-angle neutron scattering, imaging, and electrical conductivity measurements". In: *Soft Matter* 18.46 (2022), pp. 8733–8747. DOI: 10.1039/d2sm01252a.

[24] S. Perticaroli, J. Herzberger, Y. Sun, J. D. Nickels, R. P. Murphy, K. Weigandt, and P. J. Ray. "Multiscale microstructure, composition, and stability of surfactant/polymer foams". In: *Langmuir* 36.48 (2020), pp. 14763–14771. DOI: 10.1021/acs.langmuir.0c02704.

[25] J. C. Germain and J. M. Aguilera. "Multi-scale properties of protein-stabilized foams". In: *Food Structure* 1.1 (2014), pp. 55–70. DOI: 10.1016/j.foostr.2014.01.001.

[26] T. Blijdenstein, P. De Groot, and S. Stoyanov. "On the link between foam coarsening and surface rheology: Why hydrophobins are so different". In: *Soft Matter* 6.8 (2010), pp. 1799–1808. DOI: 10.1039/b925648b.

[27] A.-L. Fameau and A. Salonen. "Effect of particles and aggregated structures on the foam stability and aging". In: *Comptes Rendus Physique* 15.8-9 (2014), pp. 748–760. DOI: 10.1016/j.crhy.2014.09.009.

[28] B. S. Murray, E. Dickinson, C. K. Lau, P. V. Nelson, and E. Schmidt. "Coalescence of protein-stabilized bubbles undergoing expansion at a simultaneously expanding planar air-water interface". In: *Langmuir* 21.10 (2005), pp. 4622–4630. DOI: 10.1021/la047333k.

[29] B. S. Murray and R. Ettelaie. "Foam stability: proteins and nanoparticles". In: *Current Opinion in Colloid & Interface Science* 9.5 (2004), pp. 314–320. DOI: 10.1016/j.cocis.2004.09.004.

[30] M. Safouane, A. Saint-Jalmes, V. Bergeron, and D. Langevin. "Viscosity effects in foam drainage: Newtonian and non-newtonian foaming fluids". In: *The European Physical Journal E* 19 (2006), pp. 195–202. DOI: 10.1140/epje/e2006-00025-4.

[31] M. Safouane, M. Durand, A. Saint-Jalmes, D. Langevin, and V. Bergeron. "Aqueous foam drainage. Role of the rheology of the foaming fluid". In: *Le Journal de Physique IV* 11.PR6 (2001), Pr6-275–Pr6-280. DOI: 10.1051/jp4:2001633.

[32] C. Hill and J. Eastoe. "Foams: From nature to industry". In: *Advances in Colloid and Interface Science* 247 (2017), pp. 496–513. DOI: 10.1016/j.cis.2017.05.013.

[33] W. Drenckhan and S. Hutzler. "Structure and energy of liquid foams". In: *Advances in Colloid and Interface Science* 224 (2015), pp. 1–16. DOI: 10.1016/j.cis.2015.05.004.

[34] M. S. Sadahira, F. C. Rezende Lopes, M. I. Rodrigues, and F. M. Netto. "Influence of protein–pectin electrostatic interaction on the foam stability mechanism". In: *Carbohydrate Polymers* 103 (2014), pp. 55–61. DOI: 10.1016/j.carbpol.2013.11.070.

[35] R. D. Waniska and J. E. Kinsella. "Foaming properties of proteins: Evaluation of a column aeration apparatus using ovalbumin". In: *Journal of Food Science* 44.5 (1979), pp. 1398–1402. DOI: 10.1111/j.1365-2621.1979.tb06447.x.

[36] G. A. van Koningsveld, P. Walstra, H. Gruppen, G. Wijngaards, M. A. van Boekel, and A. G. Voragen. "Formation and stability of foam made with various potato protein preparations". In: *Journal of Agricultural and Food Chemistry* 50.26 (2002), pp. 7651–7659. DOI: 10.1021/jf025587a.

[37] Ü. I. Konak, D. Ercili-Cura, J. Sibakov, T. Sontag-Strohm, M. Certel, and J. Loponen. "CO_2-defatted oats: Solubility, emulsification and foaming properties". In: *Journal of Cereal Science* 60.1 (2014), pp. 37–41. DOI: 10.1016/j.jcs.2014.01.013.

[38] O. Kaukonen, T. Sontag-Strohm, H. Salovaara, A.-M. Lampi, J. Sibakov, and J. Loponen. "Foaming of differently processed oats: Role of nonpolar lipids and tryptophanin proteins". In: *Cereal Chemistry* 88.3 (2011), pp. 239–244. DOI: 10.1094/CCHEM-11-10-0154.

[39] D. E. Evans, A. Surrel, M. Sheehy, D. C. Stewart, and L. H. Robinson. "Comparison of foam quality and the influence of hop α-acids and proteins using five foam analysis methods". In: *Journal of the American Society of Brewing Chemists* 66.1 (2008), pp. 1–10. DOI: 10.1094/ASBCJ-2007-1129-01.

[40] S. Kim and J. Kinsella. "Surface activity of food proteins: relationships between surface pressure development, viscoelasticity of interfacial films and foam stability of bovine serum albumin". In: *Journal of Food Science* 50.6 (1985), pp. 1526–1530. DOI: 10.1111/j.1365-2621.1985.tb10525.x.

[41] W. Vundla and P. Torline. "Steps toward the formulation of a model foam standard". In: *Journal of the American Society of Brewing Chemists* 65.1 (2007), pp. 21–25. DOI: 10.1094/ASBCJ-2007-0111-02.

[42] K. Engelhardt, A. Rumpel, J. Walter, J. Dombrowski, U. Kulozik, B. Braunschweig, and W. Peukert. "Protein adsorption at the electrified air-water interface: Implications on foam stability". In: *Langmuir* 28 (2012), pp. 7780–7787. DOI: 10.1021/la301368v.

[43] X. Xiong, M. T. Ho, B. Bhandari, and N. Bansal. "Foaming properties of milk protein dispersions at different protein content and casein to whey protein ratios". In: *International Dairy Journal* 109.104758 (2020), pp. 1–8. DOI: 10.1016/j.idairyj.2020.104758.

[44] E. Zielińska, M. Karaś, and B. Baraniak. "Comparison of functional properties of edible insects and protein preparations thereof". In: *LWT – Food Science and Technology* 91 (2018), pp. 168–174. DOI: 10.1016/j.lwt.2018.01.058.

[45] M. Zhao, W. Xiong, B. Chen, J. Zhu, and L. Wang. "Enhancing the solubility and foam ability of rice glutelin by heat treatment at pH12: Insight into protein structure". In: *Food Hydrocolloids* 103 (2020), p. 105626. DOI: 10.1016/j.foodhyd.2019.105626.

[46] Z. Zhu, X. Mao, Q. Wu, J. Zhang, and X. Deng. "Effects of oxidative modification of peroxyl radicals on the structure and foamability of chickpea protein isolates". In: *Journal of Food Science* 86.3 (2021), pp. 824–833. DOI: 10.1111/1750-3841.15643.

[47] Y. Yu, H. Zhang, J. Zhu, J. Liu, and T. Zhang. "Effect of ultrasound-irradiation combined pretreatment on the foamability of liquid egg white". In: *Journal of Food Science* 85.12 (2020), pp. 4312–4318. DOI: 10.1111/1750-3841.15530.

[48] X. Chen, Y. Chen, L. Zou, X. Zhang, Y. Dong, J. Tang, D. J. McClements, and W. Liu. "Plant-based nanoparticles prepared from proteins and phospholipids consisting of a core–multilayer-shell structure: Fabrication, stability, and foamability". In: *Journal of Agricultural and Food Chemistry* 67.23 (2019), pp. 6574–6584. DOI: 10.1021/acs.jafc.9b02028.

[49] L. Cui, N. Bandillo, Y. Wang, J.-B. Ohm, B. Chen, and J. Rao. "Functionality and structure of yellow pea protein isolate as affected by cultivars and extraction pH". In: *Food Hydrocolloids* 108 (2020), p. 106008. DOI: 10.1016/j.foodhyd.2020.106008.

[50] S. Poole, S. I. West, and C. L. Walters. "Protein–protein interactions: their importance in the foaming of heterogeneous protein systems". In: *Journal of the Science of Food and Agriculture* 35.6 (1984), pp. 701–711. DOI: 10.1002/jsfa.2740350618.

[51] A. Fidantsi and G. Doxastakis. "Emulsifying and foaming properties of amaranth seed protein isolates". In: *Colloids and Surfaces B: Biointerfaces* 21.1-3 (2001), pp. 119–124. DOI: 10.1016/S0927-7765(01)00165-5.

[52] W. Jian, J. He, Y. Sun, and J. Pang. "Comparative studies on physicochemical properties of bovine serum albumin-glucose and bovine serum albumin-mannose conjugates formed via Maillard reaction". In: *LWT - Food Science and Technology* 69 (2016), pp. 358–364. DOI: 10.1016/j.lwt.2015.11.061.

[53] S. Jeske, E. Zannini, M. F. Cronin, and E. K. Arendt. "Impact of protease and amylase treatment on proteins and the product quality of a quinoa-based milk substitute". In: *Food & Function* 9.6 (2018), pp. 3500–3508. DOI: 10.1039/c8fo00336j.

[54] T. O. Fasuan, S. O. Gbadamosi, and T. O. Omobuwajo. "Characterization of protein isolate from *Sesamum indicum* seed: In vitro protein digestibility, amino acid profile, and some functional properties". In: *Food Science & Nutrition* 6.6 (2018), pp. 1715–1723. DOI: 10.1002/fsn3.743.

[55] X. Yang and E. A. Foegeding. "The stability and physical properties of egg white and whey protein foams explained based on microstructure and interfacial properties". In: *Food Hydrocolloids* 25.7 (2011), pp. 1687–1701. DOI: 10.1016/j.foodhyd.2011.03.008.

[56] K. Gräff, S. Stock, L. Mirau, S. Bürger, L. Braun, A. Völp, N. Willenbacher, and R. von Klitzing. "Untangling effects of proteins as stabilizers for foam films". In: *Frontiers in Soft Matter* 2 (2022), p. 1035377. DOI: 10.3389/frsfm.2022.1035377.

[57] S. I. Karakashev. "Hydrodynamics of foams". In: *Experiments in Fluids* 58.91 (2017), pp. 1–40. DOI: 10.1007/s00348-017-2332-z.

[58] R. Von Klitzing, E. Thormann, T. Nylander, D. Langevin, and C. Stubenrauch. "Confinement of linear polymers, surfactants, and particles between interfaces". In: *Advances in Colloid and Interface Science* 155.1-2 (2010), pp. 19–31. DOI: 10.1016/j.cis.2010.02.003.

[59] V. Bergeron, D. Langevin, and A. Asnacios. "Thin-film forces in foam films containing anionic polyelectrolyte and charged surfactants". In: *Langmuir* 12.6 (1996), pp. 1550–1556. DOI: 10.1021/la950654z.

[60] K. Engelhardt, M. Lexis, G. Gochev, C. Konnerth, R. Miller, N. Willenbacher, W. Peukert, and B. Braunschweig. "pH effects on the molecular structure of β-lactoglobulin modified air–water interfaces and its impact on foam rheology". In: *Langmuir* 29.37 (2013), pp. 11646–11655. DOI: 10.1021/la402729g.

[61] A. Bera, K. Ojha, and A. Mandal. "Synergistic effect of mixed surfactant systems on foam behavior and surface tension". In: *Journal of Surfactants and Detergents* 16 (2013), pp. 621–630. DOI: 10.1007/s11743-012-1422-4.

[62] D. M. Abascal and J. Gracia-Fadrique. "Surface tension and foam stability of commercial calcium and sodium caseinates". In: *Food Hydrocolloids* 23.7 (2009), pp. 1848–1852. DOI: 10.1016/j.foodhyd.2009.02.012.

[63] C. Monteux, G. G. Fuller, and V. Bergeron. "Shear and dilational surface rheology of oppositely charged polyelectrolyte/surfactant microgels adsorbed at the air-water interface. Influence on foam stability". In: *The Journal of Physical Chemistry B* 108.42 (2004), pp. 16473–16482. DOI: 10.1021/jp047462+.

[64] V. Kovalchuk, E. Aksenenko, A. Makievski, V. Fainerman, and R. Miller. "Dilational interfacial rheology of tridecyl dimethyl phosphine oxide adsorption layers at the water/hexane interface". In: *Journal of Colloid and Interface Science* 539 (2019), pp. 30–37. DOI: 10.1016/j.jcis.2018.12.019.

[65] L. G. C. Pereira, O. Théodoly, H. W. Blanch, and C. J. Radke. "Dilatational rheology of BSA conformers at the air/water interface". In: *Langmuir* 19.6 (2003), pp. 2349–2356. DOI: 10.1021/la020720e.

[66] N. A. Alexandrov, K. G. Marinova, T. D. Gurkov, K. D. Danov, P. A. Kralchevsky, S. D. Stoyanov, T. B. Blijdenstein, L. N. Arnaudov, E. G. Pelan, and A. Lips. "Interfacial layers from the protein HFBII hydrophobin: Dynamic surface tension, dilatational elasticity and relaxation times". In: *Journal of Colloid and Interface Science* 376.1 (2012), pp. 296–306. DOI: 10.1016/j.jcis.2012.03.031.

[67] F. Ravera, G. Loglio, and V. I. Kovalchuk. "Interfacial dilational rheology by oscillating bubble/drop methods". In: *Current Opinion in Colloid & Interface Science* 15.4 (2010), pp. 217–228. DOI: 10.1016/j.cocis.2010.04.001.

[68] R. D. Stanimirova, T. D. Gurkov, P. A. Kralchevsky, K. T. Balashev, S. D. Stoyanov, and E. G. Pelan. "Surface pressure and elasticity of hydrophobin HFBII layers on the air–water interface: Rheology versus structure detected by AFM imaging". In: *Langmuir* 29.20 (2013), pp. 6053–6067. DOI: 10.1021/la4005104.

[69] P. Gunning, A. Mackie, A. Gunning, P. Wilde, N. Woodward, and V. Morris. "The effect of surfactant type on protein displacement from the air–water interface". In: *Food Hydrocolloids* 18.3 (2004), pp. 509–515. DOI: 10.1016/j.foodhyd.2003.08.008.

[70] S. Houmadi, F. Ciuchi, M. P. De Santo, L. De Stefano, I. Rea, P. Giardina, A. Armenante, E. Lacaze, and M. Giocondo. "Langmuir-Blodgett film of hydrophobin protein from *Pleurotus ostreatus* at the air-water interface". In: *Langmuir* 24.22 (2008), pp. 12953–12957. DOI: 10.1021/la802306r.

[71] Q. Ren, A. H. Kwan, and M. Sunde. "Solution structure and interface-driven self-assembly of NC2, a new member of the class II hydrophobin proteins". In: *Proteins: Structure, Function, and Bioinformatics* 82.6 (2014), pp. 990–1003. DOI: 10.1002/prot.24473.

[72] C. L. Pham, A. Rey, V. Lo, M. Soulès, Q. Ren, G. Meisl, T. P. Knowles, A. H. Kwan, and M. Sunde. "Self-assembly of MPG1, a hydrophobin protein from the rice blast fungus that forms functional amyloid coatings, occurs by a surface-driven mechanism". In: *Scientific Reports* 6.1 (2016), p. 25288. DOI: 10.1038/srep25288.

[73] I. Othmeni, R. Karoui, and C. Blecker. "Impact of pH on the structure, interfacial and foaming properties of pea protein isolate: Investigation of the structure–function relationship". In: *International Journal of Biological Macromolecules* 278 (2024), p. 134818. DOI: 10.1016/j.ijbiomac.2024.134818.

[74] W. Xiang, N. Preisig, A. Ketola, B. L. Tardy, L. Bai, J. A. Ketoja, C. Stubenrauch, and O. J. Rojas. "How cellulose nanofibrils affect bulk, surface, and foam properties of anionic surfactant solutions". In: *Biomacromolecules* 20.12 (2019), pp. 4361–4369. DOI: 10.1021/acs.biomac.9b01037.

[75] E. Dachmann, V. Nobis, U. Kulozik, and J. Dombrowski. "Surface and foaming properties of potato proteins: Impact of protein concentration, pH value and ionic strength". In: *Food Hydrocolloids* 107 (2020), p. 105981. DOI: 10.1016/j.foodhyd.2020.105981.

[76] J. Dombrowski, J. Dechau, and U. Kulozik. "Multiscale approach to characterize bulk, surface and foaming behavior of casein micelles as a function of alkalinisation". In: *Food Hydrocolloids* 57 (2016), pp. 92–102. DOI: 10.1016/j.foodhyd.2015.12.022.

[77] A. Audebert, A. Saint-Jalmes, S. Beaufils, V. Lechevalier, C. Le Floch-Fouéré, S. Cox, N. Leconte, and S. Pezennec. "Interfacial properties, film dynamics and bulk rheology: A multi-scale approach to dairy protein foams". In: *Journal of Colloid and Interface Science* 542 (2019), pp. 222–232. DOI: 10.1016/j.jcis.2019.02.006.

[78] V. M. Rosenoer, M. Oratz, and M. A. Rothschild, eds. *Albumin: Structure, function and uses*. Oxford: Pergamon Press, 1977.

[79] R. Curvale, M. Masuelli, and A. P. Padilla. "Intrinsic viscosity of bovine serum albumin conformers". In: *International Journal of Biological Macromolecules* 42.2 (2008), pp. 133–137. DOI: 10.1016/j.ijbiomac.2007.10.007.

[80] V. Vetri, F. Librizzi, M. Leone, and V. Militello. "Thermal aggregation of bovine serum albumin at different pH: Comparison with human serum albumin". In: *European Biophysics Journal* 36 (2007), pp. 717–725. DOI: 10.1007/s00249-007-0196-5.

[81] İ. Gülseren, D. Güzey, B. D. Bruce, and J. Weiss. "Structural and functional changes in ultrasonicated bovine serum albumin solutions". In: *Ultrasonics Sonochemistry* 14.2 (2007), pp. 173–183. ISSN: 1350-4177. DOI: 10.1016/j.ultsonch.2005.07.006.

[82] H. Zhang, G. Xu, T. Liu, L. Xu, and Y. Zhou. "Foam and interfacial properties of Tween 20–bovine serum albumin systems". In: *Colloids and Surfaces A: Physicochemical and Engineering Aspects* 416 (2013), pp. 23–31. ISSN: 0927-7757. DOI: 10.1016/j.colsurfa.2012.10.028.

[83] R. Li, Z. Wu, Y. Wangb, L. Ding, and Y. Wang. "Role of pH-induces structural change in protein aggregation in foam fractionation of bovine serum albumin". In: *Biotechnology Reports* 9 (2016), pp. 46–52. DOI: 10.1016/j.btre.2016.01.002.

[84] L. Glaser, A. Paulson, R. Speers, R. Yada, and D. Rousseau. "Foaming behavior of mixed bovine serum albumin–protamine systems". In: *Food Hydrocolloids* 21.4 (2007), pp. 495–506. ISSN: 0268-005X. DOI: 10.1016/j.foodhyd.2006.05.008.

[85] A. Jahanban-Esfahlan, A. Ostadrahimi, R. Jahanban-Esfahlan, L. Roufegarinejad, M. Tabibiazar, and R. Amarowicz. "Recent developments in the detection of bovine serum albumin". In: *International Journal of Biological Macromolecules* 138 (2019), pp. 602–617. ISSN: 0141-8130. DOI: 10.1016/j.ijbiomac.2019.07.096.

[86] K.-Y. Chiang, F. Matsumura, C.-C. Yu, D. Qi, Y. Nagata, M. Bonn, and K. Meister. "True origin of amide I shifts observed in protein spectra obtained with sum frequency generation spectroscopy". In: *The Journal of Physical Chemistry Letters* 14 (2023), pp. 4949–4954. DOI: 10.1021/acs.jpclett.3c00391.

[87] R. T. Duarte, M. C. Carvalho Simões, and V. C. Sgarbieri. "Bovine blood components: Fractionation, composition, and nutritive value". In: *Journal of Agricultural and Food Chemistry* 47.1 (1999), pp. 231–236. DOI: 10.1021/jf9806255.

[88] Z. Litwińczuk, J. Król, A. Brodziak, and J. Barłowska. "Changes of protein content and its fractions in bovine milk from different breeds subject to somatic cell count". In: *Journal of Dairy Science* 94.2 (2011), pp. 684–691. DOI: 10.3168/jds.2010-3217. URL: https://www.sciencedirect.com/science/article/pii/S0022030211000154.

[89] J. Zawala, R. Todorov, A. Olszewska, D. Exerowa, and K. Malysa. "Influence of pH of the BSA solutions on velocity of the rising bubbles and stability of the thin liquid films and foams". In: *Adsorption* 16 (2010), pp. 423–435. DOI: 10.1007/s10450-010-9232-3.

[90] P. Wilde and D. Clark. "Foam formation and stability". In: *Methods of testing protein functionality*. Ed. by G. Hall. Vol. 1. Blackie Academic and Professional London, 1996. Chap. 5, pp. 110–152.

[91] S. Yadav, S. J. Shire, and D. S. Kalonia. "Viscosity analysis of high concentration bovine serum albumin aqueous solutions". In: *Pharmaceutical Research* 28 (2011), pp. 1973–1983. DOI: 10.1007/s11095-011-0424-7.

[92] W. Van der Vegt, H. Van der Mei, H. Wösten, J. Wessels, and H. Busscher. "A comparison of the surface activity of the fungal hydrophobin SC3p with those of other proteins". In: *Biophysical Chemistry* 57.2-3 (1996), pp. 253–260. DOI: 10.1016/0301-4622(95)00059-7.

[93] W. Wohlleben, T. Subkowski, C. Bollschweiler, B. Von Vacano, Y. Liu, W. Schrepp, and U. Baus. "Recombinantly produced hydrophobins from fungal analogues as highly surface-active performance proteins". In: *European Biophysics Journal* 39 (2010), pp. 457–468. DOI: 10.1007/s00249-009-0430-4.

[94] A. R. Cox, F. Cagnol, A. B. Russell, and M. J. Izzard. "Surface properties of class II hydrophobins from *Trichoderma reesei* and influence on bubble stability". In: *Langmuir* 23.15 (2007), pp. 7995–8002. DOI: 10.1021/la700451g.

[95] J. Hakanpää, A. Paananen, S. Askolin, T. Nakari-Setälä, T. Parkkinen, M. Penttilä, M. B. Linder, and J. Rouvinen. "Atomic resolution structure of the HFBII hydrophobin, a self-assembling amphiphile". In: *Journal of Biological Chemistry* 279.1 (2004), pp. 534–539. DOI: 10.1074/jbc.M309650200.

[96] M. Dokouhaki, A. Hung, S. Kasapis, and S. L. Gras. "Hydrophobins and chaplins: Novel bio-surfactants for food dispersions; a review". In: *Trends in Food Science & Technology* 111 (2021), pp. 378–387. DOI: 10.1016/j.tifs.2021.03.001.

[97] A. J. Green, K. A. Littlejohn, P. Hooley, and P. W. Cox. "Formation and stability of food foams and aerated emulsions: Hydrophobins as novel functional ingredients". In: *Current Opinion in Colloid & Interface Science* 18.4 (2013), pp. 292–301. DOI: 10.1016/j.cocis.2013.04.008.

[98] N. D. Sallada, K. J. Dunn, and B. W. Berger. "A structural and functional role for disulfide bonds in a class II hydrophobin". In: *Biochemistry* 57.5 (2018), pp. 645–653. DOI: 10.1021/acs.biochem.7b01166.

[99] J. G. Wessels. "Hydrophobins: Proteins that change the nature of the fungal surface". In: *Advances in Microbial Physiology* 38 (1997), pp. 1–45. DOI: 10.1016/S0065-2911(08)60154-X.

[100] B. von Vacano, R. Xu, S. Hirth, I. Herzenstiel, M. Rückel, T. Subkowski, and U. Baus. "Hydrophobin can prevent secondary protein adsorption on hydrophobic substrates without exchange". In: *Analytical and Bioanalytical Chemistry* 400 (2011), pp. 2031–2040. DOI: 10.1007/s00216-011-4902-x.

[101] M. Linder, K. Selber, T. Nakari-Setälä, M. Qiao, M.-R. Kula, and M. Penttilä. "The hydrophobins HFBI and HFBII from *Trichoderma reesei* showing efficient interactions with nonionic surfactants in aqueous two-phase systems". In: *Biomacromolecules* 2.2 (2001), pp. 511–517. DOI: 10.1021/bm0001493.

[102] V. K. Morris, Q. Ren, I. Macindoe, A. H. Kwan, N. Byrne, and M. Sunde. "Recruitment of class I hydrophobins to the air:water interface initiates a multi-step process of functional amyloid formation". In: *Journal of Biological Chemistry* 286.18 (2011), pp. 15955–15963. DOI: 10.1074/jbc.M110.214197.

[103] M. L. de Vocht, I. Reviakine, H. A. Wösten, A. Brisson, J. G. Wessels, and G. T. Robillard. "Structural and functional role of the disulfide bridges in the hydrophobin SC3". In: *Journal of Biological Chemistry* 275.37 (2000), pp. 28428–28432. DOI: 10.1074/jbc.M000691200.

[104] X. Wang, F. Shi, H. Wösten, H. Hektor, B. Poolman, and G. Robillard. "The SC3 hydrophobin self-assembles into a membrane with distinct mass transfer properties". In: *Biophysical Journal* 88.5 (2005), pp. 3434–3443. DOI: 10.1529/biophysj.104.057794.

[105] V. K. Morris, A. H. Kwan, and M. Sunde. "Analysis of the structure and conformational states of DewA gives insight into the assembly of the fungal hydrophobins". In: *Journal of Molecular Biology* 425.2 (2013), pp. 244–256. DOI: 10.1016/j.jmb.2012.10.021.

[106] A. Zykwinska, T. Guillemette, J.-P. Bouchara, and S. Cuenot. "Spontaneous self-assembly of SC3 hydrophobins into nanorods in aqueous solution". In: *Biochimica et Biophysica Acta (BBA)-Proteins and Proteomics* 1844.7 (2014), pp. 1231–1237. DOI: 10.1016/j.bbapap.2014.04.003.

[107] A. R. Cox, D. L. Aldred, and A. B. Russell. "Exceptional stability of food foams using class II hydrophobin HFBII". In: *Food Hydrocolloids* 23.2 (2009), pp. 366–376. DOI: 10.1016/j.foodhyd.2008.03.001.

[108] A. Lohrasbi-Nejad, M. Torkzadeh-Mahani, and S. Hosseinkhani. "Heterologous expression of a hydrophobin HFB1 and evaluation of its contribution to producing stable foam". In: *Protein Expression and Purification* 118 (2016), pp. 25–30. DOI: 10.1016/j.pep.2015.09.025.

[109] L. M. Dimitrova, P. V. Petkov, P. A. Kralchevsky, S. D. Stoyanov, and E. G. Pelan. "Production and characterization of stable foams with fine bubbles from solutions of hydrophobin HFBII and its mixtures with other proteins". In: *Colloids and Surfaces A: Physicochemical and Engineering Aspects* 521 (2017), pp. 92–104. DOI: 10.1016/j.colsurfa.2016.06.018.

[110] T. Blijdenstein, R. Ganzevles, P. De Groot, and S. Stoyanov. "On the link between surface rheology and foam disproportionation in mixed hydrophobin HFBII and whey protein systems". In: *Colloids and Surfaces A: Physicochemical and Engineering Aspects* 438 (2013), pp. 13–20. DOI: 10.1016/j.colsurfa.2012.12.040.

[111] J. Burke, A. Cox, J. Petkov, and B. S. Murray. "Interfacial rheology and stability of air bubbles stabilized by mixtures of hydrophobin and β-casein". In: *Food Hydrocolloids* 34 (2014), pp. 119–127. DOI: 10.1016/j.foodhyd.2012.11.026.

[112] I. Cantat, S. Cohen-Addad, F. Elias, F. Graner, R. Höhler, O. Pitois, F. Rouyer, and A. Saint-Jalmes. *Foams: Structure and dynamics*. Oxford University Press, 2013.

[113] D. J. McClements and S. M. Jafari. "Improving emulsion formation, stability and performance using mixed emulsifiers: A review". In: *Advances in Colloid and Interface Science* 251 (2018), pp. 55–79. DOI: 10.1016/j.cis.2017.12.001.

[114] G. Lomolino, S. Vincenzi, D. Gazzola, A. Crapisi, and A. Curioni. "Foaming properties of potato (*Solanum tuberosum*) proteins: A study by the gas sparging method". In: *Colloids and Surfaces A: Physicochemical and Engineering Aspects* 475 (2015), pp. 75–83. DOI: 10.1016/j.colsurfa.2015.01.093.

[115] R. Bois, E. Van Hecke, I. Pezron, and A. Nesterenko. "Screening of surfactant foaming properties using the gas-sparging method: Design of an optimal protocol". In: *Journal of Surfactants and Detergents* 23.2 (2020), pp. 359–369. DOI: 10.1002/jsde.12376.

[116] KRÜSS GmbH. *Dynamic Foam Analyzer*. Accessed: 2024-02-13. URL: https://images.kruss-scientific.com/files/kruss-bro-dfa100-en.pdf.

[117] Teclis Instruments. *Foamscan: Foam analyzers and defoamer testers*. Accessed: 2024-02-13. URL: https://www.teclis-scientific.com/foam-analyzers.

[118] H.-J. Butt, K. Graf, and M. Kappl. *Physics and chemistry of interfaces*. Wiley-VCH, 2006.

[119] G. Narsimhan and N. Xiang. "Role of proteins on formation, drainage, and stability of liquid food foams". In: *Annual Review of Food Science and Technology* 9 (2018), pp. 45–63. DOI: 10.1146/annurev-food-030216-030009.

[120] A. Prins and H. K. van Kalsbeek. "Foaming behaviour and dynamic surface properties of liquids". In: *Current Opinion in Colloid & Interface Science* 3.6 (1998), pp. 639–642. DOI: 10.1016/S1359-0294(98)80093-9.

[121] A. J. Wilson. *Foams: Physics, chemistry and structure*. Springer Science & Business Media, 1989.

[122] H. Caps, N. Vandewalle, A. Saint-Jalmes, L. Saulnier, P. Yazhgur, E. Rio, A. Salonen, and D. Langevin. "How foams unstable on earth behave in microgravity?" In: *Colloids and Surfaces A: Physicochemical and Engineering Aspects* 457 (2014), pp. 392–396. DOI: 10.1016/j.colsurfa.2014.05.063.

[123] I. Ivanov and D. Dimitrov. "Hydrodynamics of thin liquid films: Effect of surface viscosity on thinning and rupture of foam films". In: *Colloid and Polymer Science* 252 (1974), pp. 982–990. DOI: 10.1007/BF01566619.

[124] S. I. Karakashev and E. D. Manev. "Hydrodynamics of thin liquid films: Retrospective and perspectives". In: *Advances in Colloid and Interface Science* 222 (2015), pp. 398–412. DOI: 10.1016/j.cis.2014.07.010.

[125] G. Narsimhan. "A model for unsteady state drainage of a static foam". In: *Journal of Food Engineering* 14.2 (1991), pp. 139–165. DOI: 10.1016/0260-8774(91)90005-D.

[126] L. L. Schramm and F. Wassmuth. "Foams: Basic principles". In: *Foams: Fundamentals and applications in the petroleum industry*. Ed. by L. L. Schramm. ACS Publications, 1994. Chap. 1, pp. 3–45. DOI: 10.1021/ba-1994-0242.ch001.

[127] C. Stubenrauch and R. von Klitzing. "Disjoining pressure in thin liquid foam and emulsion films – new concepts and perspectives". In: *Journal of Physics: Condensed Matter* 15.27 (2003), R1197–R1232. DOI: 10.1088/0953-8984/15/27/201.

[128] A. Sharma and E. Ruckenstein. "Critical thickness and lifetimes of foams and emulsions: Role of surface wave-induced thinning". In: *Journal of Colloid and Interface Science* 119.1 (1987), pp. 14–29. DOI: 10.1016/0021-9797(87)90240-2.

[129] P. Wilde. "Interfaces: Their role in foam and emulsion behaviour". In: *Current Opinion in Colloid & Interface Science* 5.3-4 (2000), pp. 176–181. DOI: 10.1016/S1359-0294(00)00056-X.

[130] R. J. Pugh. *Bubble and foam chemistry*. Cambridge University Press, 2016.

[131] I. M. Lifshitz and V. V. Slyozov. "The kinetics of precipitation from supersaturated solid solutions". In: *Journal of Physics and Chemistry of Solids* 19.1-2 (1961), pp. 35–50. DOI: 10.1016/0022-3697(61)90054-3.

[132] A. Baldan. "Review: Progress in Ostwald ripening theories and their applications to nickel-base superalloys; Part I: Ostwald ripening theories". In: *Journal of Materials Science* 37 (2002), pp. 2171–2202. DOI: 10.1023/A:1015388912729.

[133] J. A. Glazier and D. Weaire. "The kinetics of cellular patterns". In: *Journal of Physics: Condensed Matter* 4.8 (1992), pp. 1867–1894. DOI: 10.1088/0953-8984/4/8/004.

[134] D. Langevin. "Foam stabilization mechanisms". In: *Foam films and foams: Fundamentals and applications*. Ed. by D. Exerowa, G. Gochev, D. Platikanov, L. Liggieri, and R. Miller. CRC Press, Taylor & Francis Group, 2018. Chap. 11, pp. 213–232.

[135] S. Magrabi, B. Dlugogorski, and G. Jameson. "Bubble size distribution and coarsening of aqueous foams". In: *Chemical Engineering Science* 54.18 (1999), pp. 4007–4022. DOI: 10.1016/S0009-2509(99)00098-6.

[136] W. Mullins. "Estimation of the geometrical rate constant in idealized three dimensional grain growth". In: *Acta Metallurgica* 37.11 (1989), pp. 2979–2984. DOI: 10.1016/0001-6160(89)90333-7.

[137] K. G. Marinova, E. S. Basheva, B. Nenova, M. Temelska, A. Y. Mirarefi, B. Campbell, and I. B. Ivanov. "Physico-chemical factors controlling the foamability and foam stability of milk proteins: Sodium caseinate and whey protein concentrates". In: *Food Hydrocolloids* 23.7 (2009), pp. 1864–1876. DOI: 10.1016/j.foodhyd.2009.03.003.

[138] K. Martínez and C. Carrera Sanchez. "Enhancing the foamability of beverages proteins by ultrasound". In: *International Journal of Horticulture, Agriculture and Food Science* 1.3 (2017), pp. 6–9. DOI: 10.22161/ijhaf.1.3.2.

[139] A. Kato and S. Nakai. "Hydrophobicity determined by a fluorescence probe method and its correlation with surface properties of proteins". In: *Biochimica et Biophysica Acta (BBA) - Protein Structure* 624.1 (1980), pp. 13–20. DOI: 10.1016/0005-2795(80)90220-2.

[140] A. Moro, C. Gatti, and N. Delorenzi. "Hydrophobicity of whey protein concentrates measured by fluorescence quenching and its relation with surface functional properties". In: *Journal of Agricultural and Food Chemistry* 49.10 (2001), pp. 4784–4789. DOI: 10.1021/jf001132e.

[141] E. Dickinson. "Mixed proteinaceous emulsifiers: Review of competitive protein adsorption and the relationship to food colloid stabilization". In: *Food Hydrocolloids* 1.1 (1986), pp. 3–23. ISSN: 0268-005X. DOI: 10.1016/S0268-005X(86)80003-0. URL: https://www.sciencedirect.com/science/article/pii/S0268005X86800030.

[142] The UniProt Consortium. "UniProt: The Universal Protein Knowledgebase in 2023". In: *Nucleic Acids Research* 51.D1 (2022). UniProtKB: P02769, pp. D523–D531. DOI: 10.1093/nar/gkac1052.

[143] D.-M. Smilgies and E. Folta-Stogniew. "Molecular weight–gyration radius relation of globular proteins: a comparison of light scattering, small-angle X-ray scattering and structure-based data". In: *Journal of Applied Crystallography* 48.5 (2015), pp. 1604–1606. DOI: 10.1107/S1600576715015551.

[144] E. Mylonas and D. I. Svergun. "Accuracy of molecular mass determination of proteins in solution by small-angle X-ray scattering". In: *Journal of Applied Crystallography* 40.s1 (2007), s245–s249. DOI: 10.1107/S002188980700252X.

[145] S. Akiyama. "Quality control of protein standards for molecular mass determinations by small-angle X-ray scattering". In: *Journal of Applied Crystallography* 43.2 (2010), pp. 237–243. DOI: 10.1107/S002188981000138X.

[146] S. Bienert, A. Waterhouse, T. A. P. de Beer, G. Tauriello, G. Studer, L. Bordoli, and T. Schwede. "The SWISS-MODEL Repository - new features and functionality". In: *Nucleic Acids Research* 45 (2017), pp. D313–D319. DOI: 10.1093/nar/gkw1132.

[147] J. R. Brown. "Serum albumin: Amino acid sequence". In: *Albumin: Structure, function and uses*. Ed. by V. M. Rosenoer, M. Oratz, and M. A. Rothschild. Oxford: Pergamon Press, Elsevier, 1977, pp. 27–51. DOI: 10.1016/B978-0-08-019603-9.50009-0.

[148] J. F. Foster. "Some aspects of the structure and conformational properties of serum albumin". In: *Albumin: Structure, function and uses*. Ed. by V. M. Rosenoer, M. Oratz, and M. A. Rothschild. Oxford: Pergamon Press, 1977, pp. 53–84. DOI: 10.1016/B978-0-08-019603-9.50010-7.

[149] D. C. Carter and J. X. Ho. "Structure of serum albumin". In: *Lipoproteins, apolipoproteins, and lipases*. Ed. by C. Anfinsen, J. T. Edsall, F. M. Richards, and D. S. Eisenberg. Vol. 45. Advances in Protein Chemistry. Academic Press, 1994, pp. 153–203. DOI: 10.1016/S0065-3233(08)60640-3. URL: https://www.sciencedirect.com/science/article/pii/S0065323308606403.

[150] K. Baler, O. A. Martín, M. A. Carignano, G. Ameer, J. A. Vila, and I. Szleifer. "Electrostatic unfolding and interactions of albumin driven by pH changes: a molecular dynamics study". In: *The Journal of Physical Chemistry B* 118.4 (2014), pp. 921–930. DOI: 10.1021/jp409936v.

[151] M. Bukackova, P. Rusnok, and R. Marsalek. "Mathematical methods in the calculation of the zeta potential of BSA". In: *Journal of Solution Chemistry* 47 (2018), pp. 1942–1952. DOI: 10.1007/s10953-018-0830-0.

[152] D. R. Grisham and V. Nanda. "Zeta potential prediction from protein structure in general aqueous electrolyte solutions". In: *Langmuir* 36 (2020), pp. 13799–13803. DOI: 10.1021/acs.langmuir.0c02031.

[153] B. Jachimska, M. Wasilewska, and Z. Adaczyk. "Characterization of globular protein solutions by dynamic light scattering, electrophoretic mobiliy, and viscosity measurements". In: *Langmuir* 24 (2008), pp. 6866–6872. DOI: 10.1021/la800548p.

[154] A. Salis, M. Boström, L. Medda, F. Cugia, B. Barse, D. F. Parsons, B. W. Ninham, and M. Monduzzi. "Measurements and theoretical interpretation of points of zero charge/potential of BSA protein". In: *Langmuir* 27 (2011), pp. 11597–11604. DOI: 10.1021/la2024605.

[155] Q. Shi, Y. Zhou, and Y. Sun. "Influence of pH and ionic strength on the steric mass-action model parameters around the isoelectric point of protein". In: *Biotechnology Progress* 21 (2005), pp. 516–523. DOI: 10.1021/bp049735o.

[156] H. A. Wösten. "Hydrophobins: multipurpose proteins". In: *Annual Review of Microbiology* 55.1 (2001), pp. 625–646. DOI: 10.1146/annurev.micro.55.1.625.

[157] H. Wösten, F. Schuren, and J. Wessels. "Interfacial self-assembly of a hydrophobin into an amphipathic protein membrane mediates fungal attachment to hydrophobic surfaces." In: *The EMBO Journal* 13.24 (1994), pp. 5848–5854. DOI: 10.1002/j.1460-2075.1994.tb06929.x.

[158] H. J. Hektor and K. Scholtmeijer. "Hydrophobins: Proteins with potential". In: *Current Opinion in Biotechnology* 16.4 (2005), pp. 434–439. DOI: 10.1016/j.copbio.2005.05.004.

[159] M. B. Linder, G. R. Szilvay, T. Nakari-Setälä, and M. E. Penttilä. "Hydrophobins: The protein-amphiphiles of filamentous fungi". In: *FEMS Microbiology Reviews* 29.5 (2005), pp. 877–896. DOI: 10.1016/j.femsre.2005.01.004.

[160] M. B. Linder. "Hydrophobins: Proteins that self assemble at interfaces". In: *Current Opinion in Colloid & Interface Science* 14.5 (2009), pp. 356–363. DOI: 10.1016/j.cocis.2009.04.001.

[161] H. A. Wösten, M.-A. van Wetter, L. G. Lugones, H. C. van der Mei, H. J. Busscher, and J. G. Wessels. "How a fungus escapes the water to grow into the air". In: *Current Biology* 9.2 (1999), pp. 85–88. DOI: 10.1016/S0960-9822(99)80019-0.

[162] S. Perrett, A. K. Buell, and T. P. Knowles. *Biological and bio-inspired nanomaterials*. Springer, 2019.

[163] V. Aimanianda, J. Bayry, S. Bozza, O. Kniemeyer, K. Perruccio, S. R. Elluru, C. Clavaud, S. Paris, A. A. Brakhage, S. V. Kaveri, L. Romani, and J.-P. Latgé. "Surface hydrophobin prevents immune recognition of airborne fungal spores". In: *Nature* 460.7259 (2009), pp. 1117–1121. DOI: 10.1038/nature08264.

[164] N. J. Talbot, D. J. Ebbole, and J. E. Hamer. "Identification and characterization of MPG1, a gene involved in pathogenicity from the rice blast fungus *Magnaporthe grisea*". In: *The Plant Cell* 5.11 (1993), pp. 1575–1590. DOI: 10.1105/tpc.5.11.1575.

[165] R. E. Beever and G. P. Dempsey. "Function of rodlets on the surface of fungal spores". In: *Nature* 272.5654 (1978), pp. 608–610. DOI: 10.1038/272608a0.

[166] J. Bayry, V. Aimanianda, J. I. Guijarro, M. Sunde, and J.-P. Latgé. "Hydrophobins—Unique fungal proteins". In: *PLoS Pathogens* 8.5 (2012), e1002700. DOI: 10.1371/journal.ppat.1002700.

[167] K. M. Bromley, R. J. Morris, L. Hobley, G. Brandani, R. M. Gillespie, M. McCluskey, U. Zachariae, D. Marenduzzo, N. R. Stanley-Wall, and C. E. MacPhee. "Interfacial self-assembly of a bacterial hydrophobin". In: *Proceedings of the National Academy of Sciences* 112.17 (2015), pp. 5419–5424. DOI: 10.1073/pnas.1419016112.

[168] L. Hobley, A. Ostrowski, F. V. Rao, K. M. Bromley, M. Porter, A. R. Prescott, C. E. MacPhee, D. M. Van Aalten, and N. R. Stanley-Wall. "BslA is a self-assembling bacterial hydrophobin that coats the *Bacillus subtilis* biofilm". In: *Proceedings of the National Academy of Sciences* 110.33 (2013), pp. 13600–13605. DOI: 10.1073/pnas.1306390110.

[169] M. Richter, J. M. Willey, R. Süßmuth, G. Jung, and H.-P. Fiedler. "Streptofactin, a novel biosurfactant with aerial mycelium inducing activity from *Streptomyces tendae* Tü 901/8c". In: *FEMS Microbiology Letters* 163.2 (1998), pp. 165–171. DOI: 10.1111/j.1574-6968.1998.tb13041.x.

[170] A. Kwan, R. Winefield, M. Sunde, J. Matthews, R. Haverkamp, M. Templeton, and J. Mackay. "Structural basis for rodlet assembly in fungal hydrophobins". In: *Proceedings of the National Academy of Sciences* 103.10 (2006), pp. 3621–3626. DOI: 10.1073/pnas.0505704103.

[171] J. P. Mackay, J. M. Matthews, R. D. Winefield, L. G. Mackay, R. G. Haverkamp, and M. D. Templeton. "The hydrophobin EAS is largely unstructured in solution and functions by forming amyloid-like structures". In: *Structure* 9.2 (2001), pp. 83–91. DOI: 10.1016/S0969-2126(00)00559-1.

[172] M. Sunde, A. H. Kwan, M. D. Templeton, R. E. Beever, and J. P. Mackay. "Structural analysis of hydrophobins". In: *Micron* 39.7 (2008), pp. 773–784. DOI: 10.1016/j.micron.2007.08.003.

[173] J. Hakanpää, G. R. Szilvay, H. Kaljunen, M. Maksimainen, M. Linder, and J. Rouvinen. "Two crystal structures of *Trichoderma reesei* hydrophobin HFBI—The structure of a protein amphiphile with and without detergent interaction". In: *Protein Science* 15.9 (2006), pp. 2129–2140. DOI: 10.1110/ps.062326706.

[174] S. Askolin, M. Linder, K. Scholtmeijer, M. Tenkanen, M. Penttilä, M. L. de Vocht, and H. A. Wösten. "Interaction and comparison of a class I hydrophobin from *Schizophyllum commune* and class II hydrophobins from *Trichoderma reesei*". In: *Biomacromolecules* 7.4 (2006), pp. 1295–1301. DOI: 10.1021/bm050676s.

[175] H. Fan, X. Wang, J. Zhu, G. T. Robillard, and A. E. Mark. "Molecular dynamics simulations of the hydrophobin SC3 at a hydrophobic/hydrophilic interface". In: *Proteins: Structure, Function, and Bioinformatics* 64.4 (2006), pp. 863–873. DOI: 10.1002/prot.20936.

[176] A. Walther and A. H. Müller. "Janus particles". In: *Soft Matter* 4.4 (2008), pp. 663–668. DOI: 10.1039/B718131K.

[177] K. Opwis and J. S. Gutmann. "Surface modification of textile materials with hydrophobins". In: *Textile Research Journal* 81.15 (2011), pp. 1594–1602. DOI: 10.1177/0040517511404599.

[178] G. R. Szilvay, A. Paananen, K. Laurikainen, E. Vuorimaa, H. Lemmetyinen, J. Peltonen, and M. B. Linder. "Self-assembled hydrophobin protein films at the air-water interface: Structural analysis and molecular engineering". In: *Biochemistry* 46.9 (2007), pp. 2345–2354. DOI: 10.1021/bi602358h.

[179] K. Kisko, M. Torkkeli, E. Vuorimaa, H. Lemmetyinen, O. H. Seeck, M. Linder, and R. Serimaa. "Langmuir–Blodgett films of hydrophobins HFBI and HFBII". In: *Surface Science* 584.1 (2005), pp. 35–40. DOI: 10.1016/j.susc.2004.12.036.

[180] K. Kisko, G. R. Szilvay, E. Vuorimaa, H. Lemmetyinen, M. B. Linder, M. Torkkeli, and R. Serimaa. "Self-assembled films of hydrophobin protein HFBIII from *Trichoderma reesei*". In: *Journal of Applied Crystallography* 40.s1 (2007), s355–s360. DOI: 10.1107/S0021889807001331.

[181] W. Hess, M. Sassen, and C. Remsen. "Surface structures of frozen-etched Penicillium conidiospores". In: *Naturwissenschaften* 53 (1966), pp. 708–708. DOI: 10.1007/BF00602737.

[182] T. Sarlin, T. Nakari-Setälä, M. Linder, M. Penttilä, and A. Haikara. "Fungal hydrophobins as predictors of the gushing activity of malt". In: *Journal of the Institute of Brewing* 111.2 (2005), pp. 105–111. DOI: 10.1002/j.2050-0416.2005.tb00655.x.

[183] B. W. Berger and N. D. Sallada. "Hydrophobins: Multifunctional biosurfactants for interface engineering". In: *Journal of Biological Engineering* 13.10 (2019), pp. 1–8. DOI: 10.1186/s13036-018-0136-1.

[184] H. K. Valo, P. H. Laaksonen, L. J. Peltonen, M. B. Linder, J. T. Hirvonen, and T. J. Laaksonen. "Multifunctional hydrophobin: Toward functional coatings for drug nanoparticles". In: *ACS Nano* 4.3 (2010), pp. 1750–1758. DOI: 10.1021/nn9017558.

[185] H. Valo, M. Kovalainen, P. Laaksonen, M. Häkkinen, S. Auriola, L. Peltonen, M. Linder, K. Järvinen, J. Hirvonen, and T. Laaksonen. "Immobilization of protein-coated drug nanoparticles in nanofibrillar cellulose matrices—Enhanced stability and release". In: *Journal of Controlled Release* 156.3 (2011), pp. 390–397. DOI: 10.1016/j.jconrel.2011.07.016.

[186] M. Sarparanta, L. M. Bimbo, J. Rytkönen, E. Mäkilä, T. J. Laaksonen, P. Laaksonen, M. Nyman, J. Salonen, M. B. Linder, J. Hirvonen, H. A. Santos, and A. J. Airaksinen. "Intravenous delivery of hydrophobin-functionalized porous silicon nanoparticles: Stability, plasma protein adsorption and biodistribution". In: *Molecular Pharmaceutics* 9.3 (2012), pp. 654–663. DOI: 10.1021/mp200611d.

[187] H. Valo, S. Arola, P. Laaksonen, M. Torkkeli, L. Peltonen, M. B. Linder, R. Serimaa, S. Kuga, J. Hirvonen, and T. Laaksonen. "Drug release from nanoparticles embedded in four different nanofibrillar cellulose aerogels". In: *European Journal of Pharmaceutical Sciences* 50.1 (2013), pp. 69–77. DOI: 10.1016/j.ejps.2013.02.023.

[188] G. Fang, B. Tang, Z. Liu, J. Gou, Y. Zhang, H. Xu, and X. Tang. "Novel hydrophobin-coated docetaxel nanoparticles for intravenous delivery: In vitro characteristics and in vivo performance". In: *European Journal of Pharmaceutical Sciences* 60 (2014), pp. 1–9. DOI: 10.1016/j.ejps.2014.04.016.

[189] H. Paukkonen, A. Ukkonen, G. Szilvay, M. Yliperttula, and T. Laaksonen. "Hydrophobin-nanofibrillated cellulose stabilized emulsions for encapsulation and release of BCS class II drugs". In: *European Journal of Pharmaceutical Sciences* 100 (2017), pp. 238–248. DOI: 10.1016/j.ejps.2017.01.029.

[190] M. Barani, M. Mirzaei, M. Torkzadeh-Mahani, A. Lohrasbi-Nejad, and M. H. Nematollahi. "A new formulation of hydrophobin-coated niosome as a drug carrier to cancer cells". In: *Materials Science and Engineering C* 113 (2020), p. 110975. DOI: 10.1016/j.msec.2020.110975.

[191] B. Wang, Z. Han, B. Song, L. Yu, Z. Ma, H. Xu, and M. Qiao. "Effective drug delivery system based on hydrophobin and halloysite clay nanotubes for sustained release of doxorubicin". In: *Colloids and Surfaces A: Physicochemical and Engineering Aspects* 628 (2021), p. 127351. DOI: 0.1016/j.colsurfa.2021.127351.

[192] X. Wang, J. Mao, Y. Chen, D. Song, Z. Gao, X. Zhang, Y. Bai, P. E. Saris, H. Feng, H. Xu, and M. Qiao. "Design of antibacterial biointerfaces by surface modification of poly (ε-caprolactone) with fusion protein containing hydrophobin and PA-1". In: *Colloids and Surfaces B: Biointerfaces* 151 (2017), pp. 255–263. DOI: 10.1016/j.colsurfb.2016.12.019.

[193] M. Artini, P. Cicatiello, A. Ricciardelli, R. Papa, L. Selan, P. Dardano, M. Tilotta, G. Vrenna, M. L. Tutino, P. Giardina, and E. Parrilli. "Hydrophobin coating prevents *Staphylococcus epidermidis* biofilm formation on different surfaces". In: *Biofouling* 33.7 (2017), pp. 601–611. DOI: 10.1080/08927014.2017.1338690.

[194] I. Sorrentino, M. Gargano, A. Ricciardelli, E. Parrilli, C. Buonocore, D. de Pascale, P. Giardina, and A. Piscitelli. "Development of anti-bacterial surfaces using a hydrophobin chimeric protein". In: *International Journal of Biological Macromolecules* 164 (2020), pp. 2293–2300. DOI: 10.1016/j.ijbiomac.2020.07.301.

[195] M. Qin, L.-K. Wang, X.-Z. Feng, Y.-L. Yang, R. Wang, C. Wang, L. Yu, B. Shao, and M.-Q. Qiao. "Bioactive surface modification of mica and poly (dimethylsiloxane) with hydrophobins for protein immobilization". In: *Langmuir* 23.8 (2007), pp. 4465–4471. DOI: 10.1021/la062744h.

[196] M. Zhang, Z. Wang, Z. Wang, S. Feng, H. Xu, Q. Zhao, S. Wang, J. Fang, M. Qiao, and D. Kong. "Immobilization of anti-CD31 antibody on electrospun poly (ε-caprolactone) scaffolds through hydrophobins for specific adhesion of endothelial cells". In: *Colloids and Surfaces B: Biointerfaces* 85.1 (2011), pp. 32–39. DOI: 10.1016/j.colsurfb.2010.10.042.

[197] S. Boeuf, T. Throm, B. Gutt, T. Strunk, M. Hoffmann, E. Seebach, L. Mühlberg, J. Brocher, T. Gotterbarm, W. Wenzel, R. Fischer, and W. Richter. "Engineering hydrophobin DewA to generate surfaces that enhance adhesion of human but not bacterial cells". In: *Acta Biomaterialia* 8.3 (2012), pp. 1037–1047. DOI: 10.1016/j.actbio.2011.11.022.

[198] V. Sterna, S. Zute, and L. Brunava. "Oat grain composition and its nutrition benefice". In: *Agriculture and Agricultural Science Procedia* 8 (2016), pp. 252–256. DOI: 10.1016/j.aaspro.2016.02.100.

[199] H.-D. Belitz, W. Grosch, and P. Schieberle. *Food chemistry*. 4th edition. Springer-Verlag, 2009. DOI: 10.1007/978-3-540-69934-7.

[200] C. Klose and E. K. Arendt. "Proteins in oats; their synthesis and changes during germination: A review". In: *Critical Reviews in Food Science and Nutrition* 52.7 (2012), pp. 629–639. DOI: 10.1080/10408398.2010.504902.

[201] O. E. Mäkinen, N. Sozer, D. Ercili-Cura, and K. Poutanen. "Protein from oat: Structure, processes, functionality, and nutrition". In: *Sustainable protein sources*. Ed. by S. R. Nadathur, J. P. Wanasundara, and L. Scanlin. Elsevier, 2017. Chap. 6, pp. 105–119. DOI: 10.1016/B978-0-12-802778-3.00006-8.

[202] S. R. Burgess, P. R. Shewry, G. J. Matlashewski, I. Altosaar, and B. J. Miflin. "Characteristics of oat (*Avena sativa L.*) seed globulins". In: *Journal of Experimental Botany* 34.147 (1983), pp. 1320–1332. DOI: 10.1093/jxb/34.10.1320.

[203] M. A. Shotwell, S. K. Boyer, R. S. Chesnut, and B. A. Larkins. "Analysis of seed storage protein genes of oats". In: *The Journal of Biological Chemistry* 265.17 (1990), pp. 9652–9658. DOI: 10.1016/S0021-9258(19)38719-8.

[204] M. A. Shotwell, C. Afonso, E. Davies, R. S. Chesnut, and B. A. Larkins. "Molecular characterization of oat seed globulins". In: *Plant Physiology* 87.3 (1988), pp. 698–704. DOI: 10.1104/pp.87.3.698.

[205] Y. Zhao, Y. Mine, and C.-Y. Ma. "Study of thermal aggregation of oat globulin by laser light scattering". In: *Journal of Agricultural and Food Chemistry* 52.10 (2004), pp. 3089–3096. DOI: 10.1021/jf030735y.

[206] R. Lásztity. "Oat grain - A wonderful reservoir of natural nutrients and biologically active substances". In: *Food Reviews International* 14.1 (1998), pp. 99–119. DOI: 10.1080/87559129809541150.

[207] D. M. Peterson and A. C. Brinegar. "Oat storage proteins". In: *Oats: Chemistry and technology*. Ed. by F. H. Webster and P. J. Wood. American Association of Cereal Chemists, Inc (AACC), 2011, pp. 153–203.

[208] S. Chen, Q. Hou, Y. Zhu, D. Wang, and W. Li. "On the origin of foam stability: understanding from viscoelasticity of foaming solutions and liquid films". In: *Journal of Dispersion Science and Technology* 35.9 (2014), pp. 1214–1221. DOI: 10.1080/01932691.2013.833102.

[209] P. Moll, L. Grossmann, I. Kutzli, and J. Weiss. "Influence of energy density and viscosity on foam stability–A study with pea protein (*Pisum Sativum L.*)" In: *Journal of Dispersion Science and Technology* 41.12 (2020), pp. 1789–1796. DOI: 10.1080/01932691.2019.1635028.

[210] A.-A. Townsend and S. Nakai. "Relationships between hydrophobicity and foaming characteristics of food proteins". In: *Journal of Food Science* 48.2 (1983), pp. 588–594. DOI: 10.1111/j.1365-2621.1983.tb10796.x.

[211] A. M. Stephen. *Food polysaccharides and their applications*. Taylor & Francis Group, 2006.

[212] A. Imeson. *Food stabilisers, thickeners and gelling agents*. Wiley Blackwell, 2010.

[213] P. Himashree, A. S. Sengar, and C. Sunil. "Food thickening agents: Sources, chemistry, properties and applications – A review". In: *International Journal of Gastronomy and Food Science* 27 (2022), p. 100468. DOI: 10.1016/j.ijgfs.2022.100468.

[214] P. A. Williams and G. O. Phillips. "Introduction to food hydrocolloids". In: *Handbook of hydrocolloids*. Elsevier, 2021, pp. 3–26. DOI: 10.1016/B978-0-12-820104-6.00017-6.

[215] E. Dickinson. "Hydrocolloids at interfaces and the influence on the properties of dispersed systems". In: *Food Hydrocolloids* 17.1 (2003), pp. 25–39. DOI: 10.1016/S0268-005X(01)00120-5.

[216] J. Milani and G. Maleki. "Hydrocolloids in food industry". In: *Food industrial processes: Methods and equipment*. Ed. by B. Valdez. InTech, 2012. Chap. 2.

[217] J. Hege, T. Palberg, and T. A. Vilgis. "Interactions of different hydrocolloids with milk proteins". In: *Journal of Physics: Materials* 3.4 (2020), p. 044003. DOI: 10.1088/2515-7639/aba2b7.

[218] J. Doublier and B. Launay. "Rheology of galactomannan solutions: Comparative study of guar gum and locust bean gum". In: *Journal of Texture Studies* 12.2 (1981), pp. 151–172. DOI: 10.1111/j.1745-4603.1981.tb01229.x.

[219] G. Robinson, S. B. Ross-Murphy, and E. R. Morris. "Viscosity-molecular weight relationships, intrinsic chain flexibility, and dynamic solution properties of guar galactomannan". In: *Carbohydrate Research* 107.1 (1982), pp. 17–32. DOI: 10.1016/S0008-6215(00)80772-7.

[220] J. A. Casas, A. F. Mohedano, and F. García-Ochoa. "Viscosity of guar gum and xanthan/guar gum mixture solutions". In: *Journal of the Science of Food and Agriculture* 80.12 (2000), pp. 1722–1727. DOI: 10.1002/1097-0010(20000915)80:12<1722::AID-JSFA708>3.0.CO;2-X.

[221] A. K. Raychaudhuri. *Classical theory of electricity and magnetism*. Vol. 21. Springer, 2022. DOI: 10.1007/978-981-16-8139-4.

[222] J. N. Israelachvili. *Intermolecular and surface forces*. 3rd edition. Elsevier, 2011.

[223] J. K. Dhont. *An introduction to dynamics of colloids*. Elsevier, 1996.

[224] P. Atkins, G. Ratcliffe, M. Wormald, and J. de Paula. *Physical chemistry for the life sciences*. 3rd edition. Oxford University Press, 2023.

[225] J. Lyklema. *Fundamentals of interface and colloid science. Volume I: Fundamentals*. Vol. 1. Academic Press, 1991.

[226] J. Israelachvili and R. Pashley. "The hydrophobic interaction is long range, decaying exponentially with distance". In: *Nature* 300 (1982), pp. 341–342. DOI: 10.1038/300341a0.

[227] S. H. Donaldson Jr, A. Røyne, K. Kristiansen, M. V. Rapp, S. Das, M. A. Gebbie, D. W. Lee, P. Stock, M. Valtiner, and J. Israelachvili. "Developing a general interaction potential for hydrophobic and hydrophilic interactions". In: *Langmuir* 31.7 (2014), pp. 2051–2064. DOI: 10.1021/la502115g.

[228] M. U. Hammer, T. H. Anderson, A. Chaimovich, M. S. Shell, and J. Israelachvili. "The search for the hydrophobic force law". In: *Faraday Discussions* 146 (2010), pp. 299–308. DOI: 10.1039/b926184b.

[229] E. E. Meyer, K. J. Rosenberg, and J. Israelachvili. "Recent progress in understanding hydrophobic interactions". In: *Proceedings of the National Academy of Sciences* 103.43 (2006), pp. 15739–15746. DOI: 10.1073/pnas.0606422103.

[230] A. Einstein. "Eine neue Bestimmung der Moleküldimensionen". In: *Annalen der Physik* (1906), pp. 289–306.

[231] A. Einstein. "Berichtigung zu meiner Arbeit: Eine neue Bestimmung der Moleküldimensionen". In: *Annalen der Physik* (1911), pp. 591–592.

[232] G. B. Jeffery. "The motion of ellipsoidal particles immersed in a viscous fluid". In: *Proceedings of the Royal Society of London. Series A, Containing papers of a mathematical and physical character* 102.715 (1922), pp. 161–179. DOI: 10.1098/rspa.1922.0078.

[233] S. E. Harding. "Dilute solution viscometry of food biopolymers". In: *Functional Properties of Food Macromolecules* 149 (1998), pp. 77–142.

[234] G. D'Avino, F. Greco, and P. L. Maffettone. "Rheology of a dilute viscoelastic suspension of spheroids in unconfined shear flow". In: *Rheologica Acta* 54 (2015), pp. 915–928. DOI: 10.1007/s00397-015-0881-8.

[235] IUPAC. "Terminology and Symbols in Colloid and Surface Chemistry Part 1.13. Definitions, Terminology and Symbols for Rheological Properties". In: *Pure and Applied Chemistry* 51.5 (1979), pp. 1213–1218. DOI: 10.1351/pac197951051213.

[236] C. Tanford and J. G. Buzzell. "The viscosity of aqueous solutions of bovine serum albumin between pH 4.3 and 10.5." In: *The Journal of Physical Chemistry* 60.2 (1956), pp. 225–231. DOI: 10.1021/J150536A020.

[237] F. Booth and H. Wills. "The electroviscous effect for suspensions of solid spherical particles". In: *Proceedings of the Royal Society of London. Series A. Mathematical and Physical Sciences* 203.1075 (1950), pp. 533–551. DOI: 10.1098/rspa.1950.0155.

[238] S. Tesch and H. Schubert. "Influence of increasing viscosity of the aqueous phase on the short-term stability of protein stabilized emulsions". In: *Journal of Food Engineering* 52.3 (2002), pp. 305–312. DOI: 10.1016/S0260-8774(01)00120-0.

[239] P. Kováts, D. Thévenin, and K. Zähringer. "Influence of viscosity and surface tension on bubble dynamics and mass transfer in a model bubble column". In: *International Journal of Multiphase Flow* 123 (2020), p. 103174. DOI: 10.1016/j.ijmultiphaseow.2019.103174.

[240] K. Koczo, D. T. Wasan, R. P. Borwankar, and A. Gonsalves. "Flocculation of food dispersions by gums: isotropic/anisotropic dispersion separation by xanthan gum". In: *Food Hydrocolloids* 12.1 (1998), pp. 43–53. DOI: 10.1016/S0268-005X(98)00044-7.

[241] P. J. Flory. "Phase equilibria in solutions of rod-like particles". In: *Proceedings of the Royal Society of London. Series A. Mathematical and Physical Sciences* 234.1196 (1956), pp. 73–89. DOI: 10.1098/rspa.1956.0016.

[242] P. J. Flory and A. Abe. "Statistical thermodynamics of mixtures of rodlike particles. 1. Theory for polydisperse systems". In: *Macromolecules* 11.6 (1978), pp. 1119–1122. DOI: 10.1021/ma60066a011.

[243] P. J. Flory. "Statistical thermodynamics of mixtures of rodlike particles. 5. Mixtures with random coils". In: *Macromolecules* 11.6 (1978), pp. 1138–1141. DOI: 10.1021/ma60066a015.

[244] M. M. Castellanos, J. A. Pathak, and R. H. Colby. "Both protein adsorption and aggregation contribute to shear yielding and viscosity increase in protein solutions". In: *Soft Matter* 10.1 (2014), pp. 122–131. DOI: 10.1039/c3sm51994e.

[245] D. Y. Abramovitch, S. B. Andersson, L. Y. Pao, and G. Schitter. "A tutorial on the mechanisms, dynamics, and control of atomic force microscopes". In: *2007 American Control Conference*. IEEE. 2007, pp. 3488–3502. DOI: 10.1109/ACC.2007.4282300.

[246] M. R. Ragazzon, J. T. Gravdahl, and K. Y. Pettersen. "Model-based identification of nanomechanical properties in atomic force microscopy: Theory and experiments". In: *IEEE Transactions on Control Systems Technology* 27.5 (2018), pp. 2045–2057. DOI: 10.1109/TCST.2018.2847644.

[247] G. Binnig, C. F. Quate, and C. Gerber. "Atomic Force Microscope". In: *Physical Review Letters* 56.9 (1986), p. 930. DOI: 10.1103/PhysRevLett.56.930.

[248] P. Eaton and P. West. *Atomic force microscopy*. Oxford University Press, 2010.

[249] W. Daear, M. Mahadeo, and E. J. Prenner. "Applications of Brewster angle microscopy from biological materials to biological systems". In: *Biochimica et Biophysica Acta (BBA)-Biomembranes* 1859.10 (2017), pp. 1749–1766. DOI: 10.1016/j.bbamem.2017.06.016.

[250] D. Hoenig and D. Moebius. "Direct visualization of monolayers at the air-water interface by Brewster angle microscopy". In: *The Journal of Physical Chemistry* 95.12 (1991), pp. 4590–4592. DOI: 10.1021/j100165a003.

[251] S. Hénon and J. Meunier. "Microscope at the Brewster angle: Direct observation of first-order phase transitions in monolayers". In: *Review of Scientific Instruments* 62.4 (1991), pp. 936–939. DOI: 10.1063/1.1142032.

[252] A. Blume. "Lipids at the air–water interface". In: *ChemTexts* 4.1 (2018), p. 3. DOI: 10.1007/s40828-018-0058-z.

[253] D. Vollhardt. "Brewster angle microscopy: A preferential method for mesoscopic characterization of monolayers at the air/water interface". In: *Current Opinion in Colloid & Interface Science* 19.3 (2014), pp. 183–197. DOI: 10.1016/j.cocis.2014.02.001.

[254] C. H. Spink. "Differential scanning calorimetry". In: *Methods in Cell Biology* 84 (2008), pp. 115–141. DOI: 10.1016/S0091-679X(07)84005-2.

[255] E. S. Watson and M. J. O'Neill. "Differential microcalorimeter". In: *US 3,263,484 patent* (1962).

[256] NETZSCH-Gerätebau GmbH. *Differential scanning calorimetry (DSC) / differential thermal analysis (DTA)*. Accessed: 2024-06-07. 2024. URL: https://analyzing-testing.netzsch.com/en/products/differential-scanning-calorimeter-dsc-differential-thermal-analyzer-dta.

[257] J. Kurreck, J. W. Engels, and F. Lottspeich, eds. *Bioanalytik*. Springer Spektrum, 2022. DOI: 10.1007/978-3-662-61707-6.

[258] P. Gill, T. T. Moghadam, and B. Ranjbar. "Differential scanning calorimetry techniques: Applications in biology and nanoscience". In: *Journal of Biomolecular Techniques* 21.4 (2010), pp. 167–193.

[259] Wyatt Technology Corporation. *Dynamische Lichtstreuung (DLS)*. Accessed: 2024-07-17. 2024. URL: https://www.wyatt.com/de/solutions/techniques/dynamic-light-scattering-nanoparticle-size.html?gad_source=1&gclid=EAIaIQobChMIsPvIjN2thwMVp5-DBx05UgdVEAAYASAAEgLAu_D_BwE.

[260] J. Stetefeld, S. A. McKenna, and T. R. Patel. "Dynamic light scattering: a practical guide and applications in biomedical sciences". In: *Biophysical Reviews* 8 (2016), pp. 409–427. DOI: 10.1007/s12551-016-0218-6.

[261] Wyatt Technology™, a portfolio of Waters Corporation™. *Understanding dynamic light scattering*. Accessed: 2024-07-17. 2024. URL: https://www.wyatt.com/library/theory/dynamic-light-scattering-theory.html.

[262] J. N. Weiss. "Dynamic light scattering (DLS) spectroscopy". In: *Dynamic light scattering spectroscopy of the human eye*. Springer, 2022, pp. 13–17. DOI: 10.1007/978-3-031-06624-5.

[263] B. J. Berne and R. Pecora. *Dynamic light scattering: With applications to chemistry, biology, and physics*. Dover Publications, Inc., 2000.

[264] D. Ferreira, R. Bachelard, W. Guerin, R. Kaiser, and M. Fouché. "Connecting field and intensity correlations: The Siegert relation and how to test it". In: *American Journal of Physics* 88.10 (2020), pp. 831–837. DOI: 10.1119/10.0001630.

[265] S. W. Provencher. "Inverse problems in polymer characterization: Direct analysis of polydispersity with photon correlation spectroscopy". In: *Die Makromolekulare Chemie / Macromolecular Chemistry and Physics* 180.1 (1979), pp. 201–209. DOI: 10.1002/macp.1979.021800119.

[266] S. W. Provencher. "A constrained regularization method for inverting data represented by linear algebraic or integral equations". In: *Computer Physics Communications* 27.3 (1982), pp. 213–227. DOI: 10.1016/0010-4655(82)90173-4.

[267] S. W. Provencher and P. Štêpánek. "Global analysis of dynamic light scattering autocorrelation functions". In: *Particle & Particle Systems Characterization* 13.5 (1996), pp. 291–294. DOI: 10.1002/ppsc.19960130507.

[268] S. Damodaran. "Amino acids, peptides, and proteins". In: *Food chemistry*. Ed. by O. R. Fennema. 3rd edition. Marcel Dekker, Inc., 1996. Chap. 6, pp. 321–430.

[269] Thermo Fisher Scientific. *HPLC basics*. Accessed: 2024-06-04. URL: https://www.thermofisher.com/de/en/home/industrial/chromatography/chromatography-learning-center/liquid-chromatography-information/hplc-basics.html.

[270] M. S. Tsvet. "On a new category of adsorption phenomena and their application to biochemical analysis". In: *Tr. Varshavskogo obschestva estestvoispytatelei, Otd. Biolol* 14.6 (1903), pp. 1–20.

[271] E. Heftmann. "Liquid chromatography–past and future". In: *Journal of Chromatographic Science* 11.6 (1973), pp. 295–298. DOI: 10.1093/chromsci/11.6.295.

[272] A. J. Martin and R. L. Synge. "A new form of chromatogram employing two liquid phases: A theory of chromatography. 2. Application to the micro-determination of the higher monoamino-acids in proteins". In: *Biochemical Journal* 35.12 (1941), pp. 1358–1368. DOI: 10.1042/bj0351358.

[273] S. Aryal. *HPLC: Principle, parts, types, uses, diagram*. Accessed: 2024-06-04. 2024. URL: https://microbenotes.com/high-performance-liquid-chromatography-hplc/.

[274] Keyence corporation. *Optical microscopes*. Accessed: 2024-06-11. 2024. URL: https://www.keyence.eu/ss/products/microscope/microscope_glossary/optical_microscopes/.

[275] E. Hecht. *Optik*. 8th edition. Walter de Gruyter GmbH, 2023.

[276] Keyence corporation. *Basic structure and principle of microscopes*. Accessed: 2024-06-11. 2024. URL: https://www.keyence.eu/ss/products/microscope/microscope_glossary/basic/basic_structure_and_principle_of_microscopes.jsp.

[277] A. A. Al-Tubuly. "SDS-PAGE and Western Blotting". In: *Diagnostic and therapeutic antibodies*. Ed. by A. J. T. George and C. E. Urch. Humana Press Inc., 2000. Chap. 32, pp. 391–405.

[278] Creative Proteomics. *SDS-PAGE service*. Accessed: 2024-06-18. 2024. URL: https://www.creative-proteomics.com/pronalyse/sds-page-service.html.

[279] KRÜSS GmbH. *Tensiometer*. Accessed: 2024-06-11. URL: https://www.kruss-scientific.com/en/know-how/glossary/tensiometer.

[280] S. Laurén. *White paper: Surface and interfacion tension – How to select the best measurement method*. Västra Frölunda, Sweden: Biolin Scientific AB, 2018.

[281] L. Wilhelmy. "Ueber die Abhängigkeit der Capillaritäts-Constanten des Alkohols von Substanz und Gestalt des benetzten festen Körpers". In: *Annalen der Physik und Chemie* 195.6 (1863), pp. 177–217. DOI: 10.1002/andp.18631950602.

[282] C. D. Volpe and S. Siboni. "The Wilhelmy method: A critical and practical review". In: *Surface Innovations* 6.3 (2018), pp. 120–132. DOI: 10.1680/jsuin.17.00059.

[283] D. I. GmbH. *Wilhelmy plate method*. Accessed: 2024-06-11. URL: https://www.dataphysics-instruments.com/knowledge/understanding-interfaces/wilhelmy-plate-method/.

[284] KRÜSS GmbH. *Wilhelmy plate method*. Accessed: 2024-06-11. URL: https://www.kruss-scientific.com/en/know-how/glossary/wilhelmy-plate-method.

[285] KRÜSS GmbH. *Technical note: Force tensiometry with ring and plate*. Hamburg, Germany, 2004.

[286] Anton Paar GmbH. *How to measure viscosity*. Accessed: 2023-09-19 and 2024-07-15. 2023. URL: https://wiki.anton-paar.com/en/how-to-measure-viscosity/.

[287] Anton Paar GmbH. *Rolling-ball viscometer: Lovis 2000 M/ME*. Accessed: 2023-09-19. 2023. URL: https://www.anton-paar.com/uk-en/products/details/rolling-ball-viscometer-lovis-2000-mme/.

[288] J. Spurk and N. Aksel. *Strömungslehre: Einführung in die Theorie der Strömungen*. 9th edition. Springer, 2019. DOI: 10.1007/978-3-662-58764-5.

[289] T. G. Mezger. *Das Rheologie Handbuch*. 3rd edition. Vincentz Network, 2010.

[290] R. M. Hubbard and G. G. Brown. "The rolling ball viscometer". In: *Industrial & Engineering Chemistry Analytical Edition* 15.3 (1943), pp. 212–218. DOI: 10.1021/i560115a018.

[291] J. H. Masliyah and S. Bhattacharjee. *Electrokinetic and colloid transport phenomena*. John Wiley & Sons, 2006.

[292] S. Seiffert, C. Kummerlöwe, and N. Vennemann, eds. *Makromolekulare Chemie*. 6th edition. Springer, 2020. DOI: 10.1007/978-3-662-61109-8.

[293] Malvern Instruments Ltd. *Zetasizer nano series: User manual*. Worcestershire, United Kingdom, 2013.

[294] J. Lyklema. *Fundamentals of interface and colloid science. Volume II: Solid-liquid interfaces*. Vol. 2. Reprint 2001. Academic Press, 1995.

[295] A. S. Khair. "Nonlinear electrophoresis of colloidal particles". In: *Current Opinion in Colloid & Interface Science* 59 (2022), p. 101587. DOI: 10.1016/j.cocis.2022.101587.

[296] S. Wall. "The history of electrokinetic phenomena". In: *Current Opinion in Colloid & Interface Science* 15.3 (2010), pp. 119–124. DOI: 10.1016/j.cocis.2009.12.005.

[297] D. Henry. "The cataphoresis of suspended particles. Part I.—The equation of cataphoresis". In: *Proceedings of the Royal Society of London. Series A* 133.821 (1931), pp. 106–129. DOI: 10.1098/rspa.1931.0133.

[298] H. Ohshima. "A simple expression for Henry's function for the retardation effect in electrophoresis of spherical colloidal particles". In: *Journal of Colloid and Interface Science* 168.1 (1994), pp. 269–271. DOI: 10.1006/jcis.1994.1419.

[299] C. Stringer, T. Wang, M. Michaelos, and M. Pachitariu. "Cellpose: A generalist algorithm for cellular segmentation". In: *Nature Methods* 18.1 (2021), pp. 100–106. DOI: 10.1038/s41592-020-01018-x.

[300] M. Pachitariu and C. Stringer. "Cellpose 2.0: How to train your own model". In: *Nature Methods* 19.12 (2022), pp. 1634–1641. DOI: 10.1038/s41592-022-01663-4.

[301] T. Lohtander, R. Herrala, P. Laaksonen, S. Franssila, and M. Österberg. "Lightweight lignocellulosic foams for thermal insulation". In: *Cellulose* 29.3 (2022), pp. 1855–1871. DOI: 10.1007/s10570-021-04385-6.

[302] J. Krom, K. Meister, and T. A. Vilgis. "Simple method to assess foam structure and stability using hydrophobin and BSA as model systems". In: *ChemPhysChem* (2024), e202400050. DOI: 10.1002/cphc.202400050.

[303] M. V. Kempin, M. Kraume, and A. Drews. "W/O Pickering emulsion preparation using a batch rotor-stator mixer – Influence on rheology, drop size distribution and filtration behavior". In: *Journal of Colloid and Interface Science* 573 (2020), pp. 135–149. DOI: 10.1016/j.jcis.2020.03.103.

[304] C. Plikat, A. Drews, and M. B. Ansorge-Schumacher. "Effects of protein content on Pickering-assisted interfacial enzyme catalysis". In: *ChemCatChem* 14.18 (2022), e202200444. DOI: 10.1002/cctc.202200444.

[305] IKA-Werke GmbH & Co. KG. *T 25 digital ULTRA-TURRAX: Operating instructions*. Staufen, Germany, 2023.

[306] GeeksforGeeks. *Python — Thresholding techniques using OpenCV — Set-1 (Simple thresholding)*. Accessed: 2024-05-10. 2023. URL: https://www.geeksforgeeks.org/python-thresholding-techniques-using-opencv-set-1-simple-thresholding/.

[307] A. Rosebrock. *OpenCV thresholding (cv2.threshold)*. Accessed: 2024-05-10. 2021. URL: https://pyimagesearch.com/2021/04/28/opencv-thresholding-cv2-threshold/.

[308] K. Oetjen, C. Bilke-Krause, M. Madani, and T. Willers. "Temperature effect on foamability, foam stability, and foam structure of milk". In: *Colloids and Surfaces A: Physicochemical and Engineering Aspects* 460 (2014), pp. 280–285. DOI: 10.1016/j.colsurfa.2014.01.086.

[309] M. Brüls, S. Foroutanparsa, T. Merland, C. E. P. Maljaars, M. M. Olsthoorn, R. P. Tas, and I. K. Voets. "Quantitative image analysis of influence of polysaccharides on protein network formation in GDL-acidified milk gels". In: *Food Structure* 38 (2023), p. 100352. DOI: 10.1016/j.foostr.2023.100352.

[310] L. L. Olijve, A. S. Oude Vrielink, and I. K. Voets. "A simple and quantitative method to evaluate ice recrystallization kinetics using the circle Hough Transform algorithm". In: *Crystal Growth & Design* 16.8 (2016), pp. 4190–4195. DOI: 10.1021/acs.cgd.5b01637.

[311] J. Schindelin, I. Arganda-Carreras, E. Frise, V. Kaynig, M. Longair, T. Pietzsch, S. Preibisch, C. Rueden, S. Saalfeld, B. Schmid, J.-Y. Tinevez, D. J. White, V. Hartenstein, K. Eliceiri, P. Tomancak, and A. Cardona. "Fiji: An open-source platform for biological-image analysis". In: *Nature Methods* 9.7 (2012), pp. 676–682. DOI: 10.1038/nmeth.2019.

[312] J. Saad, M. Fomich, V. P. Día, and T. Wang. "A novel automated protocol for ice crystal segmentation analysis using Cellpose and Fiji". In: *Cryobiology* 111 (2023), pp. 1–8. DOI: 10.1016/j.cryobiol.2023.02.002.

[313] D. K. Sarker, D. Bertrand, Y. Chtioui, and Y. Popineau. "Characterisation of foam properties using image analysis". In: *Journal of Texture Studies* 29.1 (1998), pp. 15–42. DOI: 10.1111/j.1745-4603.1998.tb00151.xopen_in_newISSN002.

[314] L. Nichele, V. Persichetti, M. Lucidi, and G. Cincotti. "Quantitative evaluation of ImageJ thresholding algorithms for microbial cell counting". In: *OSA Continuum* 3.6 (2020), pp. 1417–1427. DOI: 10.1364/OSAC.393971.

[315] S. M. Hartig. "Basic image analysis and manipulation in ImageJ". In: *Current Protocols in Molecular Biology* 102.1 (2013), pp. 14.15.1–14.15.12. DOI: 10.1002/0471142727.mb1415s102.

[316] J.-C. Isarin, A. D. Kaasjager, and R. B. Holweg. "Bubble size distribution during the application of foam to fabrics and its effects on product quality". In: *Textile Research Journal* 65.2 (1995), pp. 61–69. DOI: 10.1177/004051759506500201.

[317] S. P. Gido, D. E. Hirt, S. M. Montgomery, R. K. Prud'homme, and L. Rebenfeld. "Foam bubble size measured using image analysis before and after passage through a porous medium". In: *Journal of Dispersion Science and Technology* 10.6 (1989), pp. 785–793. DOI: 10.1080/01932698908943199.

[318] N. J. Apthorpe, A. J. Riordan, R. E. Aguilar, J. Homann, Y. Gu, D. W. Tank, and H. S. Seung. "Automatic neuron detection in calcium imaging data using convolutional networks". In: *Advances in Neural Information Processing Systems* 29 (2016).

[319] F. A. Guerrero-Pena, P. D. Marrero Fernandez, T. I. Ren, M. Yui, E. Rothenberg, and A. Cunha. "Multiclass weighted loss for instance segmentation of cluttered cells". In: *2018 25th IEEE International Conference on Image Processing (ICIP)*. IEEE, 2018, pp. 2451–2455. DOI: 10.1109/ICIP.2018.8451187.

[320] Y. Al-Kofahi, A. Zaltsman, R. Graves, W. Marshall, and M. Rusu. "A deep learning-based algorithm for 2-D cell segmentation in microscopy images". In: *BMC Bioinformatics* 19.365 (2018), pp. 1–11. DOI: 10.1186/s12859-018-2375-z.

[321] J. Chen, L. Ding, M. P. Viana, H. Lee, M. F. Sluezwski, B. Morris, M. C. Hendershott, R. Yang, I. A. Mueller, and S. M. Rafelski. "The Allen Cell and Structure Segmenter: A new open source toolkit for segmenting 3D intracellular structures in fluorescence microscopy images". In: *BioRxiv* (2020). DOI: 10.1101/491035.

[322] J. Funke, L. Mais, A. Champion, N. Dye, and D. Kainmueller. "A benchmark for epithelial cell tracking". In: *Proceedings of The European Conference on Computer Vision (ECCV) Workshops*. Computer Vision Foundation, 2018, pp. 1–9.

[323] J. Yi, H. Tang, P. Wu, B. Liu, D. J. Hoeppner, D. N. Metaxas, L. Han, and W. Fan. "Object-guided instance segmentation for biological images". In: *Proceedings of the AAAI Conference on Artificial Intelligence*. Vol. 34. 2020, pp. 12677–12684. DOI: 10.1609/aaai.v34i07.6960.

[324] M. Aggarwal, A. K. Tiwari, M. P. Sarathi, and A. Bijalwan. "An early detection and segmentation of Brain Tumor using Deep Neural Network". In: *BMC Medical Informatics and Decision Making* 23.78 (2023), pp. 1–12. DOI: 0.1186/s12911-023-02174-8.

[325] L. Ahmed, M. M. Iqbal, H. Aldabbas, S. Khalid, Y. Saleem, and S. Saeed. "Images data practices for semantic segmentation of breast cancer using deep neural network". In: *Journal of Ambient Intelligence and Humanized Computing* 14.11 (2023), pp. 15227–15243. DOI: 0.1007/s12652-020-01680-1.

[326] X. Liu, L. Song, S. Liu, and Y. Zhang. "A review of deep-learning-based medical image segmentation methods". In: *Sustainability* 13.3 (2021), p. 1224. ISSN: 2071-1050. DOI: 10.3390/su13031224. URL: https://www.mdpi.com/2071-1050/13/3/1224.

[327] C. McQuin, A. Goodman, V. Chernyshev, L. Kamentsky, B. A. Cimini, K. W. Karhohs, M. Doan, L. Ding, S. M. Rafelski, D. Thirstrup, W. Wiegraebe, S. Singh, T. Becker, J. C. Caicedo, and A. E. Carpenter. "CellProfiler 3.0: Next-generation image processing for biology". In: *PLoS Biology* 16.7 (2018), e2005970. DOI: 10.1371/journal.pbio.2005970.

[328] J. C. Bonilla, J. L. Sørensen, A. S. Warming, and M. P. Clausen. "Quantitative image analysis of protein foam microstructure and its correlation with rheological properties: Egg white foam". In: *Food Hydrocolloids* 133 (2022), p. 108010. DOI: 10.1016/j.foodhyd.2022.108010.

[329] S. Tcholakova, Z. Mitrinova, K. Golemanov, N. D. Denkov, M. Vethamuthu, and K. P. Ananthapadmanabhan. "Control of Ostwald ripening by using surfactants with high surface modulus". In: *Langmuir* 27.24 (2011), pp. 14807–14819. DOI: 10.1021/la203952p.

[330] D. Langevin. "Coalescence in foams and emulsions: Similarities and differences". In: *Current Opinion in Colloid & Interface Science* 44 (2019), pp. 23–31. ISSN: 1359-0294. DOI: 10.1016/j.cocis.2019.09.001,MemorialVolume. URL: https://www.sciencedirect.com/science/article/pii/S1359029419300391.

[331] R. Gilbert, M. Hess, A. Jenkins, R. Jones, P. Kratochvil, and R. Stepto. "Dispersity in polymer science". In: *Pure and Applied Chemistry* 81.2 (2009), pp. 351–353. DOI: 10.1351/PAC-REC-08-05-02.

[332] S. Koltzenburg, M. Maskos, and O. Nuyken. *Polymer chemistry*. Springer, 2017.

[333] O. Pitois. "Foam ripening". In: *Foam engineering: Fundamentals and applications*. Ed. by P. Stevenson. Wiley Online Library, 2012. Chap. 4, pp. 59–73.

[334] S. González-Pérez, J. M. Vereijken, G. A. van Koningsveld, H. Gruppen, and A. G. Voragen. "Formation and stability of foams made with sunflower (*Helianthus annuus*) proteins". In: *Journal of Agricultural and Food Chemistry* 53.16 (2005), pp. 6469–6476. DOI: 10.1021/jf0501793.

[335] S. Omirbekov, H. Davarzani, S. Colombano, and A. Ahmadi-Senichault. "Experimental and numerical upscaling of foam flow in highly permeable porous media". In: *Advances in Water Resources* 146 (2020), p. 103761. DOI: 10.1016/j.advwatres.2020.103761.

[336] C. A. Schneider, W. S. Rasband, and K. W. Eliceiri. "NIH Image to ImageJ: 25 years of image analysis". In: *Nature Methods* 9.7 (2012), pp. 671–675. DOI: 10.1038/nmeth.2089.

[337] P. Fox, T. Uniacke-Lowe, P. McSweeney, and J. O'Mahony. "Milk proteins". In: *Dairy chemistry and biochemistry*. Springer, 2015. Chap. 4, pp. 145–239.

[338] P. Fox. "Milk proteins: General and historical aspects". In: *Advanced dairy chemistry – 1 Proteins: Part A*. Springer, 2003, pp. 1–48. DOI: 10.1007/978-1-4419-8602-3_1.

[339] K. Nishinari, Y. Fang, S. Guo, and G. Phillips. "Soy proteins: A review on composition, aggregation and emulsification". In: *Food Hydrocolloids* 39 (2014), pp. 301–318. DOI: 10.1016/j.foodhyd.2014.01.013.

[340] X. Wang, J. F. Graveland-Bikker, C. G. De Kruif, and G. T. Robillard. "Oligomerization of hydrophobin SC3 in solution: From soluble state to self-assembly". In: *Protein Science* 13.3 (2004), pp. 810–821. DOI: 10.1110/ps.03367304.

[341] M. Torkkeli, R. Serimaa, O. Ikkala, and M. Linder. "Aggregation and self-assembly of hydrophobins from *Trichoderma reesei*: Low-resolution structural models". In: *Biophysical Journal* 83.4 (2002), pp. 2240–2247. DOI: 10.1016/S0006-3495(02)73984-2.

[342] C. E. Barquilha and M. C. Braga. "Adsorption of organic and inorganic pollutants onto biochars: Challenges, operating conditions, and mechanisms". In: *Bioresource Technology Reports* 15 (2021), p. 100728. DOI: 10.1016/j.biteb.2021.100728.

[343] K. E. Riley and P. Hobza. "Noncovalent interactions in biochemistry". In: *Wiley Interdisciplinary Reviews: Computational Molecular Science* 1.1 (2011), pp. 3–17. DOI: 10.1002/wcms.8.

[344] A. Karshikoff. "Introduction". In: *Non-covalent interactions in proteins*. 2nd edition. World Scientific, 2021. Chap. 1, pp. 1–26. DOI: 10.1142/9789811228094_0001.

[345] P. A. Kollman. "Noncovalent Interactions". In: *Accounts of Chemical Research* 10.10 (1977), pp. 365–371.

[346] J. Wessels. "Developmental regulation of fungal cell wall formation". In: *Annual Review of Phytopathology* 32.188 (1994), pp. 413–437. DOI: 10.1146/annurev.py.32.090194.002213.

[347] I. N. Berezovsky and E. I. Shakhnovich. "Physics and evolution of thermophilic adaptation". In: *Proceedings of the National Academy of Sciences* 102.36 (2005), pp. 12742–12747. DOI: 10.1073/pnas.0503890102.

[348] A. Michnik. "Thermal stability of bovine serum albumin DSC study". In: *Journal of Thermal Analysis and Calorimetry* 71 (2003), pp. 509–519. DOI: 10.1023/A:1022851809481.

[349] A. Michnik, K. Michalik, and Z. Drzazga. "Stability of bovine serum albumin at different pH". In: *Journal of Thermal Analysis and Calorimetry* 80.2 (2005), pp. 399–406. DOI: 10.1007/s10973-005-0667-9.

[350] A. Michnik, K. Michalik, A. Kluczewska, and Z. Drzazga. "Comparative DSC study of human and bovine serum albumin". In: *Journal of Thermal Analysis and Calorimetry* 84.1 (2006), pp. 113–117. DOI: 10.1007/s10973-005-7170-1.

[351] M. Matejak and J. Kofranek. "Molar amount of water". In: *Medsoft* 32.1 (2020), pp. 85–88. DOI: 10.35191/medsoft_2020_1_32_85_88.

[352] International Association for the Properties of Water and Steam. *Guideline on the use of fundamental physical constants and basic constants of water*. IAPWS G5-01. 2020.

[353] N. Vargaftik, B. Volkov, and L. Voljak. "International tables of the surface tension of water". In: *Journal of Physical and Chemical Reference Data* 12.3 (1983), pp. 817–820. DOI: 10.1063/1.555688.

[354] J. D. Paulsen, R. Carmigniani, A. Kannan, J. C. Burton, and S. R. Nagel. "Coalescence of bubbles and drops in an outer fluid". In: *Nature Communications* 5.3182 (2014), pp. 1–7. DOI: 10.1038/ncomms4182.

[355] M. Alheshibri, J. Qian, M. Jehannin, and V. S. Craig. "A history of nanobubbles". In: *Langmuir* 32.43 (2016), pp. 11086–11100. DOI: 10.1021/acs.langmuir.6b02489.

[356] M. Holmberg, A. Kühle, J. Garnæs, K. A. Mørch, and A. Boisen. "Nanobubble trouble on gold surfaces". In: *Langmuir* 19.25 (2003), pp. 10510–10513. DOI: 10.1021/la0352669.

[357] Z. Wu, X. Zhang, X. Zhang, J. Sun, Y. Dong, and J. Hu. "In situ AFM observation of BSA adsorption on HOPG with nanobubble". In: *Chinese Science Bulletin* 52.14 (2007), pp. 1913–1919. DOI: 10.1007/s11434-007-0288-8.

[358] M. Switkes and J. Ruberti. "Rapid cryofixation/freeze fracture for the study of nanobubbles at solid–liquid interfaces". In: *Applied Physics Letters* 84.23 (2004), pp. 4759–4761. DOI: 10.1063/1.1755837.

[359] X. H. Zhang, X. D. Zhang, S. T. Lou, Z. X. Zhang, J. L. Sun, and J. Hu. "Degassing and temperature effects on the formation of nanobubbles at the mica/water interface". In: *Langmuir* 20.9 (2004), pp. 3813–3815. DOI: 10.1021/la0364542.

[360] P. Klapetek, D. Nečas, and C. Anderson. *Data processing and analysis: Statistical analysis*. Accessed: 2024-07-23. 2023. URL: http://gwyddion.net/documentation/user-guide-en/statistical-analysis.html.

[361] G. R. Szilvay, T. Nakari-Setälä, and M. B. Linder. "Behavior of *Trichoderma reesei* hydrophobins in solution: Interactions, dynamics, and multimer formation". In: *Biochemistry* 45.28 (2006), pp. 8590–8598. DOI: 10.1021/bi060620y.

[362] K. L. Vergunst, C. Kenward, and D. N. Langelaan. "Characterization of the structure and self-assembly of two distinct class IB hydrophobins". In: *Applied Microbiology and Biotechnology* 106.23 (2022), pp. 7831–7843. DOI: 10.1007/s00253-022-12253-x.

[363] V. C. Lo, Q. Ren, C. L. Pham, V. K. Morris, A. H. Kwan, and M. Sunde. "Fungal hydrophobin proteins produce self-assembling protein films with diverse structure and chemical stability". In: *Nanomaterials* 4.3 (2014), pp. 827–843. DOI: 10.3390/nano4030827.

[364] J. Yang, L. Ge, B. Song, Z. Ma, X. Yang, B. Wang, Y. Dai, H. Xu, and M. Qiao. "A novel hydrophobin encoded by HGFII from *Grifola frondosa* exhibiting excellent self-assembly ability". In: *Frontiers in Microbiology* 13 (2022), p. 990231. DOI: 10.3389/fmicb.2022.990231.

[365] W. Hess, M. Sassen, and C. Remsen. "Surface characteristics of Penicillium conidia". In: *Mycologia* 60.2 (1968), pp. 290–303. DOI: 10.1080/00275514.1968.12018570.

[366] H. A. Wösten, O. M. De Vries, and J. G. Wessels. "Interfacial self-assembly of a fungal hydrophobin into a hydrophobic rodlet layer." In: *The Plant Cell* 5.11 (1993), pp. 1567–1574. DOI: 10.1105/tpc.5.11.1567.

[367] N. Takahashi, Y. Terauchi, T. Tanaka, A. Yoshimi, H. Yabu, and K. Abe. "Involvement of ionic interactions in self-assembly and resultant rodlet formation of class I hydrophobin RolA from *Aspergillus oryzae*". In: *Bioscience, Biotechnology, and Biochemistry* 87.8 (2023), pp. 857–864. DOI: 10.1093/bbb/zbad066.

[368] I. Valsecchi, J. I. Lai, E. Stephen-Victor, A. Pillé, A. Beaussart, V. Lo, C. L. Pham, V. Aimanianda, A. H. Kwan, M. Duchateau, Q. G. Gianetto, M. Matondo, M. Lehoux, D. C. Sheppard, Y. F. Dufrene, J. Bayry, J. I. Guijarro, M. Sunde, and J.-P. Latgé. "Assembly and disassembly of *Aspergillus fumigatus* conidial rodlets". In: *The Cell Surface* 5 (2019), p. 100023. DOI: 10.1016/j.tcsw.2019.100023.

[369] L. Yu, B. Zhang, G. R. Szilvay, R. Sun, J. Jänis, Z. Wang, S. Feng, H. Xu, M. B. Linder, and M. Qiao. "Protein HGFI from the edible mushroom *Grifola frondosa* is a novel 8 kDa class I hydrophobin that forms rodlets in compressed monolayers". In: *Microbiology* 154.6 (2008), pp. 1677–1685. DOI: 10.1099/mic.0.2007/015263-0.

[370] M. L. de Vocht, K. Scholtmeijer, E. W. van der Vegte, O. M. de Vries, N. Sonveaux, H. A. Wösten, J.-M. Ruysschaert, G. Hadziioannou, J. G. Wessels, and G. T. Robillard. "Structural characterization of the hydrophobin SC3, as a monomer and after self-assembly at hydrophobic/hydrophilic interfaces". In: *Biophysical Journal* 74.4 (1998), pp. 2059–2068. DOI: 10.1016/S0006-3495(98)77912-3.

[371] M. L. De Vocht, I. Reviakine, W.-P. Ulrich, W. Bergsma-Schutter, H. A. Wösten, H. Vogel, A. Brisson, J. G. Wessels, and G. T. Robillard. "Self-assembly of the hydrophobin SC3 proceeds via two structural intermediates". In: *Protein Science* 11.5 (2002), pp. 1199–1205. DOI: 10.1110/ps.4540102.

[372] X. Wang, H. Permentier, R. Rink, J. Kruijtzer, R. Liskamp, H. Wösten, B. Poolman, and G. Robillard. "Probing the self-assembly and the accompanying structural changes of hydrophobin SC3 on a hydrophobic surface by mass spectrometry". In: *Biophysical Journal* 87.3 (2004), pp. 1919–1928. DOI: 10.1529/biophysj.104.041616.

[373] J. Yang, B. Wang, L. Ge, X. Yang, X. Wang, Y. Dai, B. Niu, H. Xu, and M. Qiao. "The enhancement of surface activity and nanoparticle stability through the alteration of charged amino acids of HGFI". In: *Colloids and Surfaces B: Biointerfaces* 175 (2019), pp. 703–712. DOI: 10.1016/j.colsurfb.2018.12.044.

[374] H. A. Wösten and M. L. de Vocht. "Hydrophobins, the fungal coat unravelled". In: *Biochimica et Biophysica Acta (BBA)-Reviews on Biomembranes* 1469.2 (2000), pp. 79–86. DOI: 10.1016/S0304-4157(00)00002-2.

[375] Z. Wang, M. Lienemann, M. Qiau, and M. B. Linder. "Mechanisms of protein adhesion on surface films of hydrophobin". In: *Langmuir* 26.11 (2010), pp. 8491–8496. DOI: 10.1021/la101240e.

[376] W. Ternes. *Naturwissenschaftliche Grundlagen der Lebensmittelzubereitung*. Behr's Verlag, 2008.

[377] P.-G. De Gennes. *Scaling concepts in polymer physics*. Cornell University Press, 1979.

[378] A. Imeson, ed. *Thickening and gelling agents for food*. 2nd edition. Aspen Publishers, 1999.

[379] S. Iglauer, Y. Wu, P. Shuler, Y. Tang, and W. A. Goddard III. "Dilute iota- and kappa-carrageenan solutions with high viscosities in high salinity brines". In: *Journal of Petroleum science and Engineering* 75.3-4 (2011), pp. 304–311. DOI: 10.1016/j.petrol.2010.11.025.

[380] J. E. Martín-Alfonso, A. Cuadri, M. Berta, and M. Stading. "Relation between concentration and shear-extensional rheology properties of xanthan and guar gum solutions". In: *Carbohydrate Polymers* 181 (2018), pp. 63–70. DOI: 10.1016/j.carbpol.2017.10.057.

[381] V. Calabrese, S. J. Haward, and A. Q. Shen. "Effects of shearing and extensional flows on the alignment of colloidal rods". In: *Macromolecules* 54.9 (2021), pp. 4176–4185. DOI: 10.1021/acs.macromol.0c02155.

[382] M. Detert, T. P. Santos, A. Q. Shen, and V. Calabrese. "Alignment–rheology relationship of biosourced rod-like colloids and polymers under flow". In: *Biomacromolecules* 24.7 (2023), pp. 3304–3312. DOI: 10.1021/acs.biomac.3c00347.

[383] E. S. De Preval, D. Fabrice, M. Gilles, C. Gérard, and M. Samir. "Influence of surface properties and bulk viscosity on bubble size prediction during foaming operation". In: *Colloids and Surfaces A: Physicochemical and Engineering Aspects* 442 (2014), pp. 88–97. DOI: 10.1016/j.colsurfa.2013.05.025.

[384] N. Politova, S. Tcholakova, Z. Valkova, K. Golemanov, and N. D. Denkov. "Self-regulation of foam volume and bubble size during foaming via shear mixing". In: *Colloids and Surfaces A: Physicochemical and Engineering Aspects* 539 (2018), pp. 18–28. DOI: 10.1016/j.colsurfa.2017.12.006.

[385] N. Denkov, S. Tcholakova, and N. Politova-Brinkova. "Physicochemical control of foam properties". In: *Current Opinion in Colloid & Interface Science* 50 (2020), p. 101376. DOI: 10.1016/j.cocis.2020.08.001.

[386] P. A. Gunning, D. J. Hibberd, A. M. Howe, and M. M. Robins. "Gravitational destabilization of emulsions flocculated by non-adsorbed xanthan". In: *Food Hydrocolloids* 2.2 (1988), pp. 119–129. DOI: 10.1016/S0268-005X(88)80010-9.

[387] E. A. Foegeding, P. Luck, and J. Davis. "Factors determining the physical properties of protein foams". In: *Food Hydrocolloids* 20.2 (2006). 7th International Hydrocolloids Conference, pp. 284–292. ISSN: 0268-005X. DOI: 10.1016/j.foodhyd.2005.03.014.

[388] M. A. Masuelli. "Study of bovine serum albumin solubility in aqueous solutions by intrinsic viscosity measurements". In: *Advances in Physical Chemistry* (2013), pp. 1–8. DOI: 10.1155/2013/360239.

[389] J. E. Kinsella. "Protein structure and functional properties: Emulsification and flavor binding effects". In: *Food protein deterioration*. ACS Publications, 1982, pp. 301–326. DOI: 10.1021/bk-1982-0206.ch012.

[390] S. Etemad, A. Kantzas, and S. Bryant. "A systematic analysis of foam drainage: Experiment and model". In: *Results in Engineering* 15 (2022), p. 100551. DOI: 10.1016/j.rineng.2022.100551.

[391] B. M. Yapo. "Lemon juice improves the extractability and quality characteristics of pectin from yellow passion fruit by-product as compared with commercial citric acid extractant". In: *Bioresource Technology* 100 (2009), pp. 3147–3151. DOI: 10.1016/j.biortech.2009.01.039.

[392] F. G. Silversides and K. Budgell. "The relationships among measures of egg albumen height, pH, and whipping volume". In: *Poultry Science* 83 (2004), pp. 1619–1623. DOI: 10.1093/ps/83.10.1619.

[393] B. C. Tripp, J. J. Magda, and J. D. Andrade. "Adsorption of globular proteins at the air/water interface as measured via dynamic surface tension: Concentration dependence, mass-transfer considerations, and adsorption kinetics". In: *Journal of Colloid and Interface Science* 173.1 (1995), pp. 16–27. DOI: 10.1006/jcis.1995.1291.

[394] P. Kruglyakov, S. Karakashev, A. Nguyen, and N. Vilkova. "Foam drainage". In: *Current Opinion in Colloid & Interface Science* 13.3 (2008), pp. 163–170. DOI: 10.1016/j.cocis.2007.11.003.

[395] G. A. Ross, G. M. Morris, and P. C. Biggin. "Rapid and accurate prediction and scoring of water molecules in protein binding sites". In: *PloS One* 7.3 (2012), e32036. DOI: 10.1371/journal.pone.0032036.

[396] Z. Li and T. Lazaridis. "Water at biomolecular binding interfaces". In: *Physical Chemistry Chemical Physics* 9.5 (2007), pp. 573–581. DOI: 10.1039/B612449F.

[397] A. Saint-Jalmes and D. Langevin. "Time evolution of aqueous foams: Drainage and coarsening". In: *Journal of Physics: Condensed Matter* 14.40 (2002), pp. 9397–9412. DOI: 10.1088/0953-8984/14/40/325.

[398] D. J. Durian, D. Weitz, and D. Pine. "Scaling behavior in shaving cream". In: *Physical Review A* 44.12 (1991), R7902–R7905. DOI: 10.1103/PhysRevA.44.R7902.

[399] J. A. Glazier, S. P. Gross, and J. Stavans. "Dynamics of two-dimensional soap froths". In: *Physical Review A* 36.1 (1987), pp. 306–312. DOI: 10.1103/PhysRevA.36.306.

[400] P. Móritz. "Über einen Zusammenhang zwischen Viskosität und Oberflächenspannung der Flüssigkeiten". In: *Periodica Polytechnica Chemical Engineering* 3.3 (1959), pp. 167–176.

[401] A. H. Pelofsky. "Surface Tension-Viscosity Relation for Liquids". In: *Journal of Chemical and Engineering Data* 11.3 (1966), pp. 394–397. DOI: 10.1021/je60030a031.

[402] H. Schonhorn. "Surface tension-viscosity relationship for liquids". In: *Journal of Chemical and Engineering Data* 12.4 (1967), pp. 524–525. DOI: 10.1021/je60035a016.

[403] A. J. Queimada, I. M. Marrucho, E. H. Stenby, and J. A. Coutinho. "Generalized relation between surface tension and viscosity: A study on pure and mixed *n*-alkanes". In: *Fluid Phase Equilibria* 222–223 (2004), pp. 161–168. DOI: 10.1016/j.fluid.2004.06.016.

[404] J. Reeh. "Der Einfluss von Enzymen auf die physikalischen und sensorischen Eigenschaften bei Herstellung einer Hafermilch". MA thesis. Justus-Liebig-Universiät Gießen, 2022.

[405] A.-L. Schlichting. "Hafermilchschäume: Struktur und Stabilität". MA thesis. Justus-Liebig-Universiät Gießen, 2022.

[406] J. Krom, J. Reeh, A. Schlichting, and T. A. Vilgis. "Haferdrink: Formulierung und Schaum – eine physikalische Perspektive". In: *RFL – Rundschau für Fleischhygiene und Lebensmittelüberwachung* 75.2 (2023), pp. 52–56.

[407] J. Krom, J. Reeh, A. Schlichting, and T. A. Vilgis. "Haferdrink – physikalische Einblicke". In: *Der Lebensmittelbrief* 34.5 (2023), pp. 52–57.

[408] Statista GmbH. *Market value of oat beverages worldwide in 2019 and 2027*. Accessed: 5th January, 2023. 2022. URL: https://www.statista.com/statistics/1098378/global-oat-drinks-market-value/.

[409] Statista GmbH. *Leading oat producing countries worldwide in 2023*. Accessed: 21st January, 2025. 2024. URL: https://www.statista.com/statistics/1073550/global-leading-oats-producers/.

[410] J. Poore and T. Nemecek. "Reducing food's environmental impacts through producers and consumers". In: *Science* 360.6392 (2018), pp. 987–992. DOI: 10.1126/science.aaq0216.

[411] E. Röös, M. Patel, and J. Spångberg. "Producing oat drink or cow's milk on a Swedish farm – Environmental impacts considering the service of grazing, the opportunity cost of land and the demand for beef and protein". In: *Agricultural Systems* 142 (2016), pp. 23–32. DOI: 10.1016/j.agsy.2015.11.002.

[412] D. Stewart and G. McDougall. "Oat agriculture, cultivation and breeding targets: Implications for human nutrition and health". In: *British Journal of Nutrition* 112.S2 (2014), S50–S57. DOI: 10.1017/S0007114514002736.

[413] C. Klose, B. D. Schehl, and E. K. Arendt. "Fundamental study on protein changes taking place during malting of oats". In: *Journal of Cereal Science* 49 (2009), pp. 83–91. DOI: 10.1016/j.jcs.2008.07.014.

[414] A. R. A. Silva, M. M. N. Silva, and B. D. Ribeiro. "Health issues and technological aspects of plant-based alternative milk". In: *Food Research International* 131 (2020), pp. 1–17. DOI: 10.1016/j.foodres.2019.108972.

[415] M. Havrlentová and J. Kraic. "Content of beta-d-glucan in cereal grains". In: *Journal of Food and Nutrition Research (Slovak Republic)* (2006).

[416] A. Deswal, N. S. Deora, and H. N. Mishra. "Effect of concentration and temperature on the rheological properties of oat milk". In: *Food and Bioprocess Technology* 7.8 (2014), pp. 2451–2459. DOI: 10.1007/s11947-014-1332-8.

[417] W. Biel, K. Kazimierska, and U. Bashutska. "Nutritional value of wheat, triticale, barley and oat grains". In: *Acta Scientiarum Polonorum Zootechnica* 19 (2020), pp. 19–28. DOI: 10.21005/asp.2020.19.2.03.

[418] F. Zhu. "Structures, properties, modifications, and uses of oat starch". In: *Food Chemistry* 229 (2017), pp. 329–340. DOI: 10.1016/j.foodchem.2017.02.064.

[419] C. Y. Ma and V. R. Harwalkar. "Chemical characterization and functionality assessment of oat protein fractions". In: *Journal of Agricultural and Food Chemistry* 32.1 (1984), pp. 144–149.

[420] C. Y. Ma and V. R. Harwalkar. "Studies of thermal denaturation of oat globulin by differential scanning calorimetry". In: *Journal of Food Science* 53.2 (1988), pp. 531–534. DOI: 10.1111/j.1365-2621.1988.tb07749.x.

[421] D. Bhaskar, S. K. Khatkar, R. Chawla, H. Panwar, and S. Kapoor. "Effect of β-glucan fortification on physico-chemical, rheological, textural, colour and organoleptic characteristics of low fat dahi". In: *Journal of Food Science and Technology* 54.9 (2017), pp. 2684–2693. DOI: 10.1007/s13197-017-2705-6.

[422] A. K. Stone, M. G. Nosworthy, C. Chiremba, J. D. House, and M. T. Nickerson. "A comparative study of the functionality and protein quality of a variety of legume and cereal flours". In: *Cereal Chemistry* 96.6 (2019), pp. 1159–1169. DOI: 10.1002/cche.10226.

[423] P. Zakidou, E.-M. Varka, and A. Paraskevopoulou. "Foaming properties and sensory acceptance of plant-based beverages as alternatives in the preparation of cappuccino style beverages". In: *International Journal of Gastronomy and Food Science* 30 (2022), p. 100623. DOI: 10.1016/j.ijgfs.2022.100623.

[424] B. Zhang, S. Dhital, and M. J. Gidley. "Densely packed matrices as rate determining features in starch hydrolysis". In: *Trends in Food Science & Technology* 43.1 (2015), pp. 18–31. ISSN: 0924-2244. DOI: 10.1016/j.tifs.2015.01.004. URL: https://www.sciencedirect.com/science/article/pii/S0924224415000242.

[425] A. Deswal, N. S. Deora, and H. N. Mishra. "Optimization of enzymatic production process of oat milk using response surface methodology". In: *Food and Bioprocess Technology* 7.2 (2014), pp. 610–618. DOI: 10.1007/s11947-013-1144-2.

[426] C. R. Soccol, P. J. Rojan, A. K. Patel, A. L. Woiciechowski, L. P. Vandenberghe, and A. Pandey. "Glucoamylase". In: *Enzyme technology*. Ed. by A. Pandey, C. Webb, C. R. Soccol, and C. Larroche. Springer, 2006. Chap. 11, pp. 221–237.

[427] T. Patra, C. Axel, Å. Rinnan, and K. Olsen. "The physicochemical stability of oat-based drinks". In: *Journal of Cereal Science* 104 (2022), p. 103422. ISSN: 0733-5210. DOI: 10.1016/j.jcs.2022.103422.

[428] C. Sandhya, A. Sumantha, and A. Pandey. "Protease". In: *Enzyme technology*. Ed. by A. Pandey, C. Webb, C. R. Soccol, and C. Larroche. Springer, 2006. Chap. 16, pp. 319–332.

[429] M. Brückner-Gühmann, T. Heiden-Hecht, N. Sözer, and S. Drusch. "Foaming characteristics of oat protein and modification by partial hydrolysis". In: *European Food Research and Technology* 244 (2018), pp. 2095–2106. DOI: 10.1007/s00217-018-3118-0.

[430] X. Guan, H. Yao, Z. Chen, L. Shan, and M. Zhang. "Some functional properties of oat bran protein concentrate modified by trypsin". In: *Food Chemistry* 101.1 (2007), pp. 163–170. DOI: 10.1016/j.foodchem.2006.01.011.

[431] M. Flemming. "Untersuchungen zur proteolytischen Aktivität pflanzlicher Milchsäfte und deren Einfluss auf die Hämostase und Fibrinolyse". PhD thesis. Freie Universität Berlin, 2015.

[432] N. Russ, B. I. Zielbauer, M. Ghebremedhin, and T. A. Vilgis. "Pre-gelatinized tapioca starch and its mixtures with xanthan gum and ι-carrageenan". In: *Food Hydrocolloids* 56 (2016), pp. 180–188. DOI: 10.1016/j.foodhyd.2015.12.021.

[433] D. Paton. "Differential scanning calorimetry of oat starch pastes". In: *Cereal Chemistry* 64 (1987), pp. 394–399.

[434] M. Gudmundsson and A.-C. Eliasson. "Some physico-chemical properties of oat starches extracted from varieties with different oil content". In: *Acta Agriculturae Scandinavica* 39 (1989), pp. 101–111. DOI: 10.1080/00015128909438502.

[435] R. F. Tester and J. Karkalas. "Swelling and gelatinization of oat starches". In: *Cereal Chemistry* 73.2 (1996), pp. 271–277.

[436] D. R. Lineback. "The starch granule organization and properties". In: *Baker's Dig.* 13 (1984), pp. 16–21.

[437] M. Hartunian-Sowa and P. J. White. "Characterisation of starch isolated from oat groats with different amount of lipid". In: *Cereal Chemistry* 69 (1992), pp. 521–527.

[438] M. Zhou, K. Robards, M. Glennie-Holmes, and S. Helliwell. "Structure and pasting properties of oat starch". In: *Cereal Chemistry* 75.3 (1998), pp. 273–281. DOI: 10.1094/CCHEM.1998.75.3.273.

[439] S. Punia, K. S. Sandhu, S. B. Dhull, A. K. Siroha, S. S. Purewal, M. Kaur, and M. K. Kidwai. "Oat starch: Physico-chemical, morphological, rheological characteristics and its applications–A review". In: *International Journal of Biological Macromolecules* 154 (2020), pp. 493–498. DOI: 10.1016/j.ijbiomac.2020.03.083.

[440] T. Suzuki, A. Chiba, and T. Yarno. "Interpretation of small angle X-ray scattering from starch on the basis of fractals". In: *Carbohydrate Polymers* 34.4 (1997), pp. 357–363. DOI: 10.1016/S0144-8617(97)00170-7.

[441] L. A. Archer. "Polymer disentanglement in steady-shear flow". In: *Journal of Rheology* 43.6 (1999), pp. 1617–1633. DOI: 10.1122/1.551063.

[442] S. Shin, K. D. Dorfman, and X. Cheng. "Shear-banding and superdiffusivity in entangled polymer solutions". In: *Physical Review E* 96.6 (2017), p. 062503. DOI: 10.1103/PhysRevE.96.062503.

[443] R. H. Colby, D. Boris, W. Krause, and S. Dou. "Shear thinning of unentangled flexible polymer liquids". In: *Rheologica Acta* 46.5 (2007), pp. 569–575. DOI: 10.1007/s00397-006-0142-y.

[444] L. A. Pereira Alcântara, R. da Costa Ilhéu Fontan, R. C. Ferreira Bonomo, E. Cardozo de Souza, Jr., V. Santos Sampaio, and R. Gonçalves Pereira. "Density and dynamic viscosity of bovine milk affect by temperature and composition". In: *International Journal of Food Engineering* 8.1 (2012). DOI: 10.1515/1556-3758.1860.

[445] J.-i. Horinaka, R. Yasuda, and T. Takigawa. "Entanglement properties of cellulose and amylose in an ionic liquid". In: *Journal of Polymer Science Part B: Polymer Physics* 49.13 (2011), pp. 961–965. DOI: 10.1002/polb.22262.

[446] B. Jauregui, M. Muñoz, and A. Santamaria. "The onset of entangled behaviour in amylose solutions". In: *Polymer* 34.8 (1993), pp. 1776–1779. DOI: 10.1016/0032-3861(93)90342-8.

[447] C. Zielke, O. Kosik, M.-L. Ainalem, A. Lovegrove, A. Stradner, and L. Nilsson. "Characterization of cereal β-glucan extracts from oat and barley and quantification of proteinaceous matter". In: *PLoS One* 12.2 (2017), e0172034. DOI: 10.1371/journal.pone.0172034.

[448] A. Shah, F. Masoodi, A. Gani, and B. Ashwar. "Dual enzyme modified oat starch: Structural characterisation, rheological properties, and digestibility in simulated GI tract". In: *International Journal of Biological Macromolecules* 106 (2018), pp. 140–147. DOI: 10.1016/j.ijbiomac.2017.08.013.

[449] The UniProt Consortium. "UniProt: the Universal Protein Knowledgebase in 2023". In: *Nucleic Acids Research* (Nov. 2022). DOI: 10.1093/nar/gkac1052.

[450] D. Li, G. Wu, H. Zhang, and X. Qi. "Preparation of crocin nanocomplex in order to increase its physical stability". In: *Food Hydrocolloids* 120 (2021), p. 106415. DOI: 10.1016/j.foodhyd.2020.106415.

[451] W. Ramsden. "Separation of solids in the surface-layers of solutions and 'suspensions' (observations on surface-membranes, bubbles, emulsions, and mechanical coagulation). – Preliminary account". In: *Proceedings of the Royal Society of London* 72.477-486 (1904), pp. 156–164. DOI: 10.1098/rspl.1903.0034.

[452] S. U. Pickering. "CXCVI. – Emulsions". In: *Journal of the Chemical Society, Transactions* 91 (1907), pp. 2001–2021. DOI: 10.1039/CT9079102001.

[453] J. Wu and G.-H. Ma. "Recent studies of Pickering emulsions: Particles make the difference". In: *Small* 12.34 (2016), pp. 4633–4648. DOI: 10.1002/smll.201600877.

[454] D. G. Ortiz, C. Pochat-Bohatier, J. Cambedouzou, M. Bechelany, and P. Miele. "Current trends in Pickering emulsions: Particle morphology and applications". In: *Engineering* 6.4 (2020), pp. 468–482. DOI: 10.1016/j.eng.2019.08.017.

[455] N. D. Denkov. "Mechanisms of foam destruction by oil-based antifoams". In: *Langmuir* 20.22 (2004), pp. 9463–9505. DOI: 10.1021/la049676o.

[456] K. J. Mysels and M. N. Jones. "Direct measurement of the variation of double-layer repulsion with distance". In: *Discussions of the Faraday Society* 42 (1966), pp. 42–50. DOI: 10.1039/DF9664200042.

[457] T. Morokuma, Y. Utaka, and M. Shoji. "Measurement of liquid film thickness between coalescing twin air bubbles in a water pool using a modified laser extinction method". In: *Heat Transfer Engineering* 36.14-15 (2015), pp. 1266–1274. DOI: 10.1080/01457632.2015.994994.

[458] L. Chiappisi. "Liquid foams: New insights and perspectives from neutron and synchrotron scattering experiments". In: *Current Opinion in Colloid & Interface Science* 72 (2024), p. 101823. DOI: 10.1016/j.cocis.2024.101823.

[459] S. Van der Walt, J. L. Schönberger, J. Nunez-Iglesias, F. Boulogne, J. D. Warner, N. Yager, E. Gouillart, T. Yu, and the scikit-image contributors. "scikit-image: image processing in Python". In: *PeerJ* 2 (2014), e453. DOI: 10.7717/peerj.453.

[460] S. Bhattiprolu. *python_for_microscopists/032-grain_analysis_saving_to_csv.py*. Accessed: 2025-02-14. 2020. URL: https://github.com/bnsreenu/python_for_microscopists/blob/master/032-grain_analysis_saving_to_csv.py.

[461] F. L. González Flecha and V. Levi. "Determination of the molecular size of BSA by fluorescence anisotropy". In: *Biochemistry and Molecular Biology Education* 31.5 (2003), pp. 319–322. DOI: 10.1002/bmb.2003.494031050261.

[462] R. H. Ewoldt, M. T. Johnston, and L. M. Caretta. "Experimental challenges of shear rheology: How to avoid bad data". In: *Complex fluids in biological systems: Experiment, theory, and computation*. Ed. by S. E. Spagnolie. Springer, 2015. Chap. 6, pp. 207–241.

[463] Q. Ying and B. Chu. "Overlap concentration of macromolecules in solution". In: *Macromolecules* 20.2 (1987), pp. 362–366. DOI: 10.1021/ma00168a023.

[464] M. Ganesan, E. J. Stewart, J. Szafranski, A. E. Satorius, J. G. Younger, and M. J. Solomon. "Molar mass, entanglement, and associations of the biofilm polysaccharide of *Staphylococcus epidermidis*". In: *Biomacromolecules* 14.5 (2013), pp. 1474–1481. DOI: 10.1021/bm400149a.

[465] G. Scatchard and E. S. Black. “The effect of salts on the isoionic and isoelectric points of proteins”. In: *The Journal of Physical Chemistry* 53.1 (1949), pp. 88–100. DOI: 10.1021/j150466a007.

[466] E. Limpert, W. A. Stahel, and M. Abbt. “Log-normal distributions across the sciences: Keys and clues”. In: *BioScience* 51.5 (2001), pp. 341–352. DOI: 10.1641/0006-3568(2001)051[0341:LNDATS]2.0.CO;2.

[467] J. M. de la Rubia. “Lognormal distribution for social researchers: A probability classic”. In: *International Journal of Psychology and Counselling* 16.2 (2024), pp. 10–25. DOI: 10.5897/IJPC2024.0702.

List of Figures

List of Tables

List of Acronyms

AFM	Atomic force microscopy
BAM	Brewster angle microscopy
BSA	Bovine serum albumin
DAD	Photodiode array detector
DLS	Dynamic light scattering
DSC	Differential scanning calorimetry
ELSD	Evaporative light scattering detector
EP1	Enzyme preparation 1 (α-amylase)
EP2	Enzyme preparation 2 (glucoamylase, α-amylase, protease)
EP3	Enzyme preparation 3 (β-glucanase, cellulase, pentosanase)
GG	Guar gum
HP	Hydrophobin, H*B hydrophobin
HPLC	High-performance liquid chromatography
HOPG	Highly-oriented pyrolytic graphite
IC	Iota-carrageenan
IEP	Isoelectric point
Oi0	No addition of canola oil
Oi1	1 % canola oil
Oi2	2 % canola oil
Oi3	3 % canola oil
Pa	Protease active
Pap	Protease active, pasteurization
Pi	Protease inactive
Pip	Protease inactive, pasteurization
S1	Treatment with EP1 only
S2	Treatment with EP1 and EP2
S3	Treatment with EP1, EP2, and EP3
S3Oi	Treatment with EP1, EP2, and EP3, addition of canola oil and salt
SDS-PAGE	Sodium dodecyl sulfate-polyacrylamid gel electrophoresis
vdW interaction	Van der Waals interaction
XG	Xanthan gum

Acknowledgements

Eigenständigkeitserklärung

Hiermit erkläre ich,

dass ich die vorliegende Arbeit selbstständig verfasst und keine anderen als die angegebenen Quellen und Hilfsmittel (dazu zählen auch KI-basierte Anwendungen oder Werkzeuge*) benutzt habe. Sämtliche wörtlichen oder sinngemäßen Übernahmen und Zitate sind kenntlich gemacht und nachgewiesen.

Im Anhang „Nutzung KI-Tools“ habe ich die verwendeten KI-Tools dokumentiert.

Mit Abgabe der vorliegenden Leistung übernehme ich die Verantwortung für das eingereichte Gesamtprodukt. Ich verantworte damit auch jegliche KI-generierten Inhalte, die ich in meine Arbeit übernommen habe. Die Richtigkeit übernommener (KI-generierter) Aussagen und Inhalte habe ich nach bestem Wissen und Gewissen geprüft.

Ich habe die Arbeit nicht zum Erwerb eines anderen Leistungsnachweises in gleicher oder ähnlicher Form eingereicht.

Mir ist bekannt, dass ein Verstoß gegen die genannten Punkte prüfungsrechtliche Konsequenzen hat.

Mainz, den [Datum] [Unterschrift]

* Weiterführende Informationen zu KI-basierte Anwendungen oder Werkzeuge unter: `https://digitale-lehre.uni-mainz.de/lehren-pruefen/ki-in-der-hochschulbildung/`

Nutzung KI-Tools

KI-Tool	Genutzt für	Warum	Wann bzw. Wo
Cellpose	Detektion von Schaumbläschen	Präzise Bestimmung der Bläschengröße	Analyse der Mikroskopiebilder zur Bestimmung der Bläschengröße in Kapitel 3.6 und 6 wie im Methodenteil beschrieben
ChatGPT	Unterstützung bei der Kommentierung von Python Code	Vereinheitlichung des Stils der Kommentare	Appendix A
DeepL Translate	Übersetzung einzelner Wörter oder Wortgruppen (Wörterbuch)	Wortfindung, zum Vergleich mit anderen Online-Wörterbüchern	Punktuelle Unterstützung beim Verfassen der Thesis
DeepL Write	Zusätzliche Formulierungsoptionen einzelner Teilsätze oder Sätze	Bessere Lesbarkeit	Punktuelle Unterstützung beim Überarbeiten der Texte